

Measurement of elastic proton–proton scattering at $\sqrt{s} = 7$ TeV with the ALFA sub-detector of ATLAS at the LHC

Messung elastischer Proton–Proton Streuung bei $\sqrt{s} = 7$ TeV mit dem ALFA Teildetektor von ATLAS am LHC

Dissertation zur Erlangung des Doktorgrades der Naturwissenschaften

im Fachbereich 07 (Mathematik und Informatik, Physik, Geographie)
der Justus-Liebig-Universität Gießen

vorgelegt von

Kristof Kreuzfeldt

aus Schotten

II. Physikalisches Institut
Justus-Liebig-Universität Gießen

15. Dezember 2014

There is a theory which states that if ever anyone discovers exactly what the Universe is for and why it is here, it will instantly disappear and be replaced by something even more bizarre and inexplicable.

There is another theory which states that this has already happened.

— Douglas Adams, *The Restaurant at the End of the Universe*

Abstract

The ATLAS experiment with the ALFA sub-detector, provides a unique opportunity to measure elastic proton–proton scattering at the LHC at a centre-of-mass energy of $\sqrt{s} = 7$ TeV, that has never been reached before. The ALFA detector is a tracking detector housed in Roman Pots, which makes it possible to measure elastically scattered protons down to very small scattering angles. From the proton tracks, measured during a LHC fill with special $\beta^* = 90$ m beam optics, the differential elastic cross-section as a function of the four-momentum transfer squared t is determined, and the total hadronic cross-section σ_{tot} , the nuclear slope parameter B and further derived quantities are extracted by utilizing the optical theorem. The total hadronic cross-section is a fundamental parameter of strong interaction depending on the centre-of-mass energy. It has been measured for more than 50 years at different energies and accelerators, where a rise with energy was observed.

A newly developed fully data-driven method is used to determine the t -independent event reconstruction efficiency in the two spectrometer arms to be $\varepsilon_{\text{rec}}(\text{Arm 1368}) = 0.8974 \pm 0.0005$ (stat.) ± 0.0061 (syst.) and $\varepsilon_{\text{rec}}(\text{Arm 2457}) = 0.8800 \pm 0.0005$ (stat.) ± 0.0092 (syst.) by carefully selecting elastic-scattering events not reconstructed in the entire ALFA detector. Special care is also taken of other important aspects of the analysis like the determination of the luminosity and beam optics parameters.

An integrated luminosity of $\mathcal{L} = 80 \mu\text{b}^{-1}$ is accumulated to measure the differential elastic cross-section from which the total hadronic cross-section is extracted from a fit in the range $0.01 \text{ GeV}^2 \leq -t \leq 0.1 \text{ GeV}^2$ to be $\sigma_{\text{tot}} = 95.35 \pm 0.38$ (stat.) ± 1.25 (exp.) ± 0.37 (extr.) mb. In addition, the nuclear slope parameter at small $|t|$ is determined to be $B = 19.73 \pm 0.14$ (stat.) ± 0.26 (syst.) GeV^{-2} .

Zusammenfassung

Das ATLAS Experiment mit dem ALFA Subdetektor, bietet die einmalige Gelegenheit elastische Proton-Proton Streuung am LHC bei einer Schwerpunktsenergie von $\sqrt{s} = 7$ TeV, die niemals zuvor erreicht wurde, zu messen. Der ALFA Detektor ist ein in Roman Pots untergebrachter Spurdetektor, mit dem es möglich ist elastisch gestreute Protonen bis hin zu sehr kleinen Streuwinkeln zu messen. Aus den Protonenspuren, die während eines speziellen LHC Fills mit $\beta^* = 90$ m gemessen wurden, wird der differenzielle elastische Wirkungsquerschnitt als Funktion des quadratischen Viererimpulsübertrags t bestimmt und daraus der totale hadronische Wirkungsquerschnitt σ_{tot} , der nukleare Steigungsparameter B und weitere abgeleitete Größen entnommen, indem das optische Theorem angewendet wird. Der totale hadronische Wirkungsquerschnitt ist ein elementarer Parameter der starken Wechselwirkung, der von der Schwerpunktsenergie abhängt. Er wurde in den letzten 50 Jahren an unterschiedlichen Beschleunigern und in verschiedenen Energiebereichen gemessen, wobei ein Anstieg mit der Energie beobachtet wurde.

Ein neu entwickelter, rein datenbezogener Ansatz wird benutzt, um die nicht von t abhängige Event-Rekonstruktionseffizienz in den beiden Spektrometerarmen zu $\varepsilon_{\text{rec}}(\text{Arm 1368}) = 0.8974 \pm 0.0005$ (stat.) ± 0.0061 (syst.) und $\varepsilon_{\text{rec}}(\text{Arm 2457}) = 0.8800 \pm 0.0005$ (stat.) ± 0.0092 (syst.) zu bestimmen, wobei elastische Streueignisse, die nicht im kompletten ALFA Detektor rekonstruiert wurden, sorgfältig ausgewählt werden. Außerdem werden andere wichtige Teile der Analyse wie die Luminosität und Strahloptikparameter besonders gewissenhaft bestimmt.

Es ist eine integrierte Luminosität von $\mathcal{L} = 80 \mu\text{b}^{-1}$ angesammelt worden, um den differenziellen elastischen Wirkungsquerschnitt zu messen und daraus den totalen hadronischen Wirkungsquerschnitt mit einem Fit im Bereich $0.01 \text{ GeV}^2 \leq -t \leq 0.1 \text{ GeV}^2$ zu $\sigma_{\text{tot}} = 95.35 \pm 0.38$ (stat.) ± 1.25 (exp.) ± 0.37 (extr.) mb zu extrahieren. Außerdem wird der nukleare Steigungsparameter im Bereich kleiner $|t|$ zu $B = 19.73 \pm 0.14$ (stat.) ± 0.26 (syst.) GeV^{-2} bestimmt.

Contents

List of abbreviations	iii
1 Introduction	1
2 Elastic scattering	3
2.1 Kinematics and conventions	3
2.2 Elastic hadronic scattering in the presence of the Coulomb field	4
2.2.1 ρ parameter	7
2.2.2 Electromagnetic form factor	8
2.2.3 Coulomb phase	8
2.2.4 Nuclear scattering amplitude	9
2.3 Measurement of σ_{tot} and B from elastic scattering	11
3 Experimental setup	13
3.1 CERN and the LHC	13
3.2 The ATLAS experiment	15
3.2.1 Luminosity and Forward detectors	19
3.2.2 The ALFA detector	22
3.2.3 Coordinate systems and naming conventions	26
3.3 Data taking	28
3.3.1 Beam configuration and detector set-up	28
3.3.2 Trigger conditions and data streams	29
3.4 Track reconstruction	31
3.4.1 Tracking algorithm	32
3.4.2 Track matching	34
3.4.3 Alignment	37
4 Beam optics and t-reconstruction	43
4.1 Transverse beam dynamics	43
4.2 $\beta^* = 90$ m design beam optics	48
4.3 t -reconstruction	50
5 Monte Carlo simulations	55
5.1 Fast simulation	56
5.2 Full simulation	57
5.3 Tuning and comparison with data	58
6 Data analysis	63
6.1 Elastic-scattering event selection	64
6.1.1 Fiducial cuts	65
6.1.2 Left-right collinearity cuts	67
6.1.3 Position-angle correlation cut	68
6.1.4 Characteristics of elastic-scattering events	69
6.2 Background estimation	73
6.3 Event reconstruction efficiency	77
6.3.1 Definition	77
6.3.2 Event selection and Tag-and-probe	79

Contents

6.3.3	3/4	80
6.3.4	2/4	84
6.3.5	1+1/4	91
6.3.6	1/4	95
6.3.7	0/4	97
6.3.8	Systematic uncertainties	100
6.3.9	Result	106
6.3.10	Comparison with simulation	107
6.4	Acceptance	109
6.5	Unfolding	111
6.6	Luminosity	115
6.7	Effective beam optics	118
6.7.1	ALFA constraints	119
6.7.2	Beam optics fit	123
7	Results	127
7.1	Differential elastic cross-section	127
7.1.1	Systematic uncertainties	128
7.2	Total cross-section and nuclear slope	130
7.2.1	Experimental systematic uncertainties	135
7.2.2	Extrapolation uncertainties	136
7.2.3	Stability checks	137
7.3	Elastic and inelastic cross-section	139
7.4	Discussion	140
8	Summary	145
	Acknowledgement	147
	Bibliography	149
A	Appendix	157
A.1	Additional plots for golden elastic-scattering events	157
A.2	Additional plots for reconstruction case 3/4	160
A.3	Additional plots for reconstruction case 2/4	168
A.4	Additional plots for reconstruction case 1+1/4	174
A.5	Additional plots for reconstruction case 1/4	184
A.6	Additional plots for reconstruction case 0/4	190
A.7	Additional result tables	190

List of abbreviations

ALFA	Absolute Luminosity For ATLAS
ATLAS	A Toroidal LHC Apparatus
Athena	ATLAS offline software framework
BCId	Bunch Crossing Identifier
BCM	Beam Conditions Monitor
BeamCS	Beam Coordinate System
CERN	European Laboratory for Particle Physics (Conseil Européen pour la Recherche Nucléaire)
c.m.	centre-of-mass frame
CNI	Coulomb-nuclear interference
CTP	Central Trigger Processor
DCS	Detector Control System
DetCS	Detector Coordinate System
EM	Electromagnetic
FCal	Liquid argon Forward Calorimeter
ID	Inner Detector
IDS	Iterative Dynamically Stabilized
IP	Interaction Point
KFK	Kohara, Ferreira and Kodama
LAr	Liquid Argon
LB	Luminosity Block
LHC	Large Hadron Collider
LUCID	Luminosity measurement using Cerenkov Integrating Detector
LVDT	Linear Variable Displacement Transducers
MAD-X	Methodical Accelerator Design 10
MBTS	Minimum Bias Trigger Scintillator
MC	Monte Carlo simulation
MD	Main Detector
OD	Overlap Detector

List of abbreviations

PMT	Photomultiplier Tube
QED	Quantum Electrodynamics
QCD	Quantum Chromodynamics
RMS	Root Mean Squared
RP	Roman Pot detector
SPS	Super Proton Synchrotron
SVD	Singular Value Decomposition
TB	Test Beam
TDAQ	Trigger and Data Acquisition
Tile	Tile Calorimeter
TOTEM	Total Cross Section, Elastic Scattering and Diffraction Dissociation at the LHC
ZDC	Zero-Degree Calorimeter

1 Introduction

The LHC, a superconducting pp collider and one of its experiments, the ATLAS detector [1], provide an unique opportunity to study new physics phenomena and precisely measure Standard Model quantities at centre-of-mass energies never reached before. The ATLAS experiment is equipped with the ALFA Roman Pot detector system, which is a type of tracking detector located in the very forward region, to measure elastically scattered protons down to very small scattering angles.

The ALFA detector [2] is initially designed to provide an absolute calibration of the luminosity, whose precise knowledge is needed as a crucial ingredient for almost all measurements performed by ATLAS. It also provides the opportunity to measure the total hadronic cross-section σ_{tot} , which is a fundamental parameter of strong interactions, setting the scale of the size of the interaction region at a given energy. For the time being the total cross-section cannot be calculated from first principle based on quantum chromodynamics (QCD). However, the optical theorem, which is a general theorem in quantum scattering theory, states that a measurement of elastic scattering in the very forward direction gives information on the total cross-section. This is utilized in this thesis, which presents the measurement of the differential cross-section of elastically scattered protons at a centre-of-mass energy of $\sqrt{s} = 7$ TeV, and the extraction of the total cross-section from that measurement.

The total cross-section depends on the centre-of-mass energy \sqrt{s} , and a rise with energy was observed in the past at lower energies at the ISR [3, 4], Sp \bar{p} S [5, 6] and Tevatron [7, 8]. However, there are still open questions, that can possibly be answered, by measuring the total cross-section at the higher energies provided by the LHC. In particular, the Froissart–Martin bound [9, 10], which is based upon principles of axiomatic field theory, states that the total cross-section cannot rise asymptotically faster than $\ln^2 s$. But the actual ‘asymptotic’ energy dependence is yet to be determined. Does the total cross-section indeed rise proportionally to $\ln^2 s$ in order to saturate the bound or has the rise e.g. a $\ln s$ dependence?

A measurement of the differential elastic cross-section also allows to extract the nuclear slope parameter B , which describes the exponential t -dependence of the nuclear scattering amplitude at small $|t|$ -values, where t is the four-momentum transfer squared. In a simple geometrical model of elastic scattering B is related to the size of the proton and thus its energy dependence is strongly correlated with that of the total cross-section. Furthermore, the total elastic and inelastic cross-sections are measured, whereas the latter is considerably more precise than a previous measurement by ATLAS using minimum-bias triggers [11]. Another interesting quantity, that is derived, is the ratio of the total elastic and total hadronic cross-section, which goes in the black disk limit, where the proton is completely opaque, asymptotically to 1/2. And finally all the quantities measured here are compared to measurements by the TOTEM Collaboration [12] at the same centre-of-mass energy.

This thesis is divided into eight sections. In Section 2 the theory of elastic hadronic scattering is introduced. The parametrizations of the differential elastic cross-section are described, which are later used in the analysis to fit the measured spectrum and determine systematic uncertainties. A short overview is given, how the different quantities are extracted from the measurement.

In Section 3 a description of the experimental setup and conditions is given. The LHC and the ATLAS experiment are introduced, and in particular a more detailed overview of the ALFA detector system is given. The elastic-scattering data, analysed in this thesis, was taken in 2011 with special beam conditions also described here. In the third part of this section the

1 Introduction

first more technical stage of the data analysis with the reconstruction of particle tracks in the ALFA detector and the alignment are described.

Section 4 introduces the theoretical formulation of transverse beam optics with the transport matrix, and describes the special high- β^* optics used to measure elastic scattering. The transverse beam optics formulation is also used to derive and discuss four measurement methods to reconstruct the four-momentum transfer squared t of a given elastic-scattering event.

In Section 5 the Monte Carlo simulations used in this thesis are described, which are based on the theoretical formulation of the differential elastic cross-section and the transverse beam optics. They are used for several parts of the analysis, e.g. to determine the acceptance, the unfolding corrections and systematic uncertainties of different sources.

Section 6 is the main part of this thesis. Here the steps are described, which are needed to get from an uncorrected, raw differential t -spectrum to a corrected and normalized differential elastic cross-section. Part of this section are the selection of elastic-scattering events through different cuts, the estimation of the background correction, the determination of acceptance, unfolding corrections and resolutions. Two other crucial parts of the analysis are the determination of the luminosity, which is needed to normalize the differential cross-section, and the determination of effective beam optics from elastic-scattering data, which is needed to correctly reconstruct the four-momentum transfer squared t of each event. Furthermore, the event reconstruction efficiency is most comprehensively described in this section, since it is the author's main contribution to the measurement of the total cross-section. The reconstruction efficiency is determined with a fully data-driven 'tag-and-probe'-like method, developed by the author.

In Section 7 the results and systematic uncertainties of the uncorrected differential t -spectrum, the corrected and normalized differential cross-section, the total cross-section and further derived quantities are described, discussed and compared to measurements of the TOTEM experiment. And finally the measurement is summarized in the last Section 8.

2 Elastic scattering

2.1 Kinematics and conventions

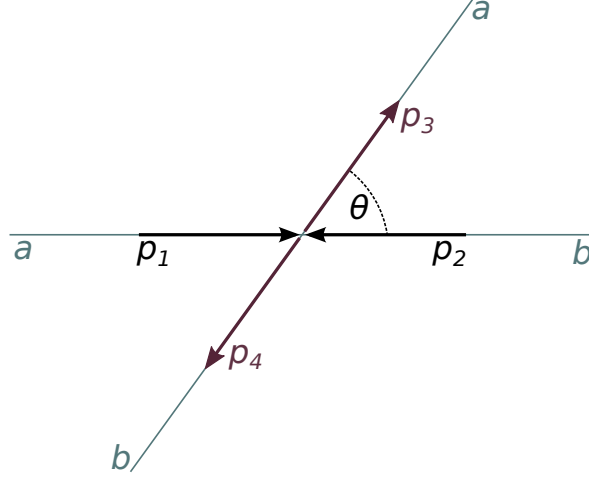


Figure 2.1: Elastic scattering in the centre-of-mass frame.

In the following the elastic hadronic scattering of $a + b \rightarrow a + b$ is described, where the initial state projectile four-momentum of a is p_1 and the initial state target four-momentum of b is p_2 , and the final state four-momentum of a is p_3 and of b is p_4 . This collision is illustrated in Figure 2.1 in the centre-of-mass frame (c.m.). In principle a and b can be protons p or anti-protons \bar{p} , but since the LHC is a proton–proton collider only the case of elastic pp scattering $p + p \rightarrow p + p$ is considered.

The Mandelstam invariant s , the square of the c.m. energy, is given by

$$s = (p_1 + p_2)^2 = m_1^2 + m_2^2 + 2 \left(\sqrt{p^2 + m_1^2} \sqrt{p^2 + m_2^2} + p^2 \right), \quad (1)$$

where p is the magnitude of the c.m. three-momentum \vec{p} (beam momentum). Since for pp scattering $m_1 = m_2 = m$ is the proton mass, one finds

$$s = 4(p^2 + m^2). \quad (2)$$

The invariant four-momentum transfer squared t is given by

$$t = (p_1 - p_3)^2 = -4p^2 \sin^2 \frac{\theta}{2}, \quad (3)$$

where θ is the c.m. scattering angle (see Figure 2.1). And for small values of $|t|$ in high-energy approximation (forward scattering) the four-momentum transfer reduces to

$$t \approx -(p\theta)^2. \quad (4)$$

The third Mandelstam invariant u is finally given by

$$u = (p_1 - p_4)^2 \quad (5)$$

and one gets

$$s + t + u = 4m^2. \quad (6)$$

2 Elastic scattering

In the following units with $\hbar = c = 1$ are used. Two elastic scattering amplitudes with different normalizations are considered. The c.m. amplitude f is given by the differential cross-sections

$$\frac{d\sigma}{d\Omega_{\text{c.m.}}} = |f|^2, \quad (7)$$

$$\frac{d\sigma}{dt} = \frac{\pi}{p^2} |f|^2 \quad (8)$$

and the optical theorem (see for example Reference [13])

$$\sigma_{\text{tot}} = \frac{4\pi}{p} \text{Im} f(\theta \rightarrow 0), \quad (9)$$

where $\sigma_{\text{tot}} = \sigma_{\text{elastic}} + \sigma_{\text{inelastic}}$ is the total hadronic cross-section of $p + p \rightarrow X$ and $f(\theta \rightarrow 0)$ is the elastic-scattering amplitude extrapolated to the forward direction, i.e. at $\theta \rightarrow 0$ and $t \rightarrow 0$ respectively.

And secondly the amplitude F is given by the properties

$$\frac{d\sigma}{dt} = |F|^2 \quad (10)$$

and

$$\sigma_{\text{tot}} = 4\sqrt{\pi} \text{Im} F(t \rightarrow 0). \quad (11)$$

The two amplitudes are related by

$$f = \frac{p}{\sqrt{\pi}} F \quad (12)$$

and they are interchangeably used whenever convenient.

2.2 Elastic hadronic scattering in the presence of the Coulomb field

At first the effects of either a Coulombic or hadronic field alone are considered separately. Later these fields are combined to act simultaneously. For elastic pp Coulomb scattering a ‘spinless’ ansatz is used [14], without considering magnetic scattering, since this is what experiments typically used in the past. The relevant Feynman diagram is shown in Figure 2.2, with $V^\mu = G(p_i + p_f)^\mu$, where $G(t)$ is the electromagnetic charge form factor of the proton, and the electromagnetic differential cross-section is readily evaluated as

$$\frac{d\sigma_{\text{C}}}{dt} = \pi \left| \frac{-2\alpha G^2(t)}{\beta_{\text{lab}} |t|} \left(1 - \frac{|t|}{4mE_{\text{lab}}} \right) \right|^2, \quad (13)$$

where $\alpha \approx 1/137$ is the electromagnetic coupling constant and β_{lab} and E_{lab} are the speed and energy of the initial projectile proton in the laboratory frame. For forward scattering at high energies, the correction term $|t|/(4mE_{\text{lab}})$ becomes negligible and $\beta_{\text{lab}} \rightarrow 1$. Hence Equation (13) goes over into the well-known Rutherford scattering formula

$$\frac{d\sigma_{\text{C}}}{dt} = \pi \left| \frac{-2\alpha G^2(t)}{|t|} \right|^2, \quad (14)$$

2.2 Elastic hadronic scattering in the presence of the Coulomb field

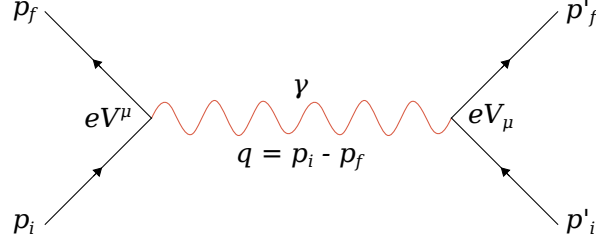


Figure 2.2: One-photon Feynman diagram for elastic pp Coulomb scattering, $p_i + p'_i \rightarrow p_f + p'_f$, with couplings eV^μ and eV_μ .

where the electromagnetic charge form factor $G(t)$ is commonly parametrized by the dipole form [15]

$$G(t) = \left(\frac{\Lambda^2}{\Lambda^2 + |t|} \right)^2, \quad (15)$$

with $\Lambda^2 = 0.71 \text{ GeV}^2$. Thus the 'spinless' Coulomb amplitude $F_C(t)$, which is generally used in analyses, is given in the notation of Equation (10) by

$$F_C(t) = -\frac{2\sqrt{\pi}\alpha G^2(t)}{|t|}. \quad (16)$$

For the nuclear (hadronic) elastic scattering cross-section in the small $|t|$ -region previous experiments have shown [8, 16, 17], that it can be adequately parametrized with a simple exponential by

$$\frac{d\sigma_N}{dt} = \left[\frac{d\sigma_N}{dt} \right]_{t=0} e^{-B|t|}. \quad (17)$$

Hence, if one plots $\ln(d\sigma_N/dt)$ as a function of $|t|$ for small $|t|$, one obtains a straight line whose slope is B , the nuclear slope parameter. With Equations (7), (8) and the optical theorem (9) one can write the differential cross-section at $t = 0$ as

$$\left[\frac{d\sigma_N}{dt} \right]_{t=0} = \frac{\pi}{p^2} \left[\frac{d\sigma_N}{d\Omega_{\text{c.m.}}} \right]_{\theta=0} \quad (18)$$

$$= \frac{\pi}{p^2} |\text{Re } f(0) + i \text{Im } f(0)|^2 \quad (19)$$

$$= \pi \left| \frac{(\rho + i) \text{Im } f(0)}{p} \right|^2 \quad (20)$$

$$= \pi \left| \frac{(\rho + i) \sigma_{\text{tot}}}{4\pi} \right|^2, \quad (21)$$

where the parameter $\rho = \frac{\text{Re } f(0)}{\text{Im } f(0)}$ is introduced. Therefore, one can now write the elastic hadronic scattering cross-section at small $|t|$ as

$$\frac{d\sigma_N}{dt} = \pi \left| (\rho + i) \frac{\sigma_{\text{tot}}}{4\pi} e^{-B|t|/2} \right|^2. \quad (22)$$

And finally the nuclear scattering amplitude in the notation of Equation (10) is given by

$$F_N(t) = (\rho + i) \frac{\sigma_{\text{tot}}}{4\sqrt{\pi}} e^{-B|t|/2}. \quad (23)$$

2 Elastic scattering

These results treat the case of only one interaction at a time. However, the simultaneous presence of both the nuclear and Coulomb fields, although coherent, does not allow for a simple superimposition of the amplitudes $F_N(t)$ and $F_C(t)$. Instead a phase factor $\alpha\phi(t)$ has to be introduced into the Coulomb amplitude, such that the complete differential elastic cross-section is given by

$$\frac{d\sigma}{dt} = \left| F_C(t)e^{i\alpha\phi(t)} + F_N(t) \right|^2 \quad (24)$$

$$= \pi \left| -\frac{2\alpha G^2(t)}{|t|} e^{i\alpha\phi(t)} + (\rho + i) \frac{\sigma_{\text{tot}}}{4\pi} e^{-B|t|/2} \right|^2, \quad (25)$$

where implicitly is assumed, that ρ varies negligibly over the very small $|t|$ -region. The phase factor $\alpha\phi(t)$ reflects the distortion of the pure amplitudes $F_N(t)$ and $F_C(t)$ due to the simultaneous presence of both hadronic and Coulombic scattering. This can be nicely understood by using the language of Feynman diagrams, in which $F_N(t)$ corresponds to summing over all diagrams in which only hadronic exchanges are present, and $F_C(t)$ corresponds to summing all diagrams in which only photons are present. Simply summing $F_N(t)$ and $F_C(t)$ and squaring would now miss all of those mixed diagrams, in which both photons and hadronic exchanges are present. This problem is solved by the introduction of the phase $\phi(t)$, which was first investigated by Bethe [18] and later by West and Yennie [19], who used quantum electrodynamics (QED) calculations of Feynman diagrams. For the fit of the differential elastic cross-section later in the analysis the calculation of West and Yennie is used, given by

$$\phi(t) = - \left\{ \gamma_E + \ln \left(\frac{B|t|}{2} \right) \right\}, \quad (26)$$

where $\gamma_E = 0.577 \dots$ is Euler's constant. Using these parametrizations the complete form of the differential elastic cross-section is

$$\frac{d\sigma}{dt} = \frac{d\sigma_C}{dt} + \frac{d\sigma_{\text{CNI}}}{dt} + \frac{d\sigma_N}{dt} \quad (27)$$

$$= \frac{4\pi\alpha^2}{t^2} G^4(t) - \sigma_{\text{tot}} \frac{\alpha G^2(t)}{|t|} [\rho + \alpha\phi(t)] e^{-B|t|/2} + \sigma_{\text{tot}}^2 \frac{1 + \rho^2}{16\pi} e^{-B|t|}. \quad (28)$$

This form is later used to fit the measured differential elastic cross-section to extract σ_{tot} and B . The differential cross-section is shown in Figure 2.3 in the CNI region for values of $\sigma_{\text{tot}} = 95 \text{ mb}$ and $B = 19.5 \text{ GeV}^{-2}$. Also shown are the Coulomb and nuclear terms and the (negative) CNI term mirrored at the horizontal axis for illustration purposes. For the fit several inputs are needed: the parametrization of the electromagnetic form factor $G(t)$, the Coulomb phase $\phi(t)$, the nuclear scattering amplitude $F_N(t)$ and the value of the ρ parameter, which are discussed in the following sub-sections.

The differential cross-section is split into three terms given by Equation (27): the Coulomb term, the Coulomb-nuclear interference (CNI) term and the nuclear term. The importance of the CNI term is maximal when $|F_C(t)| = |F_N(t)|$ i.e. when $d\sigma_C/dt = d\sigma_N/dt$. For pp scattering the interference is destructive. Assuming σ_{tot} is known, the presence of the CNI term allows the measurement of the ρ parameter. Inspecting Equation (25) indicates, that the CNI term is of maximum significance when

$$|t_{\text{CNI}}| \approx \frac{8\pi\alpha}{\sigma_{\text{tot}}}, \quad (29)$$

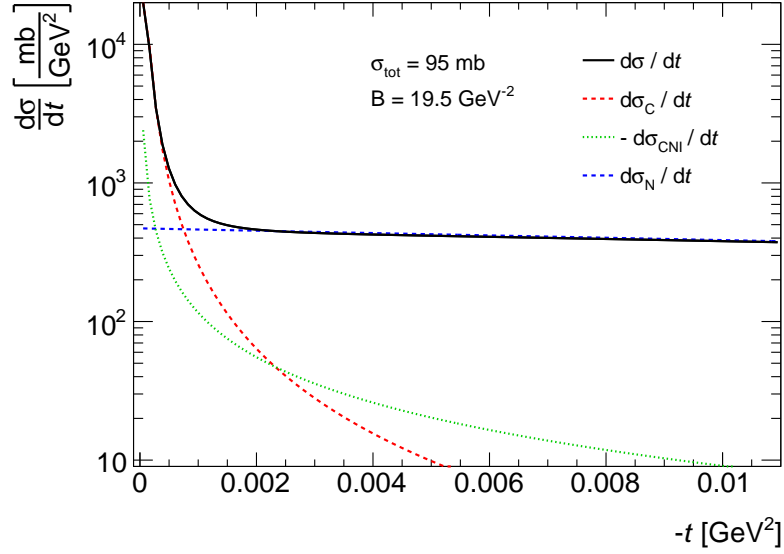


Figure 2.3: Theoretical form of the differential elastic cross-section $d\sigma/dt$ for $\sigma_{\text{tot}} = 95$ mb and $B = 19.5$ GeV^{-2} in the CNI region $|t_{\text{CNI}}| \approx 0.0018$ GeV^2 . In addition the Coulomb, nuclear and CNI term are shown alone. The CNI term is normally negative for pp scattering and therefore mirrored at the horizontal axis.

where σ_{tot} is in mb and t_{CNI} in GeV^2 . The differential elastic cross-section given by Equation (28) divides up naturally into three distinct t regions. In the first region for $|t| \ll |t_{\text{CNI}}|$ the Coulomb scattering dominates and $d\sigma/dt$ goes nearly as $1/t^2$. The second region for $|t| \simeq |t_{\text{CNI}}|$ is the CNI region. And in the third region for $|t| \gg |t_{\text{CNI}}|$ the nuclear scattering dominates and $d\sigma/dt$ goes nearly as $e^{-B|t|}$.

2.2.1 ρ parameter

As input for the fit of $d\sigma/dt$ the ρ value is needed. It can be inferred from lower energy elastic scattering data available for various initial state particles. Usually this is done analytically from dispersion relations and an explicit parametrization of the energy evolution of the total cross-section in a given model. Such a global fit was performed by COMPETE [20, 21] yielding a value of $\rho = 0.1403 \pm 0.0016$, where the uncertainty accounts only for the fit uncertainty of the model parameters. Further systematic uncertainties attributed to the choice of the model are addressed in Reference [22], where a possible range as large as ± 0.04 is indicated. New global fits were done by the COMPAS IHEP Protvino group [23], which include new cosmic ray data and the first TOTEM results [17], and use the COMPETE global fit framework. Their best fit yields $\rho = 0.1326$, but it has been criticized that the new fit underestimates the total cross-section measurement by TOTEM. Therefore, an alternative global fit was performed in Reference [24] which results in a value of $0.1403 \leq \rho \leq 0.1432$ with an uncertainty of ± 0.005 . A summary of several estimates of ρ is given in Table 2.1.

In the analysis and fit of $d\sigma/dt$ an estimate of $\rho = 0.140 \pm 0.008$ is used, where the uncertainty is taken from the difference between the COMPETE and COMPAS estimates. This choice appears to be safe, because of the model dependence of the global fits and their sensitivity to the included data sets, as recently observed in the significant change of COMPETE/COMPAS results.

Table 2.1: Summary of ρ parameter estimates.

Model	ρ	Reference
COMPETE 2005	0.1403 to 0.1420	[20, 21]
Multi-pole pomeron	0.1060 to 0.1860	[22]
COMPAS 2012	0.1326	[23]
\ln^γ	0.1403 to 0.1432	[24]

2.2.2 Electromagnetic form factor

As stated before the electromagnetic charge form factor of the proton $G(t)$ is commonly parametrized as a dipole [15] like in Equation (15). However, measurements of low energy elastic ep scattering [25] indicate a deviation from the dipole form at the level of a few percent. Recently high precision data were recorded by the A1 experiment [26] at the Mainz electron accelerator (MAMI). Both the electric and magnetic form factor $G_E(t)$ and $G_M(t)$ were re-analysed, and a large variety of models and parametrizations were fit to their data. The resulting electromagnetic form factors are shown in Figure 2.4 (left) in the t -range accessible in the measurement presented in this thesis. Deviations between the new models and the dipole parametrization increase with larger $|t|$ and reach a maximum of about 4%. The largest difference is observed for the double dipole form while the other models are quite similar. This difference between dipole and double dipole is used as an conservative estimate of the form factor uncertainty. Since the Coulomb and CNI terms—where $G(t)$ enters—only contribute to $d\sigma/dt$ at the percent level in the accessible t -range even such a conservative estimate is at the limit of the sensitivity of the cross-section measurement.

2.2.3 Coulomb phase

For the fit of the differential elastic cross-section the parametrization of the Coulomb phase $\phi(t)$ from West and Yennie, as written in Equation (26), is used. Other different parametrizations of the phase are considered when the Coulomb and nuclear amplitudes are combined to estimate the uncertainty and impact on the fit. An approach of Cahn [15] was to evaluate the phase using an eikonal formulation given by

$$\phi(t) = - \left\{ \gamma_E + \ln \left(\frac{B|t|}{2} \right) + \ln \left(1 + \frac{8}{B\Lambda^2} \right) + \frac{4|t|}{\Lambda^2} \ln \left(\frac{4|t|}{\Lambda^2} \right) + \frac{2|t|}{\Lambda^2} \right\}, \quad (30)$$

which extends the calculation by West and Yennie with further terms. Furthermore, another model was proposed recently by Kohara, Ferreira and Kodama (KFK) [27], where different slopes are considered for real and imaginary amplitudes. The relevant model parameters are fit to measurements from TOTEM [17, 28] and an approximate expression for the real phase is given by

$$\phi_R(s, t) = - \left\{ \ln \frac{-t}{s} + \frac{1}{c^2 + 1} [c^2 I(B_R) + I(B_I)] \right\} \quad (31)$$

with

$$I(B) = \int_{-4p^2}^0 \frac{dt'}{|t' - t|} \left[1 - e^{B(t' - t)/2} \right] \quad (32)$$

$$= E_1 \left[\frac{B}{2} (4p^2 + t) \right] - E_i \left[-\frac{Bt}{2} \right] + \ln \left[\frac{B}{2} (4p^2 + t) \right] + \ln \left[-\frac{Bt}{2} \right] + 2\gamma_E \quad (33)$$

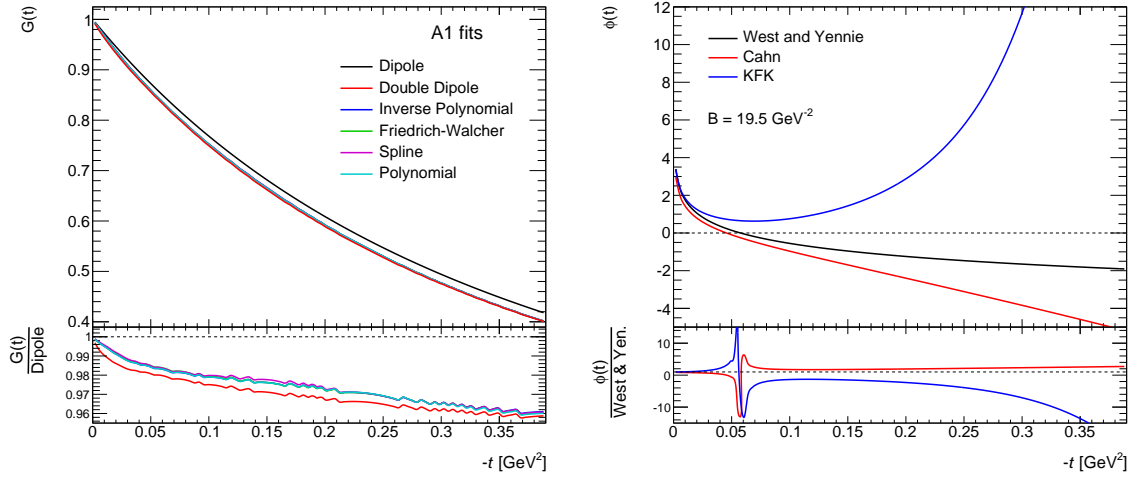


Figure 2.4: The left plot shows different parametrizations of the electromagnetic form factor of the proton $G(t)$ obtained by the A1 collaboration [26], and the bottom part shows the ratio of the models to the nominal dipole parametrization.

The right plot shows different calculations of the Coulomb phase $\phi(t)$, and the bottom part shows the ratio of the models to the nominal parametrization from West and Yennie.

and

$$c = \rho e^{(B_R - B_I)t/2}, \quad (34)$$

where $B_I = B$ is the (imaginary) nuclear slope, $B_R = 30.2 \text{ GeV}^2$ was fit by KFK and $E_{1,i}$ are exponential integral functions [29].

The different phase calculations as a function of t are compared in Figure 2.4 (right). All three models agree at small $|t|$, but substantial discrepancies appear with increasing $|t|$, in particular for the KFK model. Therefore the difference between Cahn and KFK is taken as a conservative estimate of the uncertainty related to the t -dependence of the Coulomb phase $\phi(t)$. Since the Coulomb phase only enters in the CNI term, which is small compared to the nuclear term in the relevant t -region, the impact on the fit result is at the limit of the sensitivity, although the difference is large at larger $|t|$.

2.2.4 Nuclear scattering amplitude

The nuclear scattering amplitude is parametrized in Equation (23) by a simple exponential with constant nuclear slope B . This is only an approximation for small $|t|$ values, since there is experimental evidence at larger $|t|$ in $d\sigma/dt$ of an increasing slope before a diffractive minimum, the so called ‘dip’. The position of this dip depends on the centre-of-mass energy \sqrt{s} and moves towards smaller $|t|$ with increasing energy. At LHC energies the dip position is around $t = -0.5 \text{ GeV}^2$ as seen by TOTEM [30] and shown in Figure 2.5.

Later the measured differential elastic cross-section is fit with Equation (28), which uses the simple exponential model for the nuclear amplitude. Several other models predict a t -dependent slope and have been used to fit $d\sigma/dt$ in a range extended to larger $|t|$. A detailed analysis of these models is not possible here, but to study the dependence of the extracted total cross-section on the simple exponential model several empirical parametric forms, decoupled from actual models, are considered, which involve additional parameters supposed to model the larger $|t|$ region (compare Section 7.2.3).

2 Elastic scattering

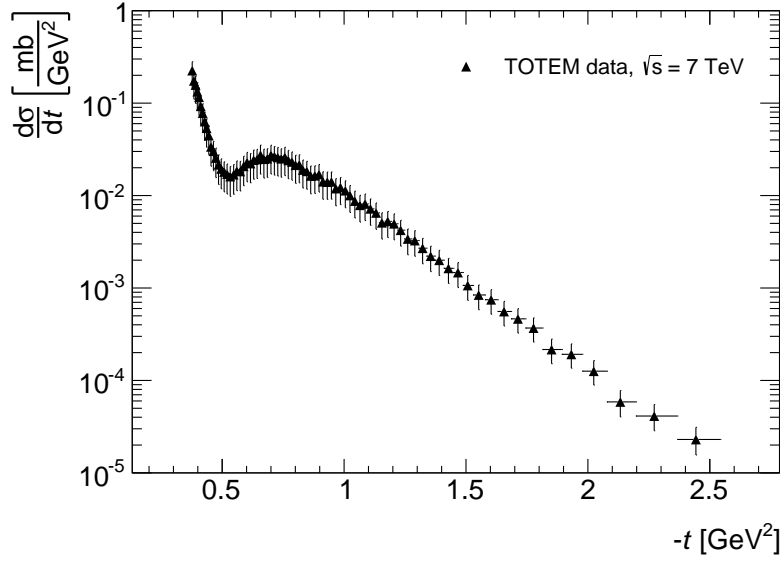


Figure 2.5: Differential elastic cross-section $d\sigma/dt$ in the larger $|t|$ region as measured by TOTEM at $\sqrt{s} = 7$ TeV at the LHC in 2011 [30]. The diffractive minimum is visible at $-t \approx 0.5$ GeV². The error bars represent total uncertainties.

A simple extension, which provides a t -dependent slope, consists of an additional term in the exponential with a dependence on t^2 , accounting for a possible slope change, given by

$$F_N(t) = (\rho + i) \frac{\sigma_{\text{tot}}}{4\sqrt{\pi}} e^{-B|t|/2 - Ct^2/2}, \quad (35)$$

where C is an additional fit parameter. Such an extension was previously used in experiments [7] and discussed in theory by West and Yennie [19] and Block and Cahn [31].

Another extension was recently proposed by Selyugin [32], which considers hadron spin non-flip amplitudes to a non-exponential form, given by

$$F_N(t) = (\rho + i) \frac{\sigma_{\text{tot}}}{4\sqrt{\pi}} e^{-Bt/2 - c(\sqrt{4\mu^2 - t} - 2\mu)/2}, \quad (36)$$

where μ is taken to be the pion mass m_π and c is an additional fit parameter.

A third extension was proposed by KFK [27] which assumes constant but possibly different slopes for the real and imaginary amplitudes separately, given by

$$F_N(t) = \rho \frac{\sigma_{\text{tot}}}{4\sqrt{\pi}} e^{-B_R t/2} + i \frac{\sigma_{\text{tot}}}{4\sqrt{\pi}} e^{-B_I |t|/2}, \quad (37)$$

where B_R and B_I are the real and imaginary nuclear slopes as introduced by Equation (31) which are both fit parameters. This form of the nuclear amplitude reduces to the simple exponential form for $B_R = B_I = B$.

The three forms above are to be used in union with the Coulomb phase ϕ . Another possibility is to use a parametrisation with even more model-independent parametric forms, absorbing to some extent Coulomb effects. Such a form was proposed by Phillips and Barger [33] and recently applied to analysis of LHC data [34], given by

$$F_N(t) = i \left[G^2(t) \sqrt{A} e^{-Bt/2} + e^{i\Phi} \sqrt{C} e^{-Dt/2} \right], \quad (38)$$

where the first exponential with amplitude \sqrt{A} and slope B is modified by the electromagnetic form factor of the proton $G(t)$, and between the first and second exponential with amplitude \sqrt{C} and slope D a relative phase Φ is introduced. These are in total five free parameters, and with the fully parametric amplitude normalisation the total cross-section is obtained from the evaluation of the fitted form at $t = 0$, which has a finite value in absence of the Coulomb term.

The last parametrisation considered here is also a model-independent one with even more free parameters as proposed by Bourrely, Soffer and Wu [35]. It consists of symmetric expressions for real and imaginary amplitudes, given by

$$\text{Re } F_{\text{N}}(t) = c_1(t_1 + t)e^{-b_1 t/2} \quad (39)$$

$$\text{Im } F_{\text{N}}(t) = c_2(t_2 + t)e^{-b_2 t/2}, \quad (40)$$

where each amplitude is multiplied by a term linear in t with an offset t_1, t_2 , and has its own normalisation c_1, c_2 and exponential slope b_1, b_2 , yielding in total six free parameters.

2.3 Measurement of σ_{tot} and B from elastic scattering

In experiments, just as in the measurement described in this thesis, cross-sections are not directly measured, but counting rates are the measured quantities. Therefore, in an elastic scattering experiment the differential counting rate $\Delta\dot{N}(t)$ at t is determined, i.e. the number of counts per second per Δt in a small interval Δt (bin size) around t , after corrections for background and inefficiencies such as dead-time, acceptance, etc. This rate has to be normalized in order to obtain the differential elastic nuclear slope $d\sigma_{\text{el}}/dt$ by

$$\Delta\dot{N}(t) = \mathcal{L} \left(\frac{d\sigma_{\text{el}}}{dt} \right), \quad (41)$$

where \mathcal{L} is a normalization factor with units of $(\text{area})^{-1} \times (\text{time})^{-1}$, which is for colliding beam experiments like ATLAS at the LHC, equal to the instantaneous luminosity at the interaction point.

If the experiment is able to reach the Coulomb region $|t| \ll |t_{\text{CNI}}|$, then $d\sigma_{\text{el}}/dt$ is given by the differential Coulomb cross-section from Equation (27) $d\sigma_{\text{C}}/dt \approx 4\pi(\alpha/t)^2$. This self-normalization of the experiment allows one to obtain \mathcal{L} directly from Equation (41). Unfortunately this was not possible in the measurement presented in this thesis, and the luminosity had to be directly calibrated by means of van-der-Meer scans (see Section 6.6). If \mathcal{L} is known, one can go to the nuclear region where $|t| \gg |t_{\text{CNI}}|$, and plot the logarithms of the counting rates against $-t$. A straight line can be fit to the data and extrapolated to $-t = 0$ to obtain the hadronic counting rate $\Delta\dot{N}(0)$, also called the optical point. And with Equations (17), (21) and (41) one can write

$$\sigma_{\text{tot}}^2 = \frac{16\pi}{1 + \rho^2} \left(\frac{d\sigma_{\text{N}}}{dt} \right)_{t=0} = \frac{16\pi}{1 + \rho^2} \frac{\Delta\dot{N}(0)}{\mathcal{L}} \quad (42)$$

to obtain the total cross-section, where the Coulomb scattering amplitude is neglected since $|t| \gg |t_{\text{CNI}}|$. This technique is called the ‘luminosity-dependent’ method, which needs a separate direct measurement of the luminosity. For the measurement presented in this thesis this method is used.

2 Elastic scattering

Another important technique for determining the total cross-section is the ‘luminosity-independent’ method, where one has to simultaneously measure $\dot{N}_{\text{tot}} = \dot{N}_{\text{elastic}} + \dot{N}_{\text{inelastic}}$, the total counting rate due to any interaction, together with $\Delta\dot{N}(0)$:

$$\Delta\dot{N}(0) = \mathcal{L} \left(\frac{d\sigma_{\text{N}}}{dt} \right)_{t=0}, \quad (43)$$

$$\dot{N}_{\text{tot}} = \mathcal{L}\sigma_{\text{tot}}. \quad (44)$$

With Equations (42) and (43) one finds and substitutes \mathcal{L} in Equation (44) to obtain

$$\sigma_{\text{tot}} = \frac{16\pi}{1 + \rho^2} \frac{\Delta\dot{N}(0)}{\dot{N}_{\text{tot}}}. \quad (45)$$

Both of these methods only weakly depend on ρ when ρ is small—a very good approximation for high energies—so very inaccurate measurements of ρ still can yield a highly accurate measurement of σ_{tot} .

Using only the parametrization of the nuclear term in Equation (17) together with (42), the total elastic cross-section σ_{el} is given by

$$\sigma_{\text{el}} = \int_{-\infty}^0 \frac{d\sigma_{\text{N}}}{dt} dt \quad (46)$$

$$= \int_0^{\infty} \left(\frac{d\sigma_{\text{N}}}{dt} \right)_{t=0} e^{-B|t|} d|t| \quad (47)$$

$$= \frac{1}{B} \left(\frac{d\sigma_{\text{N}}}{dt} \right)_{t=0} \quad (48)$$

$$= \sigma_{\text{tot}}^2 \frac{1 + \rho^2}{16\pi B}, \quad (49)$$

which can be written in the form

$$\frac{\sigma_{\text{el}}}{\sigma_{\text{tot}}} = \sigma_{\text{tot}} \frac{1 + \rho^2}{16\pi B}. \quad (50)$$

At high energies where ρ is small this essentially says that the ratio of the elastic to the total cross-section $\sigma_{\text{el}}/\sigma_{\text{tot}}$ varies as the ratio of the total cross section to the nuclear slope parameter B . For $s \rightarrow \infty$ the ratio $\sigma_{\text{el}}/\sigma_{\text{tot}}$ asymptotically approaches in many high-energy scattering models [14] the black disk limit with $\sigma_{\text{el}}/\sigma_{\text{tot}} = 1/2$, in which the proton is completely opaque. Thus the ratio σ_{tot}/B also approaches a constant, i.e. σ_{tot} and B have the same dependence on s as $s \rightarrow \infty$.

With the knowledge of σ_{tot} and σ_{el} the total inelastic cross-section can also be determined as

$$\sigma_{\text{inel}} = \sigma_{\text{tot}} - \sigma_{\text{el}}. \quad (51)$$

And finally the nuclear slope parameter B is found by plotting the un-normalized curve $\ln \Delta N(t)$ as a function of $-t$ in the purely hadronic region and extracting the slope of this straight line. Thus the measurement of B does not depend on the normalization with the luminosity \mathcal{L} .

3 Experimental setup

3.1 CERN and the LHC

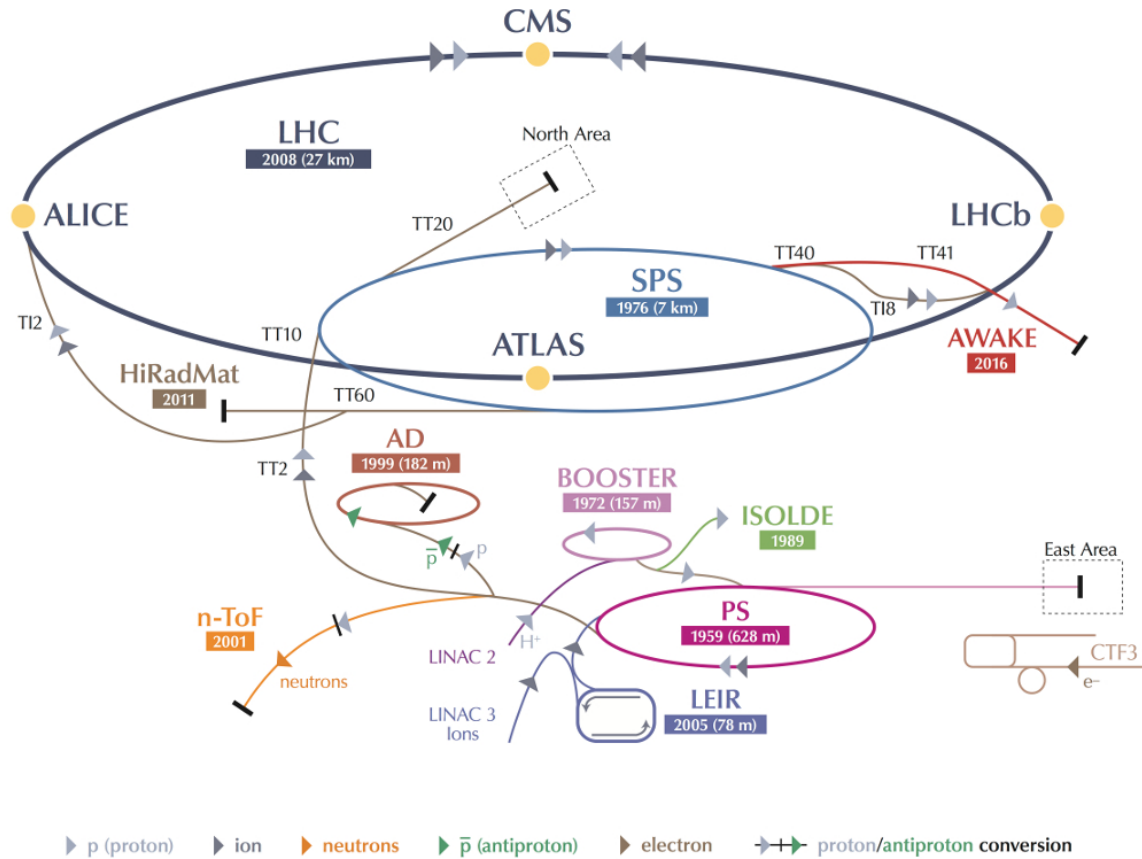


Figure 3.1: The CERN accelerator complex [36]. The colour of the arrows indicates the type of the particle beams.

The European Organisation for Nuclear Research CERN [37] is located near Geneva at the border between Switzerland and France. The organization was founded in 1954 by 12 European countries and currently has 21 member states and about 2400 employees and 10 500 users from about 600 institutes and universities. When CERN was founded its primary research concentrated on nuclear and atomic physics. Today CERN's main focus is particle physics – the study of the fundamental constituents of matter and the forces acting between them – but the physics programme at the laboratory is much broader, ranging from nuclear to high-energy physics, from studies of antimatter to the possible effects of cosmic rays on clouds. Since the beginning CERN housed many different particle accelerators, which provided and still provide high-energy beams for several experiments. Some of the older accelerators were expanded and updated over the years and are used today as injectors for the newer ones or provide beams with lower energies. The current accelerator complex with the Large Hadron Collider (LHC) at the top of the chain and some of the experiments are shown in Figure 3.1. Scientists from all over the world use the particle beams from these accelerators to do research in many different fields. The fundamental mission of CERN is to seek

3 Experimental setup

and find answers to the questions about the universe, to advance the frontiers of technology, to bring nations together through science, and to train the scientists of tomorrow.

The Large Hadron Collider (LHC) is a two-ring-superconducting-hadron accelerator and collider for protons and ions installed in the 26.7 km LEP (Large Electron Positron Collider) tunnel. The tunnel has eight straight sections and eight arcs, and there are two transfer tunnels linking the LHC to the CERN accelerator complex that acts as injector. Being a particle-particle collider, there are two rings with counter-rotating beams, unlike particle-antiparticle colliders that can have both beams sharing the same space in a single ring. The two beams only share a common beam pipe in the straight sections where the experiments are located. Four of the possible eight interaction regions are equipped with experiments: ATLAS at Point 1, CMS (and TOTEM) at Point 5, ALICE at Point 2, and LHCb at Point 8. The layout with the four experiments can be seen in Figure 3.2.

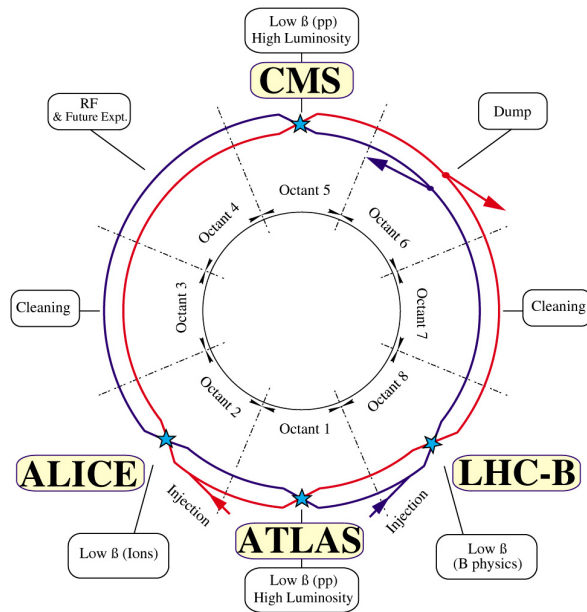


Figure 3.2: Layout of the LHC with the four experiments ATLAS at Point 1, CMS (and TOTEM) at Point 5, ALICE at Point 2, and LHCb at Point 8 [38].

ATLAS and CMS are general purpose detectors and designed for high peak luminosities. ATLAS is described further in Section 3.2. The CMS (Compact Muon Solenoid) experiment is optimized for proton runs and has a classical onion-layer configuration, which aims to cover almost the entire solid angle. Compared to ATLAS the CMS experiment is fairly small with a diameter of 15 m and a length of 21.5 m. It uses a 4 T superconducting solenoid, silicon detectors and a crystal electromagnetic calorimeter.

ALICE (A large Ion Collider Experiment) is designed for heavy ion collisions and also has an onion-layer structure intended to cover the complete solid angle. The main characteristic of ALICE is its large Time Projection Chamber.

The LHCb experiment is designed to study B meson decays and measure CP violation. It is a forward spectrometer with only a single arm and does not cover the complete solid angle.

In the forward region of CMS the TOTEM (Total Elastic and diffractive cross-section Measurement) experiment [12] is located, which is designed to measure elastic and diffractive scattering in the very forward region. It consists of Roman Pots with silicon strip detectors

inside to measure elastic scattering, and a silicon forward telescope surrounding the beam pipe to measure the inelastic rate.

The LHC is designed to operate with proton beams up to a centre of mass collision energy of $\sqrt{s} = 14$ TeV. However, in 2011 the LHC was operated with a collision energy of only 7 TeV and in 2012 of 8 TeV. In addition, the LHC has been designed to be operated with ion beams, and lead–lead and lead–proton collisions were carried out from 2011 to 2013. The two experiments ATLAS and CMS aim at a high peak luminosity of $\mathcal{L} = 10^{34} \text{ cm}^{-2}\text{s}^{-1}$ for proton operation, LHCb aims at a lower luminosity of $\mathcal{L} = 10^{32} \text{ cm}^{-2}\text{s}^{-1}$, and ALICE, which is a dedicated ion experiment, aims at $\mathcal{L} = 10^{27} \text{ cm}^{-2}\text{s}^{-1}$ for nominal lead–lead ion operation. Furthermore, LHC is designed to operate with up to 2808 proton bunches in each beam with a nominal bunch spacing of 25 ns and 1.1×10^{11} protons per bunch.

The LHC uses NbTi superconducting magnets that are cooled to a temperature below 2 K, using superfluid helium, and operate at fields above 8 T. Because there is not enough room for two separate rings of magnets in the tunnel, the LHC uses twin bore magnets that consists of two sets of coils and beam channels within the same mechanical structure and cryostat. The ring accommodates 9593 magnets of which 1232 are main dipole magnets for bending to keep the particles inside the circular trajectory. The rest of the magnets are quadrupole and multipole magnets for focusing, defocusing and correcting. A superconducting system of eight radiofrequency cavities per beam is used to capture, accelerate and store the injected beams in the LHC.

3.2 The ATLAS experiment

The ATLAS detector (A Toroidal LHC Apparatus) is one of two general purpose detectors, which have been built to probe proton–proton and lead–lead collisions at the LHC. High interaction rates, radiation doses, particle multiplicities, energies and the requirement for high precision measurements have set the standards for the design of ATLAS. The overall layout of the main ATLAS detector is shown in Figure 3.3. Several additional sub-detectors in the forward region are not depicted here, but are described in Section 3.2.1. Like most other detectors in high-energy physics, ATLAS is forward-backward symmetric with respect to the interaction point (IP) and consists of several sub-detectors in an onion-layer like configuration and a magnetic system around the IP. These different sub-detectors and magnets are used to track and identify particles created by proton–proton interactions at the IP. The detector is shaped like a cylinder, where the surface is referred to as the barrel region in the pseudorapidity range $|\eta| \lesssim 1.5$ and the end-cap regions in the range $1.5 \lesssim |\eta| \lesssim 4.9$. Pseudorapidity is defined as $\eta = -\ln \tan \theta/2$ where the polar angle θ is the angle from the beam axis.

The IP is enclosed by the inner detector which achieves momentum and vertex measurements with a combination of semiconductor pixel and strip detectors and straw-tube tracking detectors. For the tracking the detectors are immersed in a magnetic field generated by a solenoid magnet positioned outside of the inner detector. This inner tracking system is surrounded by calorimeters for energy determination. A high granularity liquid-argon (LAr) electromagnetic calorimeter is used together with a scintillating-tile hadronic calorimeter. The most exterior part of ATLAS is the muon spectrometer, which consists of a large air-core toroidal magnet system and three layers of tracking chambers. A long barrel and two inserted end-cap toroidal magnets generate a strong bending power within the large muon tracking volume and define the overall dimensions of ATLAS (44 m \times 25 m). In Figure 3.4 the different detector layers are shown along with exemplary particles and how they would

3 Experimental setup

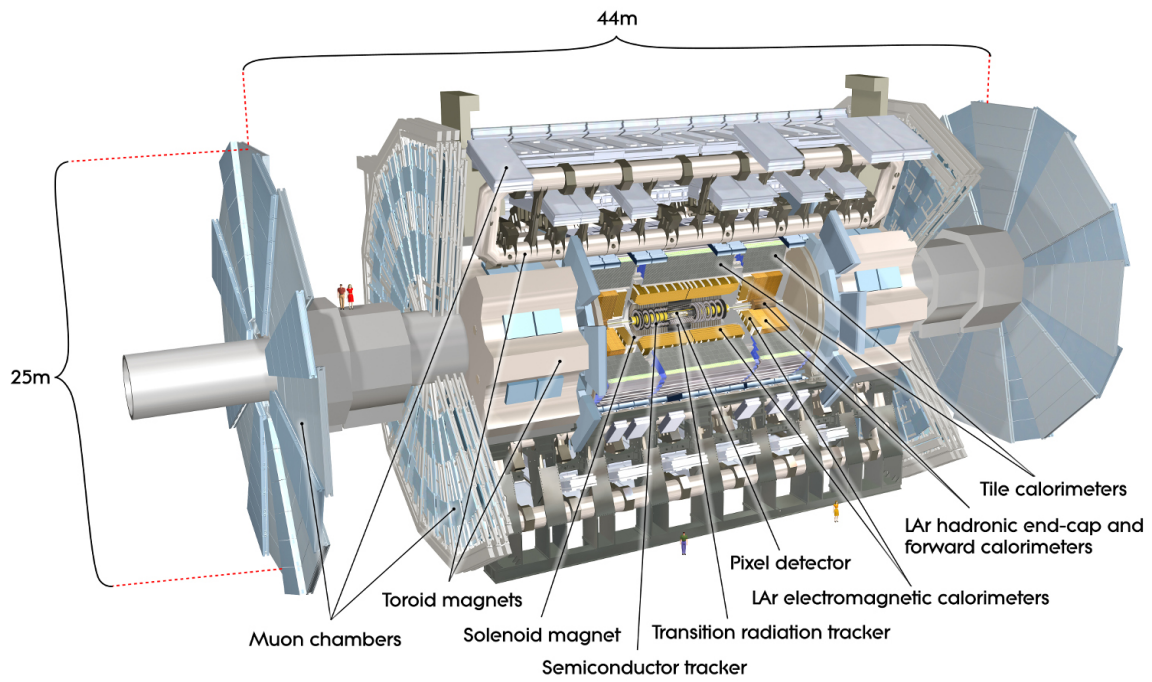


Figure 3.3: Schematic overview of the ATLAS experiment without forward detectors [39].

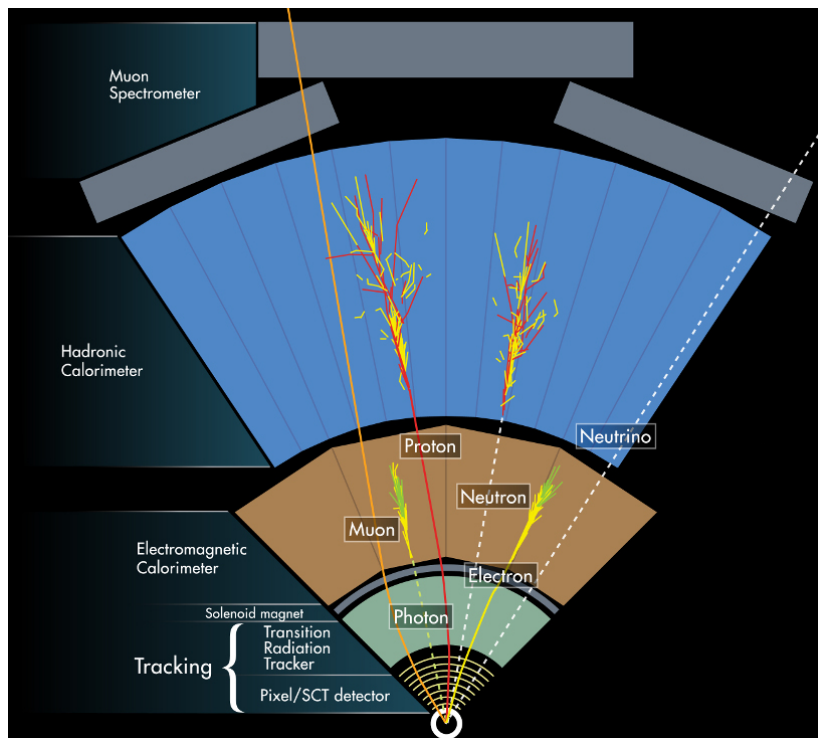


Figure 3.4: Principle of particle detection in ATLAS [40]. Dashed tracks are invisible to the detector.

be detected in the layers. The detectors, trigger system and data acquisition together with luminosity and forward detectors, which are especially important for the total cross-section analysis in this thesis, are described in the following. More details about the components of the main ATLAS detector can be found in Reference [1].

The ATLAS detector system has been built with requirements that utilize the rich physics potential of the LHC at the TeV scale. The high luminosity and increased cross-sections at the LHC enable more precise measurements of Standard Model parameters, minimum-bias events, elastic and diffractive scattering, jet- and photon physics, tests of QCD, electroweak interactions, heavy flavour and B physics. To establish the performance of important sub-detectors the search for the Standard Model Higgs boson and other new phenomena beyond the Standard Model have been used as a benchmark. This searches include new heavy gauge bosons W' and Z' , flavour-changing neutral currents, triple and quartic-gauge couplings, supersymmetry, extra dimensions as well as microscopic black holes. In addition, lead-lead collisions provide the opportunity to study the properties of strongly interacting matter at extreme energy density. Details about the ATLAS physics program can be found in Reference [41]. The analysis of data taken during the first LHC run from 2010 to 2013 has already produced several significant results including the observation of a Higgs boson [42].

Inner Detector

The Inner Detector (ID) provides hermetic and robust pattern recognition, excellent momentum resolution and both primary and secondary vertex measurements within the pseudorapidity range $|\eta| < 2.5$. The ID consists of three independent but complementary sub-detectors which are contained within a cylindrical envelope and a solenoidal magnetic field of 2 T. At inner radii silicon pixel layers and stereo pairs of silicon microstrip (SCT) layers provide discrete space points for high-resolution pattern recognition. Pixel modules are arranged in three barrel layers and two end-caps each with three disk layers, and SCT modules tile four coaxial cylindrical layers in the barrel region and two end-caps each containing nine disk layers. At the outer radii a transition radiation tracker (TRT) comprises many layers of gaseous straw tube elements interleaved with transition radiation material and provides continuous tracking to improve the momentum resolution and electron identification. The TRT contains up to 73 straw layers interleaved with fibres in the barrel region and 160 straw planes interleaved with foils in the two end-caps. The tubes are filled with a Xe/CO₂/O₂ gas mixture. Because of the high-radiation environment the pixel inner layer will have to be replaced after approximately three years of operation at design luminosity.

Calorimetry

The calorimeters of ATLAS cover the range $|\eta| < 4.9$ and use different techniques and granularities suited to the varying requirements of the interesting physics processes. The electromagnetic (EM) calorimeter is a lead-liquid argon (LAr) sampling calorimeter with accordion-shaped kapton electrodes and lead absorber plates. The lead plates are interleaved with LAr gaps, which provide the active medium. It is divided into a barrel part and two end-cap components, each housed in their own cryostat. The barrel part consists of two identical half-barrels, separated by a small gap and each end-cap calorimeter is divided into two coaxial wheels. Furthermore the calorimeter is segmented in three sections in depth except for the end-cap inner wheel which has only two segments. The EM calorimeter has a thickness of more than 22 radiation length (X_0) in the barrel region and $> 24X_0$ in the end-caps.

3 Experimental setup

Three different hadronic calorimeters are used in the ATLAS detector: the Tile calorimeter, the LAr Hadronic End-cap Calorimeter (HEC) and the LAr Forward Calorimeter (FCal). They have a total thickness of 11 interaction lengths (λ) in the barrel and 10λ in the end-caps.

The Tile is a sampling calorimeter using scintillating tiles as the active material and steel as absorber. It is placed directly outside the EM calorimeter envelope, is divided into a barrel part and two extended barrels and is also segmented in depths into three layers. The tiles are read out from two sides by wavelength shifting fibres into two photomultiplier tubes (PMT).

The HEC is a copper-LAr sampling calorimeter and consists of two independent wheels per end-cap, each segmented into two layers in depth and placed behind the end-cap EM calorimeter.

The FCal is also a sampling calorimeter consisting of three modules in each end-cap. The first module uses copper as absorber and is optimised for electromagnetic measurements, while the other two use tungsten as absorber and predominantly measure the energy of hadronic interactions. All three use again LAr gaps as active medium.

Muon spectrometer

The ATLAS muon spectrometer is based on the magnetic deflection of muon tracks in the large superconducting air-core toroid magnets, instrumented with separate trigger and high precision tracking chambers covering the range $|\eta| < 2.7$. It is designed to detect charged particles exiting the calorimeters and to measure their momentum and trigger on them. Chambers are arranged in three concentric cylindrical layers around the beam axis in the barrel region, and the chambers in the end-cap region are installed in planes forming large wheels perpendicular to the beam axis also in three layers. They are located between and on the eight coils of the superconducting barrel toroid magnet, and in front and behind the two end-cap toroid magnets.

Four types of chambers are used depending on the η -range and function. Over most of the range a measurement of the track coordinates in the principal bending direction of the magnetic field is provided by Monitored Drift Tubes (MDT) consisting of three to eight layers of tubes. At large $|\eta|$ Cathode Strip Chambers (CSC), which are multiwire proportional chambers with cathodes segmented into strips, are used. In the barrel region Resistive Plate Chambers (RPC) are used as muon triggers and in the end-caps Thin Gap Chambers (TGC) are utilized. These trigger chambers serve three purposes: provide bunch-crossing identification, provide well-defined transverse momentum (p_T) thresholds, and measure the muon coordinate in the direction orthogonal to the one from the tracking chambers.

Magnet system

The ATLAS magnet system is a hybrid system consisting of four large superconducting magnets. A solenoid provides a 2 T axial magnetic field for the inner detector. It is aligned on the beam axis and placed outside of the ID and in front of the barrel EM calorimeter. Because of calorimeter performance the layout was optimised to keep the material in front of the calorimeter as thin as possible. It is made out of a single-layer coil wound with Al-stabilised NbTi/Cu conductor. The flux is returned by the Tile calorimeter steel and its girder structure.

A barrel toroid and two end-cap toroids produce a magnetic field of 0.5 T and 1 T for the muon chambers in the barrel and end-cap regions, respectively. The barrel toroid consists of eight coils encased in individual racetrack-shaped, stainless-steel vacuum vessels, assembled

radially and symmetrically around the beam axis. The conductor and coil-winding technology is based on winding a pure Al-stabilised NbTi/Cu conductor into pancake-shaped coils, followed by vacuum impregnation. Both end-cap toroids consist of a single cold mass built up from eight flat, square racetrack-like coils and eight keystone wedges, which are bolted and glued together into a rigid structure. They are inserted in the barrel toroid at each end and line up with the central solenoid. The resulting magnet configuration provides a field which is mostly orthogonal to the muon trajectories.

Trigger and Data Acquisition

To trigger on interesting events, read out data and control the detector systems, ATLAS has a sophisticated Trigger and Data Acquisition (TDAQ) and Detector Control System (DCS).

The trigger system has three distinct levels: Level-1 (L1), Level-2 (L2) and the event filter. In each trigger level the decisions made at the previous level are refined and additional selection criteria are applied. The L1 trigger uses a limited amount of detector information to select events with a decision in less than 2.5 μs and to reduce the event rate. This selection is based on information and conditions from different sub-detectors like e.g. the muon chambers, calorimeters and forward detectors. Results from this L1 sub-detector triggers are processed by the Central Trigger Processor (CTP), which implements a ‘trigger menu’ made up of up to 256 distinct items, each item being a combinations of requirements on the input data. It is also possible to pre-scale trigger menu items to allow for an optimal use of the bandwidth as e.g. background conditions change. In the pre-scaling process the rate of trigger menu items is reduced by a certain factor by discarding events. The L1 trigger defines one or more Regions-of-Interest in each event, i.e. the geographical coordinates of those regions within the detector where its selection process has identified interesting features, with information that is used by the high-level trigger (L2 and event filter).

The L2 trigger selection is seeded by the Regions-of-Interest information from the L1 trigger and uses all the available detector data with full precision within this region to make a decision in about 40 ms. The event filter is the final stage of the event selection. It uses offline analysis procedures to select events within an average event processing time of the order of 4 s down to a rate, which can be recorded for subsequent offline analysis.

The data acquisition system receives and buffers event data from the detector-specific readout electronics, which gather information from several front-end data streams. After an event is accepted by the L1 trigger the data are transferred off the detector, whereas digitised signals are formatted as raw data. Then the readout system receives and temporarily stores the data in local buffers where it is subsequently solicited by the L2 trigger. Those events selected by the L2 trigger are transferred to the event-building system and finally to the event filter for final selection. Events selected by the event filter are moved to permanent storage on tape at the CERN computer centre.

The DCS controls, continuously monitors and archives the operational parameters, signals any abnormal behaviour to the operator and allows automatic or manual corrective actions to be taken. It permits the coherent and safe operation of the ATLAS detector hardware (gas systems, power-supply voltages, etc.), and serves as a interface for operators of the experiment to all sub-detectors and the technical infrastructure.

3.2.1 Luminosity and Forward detectors

The ATLAS experiment has several sub-detectors dedicated to different tasks. Three of these detector systems are placed in the very forward region: LUCID (Luminosity measurement

3 Experimental setup

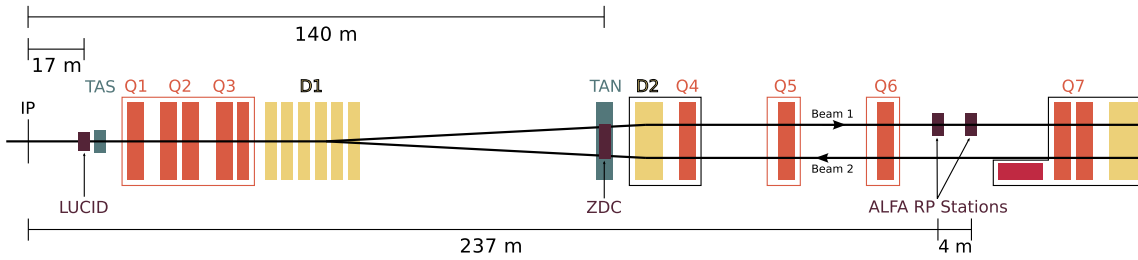


Figure 3.5: Top view of the location of forward detectors, dipole magnets (D), quadrupole magnets (Q) and absorber systems (TAS, TAN) in the two beams on C-Side. The distance from the ATLAS IP of the forward detectors is also quoted.

using Cherenkov Integrating Detector) is a Cherenkov detector used as relative luminosity monitor, ZDC's (Zero-Degree Calorimeter) primary purpose is to detect forward neutrons in heavy-ion collisions, and the ALFA (Absolute Luminosity For ATLAS) detector system measures elastically scattered protons down to very small scattering angles and is designed to provide an absolute luminosity calibration. The location of these detectors in the beam pipe of LHC and their distance from the ATLAS IP is shown in Figure 3.5 for the C-Side. All three forward detectors are symmetric to the IP and have the same components on A- and C-Side (see Section 3.2.3 for the naming convention).

The main purpose of the Beam Conditions Monitor (BCM) is to detect events with very high instantaneous rates and trigger an abort in such a case to prevent damage to the inner detector. It also proved itself as very good relative luminosity monitor, and is used as nominal luminosity detector during the first LHC run. Another minor sub-detector is the Minimum Bias Trigger Scintillator (MBTS), which is used to trigger on minimum bias events (minimum proton–proton collision activity) and also as a relative luminosity monitor.

The η -coverage of all important detector systems is depicted in Figure 3.6.

LUCID

As outlined before, ATLAS uses several detectors to measure relative luminosity (see also Section 6.6), but LUCID is the only one primarily dedicated to monitor online luminosity. Its main purpose is to detect charged particles from inelastic proton–proton scattering in the forward region, in order to measure the integrated luminosity and to provide online monitoring of the instantaneous luminosity. Because of its position in the forward region, LUCID can also be used as a tag for diffractive and minimum bias signals.

LUCID is a Cherenkov detector that consists of 16 mechanically polished aluminium tubes, which surround the beam-pipe and point towards the IP. Two detectors are located at a distance of $z = \pm 17$ m from the ATLAS IP on each side (the ATLAS coordinate system is described in Section 3.2.2), near the TAS (Target Absorber Secondaries) collimator with a radial distance of approximately 10 cm from the beam-line ($|\eta| \approx 5.8$). The tubes are filled with C_4F_{10} radiator gas to provide a Cherenkov threshold of 2.8 GeV for pions and 10 MeV for electrons. Cherenkov light emitted by particles traversing the tube has a half-angle of 3° and is reflected on average three times before the light is measured by PMTs at the back end of the tubes. The PMTs match the size of the tube and have a quartz window, which itself is also a Cherenkov radiator. The signal amplitude from the PMTs is used to distinguish the number of particles per tube, and the fast timing response provides measurements of individual bunch-crossings. LUCID also provides an independent trigger signal for use in the L1 trigger menu.

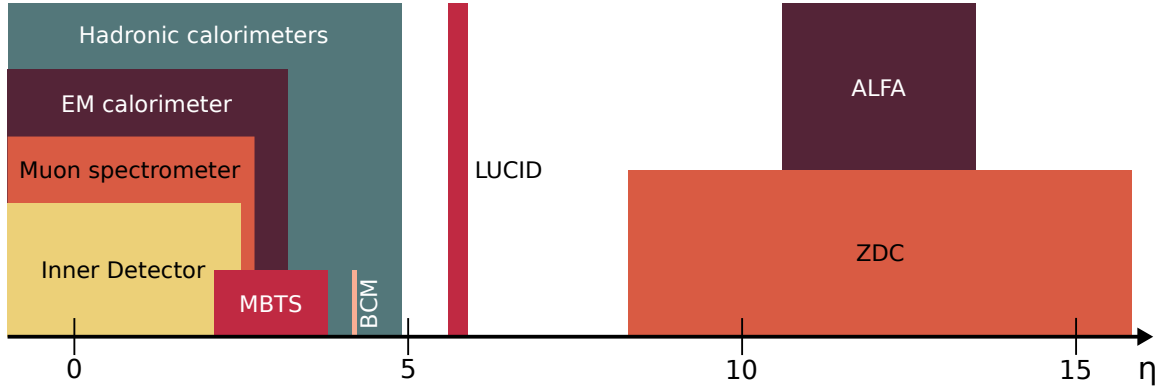


Figure 3.6: Pseudorapidity coverage of ATLAS central and forward sub-detectors. The coverage of ZDC extends to $\eta = \infty$.

As of July 2011 the radiator gas was removed and LUCID was only operated with Cherenkov signals from the quartz windows. This was done because of an increasing interaction rate during nominal physics running, which was starting to saturate the response when the detector was filled with gas.

ZDC

The main purpose of ZDC is to detect forward neutrons with $|\eta| > 8.3$ in heavy-ion collisions, because the centrality of such collisions is strongly correlated to the number of very forward neutrons. In the start-up phase of LHC with instantaneous luminosities well below $10^{33} \text{ cm}^{-2} \text{ s}^{-1}$ ZDC enhanced the acceptance of ATLAS for diffractive processes and provided an additional minimum bias trigger. This was the case until the end of 2011 and ZDC was removed for the proton-proton run in 2012 with higher luminosities. It was later inserted again for the heavy-ion run at the beginning of 2013.

The modules of ZDC are positioned in a slot in the TAN (Target Absorber Neutral) collimator, which is used to absorb forward high energy neutral particles so they do not impinge on the superconducting beam separation dipoles. The TAN is located at $z = \pm 140 \text{ m}$ from the IP on each side, at the place where the straight-section of the beam-pipe is divided into two independent beam-pipes. One electromagnetic and three hadronic calorimeter modules of ZDC are installed per side. The electromagnetic modules consist of tungsten plates as absorber with their face perpendicular to the beam direction and quartz rods as active radiator, penetrating the tungsten plates parallel to the beam in a matrix. The rods are bent upwards and viewed by multi-anode PMTs, which capture Cherenkov light produced in the quartz by shower products of incident particles. Thus it is possible to determine the transverse position of the particles from the rods and the energy from the intensity of the light. But only the EM module on the C-side ($z = -140 \text{ m}$) has these position-sensitive capabilities. To obtain a second, improved measurement of the energy, additional quartz strips are placed between the tungsten plates and read out from above by PMTs via air light-guides.

The hadronic modules are similar but in contrast to the EM modules the position-sensitive quartz rods are mapped in clusters of four into individual PMTs. Furthermore only one out of three modules on each side is equipped with the position-sensing rods.

ALFA

An in-depth description of the ALFA sub-detector can be found in Section 3.2.2.

Beam Conditions Monitor

The ATLAS Beam Conditions Monitor (BCM) system [43] consists of a set of detectors designed to detect beam losses that might damage the ID. One of such beam accident scenarios can arise, if several proton bunches hit the collimators in front of the detectors, producing enormous instantaneous rates that might cause damage to the ID. In such a case the BCM system triggers an abort signal in time to protect the ID.

The system consists of two stations, located symmetrically around the IP at $z = \pm 1.84$ m ($|\eta| = 4.2$), each with two vertical and two horizontal modules positioned less than 6 cm from the beam. Each module includes two radiation-hard diamond sensors read out in parallel by radiation-tolerant electronics with a very fast rise-time of 1 ns. The difference in time-of-flight between the two stations distinguishes particles from normal collisions at the IP from those arising from stray protons. The time-of-flight and pulse height can be measured bunch-by-bunch, and the BCM can also be used as an additional minimum bias trigger. Because of these capabilities the BCM system was discovered to be an excellent relative luminosity detector. And in fact the BCM was used in 2011 and 2012 as one of the main luminosity monitors.

Minimum Bias Trigger Scintillators

For the initial low luminosity running period ($\mathcal{L} < 10^{33} \text{ cm}^{-2} \text{ s}^{-1}$) ATLAS is equipped with a Minimum Bias Trigger Scintillator (MBTS) [44]. The main purpose of the MBTS is to provide a trigger on minimum collision activity from charged particles during proton-proton running.

The MBTS detector consists of 32 scintillator paddles (2 cm thick) organised into two disks. One of the disks is located on each side of the IP at $z = \pm 3.56$ m, positioned perpendicular to the beam direction. Each disk is separated into an inner and outer ring which together cover the region $2.09 < |\eta| < 3.84$. The rings themselves are organised into eight independent sectors. Light emitted by each scintillator segment is collected by wavelength-shifting optical fibres and guided to PMTs, which are read out by Tile electronics. During operation in 2010 and 2011 the MBTS detector was also used as a relative luminosity monitor.

3.2.2 The ALFA detector

The ALFA detector system [2] consists of eight tracking detectors housed in so-called Roman Pots (RP). These are movable insertions in the LHC beam tubes with which the tracking detectors can measure proton trajectories close to the circulating beams. The eight detectors are grouped into four stations, which are placed at $z = \pm 237.4$ m and $z = \pm 241.5$ m on both sides of the ATLAS IP in the outgoing beams (see Section 3.2.3 and Figure 3.11 for coordinate systems and naming). A station consists of two RPs (upper and lower) with tracking detectors approaching the beams in the vertical coordinate y .

Each of the eight tracking detectors is made of scintillating fibres. In the Main Detector (MD) traversing protons are detected and their position is measured. In addition, the dedicated Overlap Detectors (OD) measure precisely the distance between upper and lower MDs to align the detectors. Such a measurement is needed because the position of the movable RPs is not fixed from one data taking to another. Both MD and ODs are completed with

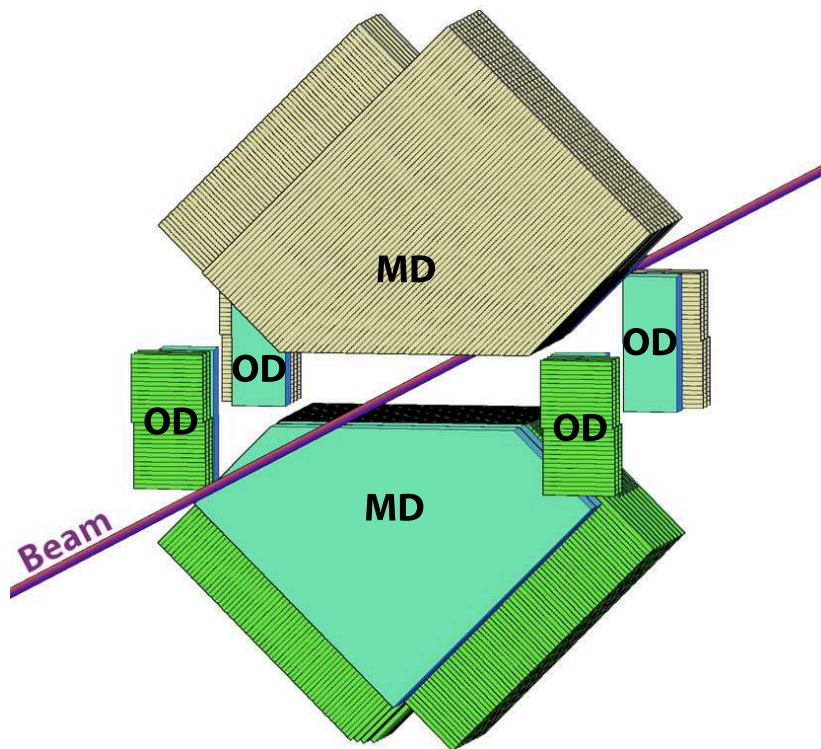


Figure 3.7: Layout of upper/lower MD and ODs with trigger counters in respect to the nominal beam position [45].

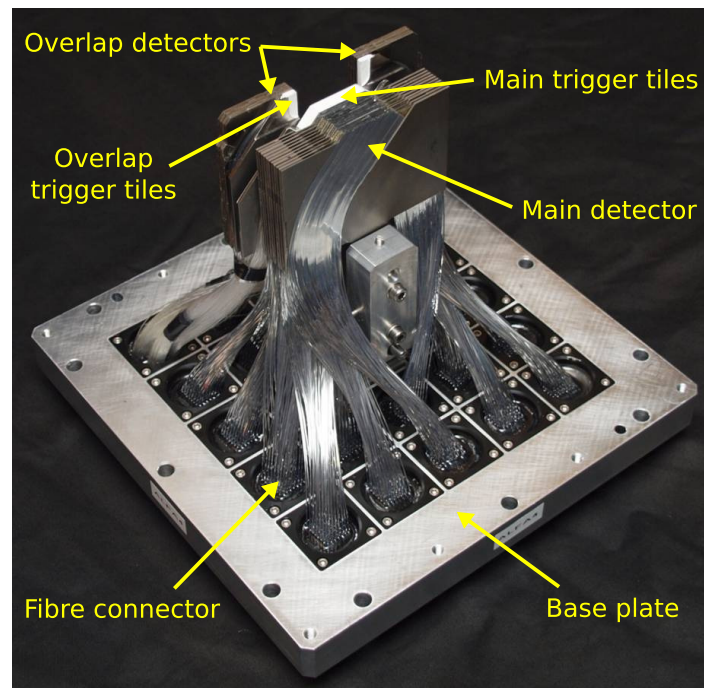


Figure 3.8: ALFA tracking detector insert without Roman Pot housing. The names of important parts are also shown.

3 Experimental setup

trigger counters, which are used to select miscellaneous event topologies of e.g. elastically or diffractively scattered protons. Figure 3.7 shows the layout of the scintillating fibres and trigger counters in the MD and ODs of the upper and lower detector in one station and their position with respect to the nominal beam. And in Figure 3.8 an actual tracking detector insert with all components is shown without the Roman Pot housing.

The main detector consists of ten fibre modules, with two layers of 64 squared single cladding scintillating fibres each. The fibres in each module are made of plastic, have a base length of $500 \mu\text{m}$, and are glued on both sides of Ti plates. They are coated with a thin Al film to minimize the optical cross-talk, which also improves the reflection at the fibre ends. At the front and back side of the plates the fibres are arranged at an angle of $\pm 45^\circ$ to the vertical coordinate y (base of the plates) in a diamond shape and perpendicular to each other. The plates are arranged after each other in the direction of the beam (z -direction), which results in a pattern of alternating fibre layers which form pixels in the so-called v and w coordinates. These pixels are illustrated in Figure 3.9, where one plane with a v and w layer is shown. The coordinates v and w are rotated 45° with respect to the horizontal and vertical coordinates x and y . For one v - w -plane the resulting pixels have a width of $d = 500 \mu\text{m}$, which corresponds to the base length of the fibres and gives a width of $d_{x,y} = \sqrt{2} \cdot 500 \mu\text{m} = 707 \mu\text{m}$ in the x - y -plane.

The theoretical resolution $\hat{\sigma}_{v,w}$ of one v - w -plane can be calculated as the Root Mean Square (RMS)

$$\hat{\sigma}_{v,w} = \sqrt{\int_{-d/2}^{d/2} \frac{(x - x_0)^2}{d} dx} \stackrel{x_0=0}{=} \sqrt{\int_{-d/2}^{d/2} \frac{x^2}{d} dx} = \frac{d}{\sqrt{12}} \approx 144 \mu\text{m}. \quad (52)$$

This is also true for $\hat{\sigma}_{x,y}$ in the x - y -plane which can be seen from the geometry. To further improve the resolution the fibre layers in the individual Ti plates are staggered by multiples of $1/10$ of the fibre size. The staggering makes the effective pixel size ten times smaller, which results in an ultimate theoretical resolution of the MD of $\sigma_{x,y} = \hat{\sigma}_{x,y}/10 = 14.4 \mu\text{m}$. In Figure 3.10 the staggering for ten fibre layers of either the v or w coordinate and the effective pixel size $d'_{v,w}$ are shown. In practice the resolution is deteriorated by imperfect staggering, cross-talk, noise and inefficient fibre channels. The actual resolution was measured in several test beams [46–49] to be between 25 and $35 \mu\text{m}$. Furthermore, the single layer efficiency to get a signal from any fibre in a layer from a traversing particle is about 93% with layer-to-

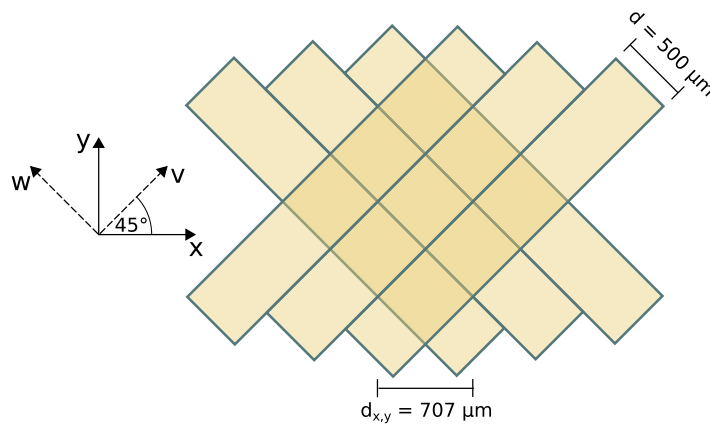


Figure 3.9: Illustration of one v and w layer forming a detector plane and pixels. The x - y -plane is rotated 45° with respect to the v - w -plane.

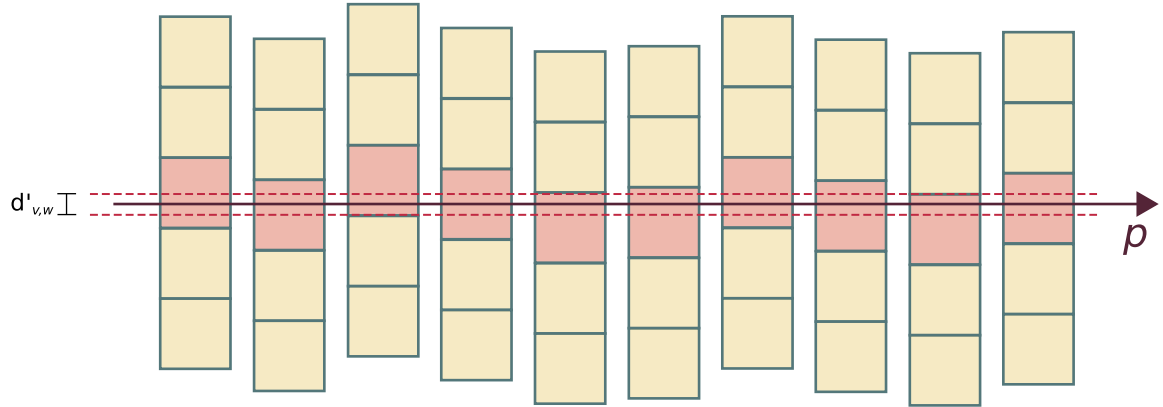


Figure 3.10: Ten fibre layers in either v or w direction with staggering of $1/10$ of the fibre size resulting in an effective pixel size $d'_{v,w}$. The resolution $\sigma_{v,w}$ of a particle track is ten times smaller then the resolution of a single layer.

layer variations of about 1 %, and the intrinsic tracking efficiency of all layers combined for minimum ionizing particles is close to 100 % per detector.

The overlap detectors consist of three layers of 30 scintillating fibres, which are glued to the front and back side of Ti plates, are staggered by $1/3$ of the fibre diameter, and are oriented horizontally. They are positioned on both sides of the MD, to measure the vertical coordinate of traversing particles (see Figure 3.7). The ODs are aligned to the MD with an uncertainty of not more than $8 \mu\text{m}$, which was measured in a test beam. The single-track resolution is about $50 \mu\text{m}$, but the precision of the distance measurement can be improved by using a large sample of beam-halo particles. A precision of $20 \mu\text{m}$ is achieved with a few thousand tracks. By using N particle tracks [50] with vertical coordinates y_i^{up} in the upper ODs and y_i^{low} in the lower ODs the distance can be calculated as

$$d_{\text{up-low}} = \frac{1}{N} \sum_{i=1}^N (y_i^{\text{up}} - y_i^{\text{low}}). \quad (53)$$

The main and overlap trigger counters consist of 3 mm thick scintillator plates, which cover the active areas of the MD and ODs. The MD detector is covered by two diamond-shaped plates of 31.5 mm base length, while for the ODs a single plate of $6 \times 15 \text{ mm}^2$ is used. The efficiency of a trigger signal in coincidence in both MD trigger counters was measured to be above 99.9 % [51].

The scintillation-light signals of the MD, ODs and trigger counters are guided by means of total internal reflection with scintillating fibres out of the RP to the photo-cathodes of multi-anode and single-channel Photomultiplier Tubes (PMT) respectively. A charged particle typically generates a signal of 4 photo-electrons, which results in a single fibre efficiency of about 89 % [48]. Each PMT is connected to front-end electronics with signal amplifiers and readout buffers to digitally store signals above a certain threshold. The digital fibre signals and analogue plus digital trigger signals are transmitted via a fibre optical link to the central ATLAS TDAQ system.

The tracking detector and trigger counters are housed in Roman Pots, which are vessels providing a secondary vacuum that allow the detector to approach the beam inside the beam pipe, but separate the detector from the primary vacuum of the beam pipe. Each RP has a thin steel window of 0.2 mm thickness at the bottom as direct separation between detector and beam. Two additional windows of 0.5 mm thickness are at the front and back side

3 Experimental setup

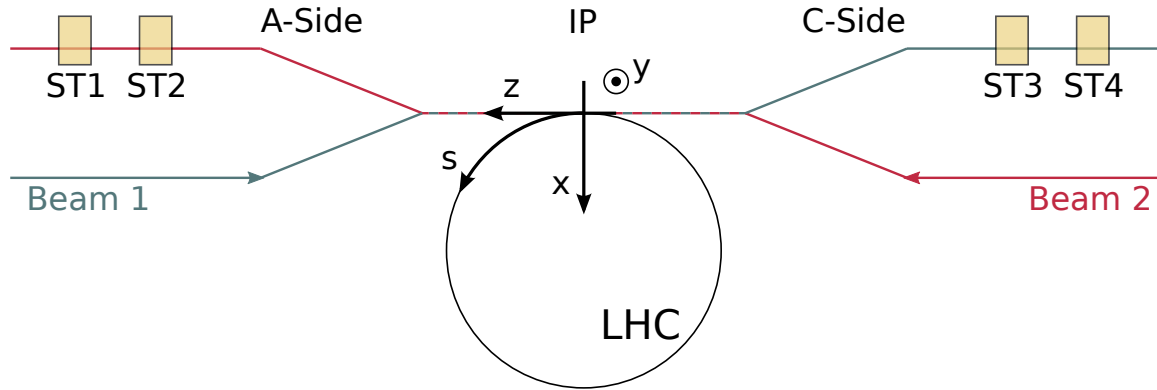


Figure 3.11: Top view of the LHC beam configuration with the ATLAS and Beam coordinate systems. The Roman Pot stations on A-Side are positioned in the outgoing beam 2 and on C-Side in the outgoing beam 1.

wall (in front and behind the MD). The pots are kept on movable flanges, and flexible bellows allow to move them close to the beam. Motors are used to achieve this positioning with 5 μm steps, and the position is measured by Linear Variable Displacement Transducers (LVDT), which were calibrated in a laser survey. The LVDT is calibrated with respect to the geometrical centre of the beam pipe, and the real beam positions are measured in special runs in which the bottom RP windows start to scrape the beam edges. Finally the occupancy of tracks in the upper and lower MDs of one station is used for a precise alignment of the detectors in respect to the beam (see Section 3.3.1).

Further details on the ALFA detector system, the commissioning and operation can be found in Reference [52].

3.2.3 Coordinate systems and naming conventions

The ALFA detector system uses three main coordinate systems: the detector (DetCS), beam (BeamCS) and ATLAS coordinate system. The DetCS is a 2D Cartesian coordinate system with its origin at the position of a precision hole in one end of the Ti plates holding the scintillating fibres. The y -axis points away (upwards for upper and downwards for lower detectors) from the scintillating fibre layers. And the x -axis is parallel to the surface of the Ti plate. An illustration of the DetCS can also be found in Figure 3.18 (left) on page 37.

The BeamCS is a right-handed Cartesian 3D coordinate system with its origin at the real ATLAS interaction point (IP) in the centre of the ATLAS detector and an s -axis along the real position of the beams. This axis follows the beams and therefore bends in the LHC arcs. The x -axis points from the IP to the centre of the LHC ring and the y -axis upwards.

The only difference of the ATLAS coordinate system compared to the BeamCS is the position of the origin and the z -axis. The origin of the ATLAS coordinate system is at the *nominal* IP and the z -axis is oriented along the *centre* of the beam pipe in an anti-clockwise direction, but does not follow the bending arcs like the s -axis. Since the nominal and real positions of the IP and the beam are not necessarily the same, these two coordinate systems are slightly different. However, the direction of the x - and y -axis is the same in both systems. An illustration of the ATLAS and Beam coordinate system with respect to the LHC ring and the Roman pot stations is shown in Figure 3.11.

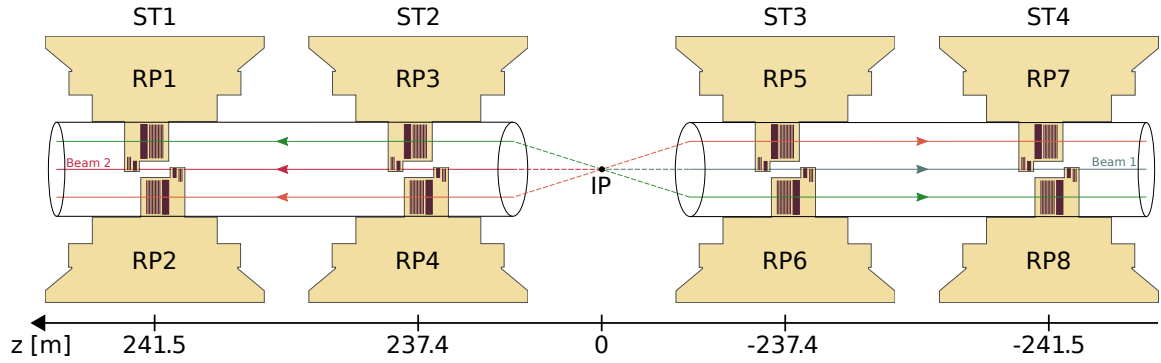


Figure 3.12: Side view from the middle of the LHC ring outwards of the four ALFA Roman Pot stations with upper and lower detectors. The dark areas represent the scintillating material of the MDs, ODs and trigger tiles. The beam pipes of beam 1 and 2 are also shown with the nominal beam positions and two possible trajectories of elastically scattered protons.

The polar angle θ (scattering angle) is defined as the angle with respect to the positive z -axis, and the azimuthal angle ϕ in the x - y -plane originates from the x -axis and increases clockwise when looking down the positive z -direction.

The positions of detectors, Roman Pot stations, LHC elements etc. are specified in the nominal BeamCS. The coordinates of particle tracks are reconstructed and stored in the DetCS of each Roman Pot and later transformed into the BeamCS (see Section 3.4.3).

Figure 3.11 also shows the position of the four ALFA stations in the two LHC beam pipes as a top view (y -axis going towards the reader). Station 1 (ST1) and 2 (ST2) are positioned on the ATLAS A-Side in the beam pipe of outgoing Beam 2 and Station 3 (ST3) and 4 (ST4) are positioned on the C-Side in the beam pipe of outgoing Beam 1. The arrows indicate the direction of the proton beams.

Figure 3.12 shows a more detailed view of the layout of the ALFA detector system. Station 1 at $z = 241.5$ m consists of upper detector RP1 (Roman Pot 1) and lower detector RP2, Station 2 at $z = 237.4$ m consists of RP3 and RP4, Station 3 at $z = -237.4$ m consists of RP5 and RP6 and Station 4 at $z = -241.5$ m consists of RP7 and RP8. The nominal position of Beam 1 is shown as blue line and the nominal position of Beam 2 as red line. The brown areas inside the Roman Pots represent the scintillating fibres of MDs and ODs and the trigger tiles. The green and orange lines represent trajectories of elastically scattered protons in back-to-back configuration. This means that proton tracks from elastic-scattering events are expected in the upper/lower detectors on A-Side and in the lower/upper ones on C-Side. Therefore, one can define two independent spectrometer arms: ‘Arm 1368’ consisting of detectors RP1, RP3, RP6 and RP8, and ‘Arm 2457’ consisting of detectors RP2, RP4, RP5 and RP7. Elastic-scattering events in the ‘golden’ back-to-back configuration are present either in arm 1368 or in arm 2457. The two spectrometer arms are basically two independent detectors systems, with which the differential elastic cross-section can be measured.

A few more notations which are used in this thesis are listed here:

- ‘Upper’ detectors are at $y > 0$ and ‘lower’ detectors are at $y < 0$ in the BeamCS;
- The ‘inner’ stations are nearer to the IP at $|z| = 237.4$ m, and the ‘outer’ stations are further from the IP at $|z| = 241.5$ m;
- ‘Armlet 13’ consists of detectors RP1 and RP3, ‘armlet 24’ consists of RP2 and RP4, ‘armlet 57’ consists of RP5 and RP7, and ‘armlet 68’ consists of RP6 and RP8;

3 Experimental setup

- ‘Golden’ events are elastic-scattering events in back-to-back configuration with reconstructed tracks in detectors of arm 1368 or arm 2457;
- ‘Anti-golden’ events are background events with reconstructed tracks in the four upper detectors (RP1, RP3, RP5, RP7) or in the four lower detectors (RP2, RP4, RP6, RP8).

3.3 Data taking

3.3.1 Beam configuration and detector set-up

The data used in the analysis described in this thesis were recorded in October 2011 in run number 191373 during a dedicated low-luminosity LHC fill using beam optics with a high- $\beta^* = 90$ m. The betatron function $\beta(s)$ determines the variation of the beam envelope around the LHC ring and depends on the focusing properties of the magnetic lattice. The value of $\beta(s)$ at the IP ($s = z = 0$) is called β^* and represents the focal length of the quadrupole system. Further details on the beam optics are found in Section 4.2. The nominal energy/momentum of the two proton beams was $E_{\text{beam}} = p_{\text{beam}} = 3.5$ TeV with a total uncertainty of $\Delta E/E = 0.65\%$ [53], which resulted in a centre-of-mass energy of $\sqrt{s} = 7$ TeV. The duration of the run was approximately four hours, in which primarily data from elastically scattered protons were recorded with the ALFA detector system.

The main pair of colliding bunches with BCID = 1 (Bunch Crossing Identifier number) were used for elastic-scattering events. Each bunch contained around 7×10^{10} protons. Twelve further low intensity pilot bunch pairs with about 1×10^{10} protons per bunch and one unpaired bunch with about 7×10^{10} protons were only used for systematic studies and background determination. To optimize the rates of the head-on collisions, several online luminosity monitors were used, including LUCID and the BCMs.

In the following the positioning of the Roman Pots and the beam characteristics are described. Further details on the beam configuration and detector set-up can be found in Reference [52].

Beam-based alignment

To achieve a precision on the position measurement of 20 to 30 μm in the horizontal and vertical plane, a very precise positioning of the RPs and detectors is needed. This is done in two steps: first with the beam-based alignment procedure the position of the RPs with respect to the proton beam is determined. And second, an off-line alignment procedure is performed to transform the reconstructed track positions from the DetCS to the BeamCS (see Section 3.4.3).

The beam-based alignment was performed in a separate dedicated LHC fill right before the fill that was used for elastic-scattering data taking. Beam settings in this fill were identical to the data-taking fill, and the duration was about three hours. During the procedure the eight RPs were individually moved into the beam by steps of 10 μm . The movement was stopped when the LHC beam-loss monitors gave a signal well above threshold. This ‘scraping’ was done for the two stations in beam 1 and beam 2 consecutively for the upper and lower RPs. After alignment of the two RPs of one station, the beams were reshaped by the primary collimators in the vertical direction.

From the vertical positions of the upper and lower RP windows with respect to the beam edges, the centre of the beams as well as the distance between the upper and lower RPs were determined. The beam centre on A-side was for both RPs off by about -0.2 mm from the

nominal position at $y = 0$ in the ATLAS coordinate system, and on C-side it was off by 0.5 to 0.6 mm. The distance between the upper and lower RPs was measured to be 8.7 mm for both inner stations and 7.8 mm for both outer stations. The difference between inner and outer stations corresponds to the expected decrease in the nominal vertical beam widths σ_y from the inner to outer stations.

For data taking the RPs were positioned as close as possible to the beams at $6.5\sigma_y$ to keep the background rates at a reasonable level. The nominal vertical beam width for the inner stations was $\sigma_{y,\text{inner}} = 897 \mu\text{m}$ and for the outer stations $\sigma_{y,\text{outer}} = 856 \mu\text{m}$. Therefore, the position at $6.5\sigma_y$ corresponds to a typical distance from the beam position in the ATLAS coordinate system of 5.83 mm for the inner and 5.56 mm for the outer stations.

Beam characteristics

To survey the horizontal and vertical beam positions during data taking, beam position monitors (BPMs) were used. These are regularly distributed along the beam line between the IP and the RP positions. Both beams were stable during data taking, with only small variations of the positions of the beams of the order of $10 \mu\text{m}$, which is equal to the precision of the measurement itself.

In the Monte Carlo simulation described in Section 5 the horizontal and vertical beam emittances ϵ_x and ϵ_y , expressed in μm (see definition in Equation (85)), are used as input to calculate the transverse momentum distributions. Therefore, the emittances were measured at various stages at the start of the fill (beam modes: injection, ramp, squeeze, adjust) using a wire-scan method [54]. Throughout the fill the emittances were monitored bunch-by-bunch by synchrotron radiation monitor systems, which were calibrated to the wire-scan measurements. The emittances increased smoothly with time during the fill from $\epsilon_x = 2.2 \mu\text{m}$ to $\epsilon_x = 3.0 \mu\text{m}$ and from $\epsilon_y = 1.9 \mu\text{m}$ to $\epsilon_y = 2.2 \mu\text{m}$ for beam 1, and from $\epsilon_x = 3.2 \mu\text{m}$ to $\epsilon_x = 4.2 \mu\text{m}$ and from $\epsilon_y = 2.0 \mu\text{m}$ to $\epsilon_y = 2.2 \mu\text{m}$ for beam 2. The systematic uncertainty on the emittances are about 10 %. For the Monte Carlo simulation a luminosity-weighted average horizontal and vertical emittance is used, which results in an angular beam divergence of about $3 \mu\text{rad}$.

3.3.2 Trigger conditions and data streams

Each Roman Pot is equipped with dedicated trigger tiles for the MD detectors. The signals from these tiles are sent to the CTP and integrated into the combined ATLAS trigger system. For ALFA data taking a special ‘ALFA trigger menu’ is implemented at the L1 trigger stage with 62 CTP bits. The rest of the 256 menu items are used for triggers from other sub-detectors.

To trigger on elastic-scattering events 18 L1 items ‘L1_ALFA_ELAST1’ to ‘_ELAST18’ are defined, but not all of them are used for the analysis. Only the loose conditions described by L1_ALFA_ELAST15 (arm 1368) and L1_ALFA_ELAST18 (arm 2457) are used to select elastic-scattering events:

$$\text{L1_ALFA_ELAST15} = (\text{RP1} \vee \text{RP3}) \wedge (\text{RP6} \vee \text{RP8}), \quad (54)$$

$$\text{L1_ALFA_ELAST18} = (\text{RP2} \vee \text{RP4}) \wedge (\text{RP5} \vee \text{RP7}). \quad (55)$$

A trigger signal needs to be present in at least one detector on A-Side and one detector on C-Side in one spectrometer arm regardless of the activity in the other arm. This is also illustrated for the arm 1368 trigger L1_ALFA_ELAST15 in Figure 3.13, where the green trigger tiles represent a trigger signal in the corresponding detector.

3 Experimental setup

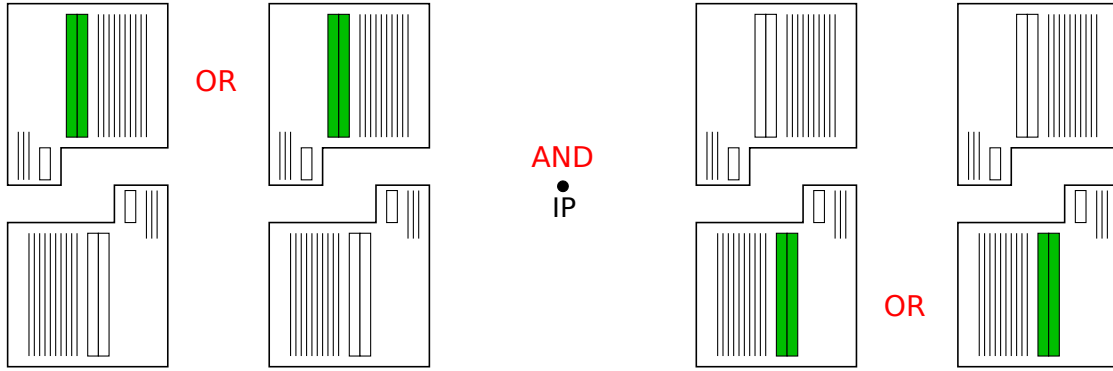


Figure 3.13: Illustration of the trigger logic of L1_ALFA_ELAST15. The green trigger tiles represent a trigger signal in the corresponding detector.

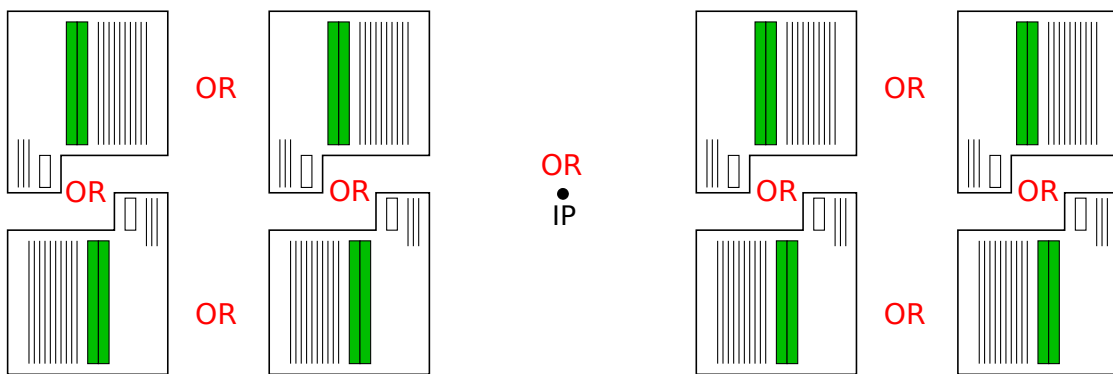


Figure 3.14: Illustration of the trigger logic of L1_ALFA_ANY. The green trigger tiles represent a trigger signal in the corresponding detector.

More trigger items are dedicated to diffractive events (8 items) and background, systematics and monitoring (31 items). The loosest possible trigger for background studies is an OR between all eight ALFA detectors:

$$L1_ALFA_ANY = RP1 \vee RP3 \vee RP6 \vee RP8 \vee RP2 \vee RP4 \vee RP5 \vee RP7. \quad (56)$$

This trigger is made in multiple bunch groups (paired, unpaired, empty, ...) and comprises five items. The most important one for the analysis, presented in this thesis, is the L1_ALFA_ANY item which is grouped with the paired bunches with BCID = 1. This loose trigger is also illustrated in Figure 3.14.

The high-level triggering (L2 and event filter) for ALFA is only a pass through of L1 items and further algorithms are not applied. Furthermore, the high-level trigger is not used for the analysis of elastic-scattering events. More details on the ALFA trigger menu can be found in References [52, 55].

Two streams with ALFA data were recorded during the data taking in October 2011: a physics stream and a calibration stream. The physics stream is mainly used for the analysis of elastic-scattering events and contains the complete data from all ATLAS sub-detectors. The readout of data in this stream was triggered by ALFA L1 items (including L1_ALFA_ELAST15 and _ELAST18) except for the very loose L1_ALFA_ANY trigger, because of bandwidth limitations. The calibration stream stored only data from the ALFA detector and was also triggered by ALFA L1 items *including* the L1_ALFA_ANY trigger, because it could handle a

higher rate of events. It is mainly used for background studies and determination of the trigger efficiency.

The trigger efficiency for the two elastic-scattering triggers `_ELAST15` and `_ELAST18` was determined from the calibration stream, which includes also data whose recording was triggered by the `_ANY` trigger. The number of events triggered by `_ELAST15` and `_ELAST18` in the physics stream was compared to the events triggered by `_ANY` in the calibration stream, to find a trigger efficiency in the geometrical acceptance of the detectors of $\varepsilon_{\text{trig}} = 99.96 \pm 0.01 \%$ [51].

Several additional trigger items from other sub-detectors related to minimum-bias and forward events (`L1_MinBias`) are used mainly in the determination of background (see Section 6.2) and the event reconstruction efficiency (see Section 6.3). The logical conditions for these items are briefly described here:

- `L1_TE20`: The total transverse energy $\sum E_T$ in the central detector needs to be larger than a threshold of 20 GeV to fire this trigger item;
- `L1_ZDC`: At least one hit in ZDC on either A- or C-Side is required to fire this trigger item;
- `L1_LUCID`: At least one hit in LUCID on either A- or C-Side is required to fire this trigger item;
- `L1_MBTS2`: At least two hits in the MBTS detector on either A- or C-side are required to fire this trigger item.

3.4 Track reconstruction

An elastic-scattering event is characterized by trajectories of two scattered protons creating local tracks in all four RP stations of one spectrometer arm. The local tracks in the MDs are reconstructed from the hit pattern of protons traversing the scintillating fibre layers. In each MD, 20 layers of fibres are arranged perpendicular to the beam direction in a v - w configuration. In this configuration the fibre planes (layers) are arranged at $\pm 45^\circ$ with respect to the vertical axis y of the DetCS. The coordinate system in which the tracks are reconstructed is called (v, w) . For simplicity and analysis the track coordinates are transformed by a simple rotation to the DetCS:

$$\begin{pmatrix} x_{\text{DetCS}} \\ y_{\text{DetCS}} \end{pmatrix} = \begin{pmatrix} \cos 45^\circ & -\sin 45^\circ \\ \sin 45^\circ & \cos 45^\circ \end{pmatrix} \begin{pmatrix} v \\ w \end{pmatrix} \quad (57)$$

The hit pattern of elastically scattered protons is characterized by an average total fibre multiplicity per detector of $M_{\text{tot}} = 23$, where typically 18 – 19 hits are attributed to the proton trajectory (ideal case: 20 hits) while the remaining 4 – 5 hits are associated to beam-related background, cross-talk and electronic noise. The total fibre multiplicity is defined as the sum of all detected hits in the 20 layers of an MD

$$M_{\text{tot}} = \sum_{i=1}^{20} h_i^{\text{layer}} = \sum_{j=1}^{1280} f_j^{\text{hit}}, \quad (58)$$

where i is the layer number, h_i^{layer} is the number of hits in a layer, j is the fibre number, $f_j^{\text{hit}} = 1$ if a hit is detected in fibre j and $f_j^{\text{hit}} = 0$ if no hit is detected.

3 Experimental setup

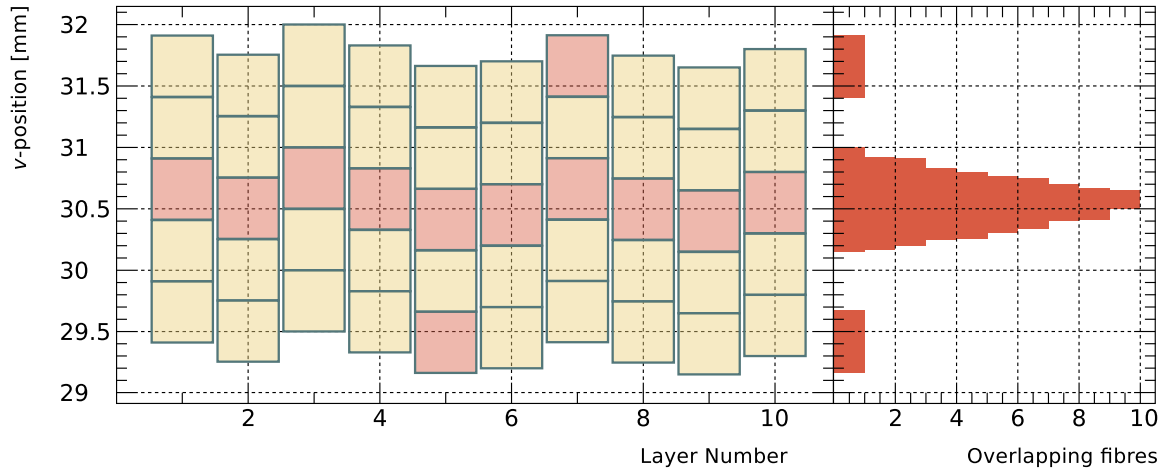


Figure 3.15: Illustration of the overlap of fibre hits in the v or w projection of the trajectory of an elastically scattered proton. The left part shows ten layers of the v direction, with fibre hits indicated in red. The right part shows the projection histogram with the overlap plateau as maximum. The height of the maximum is a measure for the number of hit fibres.

After reconstruction the track coordinates are available in the DetCS of each RP and need to be transformed into the BeamCS, in which the analysis of elastic-scattering events is performed. This is accomplished by the alignment procedure, which uses the distance between upper and lower RPs and rotations of detectors with respect to the beam, to transform the track coordinates.

3.4.1 Tracking algorithm

The ALFA fibre detectors have been built assuming, that elastically scattered protons traverse the detectors perpendicular to the fibre layers. The reconstruction algorithm [45] makes use of this assumption by using the fact, that hit fibres overlap in consecutive layers. However, a small angle below 1 mrad with respect to the beam direction has no sizeable impact on the reconstruction. In a first step the v and w coordinates of a track are determined from the two sets of ten layers which have the same orientation. The fibres are projected onto a perpendicular plane as shown in Figure 3.15, and a histogram of hits with a bin width of 1 μm is created. By going through the layers, the bins where hit fibres overlap are incremented in the histogram. The maximum of the resulting distribution is a plateau with a given overlap width, and indicates the region in the detector where the track has a uniform probability to be. This operation is done separately for the v and w projection. The centre of the overlap region plateaus give the coordinates of the track position in v and w , while the overlap width determines the resolution. The staggering of the fibres narrows the overlap region and thereby improves the resolution. In the second step the coordinates are combined to extract the position of the track in the DetCS as given by Equation (57).

Not all events are considered for the reconstruction. If the amount of hit fibres is large, e.g. because of hadronic showers or high noise levels, the tracking algorithm will in fact succeed to reconstruct a track position, however without a meaningful relation to the actual proton trajectory. On the other hand, only a few overlapping fibres in the layers cannot be the result of a proton traversing the detector. Therefore, good candidate events for the reconstruction are pre-selected based on several criteria:

- Only layers with a maximum of 10 hits are used for the reconstruction. Layers with more than 10 hits are excluded. The reconstruction is performed with less than the maximum possible ten layers per projection, if the other criteria are fulfilled.
- Out of the possible ten at least three layers are required to have between one and maximal three hits each.
- Only projections with three or more overlapping fibres are accepted for the combination of spatial tracks.

Because of these pre-selection criteria tracks are reconstructed with an average total multiplicity of $\bar{M}_{\text{tot}} = 23$ as described before. Some elastic-scattering events with $M_{\text{tot}} > 100$ survive the pre-selection criteria. These events are typically from hadronic showers developing within the detector, leaving the first layers clean enough to satisfy the criteria, and to be able to identify the real proton trajectory and reconstruct the track position (see Section 6.1.4 for total multiplicity distributions of elastic-scattering events). It is expected that some layers do not register any hit due to fibre inefficiencies or dead areas, and that some layers will have more than one fibre hit due to noise, cross talk or background. If an elastically scattered proton is not reconstructed, because its hit patterns do not fulfil the pre-selection criteria, some good elastic-scattering events would not be considered for the analysis. The amount of this reconstruction inefficiency for elastic-scattering events needs to be determined, in order to correct the measured raw differential t -spectrum. A fully data-driven procedure to estimate this event reconstruction efficiency is described in Section 6.3.

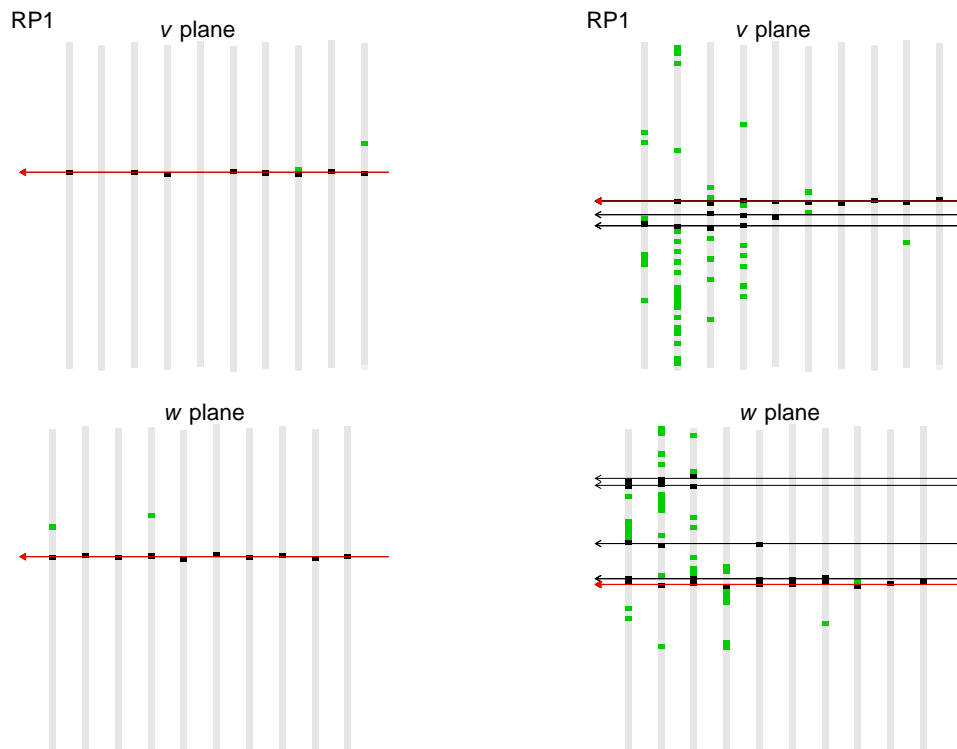


Figure 3.16: Event displays of event 4025 (left) and 4033 (right) in RP1. The arrows indicate a reconstructed track and the red one the best candidate from the track matching.

3 Experimental setup

Figure 3.16 shows two event displays of reconstructed proton tracks from elastic scattering in RP1. The displays show the hit pattern in the v and w planes, where the fibre layers are indicated in grey, the fibres hits in green and the fibre hits used to reconstruct the track in black. The reconstructed track position is also shown as red or black arrow. The red arrow indicates the best track candidate found by the track matching (see Section 3.4.2) and used for analysis. In the left display an almost clear track with only a few noisy fibres can be seen, where a single track is reconstructed. However, in the right display a lot of noise is present, because of cross-talk or background, so that multiple tracks are reconstructed. Via track matching the most elastic-like track is found, which is also the track with the most clear layers at the very right.

The tracking algorithm described here is used for the reconstruction of tracks in the MDs and ODs, whereat the precision for the ODs is reduced since only three fibre layers are available.

3.4.2 Track matching

Each of the projections v and w provide only one coordinate. If more than one particle passes through the detector in a single event, the orthogonal fibre geometry does not allow a unique formation of tracks, and two or more maxima per projection are detected. For example, if two particles pass through, two maxima per projection are formed and combined to four possible track candidates. A maximum of ten candidates are stored and sorted by decreasing number of overlapping fibres. Such multiple tracks can appear because of background associated with elastic-scattering events or elastic-scattering pileup, where elastically scattered protons from more than one reaction per bunch crossing hit the detector at the same time.

The back-to-back topology of elastic-scattering events can now be utilized to find the best combination of track candidates in the four detectors of a spectrometer arm. In the case of background in two detectors on one side it is likely that in the other two detectors of the same spectrometer arm no background tracks are reconstructed. By matching the tracks in all four detectors, the candidates belonging to the elastic-scattering event are found. For pileup events the best and most ‘elastic-like’ combination referring to one of the two events is also found with this matching. The other event in the pileup case is neglected and not used for analysis. The event display in Figure 3.16 (right) shows multiple reconstructed tracks in RP1 because of background associated to an elastic-scattering event. The black dots indicate the fibres that are used to reconstruct the tracks, which are displayed as arrows. The red arrow is the best track from elastic scattering found by the matching.

To match the tracks and find the best combination of candidates a χ^2 quality factor is calculated for every combination. For example for a pileup event with two tracks in each of the four detectors of one arm $2^4 = 16$ combinations are possible and the one with the smallest χ^2 is taken as best track candidate combination for the event. The calculation of χ^2 is based on the extrapolation of reconstructed track positions in one detector to the other three RPs of the same spectrometer arm. This extrapolation can be done by using the effective lever arms in Table 4.2 and exploiting the parallel-to-point focusing of the ALFA detector system (see Section 4.2 for a description). The track position in the detectors is directly related to the scattering angle at the IP via the effective lever arm L_{eff}

$$\theta_u^* = \frac{u_i}{L_{\text{eff},u,i}}, \quad (59)$$

where $u \in \{x, y\}$ and $i \in \{1, \dots, 8\}$ which is the number of the Roman Pot. Since the parallel-to-point focusing is only available in the vertical plane, this expression is just an approximation for the horizontal plane. This yields for two detectors i and j with $i \neq j$:

$$\theta_u^* = \frac{u_i}{L_{u,i}} = \frac{u_j}{L_{u,j}} \Rightarrow u_i = u_j \frac{L_{u,i}}{L_{u,j}}. \quad (60)$$

With this relation one can now extrapolate the position u_j in RP j to the position in RP i . The lever arm ratios $L_{u,i}/L_{u,j}$ are extracted from elastic-scattering data as part of the ALFA constraints for the beam optics fit described in Section 6.7.

For one track combination the position in three detectors is extrapolated to the fourth and compared with the reconstructed position in this detector. This is done for both coordinates x and y and for each of the four detectors of one arm. The quality factor χ^2 of one track combination of an elastic-scattering event is then defined as

$$\chi^2 = \chi_x^2 + \chi_y^2 \quad (61)$$

with

$$\chi_u^2 = \chi_u^2(i) + \chi_u^2(j) + \chi_u^2(k) + \chi_u^2(l), \quad (62)$$

where i, j, k and l are the four detectors of one arm and

$$\begin{aligned} \chi_u^2(i) = & \frac{1}{\sigma_u^2(j \rightarrow i)} \left(u_j \frac{L_{u,i}}{L_{u,j}} - u_i \right)^2 + \frac{1}{\sigma_u^2(k \rightarrow i)} \left(u_k \frac{L_{u,i}}{L_{u,k}} - u_i \right)^2 \\ & + \frac{1}{\sigma_u^2(l \rightarrow i)} \left(u_l \frac{L_{u,i}}{L_{u,l}} - u_i \right)^2. \end{aligned} \quad (63)$$

The factor $\sigma_u^2(j \rightarrow i)$ is a combination of different uncertainties related to the extrapolation from detector j to i

$$\sigma_u^2(j \rightarrow i) = \sigma_{\text{res}}^2(i) + \sigma_{\text{res}}^2(j) \left(\frac{L_{u,i}}{L_{u,j}} \right)^2 + \left(u_j \Delta \frac{L_{u,i}}{L_{u,j}} \right)^2 + \sigma_{\text{div}}^2(j, i). \quad (64)$$

These uncertainties include the average detector resolution for inner and outer stations (calculated from $\sigma_{x,y}^{\text{tuned}}$ in Table 5.2)

$$\sigma_{\text{res}}^2(i) = \begin{cases} 910 \mu\text{m}^2, & i = 1, 2, 7, 8 \\ 754 \mu\text{m}^2, & i = 3, 4, 5, 6, \end{cases} \quad (65)$$

the total uncertainty of the effective lever arm ratios $\Delta \frac{L_{u,i}}{L_{u,j}}$ obtained from data (see Table 6.20) and a divergence uncertainty which is important for extrapolations from one side to the other side of the IP

$$\sigma_{\text{div}}^2(j, i) = \begin{cases} 0, & i \text{ and } j \text{ on same side} \\ \sigma_{\theta,u}^2(i, j) \cdot L_{u,i}^2, & i \text{ and } j \text{ on opposite sides.} \end{cases} \quad (66)$$

The angle uncertainty $\sigma_{\theta,u}^2(i, j)$ is also obtained from data and shown in Table 3.1. Finally, the track combination with the minimum χ^2 is used for analysis.

In principle the track matching is done with golden elastic-scattering events, where in all four detectors of an spectrometer arm one or more track candidates are reconstructed. Therefore, one gets a best track candidate combination for each of these events. But it is

3 Experimental setup

Table 3.1: Scattering angle uncertainty for χ^2 quality factor calculation obtained from data. The difference comes from different divergences in the horizontal and vertical plane and in beam 1 and beam 2.

$\sigma_{\theta,x}^2(1368)$	39.49
$\sigma_{\theta,x}^2(2457)$	39.17
$\sigma_{\theta,y}^2(1368)$	3.379
$\sigma_{\theta,y}^2(2457)$	3.338

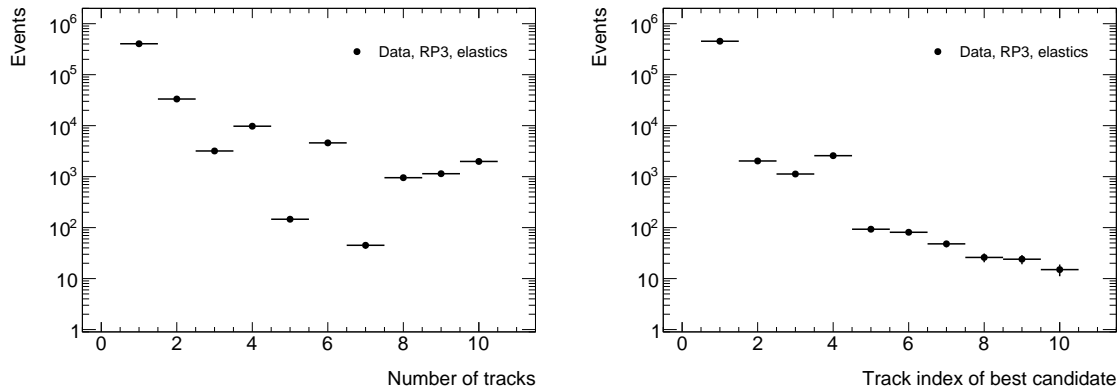


Figure 3.17: Number of reconstructed track candidates in RP3 for golden elastic-scattering events (left) and the track index that is chosen as best candidate in the track matching (right).

also possible to perform the matching with less than four detectors. Only two are needed to get a estimate of the best track candidate combination. Events with less than four detectors are only used to determine the event reconstruction efficiency later on in Section 6.3. Hence the matching is done for all events with an elastic-scattering trigger and at least two detectors with reconstructed track candidates in the triggered arm. In this case Equation (62) is reduced to the available detectors, consisting only of two or three terms.

Aligned track positions in the BeamCS have to be used for the matching. But for the alignment ideally the best track candidate combinations are used. This means an iterative procedure is done to get the final alignment and best track candidates. First the alignment is performed with the first track that is stored in the dataset, which is in most cases already the best one. Then the track matching is done with this alignment and the best candidates are found. These candidates are now used for another iteration of the alignment determination, which gives the final alignment. The matching is done one last time with this final alignment and the resulting best track candidate combinations are used for analysis. After two iterations the alignment does not change any more and no further steps are needed.

The distributions of the number of reconstructed tracks and the track index found by the matching as best candidate are shown in Figure 3.17 for RP3. The left plot shows, that most of the golden elastic-scattering events have only one or two reconstructed tracks. But there are many events with up to ten tracks, which is the maximum that the tracking algorithm can find. Events with an odd number of tracks are less common, because of the way the v and w projections are combined to provide the track candidates. The right plot shows on the x -axis the index of the track that is found as best track candidate during the matching. Track index 1 is the first one stored in the dataset, which refers to the track with the most overlapping fibres. This track is also chosen as best track candidate in most events. But there

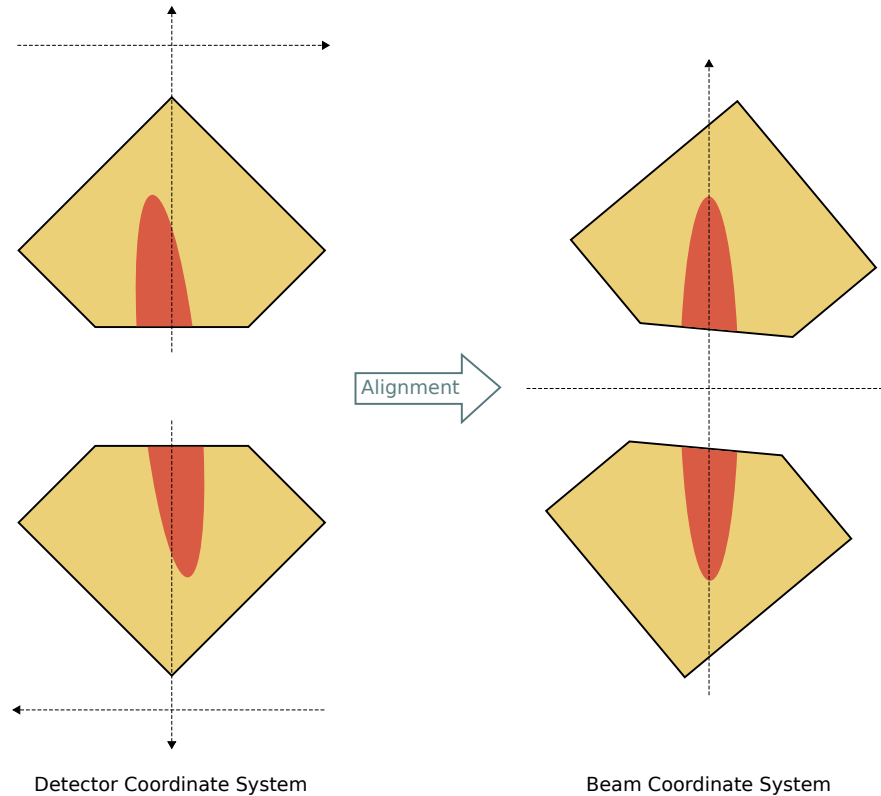


Figure 3.18: Illustration of the track based alignment procedure from the two floating reference systems (DetCS) of the upper and lower RP in a station to an absolute system of the ALFA detector system (BeamCS). The red ellipse is the distribution of elastic-scattering tracks.

are also a few events in which the best candidate is one of the tracks with a larger index. This means the whole range of reconstructed track candidates plays a role in finding the best one from elastic scattering. Tracks with index 4 seem to be favoured against indices 3 and 5. A possible explanation for this behaviour are elastic scattering pileup events in the same spectrometer arm, where four track candidates are reconstructed, and the fourth track is chosen as most elastic-like.

3.4.3 Alignment

The precision of the measurement of the elastically scattered proton kinematics and the measured differential cross-section as well as the total cross-section depends strongly on the knowledge of the detector position with respect to the beams. During data taking the detector positions were directly measured by LVDTs with a precision of 100 – 200 μm . For the analysis the positions with respect to the beams is needed with better precision. Therefore, the beam based alignment, described in Section 3.3.1, was performed. However, to obtain the most precise positioning in the vertical and horizontal coordinates, an additional track based alignment [45] is applied. With this alignment the reconstructed track coordinates in the DetCS are transformed into the BeamCS, in which their position is given in respect to the real position of the beams. This is illustrated in Figure 3.18, where two floating reference systems (DetCS of upper and lower detector) are merged into an absolute one (BeamCS).

The track based alignment procedure is based on the distribution of track positions in the detectors (MDs), and uses the full elastic-scattering event sample of the physics stream.

3 Experimental setup

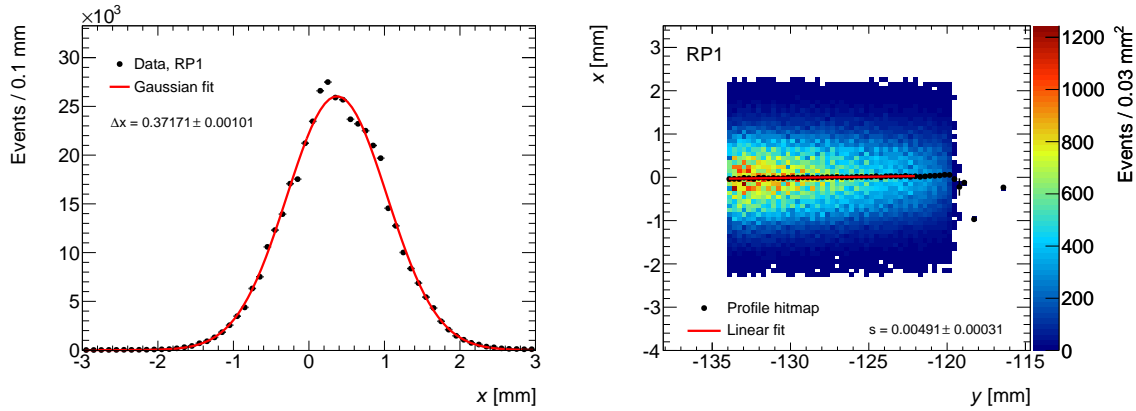


Figure 3.19: Gaussian fit of the horizontal track position in RP1 to determine the offset Δx (left). And a straight line fit to a profile histogram of the track pattern (hitmap) of RP1 to determine the rotation angle around the beam axis (right). The track coordinates in both figures are in the DetCS.

This distribution of elastic-scattering tracks forms a narrow ellipse in the x - y -plane with its major axis in the vertical direction, and with an aperture gap between the upper and lower detectors (compare Section 6.1.4). Additional constraints are the measured distance between the upper and lower detectors and the rotation symmetry of the scattering angles. For the alignment of each detector three parameters are necessary: the horizontal and vertical position offsets and the rotation angle around the beam axis z of the detectors. The possible detector rotations around the horizontal or vertical axis can be of the order of a few mrad, as deduced from survey measurements and the alignment corrections for rotations around the beam axis. However, such tiny deviations from the nominal angles result in small offsets which are effectively absorbed in the three alignment parameters. It is important to note, that the entire alignment procedure, described in the following, is independent of the beam optics parameters.

With the horizontal alignment the offset in the horizontal plane with respect to the beam centre Δx and the rotation angle around the beam axis θ_z are determined. This is done with a fit of a straight line to a profile histogram of the narrow track patterns in the upper and lower detectors to determine the rotation angle, and with a Gaussian fit to the projection of the horizontal track pattern in each detector to determine the offset. Examples of both fits are shown in Figure 3.19 for RP1. The fits use the fact, that the pattern of elastically scattered protons is symmetric to the beam centre. However, the used event sample has to be free of background, which can be achieved with the elastic-scattering event selection in Section 6.1. To apply the event selection the track coordinates have to be expressed in a common reference system, the BeamCS, which is exactly the purpose of the alignment procedure. In order to apply the event selection several iterations are required, starting with a rough selection of elastic-scattering candidates without any sophisticated cuts. Furthermore, the best track candidates, found by the track matching, are used, which requires an additional iteration. The final horizontal alignment parameters are quoted in Table 3.2. The total uncertainty of the horizontal offset parameters is about 1 to 2 μm with a statistical uncertainty of 1 μm ; and the uncertainty of the rotation is about 0.3 to 0.6 mrad with a statistical uncertainty of 0.3 mrad. Systematic uncertainties are attributed to the event selection and the range of the linear fit.

For the vertical alignment two parameters are determined: the distance between the upper and lower detectors and the vertical offset with respect to the beam centre. However, it

Table 3.2: Horizontal alignment parameters with total uncertainties.

Detector	Δx [mm]	θ_z [mrad]
RP1	0.337 ± 0.002	5.0 ± 0.5
RP2	-0.356 ± 0.002	1.4 ± 0.5
RP3	0.630 ± 0.001	3.9 ± 0.6
RP4	0.382 ± 0.001	1.6 ± 0.4
RP5	0.265 ± 0.001	0.4 ± 0.3
RP6	0.383 ± 0.002	-0.5 ± 0.3
RP7	0.428 ± 0.002	2.0 ± 0.3
RP8	0.494 ± 0.002	-1.3 ± 0.4

is not possible to apply a similar procedure as for the horizontal alignment with a Gaussian fit to the vertical track pattern in each detector to determine the offset, because of the gap between upper and lower detector. One input for the vertical alignment is the measured distance between the upper and lower detector in each RP station. The distance is determined by analysing data taken with the overlap detectors in a run right before run 191373. In this run the data was stored based on dedicated OD trigger signals. The ODs begin to overlap if the distance to the beam axis becomes smaller than 8.5 mm. If in this case halo particles pass through both ODs at the same time, two independent measurement of the vertical coordinate of the particle trajectory are performed. The principle of the distance measurement is illustrated in Figure 3.20. Here y_{up} and y_{low} are the vertical positions of the halo particle track in the DetCS of the upper and lower RP. The sum of these positions can also be written as

$$y_{\text{up}} + y_{\text{low}} = d + y_{\text{up}}^{\text{edge}} + y_{\text{low}}^{\text{edge}}, \quad (67)$$

where $y_{\text{up}}^{\text{edge}}$ and $y_{\text{low}}^{\text{edge}}$ are the vertical positions of the upper and lower detector edges (of the MD) and d the distance between the detectors. The edge positions were measured in test beams [46–49], and the sum is a constant value around $y_{\text{up}}^{\text{edge}} + y_{\text{low}}^{\text{edge}} \approx 270$ mm, depending on the station. Hence, the distance is given by

$$d = y_{\text{up}} + y_{\text{low}} - (y_{\text{up}}^{\text{edge}} + y_{\text{low}}^{\text{edge}}). \quad (68)$$

To improve the precision of the distance measurement many halo events with multiple tracks are used by averaging over larger samples. The results can be found in Table 3.3 with total uncertainties. The associated systematic uncertainties are derived from variations of the requirements on hit and track multiplicities in the ODs, from the relative alignment of the ODs with respect to the MDs and from uncertainties in the fibre positions. For the two inner stations the most precise distance values are achieved, whereas the measurement in the outer stations is degraded by shower particles from interactions in the inner stations. The large uncertainty for station 1 (RP1/RP2) is due to one detector which was not calibrated in a test beam. Further details on the distance measurement can be found in Reference [56].

With the distance from the OD measurement as input, upper and lower stations are grouped into a combined station coordinate system where the horizontal alignment is applied. To get the vertical offset to the beam centre its position is determined based on the density symmetry of tracks from elastically scattered protons in the upper and lower detectors. The density of elastic-scattering tracks at a given distance from the beam centre should be equal in the upper and lower detector. To find the centre position with equal track density

3 Experimental setup

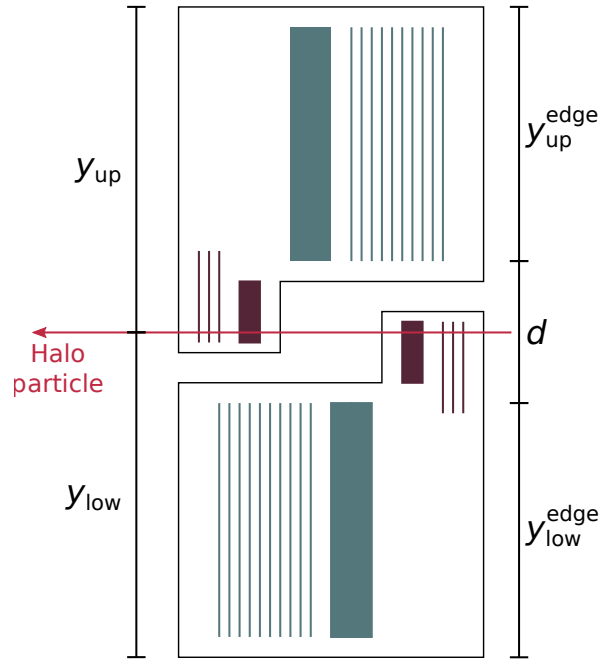


Figure 3.20: Principle of the distance measurement between upper and lower RP in one station.

a sliding window technique is applied on the vertical track position distribution. For the event reconstruction efficiency described in Section 6.3 an asymmetry of the order of 1.7 % between the two spectrometer arms is observed, which is taken into account for the vertical position distribution. Being independent with respect to the track position, the distribution of each station is scaled with a factor of $1/\epsilon_{rec}^{arm}$. The technique consists of three steps and is illustrated in Figure 3.21 for station 1: a window with random upper and lower limit is generated with a minimum width of 3 mm; the integral in the window is calculated for vertical position distribution of the lower detector; the upper detector distribution is scanned with the same window width until the closest integral is found. The vertical offset is extracted by comparing the upper window edge in the lower detector to the lower window edge in the upper detector. All steps are repeated 500 times for each station and the resulting distribution is fitted with a Gaussian function in order to extract the mean value. This is shown in Figure 3.21 for station 1.

Statistical uncertainties and systematic uncertainties related to the sliding window technique are determined from fast simulation Monte Carlo samples (compare Section 5 for a description of the samples). For other systematic uncertainties contributions from the event reconstruction efficiency and the event selection are taken into account. The uncertainty from the reconstruction efficiency is by far the dominating contribution. Finally, with the distance d and vertical offset Δy the detector edge position in the BeamCS y_{meas} can be calculated to $y_{meas} = \pm d/2 - \Delta y$, where $+$ is for upper and $-$ for lower detectors. The results of the detector edges are summarized in Table 3.3 with total uncertainties.

In order to optimize the parameters the parallel-to-point focusing is used to extrapolate the measured vertical track positions from one detector to the others using the effective lever arm ratios (see Equation (60)). The principle of this procedure is already described in Section 3.4.2 and is used here to refine the relative alignment between the stations. To be independent from the beam optics the lever arm ratios extracted from elastic-scattering data as described in Section 6.7 are used as input for the extrapolation. One station is chosen as reference and

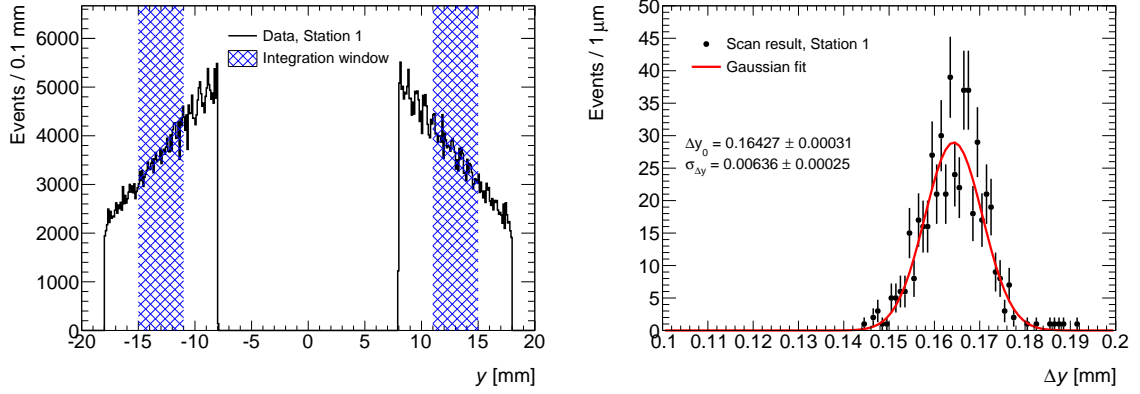


Figure 3.21: Illustration of the sliding window technique for station 1 (left): The vertical position distributions of the upper and lower detector are scaled with $1/\varepsilon_{\text{rec}}^{\text{arm}}$, and the blue integration window is randomly generated inside the range of the distributions. And the distribution of the vertical offsets in station 1 obtained with the sliding window technique fitted with a Gaussian function (right).

Table 3.3: Measured distance values between upper and lower detector, and measured and optimized detector edge positions with total uncertainties.

Station	Detector	d [mm]	y_{meas} [mm]	y_{opt} [mm]
1	RP1	11.962 ± 0.081	5.981 ± 0.093	5.934 ± 0.076
	RP2		-5.981 ± 0.093	-5.942 ± 0.076
2	RP3	12.428 ± 0.022	6.255 ± 0.079	6.255 ± 0.078
	RP4		-6.173 ± 0.079	-6.173 ± 0.080
3	RP5	12.383 ± 0.018	6.080 ± 0.077	6.036 ± 0.088
	RP6		-6.303 ± 0.077	-6.273 ± 0.087
4	RP7	11.810 ± 0.031	5.765 ± 0.073	5.820 ± 0.083
	RP8		-6.045 ± 0.073	-6.120 ± 0.084

the reconstructed vertical track positions in this station are extrapolated to the other three stations. Of course, the horizontal and vertical alignment described above is first applied to the track positions. The distribution of residuals $y_{\text{extr}} - y_{\text{meas}}$ between the extrapolated and measured position for a given elastic-scattering event is fitted with a Gaussian function to extract the mean value. This mean value y_{mis} represents the residual misalignment between the detector of the reference station and the other three detectors of the same spectrometer arm. The corrections to be applied can be interpreted as a distance error $\Delta d = y_{\text{mis}}^{\text{up}} - y_{\text{mis}}^{\text{low}}$ and a vertical misalignment $\Delta \hat{y} = (y_{\text{mis}}^{\text{up}} + y_{\text{mis}}^{\text{low}})/(-2)$. Like for the horizontal alignment several iterations are performed until the difference between iteration n and $n - 1$ is smaller than $5 \mu\text{m}$.

Station 2 is chosen as reference station for the final alignment. Taking a different station would result in other alignment parameters. However, only the two inner stations can be used, since the outer ones suffer from a larger uncertainty on the distance measurement. Additional systematic uncertainties have to be taken into account because of the optimization procedure and affect the final detector positioning: the vertical alignment parameters obtained with Station 2 as reference are compared to the ones obtained with Station 3 which gives an uncertainty on the choice of the reference station; the systematic uncertainties of the

3 *Experimental setup*

distance measurement and of the vertical offset; and the systematic uncertainties of the lever arm ratios. The final results for the detector edge positions after optimization are shown with total uncertainties in Table 3.3. The edge positions obtained after alignment are compatible within uncertainties with the measured values without optimization.

4 Beam optics and t -reconstruction

The beam optics of a particle accelerator like the LHC describe the motion of the particles in the beams. Magnetic elements in the accelerator are designed to guide and focus the particle beams along a reference circular orbit. Because of the focusing and defocusing nature of these magnetic elements, so called ‘betatron’ oscillations around the reference orbit occur for the particles. These oscillations describe the transverse motion and depend on the magnetic fields applied in the accelerator ring. The ALFA detector system is located about 240 m away from the ATLAS IP in the outgoing beams. Therefore, the position and local angle of elastically scattered protons depend on their motion along the reference orbit, and a precise knowledge of the beam optics parameters is necessary to correctly reconstruct the four-momentum transfer squared t of the elastic-scattering event. In the following some general concepts of transverse beam dynamics are introduced, the most important beam optics parameters are described and the t -reconstruction from the measured proton track positions in the ALFA detector is outlined.

4.1 Transverse beam dynamics

In general the motion of charged particles with velocity \vec{v} in electromagnetic fields is governed by the Lorentz force

$$\vec{F}_L = q(\vec{E} + \vec{v} \times \vec{B}), \quad (69)$$

where q is the electric charge of the particle, \vec{E} the electric field and \vec{B} the magnetic field. From this force a trajectory can be derived. For high energy beams magnetic fields are preferably used to guide (focus and bend) particles, because the needed field strengths can be more easily achieved than for electric fields. Electric fields are only used to accelerate the particle beams using e.g. superconducting radio frequency cavities as for the LHC. In the two-dimensional case where only a uniform magnetic field B is present the particles travel with momentum \vec{p} on a circle with radius r

$$\frac{d\vec{p}}{dt} = q(\vec{v} \times \vec{B}) \xrightarrow{\vec{B} \perp \vec{v}} Br = \frac{p}{r}. \quad (70)$$

An accelerator can now be defined as a sequence of magnets which guides the beam by bending (dipole magnets) and focusing (quadrupole magnets) [57, 58]. The trajectories of all beam particles are described around a reference orbit, which is defined as the trajectory of a particle with given momentum p_0 . In general p_0 is the nominal beam momentum and in the case of the LHC this is 3.5 TeV in 2011. The trajectories are described in a curved coordinate system similar to the BeamCS (compare Section 3.2.3) with the origin at a longitudinal position of $s = 0$. Particles perform small oscillations around the reference orbit in the transverse plane denoted by the coordinates x and y . This transverse motion is described by Hill’s equation

$$\frac{d^2}{ds^2}u(s) + K(s)u(s) = 0, \quad (71)$$

where the trajectory function $u(s)$ describes the betatron oscillation in the transverse plane and $K(s)$ are the focusing functions depending on the different magnet structure types. The oscillations in x and y are decoupled at first order and therefore $u(s)$ can be replaced by either of them: $u = \{x, y\}$. Amplitude and phase of $u(s)$ depend both on the longitudinal

position s along the reference orbit. The first derivative $u'(s)$ describes the angle of the particle trajectory with respect to the reference orbit (s -axis) in the vertical and horizontal plane, also called $\theta_u(s)$. For circular accelerators the focusing functions $K_{x,y}(s)$ are periodic with $K(s + \kappa) = K(s)$, where κ is at most the circumference of the accelerator ring but normally corresponds to the distance between two FODO cells¹. One can assume that K is constant, because of (nearly) uniform magnetic fields in the accelerator components, which gives the following linear independent principal solutions to Hill's equation:

$$u(s) = \begin{cases} a \cos(\sqrt{K}s + b) & \text{and } a \sin(\sqrt{K}s + b) & \text{if } K > 0 \text{ (focusing)} \\ as + b & & \text{if } K = 0 \text{ (drift space)} \\ a \cosh(\sqrt{|K|}s + b) & \text{and } a \sinh(\sqrt{|K|}s + b) & \text{if } K < 0 \text{ (defocusing),} \end{cases} \quad (72)$$

where a and b are integration constants which need to be determined by the initial conditions of u_0 and u'_0 . Any arbitrary solution can be expressed as a linear combination of these principal solutions.

The evolution of $u(s)$ and $u'(s)$ from the initial position $u(s_0)$ and angle $u'(s_0)$ can also be expressed with matrix formalism in the following way:

$$\begin{pmatrix} u(s) \\ u'(s) \end{pmatrix} = M_u(s, s_0) \begin{pmatrix} u(s_0) \\ u'(s_0) \end{pmatrix} = \begin{pmatrix} M_{u,11}(s, s_0) & M_{u,12}(s, s_0) \\ M_{u,21}(s, s_0) & M_{u,22}(s, s_0) \end{pmatrix} \begin{pmatrix} u(s_0) \\ u'(s_0) \end{pmatrix}. \quad (73)$$

Here $M_u(s, s_0)$ is called the 'transport matrix' and depends on the initial and final longitudinal positions s_0 and s . The transport matrix is independently defined for $u = \{x, y\}$, but for the sake of clarity the index and dependence on s will be omitted in the rest of this thesis. It relates the position and angle at s after a magnetic element to the initial position and angle at s_0 before the element. To get the transport matrix for a series of elements in an accelerator the matrices of the individual elements simply need to be multiplied. For two consecutive magnets with lengths $L_1 = s_1 - s_0$ and $L_2 = s_2 - s_1$ the overall transport matrix for $L = L_1 + L_2 = s_2 - s_0$ is given by

$$M(s_0 \rightarrow s_2) = M(s_1 \rightarrow s_2)M(s_0 \rightarrow s_1). \quad (74)$$

Based on the solution of Hill's equation in (72) the transport matrix for the three different cases of K can be written as

$$M = \begin{cases} \begin{pmatrix} \cos \sqrt{K}L & \frac{1}{\sqrt{K}} \sin \sqrt{K}L \\ -\sqrt{K} \sin \sqrt{K}L & \cos \sqrt{K}L \end{pmatrix} & \text{if } K > 0, \\ \begin{pmatrix} 1 & L \\ 0 & 1 \end{pmatrix} & \text{if } K = 0, \\ \begin{pmatrix} \cosh \sqrt{|K|}L & \frac{1}{\sqrt{|K|}} \sinh \sqrt{|K|}L \\ \sqrt{|K|} \sinh \sqrt{|K|}L & \cosh \sqrt{|K|}L \end{pmatrix} & \text{if } K < 0, \end{cases} \quad (75)$$

with the length of the magnet $L = s - s_0$. At this point it is important to notice, that the treatment of the beam dynamics described here does not consider any momentum loss $\Delta p/p$ of the beam particles. In general this is not true, so that the position $u(s)$ and angle $u'(s)$ also depend on dispersion. But for the special case of elastic scattering there is no momentum loss, and a treatment without dispersion is sufficient.

¹A typical structure of (magnet) elements used in an accelerator. 'F' stands for a Focusing magnet, 'O' for a drift space with no magnetic field and 'D' for Defocusing.

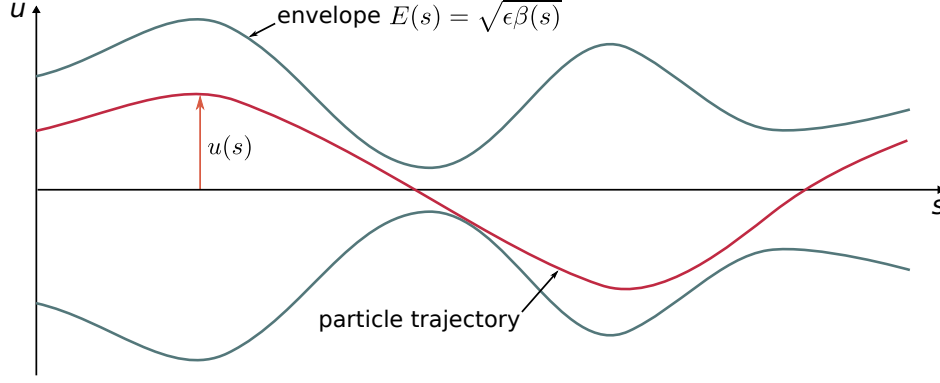


Figure 4.1: Illustration of the beam envelope $E(s) = \sqrt{\epsilon\beta(s)}$ with a particle trajectory $u(s)$ inside. The beam consists of a combination of all possible trajectories.

Furthermore, the general solution for Hill's equation (71) can be expressed with an ansatz of a quasi-harmonic oscillator with an s -dependent amplitude $\omega(s)$ and phase $\Psi(s)$, and integration constants A and Ψ_0 .

$$u(s) = A\omega(s) \cos [\Psi(s) - \Psi_0] \quad (76)$$

This means for $K > 0$ the phase is e.g. $\Psi(s) = \sqrt{K}s$. By inserting this solution and its second derivative into (71) one gets with the short cuts $\Psi(s) = \Psi$, $\omega(s) = \omega$ and $K(s) = K$

$$A(\omega^3\omega'' - \omega^4\Psi'^2 + K\omega^4) \cos(\Psi - \Psi_0) - A(2\omega\omega'\Psi' + \omega^2\Psi'') \sin(\Psi - \Psi_0) = 0. \quad (77)$$

The sum of all coefficients of the sine and cosine terms, respectively, must vanish separately to make ansatz (76) valid for all phases Ψ . This can only be satisfied for $A \neq 0$ with the two conditions

$$\omega^3\omega'' - \omega^4\Psi'^2 + K\omega^4 = 0 \quad \text{and} \quad 2\omega\omega'\Psi' + \omega^2\Psi'' = 0. \quad (78)$$

The second condition can be integrated immediately since $2\omega\omega'\Psi' + \omega^2\Psi'' = (\omega^2\Psi')'$, and yields an expression for the phase $\Psi(s)$

$$\Psi(s) = \int_0^s \frac{d\tau}{\omega^2(\tau)} = \int_0^s \frac{d\tau}{\beta(\tau)}. \quad (79)$$

Here $\beta(s)$ is the betatron or amplitude function, which depends on the beam focusing properties of the magnetic lattice, and is a measure of the beam cross-section at a given position s . With this expression Equation (76) can be written as

$$u(s) = E(s) \cos [\Psi - \Psi_0] = \sqrt{\epsilon\beta(s)} \cos [\Psi(s) - \Psi_0], \quad (80)$$

where $A = \sqrt{\epsilon}$ is the root of the 'emittance' ϵ , which is explained later in this section. The beam envelope $E(s) = \sqrt{\epsilon\beta(s)}$ is the limit of the transverse motion of particle trajectories along the reference orbit and defines the transverse size of the beam at a given point s . An illustration of the envelope is shown in Figure 4.1 with a sample particle trajectory inside the beam. And the phase advance $\Psi(s) - \Psi_0$ gives the number of oscillations between $s = 0$ and s in the magnetic lattice. From the derivative of $u(s)$ with respect to s the angle of the particle trajectory is found to be

$$u'(s) = -\sqrt{\frac{\epsilon}{\beta(s)}} \{ \sin [\Psi(s) - \Psi_0] + \alpha(s) \cos [\Psi(s) - \Psi_0] \} \quad (81)$$

4 Beam optics and t -reconstruction

where

$$\alpha(s) = -\frac{1}{2} \frac{d}{ds} \beta(s) \quad (82)$$

is the derivative of the betatron function with respect to s . The two parameters $\alpha(s)$ and $\beta(s)$ are called ‘Twiss’ functions. Together with the third Twiss function

$$\gamma(s) = \frac{1 + \alpha^2(s)}{\beta(s)} \quad (83)$$

and the emittance they fully describe the beam optics. At several points in this thesis it is referred to the ‘beam optics parameters’, which means the values of the Twiss functions and phase $\Psi(s)$ at certain points s in the LHC. For example at the ATLAS IP ($s = z = 0$) or at the positions of the Roman Pots ($s \approx 240$ m).

By substituting the phase $\Psi(s)$ in Equation (80) and (81) with Twiss functions, it is possible to get an expression for the phase-space coordinate system of the particle motion (u, u') :

$$\gamma(s)u^2(s) + 2\alpha(s)u(s)u'(s) + \beta(s)u'^2(s) = \epsilon, \quad (84)$$

which describes an ellipse in the phase-space system, that is shown in Figure 4.2. The orientation and shape of the ellipse changes and depends on the location s in the ring. However, the area $A = \pi\epsilon$ enclosed by the ellipse is an invariant of the particle motion and remains constant, according to Liouville’s theorem. This area is equal to the emittance ϵ , except for the factor π . By convention the area of the ellipse contains 68 % (1σ) of the beam particles,

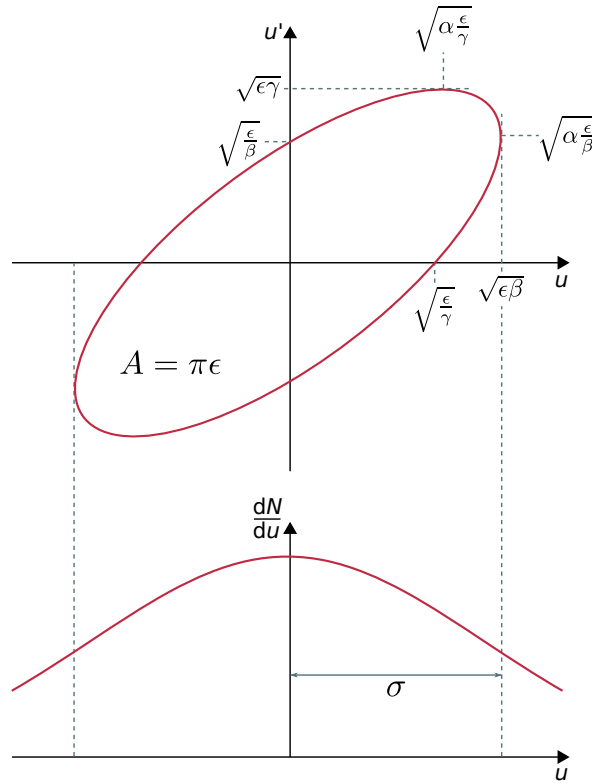


Figure 4.2: Phase ellipse with relevant quantities. The projection of the ellipse onto the u -axis represents the Gaussian beam profile with width σ .

and its projection on the u -axis represents the beam profile (see Figure 4.2). This gives a definition of the emittance in terms of the nominal beam width σ_u as the standard deviation of the Gaussian beam profile:

$$\epsilon = \frac{\sigma^2(s)}{\beta(s)}. \quad (85)$$

From this equation the beam width for a given position s can be written as

$$\sigma(s) = \sqrt{\epsilon\beta(s)}, \quad (86)$$

and by derivation the angular beam divergence

$$\sigma'(s) = \sqrt{\epsilon\gamma(s)} \quad (87)$$

can be deduced.

Since the emittance, and hence the physical size of the beam, decreases with increasing beam momentum during acceleration (adiabatic damping) it is more useful to consider the normalized emittance

$$\epsilon_N = \beta_r \gamma_r \epsilon, \quad (88)$$

where $\beta_r = v/c$ and $\gamma_r = 1/\sqrt{1-\beta_r^2}$ are the usual relativistic parameters. The normalized emittance does not change as a function of the beam momentum and therefore can track beam degradation during particle acceleration.

Now the elements of the transport matrix in Equation (73) can be expressed in terms of the optical Twiss functions, without detailed knowledge of the lattice structure, if their values at the beginning and end of the magnetic lattice are known. With the boundary conditions $s_0 = 0$, $u(0) = u^*$, $u'(0) = u'^*$, $\beta(0) = \beta^*$, $\alpha(0) = \alpha^*$ and $\Psi_0 = \Psi(0) = 0$ equations (80) and (81) are rewritten as

$$u(s) = \sqrt{\frac{\beta(s)}{\beta^*}} [\cos \Psi(s) + \alpha^* \sin \Psi(s)] \cdot u^* + \sqrt{\beta(s)\beta^*} \sin \Psi(s) \cdot u'^*, \quad (89)$$

$$u'(s) = \frac{1}{\sqrt{\beta(s)\beta^*}} [(\alpha^* - \alpha(s)) \cos \Psi(s) - (1 + \alpha(s)\alpha^*) \sin \Psi(s)] \cdot u^* + \sqrt{\frac{\beta^*}{\beta(s)}} [\cos \Psi(s) - \alpha(s) \sin \Psi(s)] \cdot u'^*. \quad (90)$$

This is finally expressed in the matrix formalism with the following transport matrix, using the short cuts $\alpha(s) = \alpha$, $\beta(s) = \beta$ and $\Psi(s) = \Psi$:

$$M_u(s) = \begin{pmatrix} \sqrt{\frac{\beta}{\beta^*}} (\cos \Psi + \alpha^* \sin \Psi) & \sqrt{\beta\beta^*} \sin \Psi \\ \frac{1}{\sqrt{\beta\beta^*}} [(\alpha^* - \alpha) \cos \Psi - (1 + \alpha\alpha^*) \sin \Psi] & \sqrt{\frac{\beta^*}{\beta}} (\cos \Psi - \alpha \sin \Psi) \end{pmatrix}, \quad (91)$$

which relates the position and angle of beam particles at an initial longitudinal position $s_0 = z_0 = 0$ to an arbitrary position s in the accelerator. In the case of the ALFA detector s_0 is the ATLAS interaction point and $s = z = \pm 237.4$ m and $s = z = \pm 241.5$ m are the positions of the four Roman Pot stations. Therefore, the optical parameters needed for the reconstruction of elastic-scattering events in the ALFA detector (see Section 4.3) are completely described by eight transport matrices $M_x(-241.5$ m), $M_x(-237.4$ m), $M_x(237.4$ m), $M_x(241.5$ m), $M_y(-241.5$ m), $M_y(-237.4$ m), $M_y(237.4$ m) and $M_y(241.5$ m).

Table 4.1: Beam optics parameters of the $\beta^* = 90$ m design optics for beam 1 [59].

IP		ALFA		
			RP _{inner}	RP _{outer}
ϵ_N [μm]	3.75	β_x [m]	139.5	124.2
β_x^* [m]	90	β_y [m]	857.5	780.4
β_y^* [m]	90	σ_x [μm]	374	353
α_u^*	0.0	σ_y [μm]	926	883
D_y^* [m]	0.0	σ_x' [μrad]	2.67	2.83
$D_y'^*$	0.0	σ_y' [μrad]	1.08	1.13
σ_u^* [μm]	300	Ψ_x [2π]	0.515	0.520
$\sigma_u'^*$ [μrad]	3.33	Ψ_y [2π]	0.250	0.250

4.2 $\beta^* = 90$ m design beam optics

At LHC energies protons are elastically scattered under very small angles. With the nominal collision beam optics ($\epsilon = 3.75 \mu\text{m}$, $\beta^* = 0.55$ m) it is not possible to reach the smallest $|t|$ values, which correspond to $\theta_u \lesssim 15 \mu\text{rad}$. Since for these optics the beam divergence is expected to be $\sigma' \sim 30 \mu\text{rad}$, which is on the order of the scattering angles, they are not suitable to measure elastic scattering and the total cross-section. Instead an optics with a higher value of $\beta^* = 90$ m is used in order to achieve the necessary small divergence of the beams [59, 60]. The optics parameters and characteristics for the IP and position of the Roman Pots are shown in Table 4.1 for beam 1 and in Figure 4.3 for both beams. These are the normalized emittance ϵ_N , the dispersion D , the derivative of the dispersion D' , the phase advance between the IP and Roman Pots Ψ , the beam width σ , the beam divergence σ' , the betatron function β and its derivative α . However as stated before, the dispersion is irrelevant and can be neglected for elastic scattering. One consequence of the high- β^* optics is a significantly smaller beam divergence than the smallest measurable scattering angles, but on the other hand this implies a bigger beam width at the IP relative to the nominal collision optics. Another consequence is, that the beams are quasi-parallel at the IP because of $\alpha^* = 0$ (no crossing angle), in contrast to the nominal optics, where the beams are colliding with a large vertical crossing angle. The most important property of these optics is the phase advance, which is 90° in the vertical and close to 180° in the horizontal plane.

With these parameters the transport matrix (91) is now defined and the position and local scattering angle at the Roman Pot positions of elastically scattered protons are given by Equation (89) and (90). Furthermore, both the phase advance of $\Psi_y = 90^\circ$ and the quasi-parallel beams at the IP yield the so-called ‘parallel-to-point focusing’ for the vertical plane. Through this, all particles scattered at the same angle at the IP are focused on the same position in the Roman Pot detectors, independent of their vertex position at the IP, which is illustrated in Figure 4.4. With this parallel-to-point focusing ($\alpha_y^* = 0$, $\cos \Psi_y = 0$) the measured vertical position in the Roman Pot detectors described by Equation (89) only depends on the scattering angle and reduces to

$$y(s) = \sqrt{\beta_y(s)\beta_y^*} \sin \Psi_y(s) \cdot y'^* = \sqrt{\beta_y(s)\beta_y^*} \cdot y'^*, \quad (92)$$

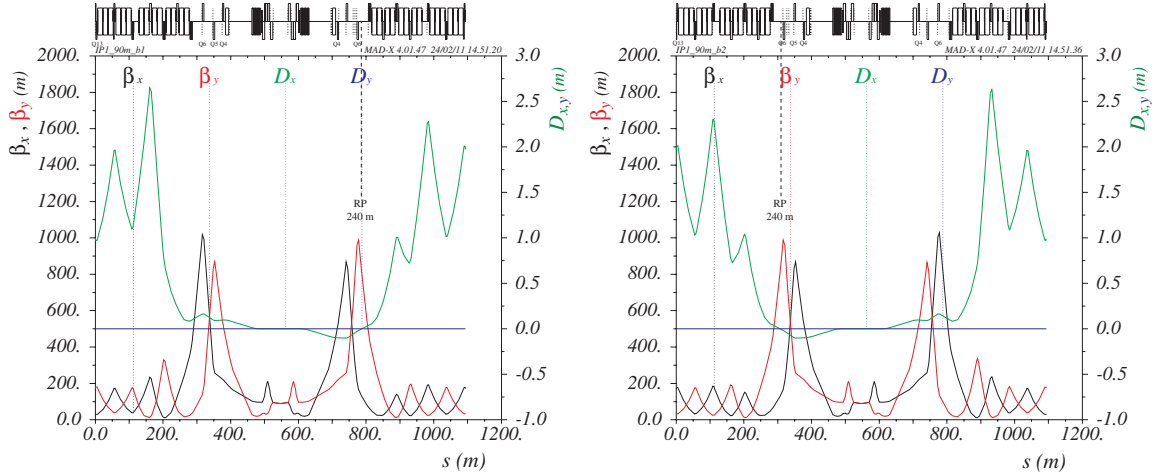


Figure 4.3: Betatron functions $\beta_{x,y}(s)$ and dispersions $D_{x,y}(s)$ of the $\beta^* = 90$ m optics in beam 1 (left) and beam 2 (right) [59]. The ATLAS IP is located at $s = 550$ m in the middle of the horizontal axes.

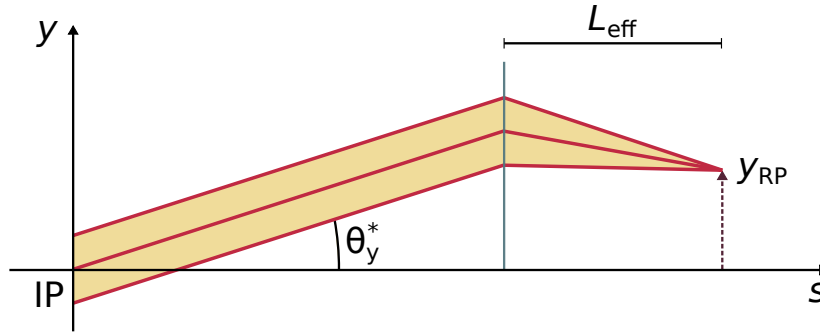


Figure 4.4: Illustration of the parallel-to-point focusing. The effective lever arm is in principle the focal length of the magnetic system in this case.

from which the vertical scattering angle at the IP $\theta_y^* = y'^*$ can be directly deduced by measuring the vertical position:

$$\theta_y^* = \frac{y(s)}{L_{\text{eff},y}(s)}. \quad (93)$$

The quantity $L_{\text{eff},y}(s)$ is called the ‘effective lever arm’ and is defined by $L_{\text{eff},y}(s) = M_{y,12}(s) = \sqrt{\beta_y(s)\beta_y^*} \sin \Psi_y(s)$. It represents the distance between the IP and Roman Pots if focusing or defocusing magnetic elements were not present in the beam line. In Table 4.2 the values of the effective lever arms in the horizontal and vertical plane are quoted for the $\beta^* = 90$ m design optics. The effective lever arm is large in the vertical plane, which provides a good separation at the level of the detector and thus a good resolution for different scattering angles at the IP. In the horizontal plane the phase advance is close to 180° , which does not yield parallel-to-point focusing, so that the vertex position can not be eliminated in Equation (89). This and the relatively small effective lever arm make it necessary to apply more sophisticated methods to reconstruct the horizontal scattering angle which are described in the next section.

From the design optics described here, along with the alignment parameters, magnet currents and field calibrations, all transport matrix elements are calculated. However, the precision of the t -reconstruction depends on the knowledge of these elements. Small corrections are allowed within the range of the systematic uncertainties, which need to be applied to

Table 4.2: Position of Roman Pot stations and effective lever arms for $\beta^* = 90$ m design optics.

Station	s [m]	$L_{\text{eff},x}$ [m]	$L_{\text{eff},y}$ [m]
1	-241.538	-13.017	265.022
2	-237.398	-10.294	277.804
3	237.398	-10.292	277.836
4	241.538	-13.016	265.073

the design optics for the measurement of the total cross-section. Therefore, an ‘effective’ $\beta^* = 90$ m optics is obtained from a global fit, which uses constraints derived from ALFA data and the design optics as a starting point. This fit procedure and the constraints are described in Section 6.7.

4.3 t -reconstruction

In order to determine the differential elastic cross-section the four-momentum transfer t needs to be calculated for each elastic-scattering event. As already described in Section 2, the t value is linked to the scattering angle at the IP θ^* through the relation

$$t = -(p\theta^*)^2 = -p^2 (\theta_x^{*2} + \theta_y^{*2}), \quad (94)$$

where p is the beam momentum and $\theta^* = \sqrt{\theta_x^{*2} + \theta_y^{*2}}$ is small. And it is shown in the previous sections, how the measured position of elastically scattered protons in the Roman Pot detectors of ALFA is related to the scattering angle. For the parallel-to-point focusing in the vertical plane the scattering angle and therefore the t value can simply be reconstructed with the relation in Equation (93). However, the phase advance in the horizontal plane is close to 180° , which means the parallel-to-point focusing is not available there. Hence, four different reconstruction methods are used, which are described in the following and use different aspects of the beam optics to reconstruct the scattering angle and t .

Subtraction method

The first and nominal method used to reconstruct t is called ‘subtraction method’. It exploits the back-to-back topology of elastically scattered protons, where the scattering angle on A- and C-Side of the ATLAS IP are approximately the same in magnitude and opposite in sign, and the protons originate from the same vertex:

$$\theta^* = \theta_A^* \approx -\theta_C^*, \quad (95)$$

$$u^* = u_A^* = u_C^*. \quad (96)$$

However, the scattering angles are only approximately of the same magnitude, because of the divergence of the incoming beams, which slightly worsens the resolution of the reconstructed scattering angle. The ALFA detector system was designed to use these facts, and the beam optics are optimized to maximize the effective lever arm $L_{\text{eff},y}$ in the vertical plane in order to access the smallest possible scattering angles. Using the relation between the measured position in ALFA and the vertex position and scattering angle in Equation (89) and taking the difference of the measured position on A- and C-Side u_A and u_C yields

$$u_A - u_C = M_{11,A}u^* + M_{12,A}\theta_u^* - M_{11,C}u^* + M_{12,C}\theta_u^*. \quad (97)$$

The matrix element M_{11} is small and in first order approximately equal for the two beams (see Table 4.3), so that Equation (97) simplifies to

$$u_A - u_C = (M_{12,A} + M_{12,C})\theta_u^*, \quad (98)$$

where the term proportional to the unknown vertex position is eliminated. This can not be further simplified because the small difference in M_{12} between A- and C-Side, which is more important in the horizontal plane, has to be taken into account. The scattering angle is then reconstructed by

$$\theta_u^* = \frac{u_A - u_C}{M_{12,A} + M_{12,C}}. \quad (99)$$

This is used with the measured horizontal position x and vertical one y , for the inner stations at $|s| = 237$ m and outer stations at $|s| = 241$ m, which yields two values for t per elastic-scattering event of which the average is taken:

$$-t(s) = \left[\theta_x^*(s)^2 + \theta_y^*(s)^2 \right] p^2, \quad (100)$$

$$-t = \frac{t(237 \text{ m}) + t(241 \text{ m})}{2}. \quad (101)$$

The subtraction method is used as nominal method in the vertical and horizontal plane, and yields the best t -resolution (see Section 6.5). The three other methods described in the following are mainly used to cross-check the subtraction method and to determine the effective beam optics parameters (see Section 6.7).

Local angle method

The second method also exploits the back-to-back topology, and is called ‘local angle method’. Instead of the measured position it uses the relation between the measured local angle in the Roman Pot detectors and the vertex position and scattering angle described in Equation (90). Again the difference between the measurement on the A- and C-Side is taken which yields

$$u'_A - u'_C = M_{21,A}u^* + M_{22,A}\theta_u^* - M_{21,C}u^* + M_{22,C}\theta_u^*. \quad (102)$$

The term proportional to the vertex position is eliminated as well under the assumption, that the transport matrix element M_{21} is small and in first order equal on both sides. This results in this equation for the reconstructed scattering angle:

$$\theta_u^* = \frac{\theta_{u,A} - \theta_{u,C}}{M_{22,A} + M_{22,C}}. \quad (103)$$

Here the local angle θ_u of the proton trajectory measured between the inner and outer station is needed. It is determined from the measured track positions in two consecutive Roman Pot detectors on one side:

$$\theta_u = \frac{u_{\text{outer}} - u_{\text{inner}}}{d}, \quad (104)$$

where $d = 4.1$ m is the distance between the two Roman Pots, which is equal on A- and C-side. In contrast to the subtraction method only one measurement of t per event can be done, since there is only one local angle between two consecutive stations. Furthermore, the matrix element M_{22} is the same at $s = 237$ m and $s = 241$, because no active magnetic element lies between the stations. Finally t is calculated according to Equation (100).

The local angle method has one crucial advantage in the horizontal plane: since the matrix element M_{22} is proportional to $\sin \Psi$ and the $\cos \Psi$ term is damped by a factor α , the matrix element is less sensitive to uncertainties in the phase advance Ψ . But on the other hand the measurement of the local angle has only a moderate resolution of about $10 \mu\text{rad}$, because of the small distance d between two consecutive stations. This results in a worse t -resolution of the local angle method compared to the subtraction method. However systematic uncertainties related to the beam optics are reduced.

Local subtraction method

A third possibility to reconstruct the scattering angle is to perform a local subtraction separately on the A- and C-Side. This method is therefore called 'local subtraction method', and starts again with Equation (89) which gives with $S = A, C$ for the inner and outer detectors on one side

$$u_S(237) = M_{11,S}(237)u^* + M_{12,S}(237)\theta_u^*, \quad (105)$$

$$u_S(241) = M_{11,S}(241)u^* + M_{12,S}(241)\theta_u^*. \quad (106)$$

This is simply a system of two linear equations with two unknown variables and a single solution, that is solved for θ^* by substituting u^* :

$$\frac{u_A(237) - M_{12,S}(237)\theta_u^*}{M_{11,S}(237)} = \frac{u_A(241) - M_{12,S}(241)\theta_u^*}{M_{11,S}(241)}. \quad (107)$$

$$\theta_S^* = \frac{M_{11,S}(241)u_A(237) - M_{11,S}(237)u_A(241)}{M_{11,S}(241)M_{12,S}(237) - M_{11,S}(237)M_{12,S}(241)}. \quad (108)$$

The method allows to fully eliminate the vertex position by combining the inner and outer stations without any assumption on the equality of the matrix elements. However, the matrix element M_{11} is used, which is proportional to $\cos \Psi$ and therefore worsens the resolution in the vertical plane. As for the subtraction method two t -values per elastic-scattering event can be reconstructed of which again the average is taken:

$$-t_S = \left(\theta_{x,S}^{*2} + \theta_{y,S}^{*2} \right) p^2, \quad (109)$$

$$-t = \frac{t_A + t_C}{2}. \quad (110)$$

Lattice method

The fourth and final method is called 'lattice method', and uses both the measured positions and local angle to determine the scattering angle. It does not exploit the elastic-scattering topology of the events. If all transport matrix elements are known, Equation (73) can be solved for (u^*, θ_u^*) by inverting the transport matrix:

$$\begin{pmatrix} u^* \\ \theta_u^* \end{pmatrix} = M_u^{-1} \begin{pmatrix} u \\ \theta_u \end{pmatrix}, \quad (111)$$

which yields from the second row

$$\theta_u^* = M_{21}^{-1}u + M_{22}^{-1}\theta_u. \quad (112)$$

Table 4.3: Transport matrix elements in the horizontal and vertical plane of the eight Roman Pot stations for $\beta^* = 90$ m effective optics.

Plane, side	M_{11}	M_{12}	M_{21}	M_{22}
$x(+237 \text{ m})$	-1.2461	-10.71	0.018 11	-0.6469
$x(+241 \text{ m})$	-1.1710	-13.39	0.018 11	-0.6469
$y(+237 \text{ m})$	0.0980	280.8	-4.65×10^{-3}	-3.114
$y(+241 \text{ m})$	0.0787	267.9	-4.65×10^{-3}	-3.114
$x(-237 \text{ m})$	-1.2458	-10.68	0.018 08	-0.6477
$x(-241 \text{ m})$	-1.1708	-13.36	0.018 08	-0.6477
$y(-237 \text{ m})$	0.0910	280.6	-4.57×10^{-3}	-3.116
$y(-241 \text{ m})$	0.0720	267.7	-4.57×10^{-3}	-3.116

Here M_{ij}^{-1} are the elements of the inverted transport matrix M^{-1} and not the inverted elements of M . With the help of Cramer's rule the inverted matrix can simply be written in terms of elements of M as

$$M^{-1} = \frac{1}{M_{11}M_{22} - M_{12}M_{21}} \begin{pmatrix} M_{22} & -M_{12} \\ -M_{21} & M_{11} \end{pmatrix}. \quad (113)$$

With this method four t -values are reconstructed per event, one for each detector in the corresponding spectrometer arm. Again the average is taken as final value:

$$-t(s) = \left[\theta_x^*(s)^2 + \theta_y^*(s)^2 \right] p^2, \quad (114)$$

$$-t = \frac{t(-241 \text{ m}) + t(-237 \text{ m}) + t(237 \text{ m}) + t(241 \text{ m})}{4}. \quad (115)$$

The matrix inversion obscures a clear dependence of the reconstructed scattering angle on the transport matrix elements and thereby on the beam optics. Since eventually all matrix elements and the local angle are used for the reconstruction, the resolution is worse than for the subtraction method. As described in Section 6.2, the first row of Equation (111) is used to reconstruct the vertex position and get an additional handle on the background for systematic purposes:

$$u^* = M_{11}^{-1}u + M_{12}^{-1}\theta_u. \quad (116)$$

The three alternative methods to the subtraction method are only considered in the horizontal plane because of the optics parameters uncertainties. In the vertical plane always the subtraction method is applied which yields the best resolution and depends less on the optics. The t -value of an elastic-scattering event is then in general reconstructed for method $i = \{\text{subtraction, local angle, local subtraction, lattice}\}$ by

$$-t_i = \left(\bar{\theta}_{x,i}^{*2} + \bar{\theta}_{y,\text{sub}}^{*2} \right) p^2, \quad (117)$$

where $\bar{\theta}_{x,i}^*$ is the average scattering angle in the horizontal plane reconstructed with method i and $\bar{\theta}_{y,\text{sub}}^*$ the average vertical scattering angle reconstructed with the subtraction method.

The final values of the transport matrix elements obtained from the effective optics fit are shown in Table 4.3. In the vertical plane the scattering angle terms $M_{y,21}$ and $M_{y,22}$ are three to four orders of magnitude larger than the vertex position terms $M_{y,11}$ and $M_{y,12}$. Therefore, an asymmetry in the vertex terms between the beams/sides of 7 % is irrelevant for the

4 *Beam optics and t-reconstruction*

t-reconstruction. In the horizontal plane the scattering angle terms are only ten times larger, however for the subtraction method the asymmetry in $M_{x,11}$ between the beams/sides is negligible and ensures a good cancellation of the vertex term. For the local angle an asymmetry of 1.7 % is present in $M_{x,21}$, which entails a small error in the scattering angle.

5 Monte Carlo simulations

Two Monte Carlo (MC) simulations—a full and a fast one—are used to calculate and estimate different properties used in the total cross-section analysis. The main difference between the two simulations is the detector response: in the full simulation the ALFA detector system is described in GEANT4 [61, 62] and the interactions of elastically scattered protons with the detector material are simulated. In the fast simulation GEANT4 is not used and the reconstructed position of the scattered protons in the detectors are smeared by just applying the detector resolution. Both simulations are described in detail in the following sub-sections.

In both simulations PYTHIA 8.1 [63, 64] is used as generator to produce elastically scattered protons with a differential elastic cross-section according to Equation (28). Two proton beams with a nominal energy of $E_{\text{beam}} = 3.5$ TeV are colliding in z -direction like it was for ATLAS in 2011. The coordinate system in the simulations is the same as for ATLAS described in Section 3.2.2. Furthermore, there is no angle between the colliding beams like it was in the $\beta^* = 90$ m run. A small difference between full and fast simulation at generator stage is the incorporation of angular divergence and energy smearing of the incoming initial state protons in the two beams which lead to a distortion of the reconstructed scattering angle spectra. The full simulation uses the ‘beam’ class of PYTHIA 8.1 in which these effects are already implemented. In this class the shape of the angular and energy distribution of the colliding beams only need to be specified by the user and the initial state protons are generated accordingly. As a result the final state protons after the elastic-scattering process also incorporate both effects. The fast simulation does not use the beam class because of several technical reasons. Instead, the initial state protons are generated as head-on colliding without angular divergence at nominal beam energy and the entire system of initial and final state protons is later transformed by a Lorentz-boost-rotation according to the beam properties to include the divergence and energy smearing. Both methods give equivalent results in terms of the distribution of the final state protons.

The parameters for the elastic-scattering process and the incoming beams are the same for both methods and are listed in Table 5.1. These parameters are taken from theoretical predictions (compare Section 2) and preliminary results of the total cross-section analysis. The widths of the vertex distributions σ_x and σ_y in Figure 5.1 are taken from beam spot measurements [65], the transverse momentum distributions σ_{p_x} and σ_{p_y} are calculated from

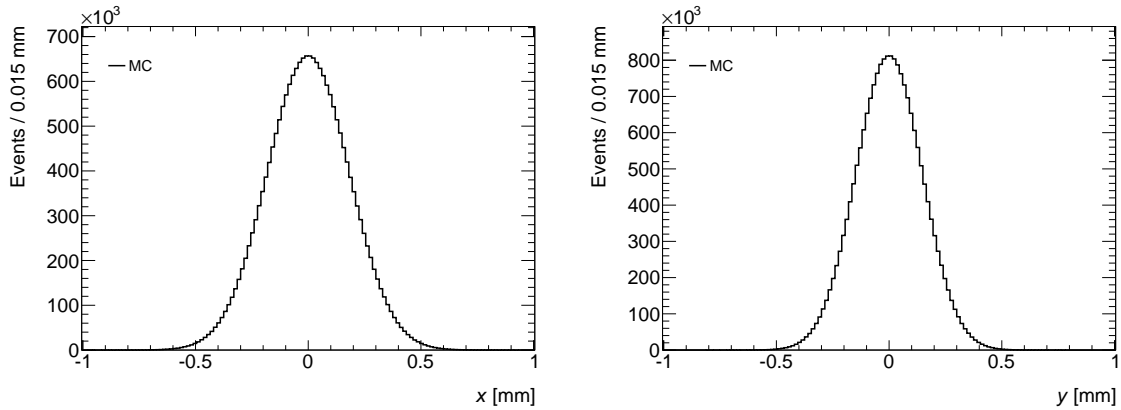


Figure 5.1: Horizontal and vertical vertex distribution at the IP of elastic-scattering events.

Table 5.1: Parameters for event generation of elastically scattered protons. B1 = Beam 1, B2 = Beam 2.

Parameter	Value	
σ_{tot}	95	mb
B	19.5	GeV^{-2}
ρ	0.14	
Λ	0.72	GeV^2
ϕ_C	0.577	
\sqrt{s}	7	TeV
σ_x	182.2	μm
σ_y	147.1	μm
σ_z	0	
$\sigma_{p_x}(\text{B1})$	10.28	MeV
$\sigma_{p_y}(\text{B1})$	8.948	MeV
$\sigma_{p_x}(\text{B2})$	11.74	MeV
$\sigma_{p_y}(\text{B2})$	8.989	MeV
σ_{p_z}	395.5	MeV

the measured emittance given in Section 3.3.1 and the beam energy smearing σ_{p_z} from the intrinsic energy uncertainty $\Delta E/E$.

The generated events are purely from elastic scattering and the complete kinematic information for initial and final state protons is available for analysis. This also includes the true t without angular divergence and energy smearing, the so called \hat{t} , for every elastic-scattering event. There are no beam-halo background, other diffractive events, pile-up or radiative corrections in the two simulations. Later only background from hadronic showers appears in the full detector simulation with GEANT4, but not in the fast simulation. After the events are generated they are injected into different beam transport codes which are also described in the following sub-sections.

5.1 Fast simulation

After generation and scattering is performed with PYTHIA the final state protons are injected into the MAD-X [66, 67] software package to perform the transport from the IP to the ALFA stations in the fast simulation. MAD-X uses a scripting language and is the standard software at CERN to describe particle accelerators, simulate beam dynamics and optimize beam optics. The polymorphic tracking code (PTC) module of MAD-X, which performs a symplectic thick-lens tracking, is used to transport the protons from one magnetic element to the following one up to the Roman Pot stations. The MAD-X software reads the elements from a configuration file, where they are defined in the LHC sequence with their actual position, strength and apertures. This file is produced according to the effective $\beta^* = 90$ m optics, that where found with the optimization (see Section 6.7). The transport from element to element is performed by means of the transport matrix formalism, which is calculated from the optical functions according to Equations (73) and (91). The optical functions are determined from the magnet strengths and positions of the effective optics. For each element a check is done, if the proton is still inside the aperture. If not, it is simply lost and the transport is stopped at this point for the particular proton. A simulation of the interaction of the proton with the absorbing material is not done in the MAD-X transport, which means that potential

hadronic showers, created in the beam line in front of the Roman Pot stations, are not taken into account. The protons are transported to the positions of the inner and outer stations at both sides of the IP and if they survive the transport, the coordinates and momenta are saved for further use. At this point no simulation of the interactions in the detector material is done and only a parametrized Gaussian smearing according to the position resolution of the detectors is applied to the coordinates in x and y . The applied smearing is tuned based on the full simulation and measured data, which is described in Section 5.3. A large sample of several million elastic-scattering events was produced with the fast simulation for various calculations and studies. Statistical uncertainties are in general negligible, because of the large number of generated events.

5.2 Full simulation

The generation, transport and reconstruction of elastic-scattering events in the full simulation is performed entirely in the ATLAS offline software framework Athena [68, 69]. After the final state protons are generated, like it is described above, they are injected into the ALFA_BeamTransport package, which performs the transport from the IP to the Roman Pot stations. The BeamTransport package is similar to MAD-X but it uses a modified version of the FPTrack code [70] called FPTracker to do the transport. It was verified in a dedicated study [71], that the differences between MAD-X and ALFA_BeamTransport are negligible and both are fully exchangeable. FPTracker uses the exact solutions of the equations of motions in the magnetic field in the small deviations approximations to calculate proton trajectories inside the LHC. It reads LHC configuration data from files (twiss files) containing information on the location, type and strength of the beam line magnets and collimator settings. These files are, like for MAD-X, also produced according to the effective $\beta^* = 90$ m optics. The proton is tracked down the beam line by iterating over the beam line elements until either the proton goes out of aperture or it traverses a plane which marks the end of the tracking. In one iteration the proton is first transported to the front face of an element by projecting from its current position at the back-end of another element in a straight line. Second if the proton is inside the aperture, a bending of the trajectory is performed according to the magnet parameters. If the proton goes out of aperture it is simply lost and the tracking is stopped for this particle. Like for MAD-X no simulation of the interaction with absorbing material is done and possible hadronic showers are not taken into account. The protons are transported to a position right in front of the inner stations on both sides of the IP and the coordinates and momenta are available for the next step.

After the transport the protons are injected into a GEANT4 simulation of the Roman Pot stations. The passage of the protons through the detector material is simulated using an exact description of the four stations. This includes the position, metrology and material of all involved detector elements (frames, fibres, ...). The position of the detectors with respect to the beam line are read from a database to be in accordance with the positions in the $\beta^* = 90$ m run at $\sqrt{s} = 7$ TeV analysed in this thesis. All possible interactions of the protons and secondary particles with the material are included and switched on. The response of the scintillating fibres of the main and overlap detectors is simulated and digitized to be used in the next step. However, the response of the trigger tiles is not simulated and therefore no triggers are available in the full simulation. Only the material of the tiles is present as an absorber, and an elastic-scattering trigger signal has to be simulated at the analysis stage with other available truth information. Cross-talk and noise effects in the fibres or PMTs are also not implemented. Because of the GEANT4 stage in the simulation, background from

5 Monte Carlo simulations

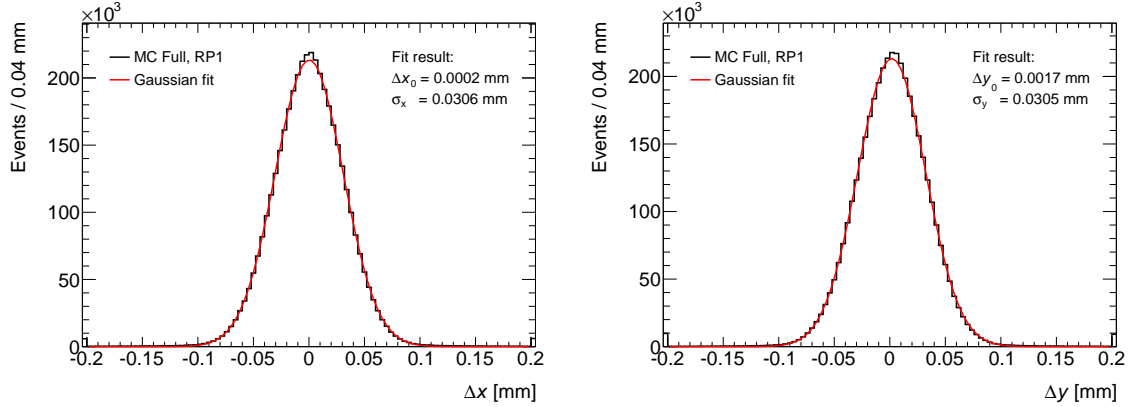


Figure 5.2: Horizontal (left) and vertical (right) position resolution in RP1 for full simulation after elastic-scattering event selection cuts. The distributions for the other detectors look similar.

hadronic showers started inside the detector material can be observed and studied. This is also the only background which is considered in any of the simulations (fast or full).

After the digitization of the scintillating fibre response the raw simulation data is available in the same format as for real data. Therefore, the same tracking algorithm as in Section 3.4 can be applied to get reconstructed tracks. This is done in the next step: The raw simulated data is reconstructed with the tracking algorithm with the same parameters as for the $\beta^* = 90$ m run.

In the last step the coordinates of the reconstructed tracks are then converted into the same n-tuple format as for real data. Except for operational parameters and trigger data all information from the reconstruction is available in this n-tuple, which can be analysed in a similar way as the measured data. In contrast to the fast simulation no additional smearing due to position resolution is applied, because this is already included as an intrinsic resolution in the GEANT4 simulation. With the full simulation also a large sample of several million elastic-scattering events was produced for resolution and shower studies.

5.3 Tuning and comparison with data

The positions of the protons after the transport in the fast simulation need to be smeared and tuned to the real position resolution of the detectors. The resolution was measured in a test beam setup (TB) in 2009 in the H6B area of the H6 beam line of the CERN SPS North Area with a 120 GeV hadron beam for every Roman Pot detector to about $30 \mu\text{m} \leq \sigma_{x,y}^{\text{TB}} \leq 36 \mu\text{m}$ and equal for horizontal and vertical position [46, 49]. The values of the eight detectors are listed in Table 5.2. A slightly better resolution is expected at higher energies at the LHC because of a reduced impact of multiple scattering and hadronic showers. On the other hand the resolution is calculated from the full simulation, by comparing the reconstructed track position in the detectors with the position after the transport, but before the GEANT4 step. Figure 5.2 shows the horizontal and vertical position resolution $\sigma_{x,y}^{\text{full}}$ of RP1 from the full simulation fitted with a Gaussian distribution. The values for the detectors are in the range $23 \mu\text{m} \leq \sigma_{x,y}^{\text{full}} \leq 31 \mu\text{m}$, where the inner detectors have a slightly better resolution than the outer ones. In Table 5.2 the results for all Roman Pots can be found. The difference between the detectors is on one side related to the alignment of fibres, which were measured by means of optical metrology and implemented in the GEANT4 simulation and on the other side to the

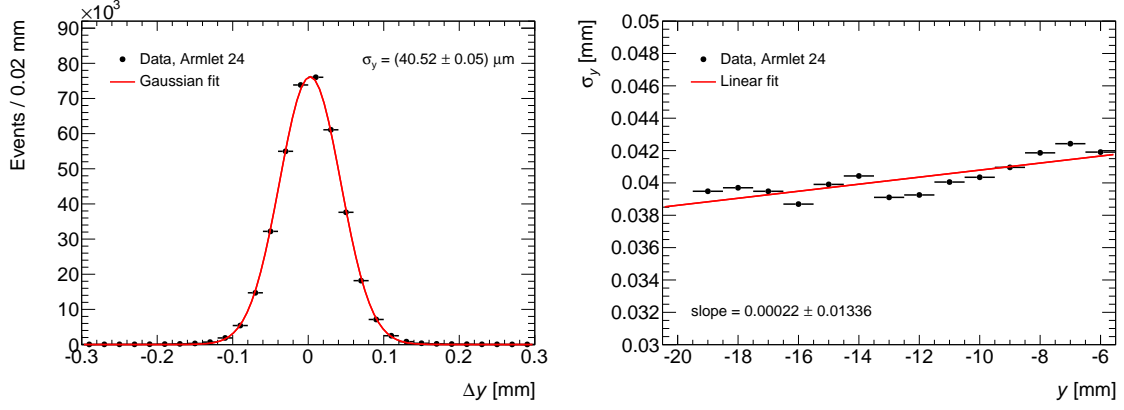


Figure 5.3: Vertical convoluted resolution for armlet 24 with Gaussian fit (left) and dependence of this resolution on the vertical track position with linear fit (right).

placement of the detectors in the inner or outer position relative to the IP. In outer detectors the resolution is deteriorated, because of hadronic interactions of the protons in the inner ones. Therefore, the resolution in outer detectors is in average larger than in the inner ones by a factor of $f_\sigma = 1.1$. Compared to the test beam data and real data from the LHC the full simulation predicts a too good resolution. This is mainly related to the absence of cross-talk and multi-track events resulting from an overlap of elastically scattered protons with beam-halo particles and to the underestimation of hadronic shower production in GEANT4. This is probably also the reason for the very small resolution of $\sigma_{x,y}^{\text{full}} = 22.9 \mu\text{m}$ in RP6, which is about 16 % smaller compared to the average of all detectors. The smallest value of the test beam resolution is e.g. only 8 % smaller than the average.

Another possibility is to determine the resolution from real data of the $\beta^* = 90$ m run. Here the residuals of the measured position in inner detectors compared to outer ones is used to get a convoluted position resolution of inner and outer detectors. The measured vertical position in the inner detector is extrapolated to the outer one on the same side by using the lever arms, like it is described in Section 3.4.2, and subtracted from the measured position in the outer detector to get the residual distribution. This distribution, shown in Figure 5.3 (left) for armlet 24, is then fitted with a Gaussian function to get the vertical convoluted resolution σ_y^{conv} . In the horizontal plane the fitted convoluted resolutions are of the order of $\sigma_x^{\text{conv}} \approx 80 \mu\text{m}$ and cannot be used. Because of a lack of parallel-to-point focusing the extrapolated positions do not only depend on the measured positions and the lever arm ratios, but also on the unknown vertex position at the IP, which dominates the residuals. Both test beam measurements and full simulation results confirm, that the resolution in the horizontal and vertical plane are the same and therefore the residuals in y are sufficient to also get the resolution in x . The convoluted position resolutions in x and y of all four detectors pairs (armlets) 13, 24, 57 and 68 are given in Table 5.2.

The fast simulation is now tuned to the data by using the convoluted position resolution $\sigma_{x,y}^{\text{conv}}$ and the deterioration factor f_σ from full simulation by considering the relations

$$\sigma_{u,\text{outer}} = f_\sigma \sigma_{u,\text{inner}} \quad (118)$$

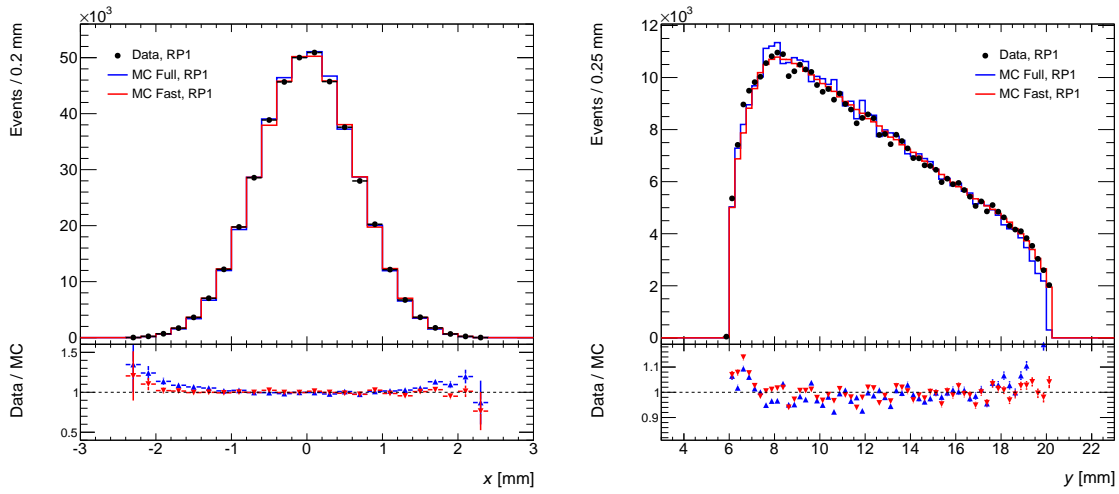
and

$$(\sigma_u^{\text{conv}})^2 = \sigma_{u,\text{inner}}^2 + \sigma_{u,\text{outer}}^2 = (1 + f_\sigma^2) \sigma_{u,\text{inner}}^2 \quad (119)$$

with $u \in \{x, y\}$. The resolution values $\sigma_{x,y}^{\text{tuned}}$ tuned in this way can also be found in Table 5.2. A slight dependence of the convoluted resolution on the vertical track position on the detec-

Table 5.2: Position resolution from test beam (TB), full simulation (full) and the tuned data values (tuned). In addition the convoluted resolutions of the detector pairs from real data are shown (conv).

RP	$\sigma_{x,y}^{\text{TB}}$ [μm]	$\sigma_{x,y}^{\text{full}}$ [μm]	$\sigma_{x,y}^{\text{conv}}$ [μm]	$\sigma_{x,y}^{\text{tuned}}$ [μm]
1	36	30.6	43.3	32
2	35	29.2	40.5	29.9
3	34.4	28.6	43.3	29.1
4	31.1	25.2	40.5	27.2
5	34.8	28.6	40.8	27.4
6	33.2	22.9	38.8	26.1
7	30.7	26.2	40.8	30.1
8	31	26.3	38.8	28.7

**Figure 5.4:** Comparison of horizontal (left) and vertical (right) position distributions in RP1 for data, fast simulation and full simulation after elastic-scattering event selection cuts.

tor surface with a systematic trend can be observed, where the resolution gets linearly worse towards the detector edge for all eight detectors. This effect is shown in Figure 5.3 (right) for armlet 24, and can be explained by a feature of the detector assembly: the scintillating fibres are glued on a special Ti support, where a high-precision edge was machined to allow an accurate alignment of the v - and w -fibres against this edge. Therefore, the first fibres in the region of larger y are precisely aligned with an optimal overlap across the staggered layers. As more fibres are glued and aligned against precedent ones, the accuracy of the alignment increasingly deteriorates with a peak at the detector edge, because glue is accumulated in the inter-fibre gaps. However, this effect has only a small impact on the fast simulation and analysis; therefore the y -integrated convoluted resolutions from before are used for nominal analysis.

Systematic uncertainties are derived from replacing the y -integrated resolution model with the y -dependent parametrization, with the test beam measurements and with the full simulation values.

A comparison of the fast and full simulation with measured observables from data is done with horizontal and vertical position distributions in Figure 5.4 and with local angle distributions in Figure 5.5. The distributions are for RP1 and include elastic-scattering events after

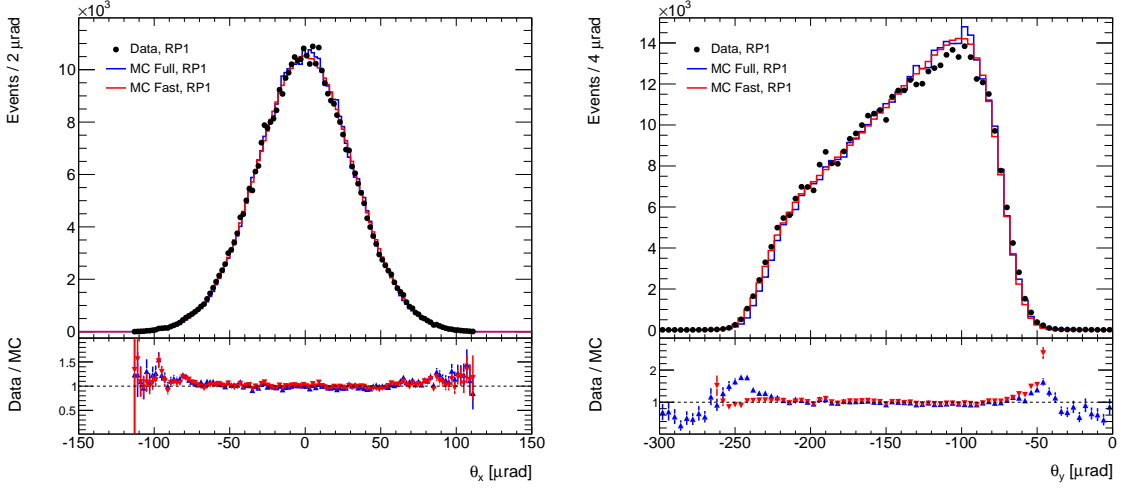


Figure 5.5: Comparison of horizontal (left) and vertical (right) local angle distributions in RP1 for data, fast simulation and full simulation after elastic-scattering event selection cuts.

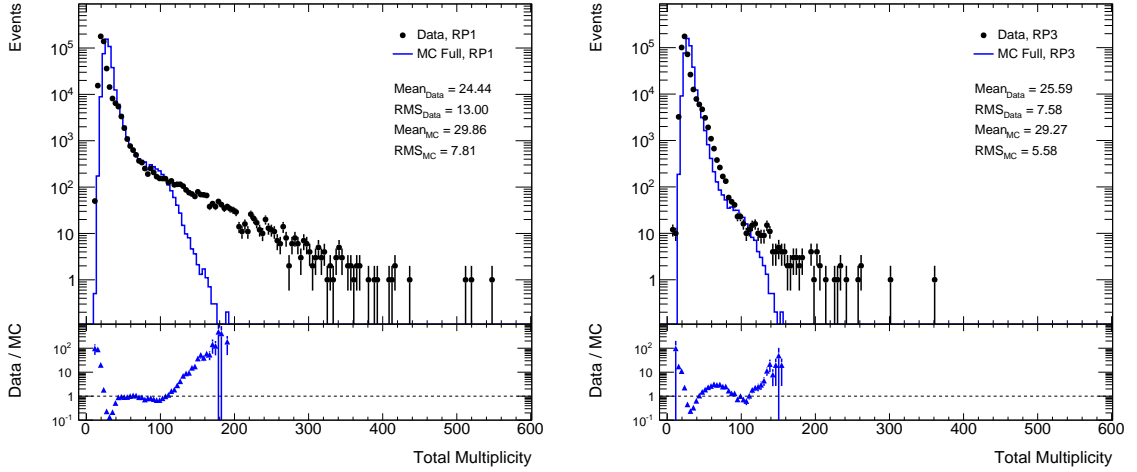


Figure 5.6: Comparison of total multiplicity distributions in outer detector RP1 (left) and inner one RP3 (right) for data and full simulation after elastic-scattering event selection cuts.

event selection cuts, which are described in Section 6.1. Cuts are applied in the same way to full, fast simulation and measured data. They show overall a good agreement between fast simulation, full simulation and data. For the vertical local angle θ_y in some bins an irregular structure in the data is observed, which is likely related to fibre metrology or mapping issues. However, this does not affect the t -reconstruction, which uses only the position in the vertical plane and not the local angle. The fractions between data and MC simulation in the lower part of the figures also show some slight deviations at the edges of all distributions. Fast and full simulation also agree very well except for this edge deviations. The agreement for the rest of the eight detectors is also very good and comparable with RP1, which is shown here as an example.

Another interesting observable which is only available in data and full simulation is the total fibre multiplicity M_{tot} , which is the sum of all fibres giving a signal. A comparison between data and full simulation can be seen in Figure 5.6 for outer detector RP1 and inner detector RP3. The agreement in the low multiplicity range is rather poor. The peak in the

full simulation, corresponding to events with only one reconstructed track and almost no noise, is shifted from $M_{\text{tot}}^{\text{data}} = 21.6$ in the data to a larger value of $M_{\text{tot}}^{\text{full}} = 28.6$. Furthermore, the data shows much more events with higher total multiplicity up to $M_{\text{tot}}^{\text{full}} \approx 350$ for the inner and $M_{\text{tot}}^{\text{full}} \approx 550$ for the outer detector. These high multiplicity events are mainly caused by hadronic showers inside the detector, elastic-scattering pile-up, beam-halo background and cross-talk. The full simulation does not include all of these background types (pile-up, beam-halo, cross-talk) and the showers created inside the detectors are apparently not modelled well enough. Especially showers created by the beam screen (a protection element) of magnet Q6 are not in the simulation, but they are clearly observed in the measured data. Therefore, more high multiplicity events and events with higher maximum multiplicity are observed in data compared to full simulation. This is one of the main reasons the full simulation is not used for critical parts of the total cross-section analysis but only for some cross checks and the tuning described above. The fast simulation also does not include any background, but it can be produced much faster with much more statistics, because of the missing `GEANT4` step. Therefore, the tuned fast simulation is used as main MC simulation for the analysis to determine among others the acceptance in Section 6.4, the t -resolution and the unfolding corrections in Section 6.5. Some more details on the issue of total multiplicity in the full simulation can be found in Section 6.3.10, where the event reconstruction efficiency determined from MC simulation is compared to the nominal method.

6 Data analysis

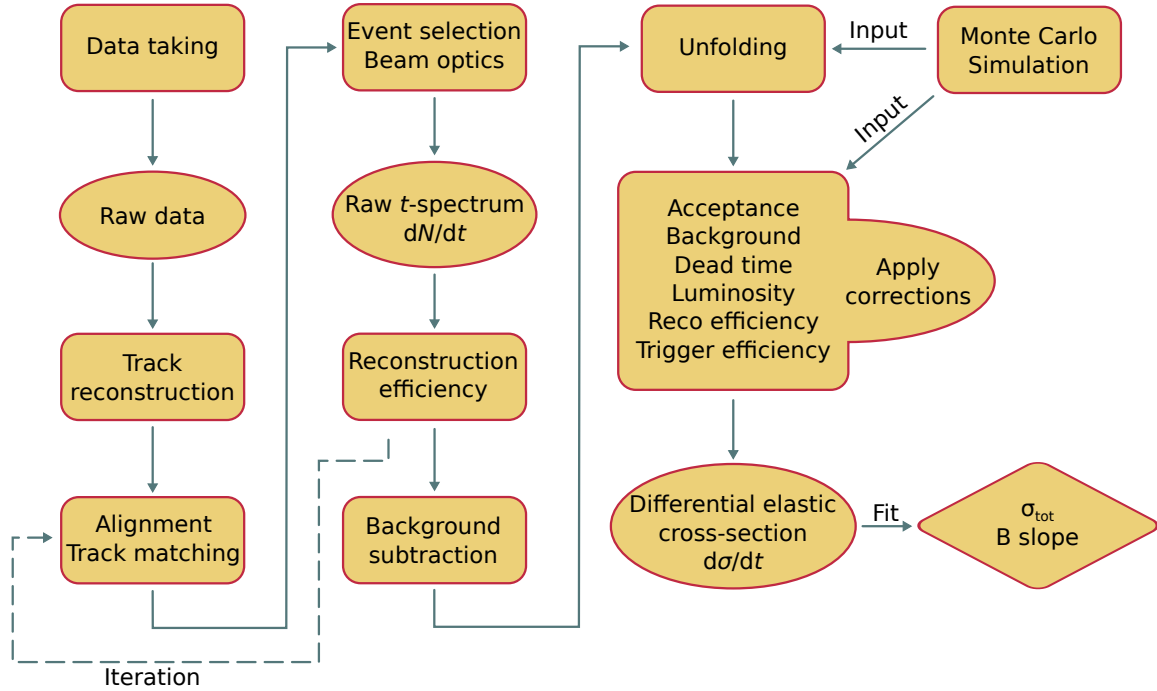


Figure 6.1: Analysis flow from data taking to the final total cross-section results with all relevant steps.

In this section several steps of the analysis of elastic-scattering events to the point of the differential elastic cross-section are described. The analysis flow is illustrated in Figure 6.1 with all relevant steps from data taking to the final results. After data taking the first steps are the reconstruction of particle tracks in the detectors, the alignment of the detector system in the beam coordinate system and the matching of tracks from elastic scattering. These three steps are already described in the Section 3.4. The next steps are the selection of elastic-scattering events and the determination of the effective optics, by using several observables sensitive to the transport matrix to fit small corrections to the relevant nominal beam parameters. The effective optics fit procedure is presented in Section 6.7. After these steps a raw and uncorrected differential t -spectrum dN/dt is reconstructed with the four different reconstruction methods described in Section 4.3 which is shown in Section 7.1. Now several corrections need to be applied to get a normalized differential elastic cross-section. First the efficiency to reconstruct elastic-scattering events in all four detectors of a spectrometer arm is determined in a newly developed data-driven way. Since this event reconstruction efficiency is the author's main contribution to the measurement of the total hadronic cross-section, it is most comprehensively described. Since the alignment needs input from the elastic-scattering event selection and the reconstruction efficiency an iterative procedure is done, in which the steps from alignment to efficiency determination are repeated. This procedure usually converges after a few reiterations, where the alignment and reconstruction efficiency changes are small compared to the previous iteration step. Next the amount of irreducible background is estimated and a background subtraction method is applied to the raw t -spectrum. Then the fast simulation, described in Section 5, is used to calculate acceptance corrections and to unfold the background subtracted data for resolution effects. The luminosity for the $\beta^* = 90$ m run is measured in a dedicated analysis by the ATLAS luminosity task-force, and

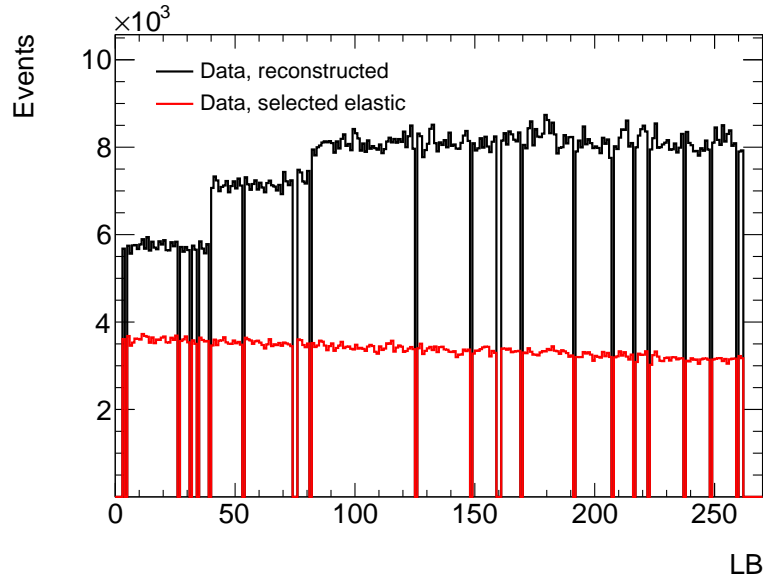


Figure 6.2: Amount of events per luminosity block. In black are all events with $BCId = 1$ and in red are elastic-scattering events after the entire event selection.

together with the other corrections applied to the unfolded differential t -spectrum to yield the differential elastic cross-section. Finally a fit with the theoretical form of the differential elastic cross-section in Equation (28) is performed in Section 7.2 to yield the results for the total cross-section and derived quantities.

6.1 Elastic-scattering event selection

Events for the analysis are selected from the single run 191373 described in the data taking section 3.3. During this run two streams with ALFA data were recorded. The physics stream and the calibration stream, which differ slightly with respect to the trigger signals and their pre-scaling. The details of that are also described in the mentioned data taking section.

Only data from collisions from a single bunch pair with $BCId = 1$ are used. This bunch had an intensity of about 7×10^{10} protons. The rest are 12 pilot bunches with an intensity of about 1×10^{10} protons and a higher beam-halo background fraction. They are not used for the analysis because of this background. In addition, the luminosity is determined reliably only for this single high intensity bunch pair.

The complete run consists of 263 luminosity blocks (LB), where a LB is defined as the data taken in 60 s of running time. Only a list of good LBs is used: The LBs have to have a dead-time which is smaller than 5 % and a duration of at least the nominal 60 s. This leaves the list with 240 good LBs for analysis with an average life fraction of $\epsilon_{DAQ} = 99.73$ %. Figure 6.2 shows the amount of events in each used good LB. The black distribution is for all events in the LB which have $BCId = 1$ and the red one is for elastic-scattering events after the entire event selection.

Elastic-scattering events with $BCId = 1$ and in these good LBs are then selected via level 1 trigger-signal bits (CTP bits). The bits `L1_ALFA_ELAST15` and `L1_ALFA_ELAST18` are used and have to be set as 'true'. They correspond to a signal in the ALFA trigger tiles of at least one detector on A-Side and one on C-Side in spectrometer arm 1368 (ELAST15) or arm 2457 (ELAST18).

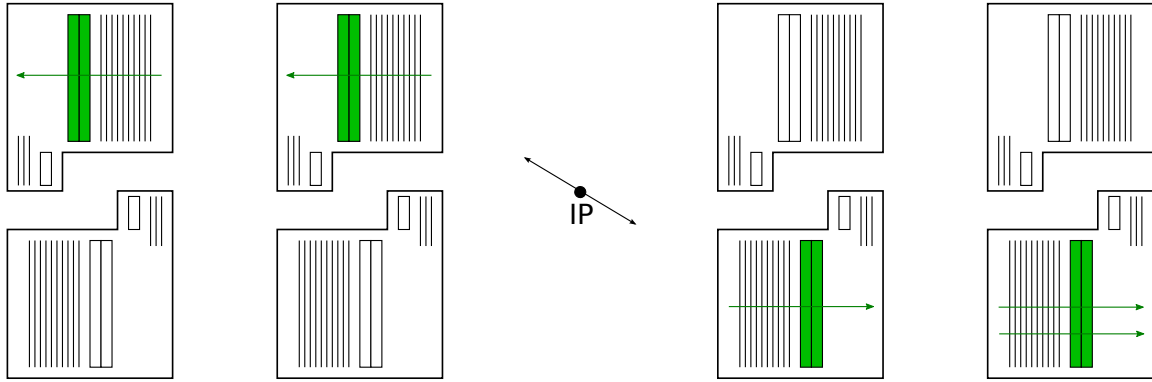


Figure 6.3: Diagram of an elastic-scattering event. An elastic-scattering trigger signal is present in arm 1368 shown by green trigger tiles. In RP1, RP3, RP6 and RP8 tracks are reconstructed shown by green arrows. RP8 has also an additional reconstructed track.

After these trigger signals are selected the events also have to have reconstructed tracks in all four detectors of the spectrometer arm that corresponds to the trigger-signal bit. There needs to be at least one track, which does not exclude events with multiple tracks, where e.g. a shower or background particle is reconstructed in addition to the elastic-scattering track. The diagram in Figure 6.3 shows a schematic of such an elastic-scattering event in arm 1368 with an elastic-scattering trigger signal and reconstructed tracks in all four detectors.

With these criteria raw elastic-scattering event candidates are selected. In the last stage several selection cuts are applied to the reconstructed tracks of the events. This is done to ensure the events are fully contained in the fiducial volume of all Roman Pot detectors, to reject background and enhance the selection of elastic-scattering events in back-to-back configuration. An event has to pass all of these cuts to be counted as an elastic-scattering event and to be used for the analysis of the differential t -spectrum. The cuts are described in detail in the following sub-sections.

6.1.1 Fiducial cuts

The tracks in all four detectors of an elastic-scattering event candidate have to be inside the fiducial volume of ALFA which defines the acceptance. This is done with two cuts on the vertical coordinate of the tracks. One cut is placed at the physical detector edge close to the beam. Tracks have to be $60 \mu\text{m}$ away from this edge to pass the cut. The fibre efficiency is above 99 % in this region, which was measured in test beams. The position of the edge was determined by means of metrology also in test beams.

Another cut is placed at the other end of the vertical range around $y \approx 20 \text{ mm}$. An increased contribution from showers, generated by protons hitting the beam screen at quadrupole magnet Q6 (compare Figure 3.5 on page 20), can be observed in this region. The protons hitting this beam screen, which is an element used to protect the magnet, are actually outside of the acceptance. But hadronic shower fragments can be reconstructed inside ALFA and might be considered as elastically scattered protons. In the distribution of the vertical track coordinate y the position of the shadow of this beam screen is visible as an edge. The cut is now placed 1 mm away from this edge, which ensures that tracks are not coming from beam screen shower particles. The edge position of the beam screen shadow in each detector is determined by fitting the vertical track distribution in the edge region with

6 Data analysis

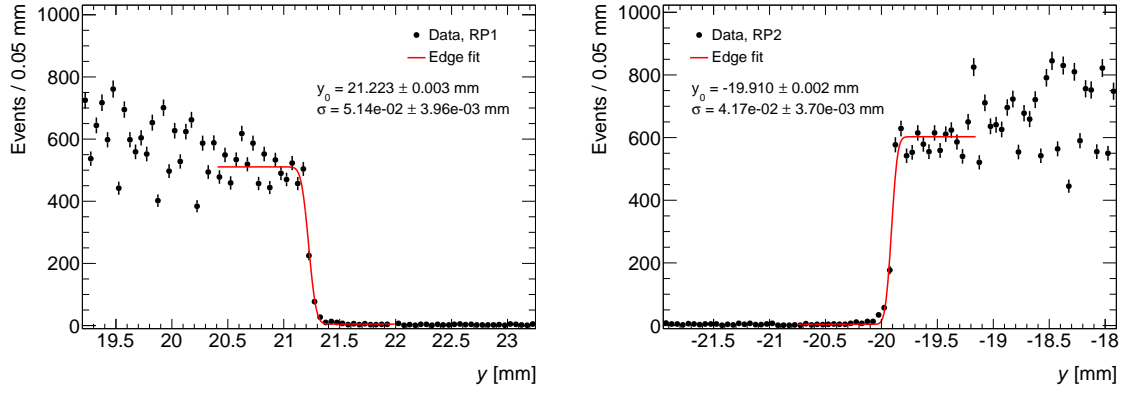


Figure 6.4: Fits of the beam screen edge in RP1 (left) and RP2 (right) with smeared edge functions.

a ‘smeared edge’ function. This function consists of a Heaviside step function convoluted with a Gaussian

$$f(y; N, y_0, \sigma) = N \int_{-\infty}^{\infty} H(a') g(a' - a) da' \quad (120)$$

$$= \frac{N}{2} \left[1 + \operatorname{erf} \left(\frac{a}{\sqrt{2}\sigma} \right) \right] \quad (121)$$

with $a = y - y_0$. Two different smeared edge functions are used depending on the detector position:

$$f_{\text{edge}}^+(y) = N_0 + \frac{N}{2} \left[1 + \operatorname{erf} \left(\frac{y - y_0}{\sqrt{2}\sigma} \right) \right] \quad (122)$$

or

$$f_{\text{edge}}^-(y) = N_0 + N - \frac{N}{2} \left[1 + \operatorname{erf} \left(\frac{y - y_0}{\sqrt{2}\sigma} \right) \right], \quad (123)$$

where $f_{\text{edge}}^+(y)$ is applied to the vertical distribution of upper detectors and $f_{\text{edge}}^-(y)$ to lower ones. The fit determines four free parameters: the edge position y_0 , the edge width and Gaussian smearing σ , the offset N_0 and the normalization N . Only y_0 is later used as location of the edge. The error function $\operatorname{erf}(x)$ is defined as

$$\operatorname{erf}(x) = \frac{2}{\sqrt{\pi}} \int_0^x e^{-x'^2} dx'. \quad (124)$$

For the fit the vertical distribution of each Roman Pot detector is divided into three segments with different x ranges. The segments are chosen in a way that the number of events in each one is nearly the same. Figure 6.4 shows two fits for an upper and lower detector for the middle segment. The average of all three segment fits yields the beam screen edge position.

In Table 6.1 the positions of all fiducial cuts are summarized. In Figure 6.5 an illustration of the cuts is shown for RP1. The hitmap of the detector shows reconstructed track positions for elastic-scattering candidates after the raw event selection. Two red lines indicate the position of the fiducial cuts. Every reconstructed track between the top beam screen and bottom detector edge line fulfilling $|y_{\text{detector edge}}| < |y_{\text{track}}| < |y_{\text{beam screen edge}}|$ passes the cuts and is used for analysis. The cuts are applied to the reconstructed track positions of all four detectors of the spectrometer arm with a trigger signal in an event.

Table 6.1: Position of vertical edge cuts for each detector. Tracks fulfilling $|y_{\text{detector edge}}| < |y_{\text{track}}| < |y_{\text{beam screen edge}}|$ pass the cuts and are used for analysis.

RP	$y_{\text{detector edge}}$ [mm]	$y_{\text{beam screen edge}}$ [mm]
1	5.994	20.221
2	-6.002	-18.910
3	6.315	21.247
4	-6.233	-19.885
5	6.096	19.528
6	-6.333	-21.379
7	5.880	18.609
8	-6.181	-20.343

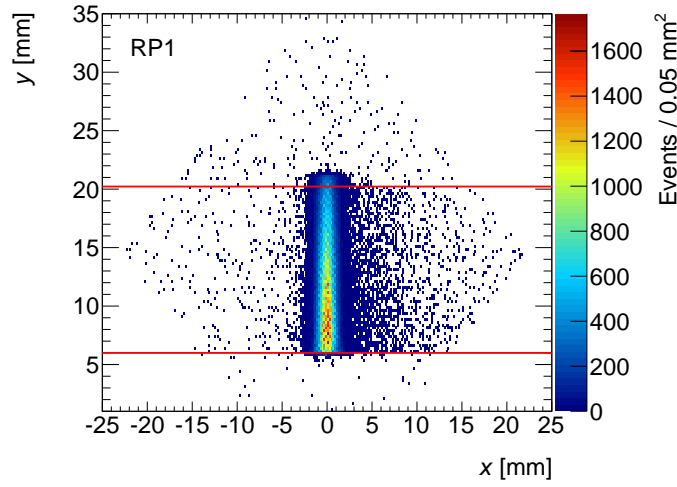


Figure 6.5: Hitmap showing x and y position of track candidates from elastic scattering in RP1. The red lines indicate the position of the fiducial cuts used to define the acceptance.

6.1.2 Left-right collinearity cuts

The back-to-back configuration of elastic-scattering events is utilized to select elastic-scattering events and reject background. Background usually does not appear in back-to-back configuration and can be handled with cuts on the correlation between vertical and horizontal positions measured left and right from the IP for inner and outer detectors. In practice the divergence of the beams and detector resolution effects dilute the perfect collinearity of the two sides. Two correlations for the x and y coordinates of reconstructed tracks in outer detectors are shown in Figure 6.6. Tracks from elastic scattering are confined in a narrow elliptical correlation pattern in the horizontal distribution and in a straight line in the vertical one. Uncorrelated bands in the horizontal and off-diagonal tracks in the vertical coordinate originate from accidental beam-halo particle coincidences. Cuts are now applied to these distributions to select the contribution from elastic scattering and reject the background from halo particles.

The elastic-scattering events in the horizontal coordinate correlation can be parametrized by a 2D Gaussian distribution. The widths σ_1 and σ_2 and the angle of rotation θ_{rot} of this distribution is determined from simulation using the fast simulation described in Section 5.1.

6 Data analysis

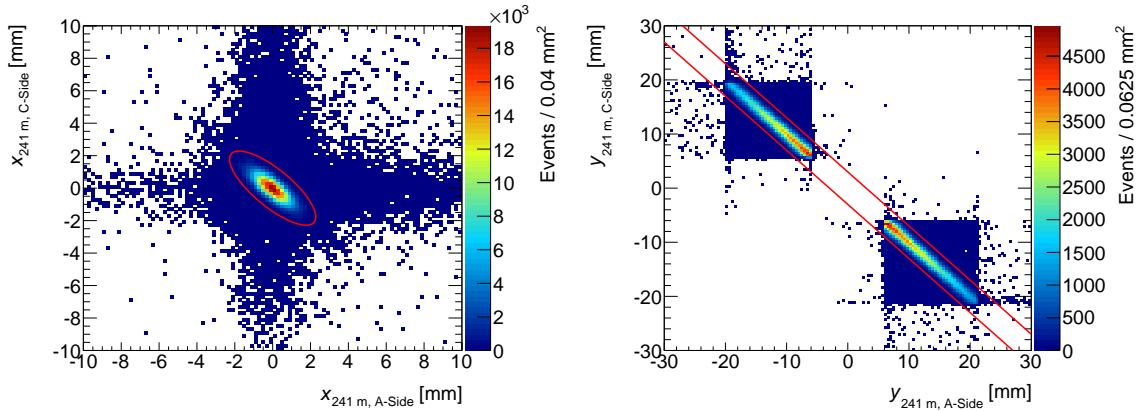


Figure 6.6: Correlation plots of horizontal (left) and vertical (right) reconstructed track coordinates for outer detectors. The red lines indicate the positions of the cuts.

Table 6.2: Values of elastic-scattering event selection cuts based on collinearity of vertical and horizontal track coordinates. A and C refer to the side of the IP.

Correlation	σ_1 [mm]	σ_2 [mm]	ϑ_{rot} [rad]
x_A vs. x_C inner	0.325	0.696	0.788
x_A vs. x_C outer	0.308	0.870	0.784
y_A vs. y_C both	distance to diagonal ± 3 mm		

The correlations are determined for simulated elastic-scattering events and a 2D Gaussian fit is performed independently for inner and outer correlations. In data the elliptical cuts are placed with $3.5\sigma_i$, which preserves about 99 % of the elastic-scattering events (see also Section 6.4). The left histogram in Figure 6.6 shows the horizontal correlation for outer detectors together with a red ellipse, which indicates the position of the cut. Reconstructed tracks inside the $3.5\sigma_i$ ellipse pass the cut and are used for analysis.

The collinearity of elastic-scattering events in the vertical correlation is much more pronounced. Therefore, a simple cut with a straight diagonal line is sufficient. The events are not allowed to be further than 3 mm away from the diagonal to pass the cut. This value again corresponds to a preservation of 99 % of the elastic-scattering events, which is determined from MC. The vertical cut is applied on the inner and outer position correlation, whereat the cut value of 3 mm is used for both. Figure 6.6 (right) shows the vertical correlation for outer detectors together with the two red lines indicating the ± 3 mm cut on the diagonal. All tracks inside these two lines are considered for the analysis and pass the cuts.

Table 6.2 summarizes the collinearity cuts for x and y and for inner and outer detectors. The cuts are applied to inner and outer detectors of the spectrometer arm with a trigger signal in an event.

6.1.3 Position-angle correlation cut

Another correlation which is used to suppress background is the one between the horizontal coordinate of the inner detectors and the local scattering angle in the horizontal plane. The local angle θ_x is calculated with the reconstructed horizontal track positions in two consecutive Roman Pots on one side described in Equation (104). Elastic-scattering events appear as a narrow, positively correlated elliptical pattern in contrast to background from beam-halo and

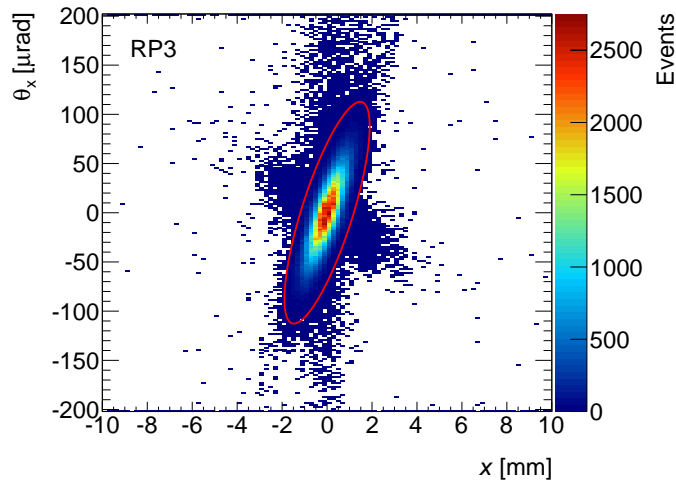


Figure 6.7: Correlation of reconstructed horizontal track position versus local angle for inner detector RP3.

Table 6.3: Values of elastic-scattering event selection cut based on correlation between horizontal track position (inner RP) and local angle.

Correlation	σ_1 [mm]	σ_2 [μrad]	ϑ_{rot} [rad]
x_{inner} vs. θ_x	0.34	32.2	-0.0131

single diffraction accidentals, which populates a narrow band and a negatively correlated ellipse. Again the widths and angle of rotation of the elliptical elastic-scattering correlation is determined from simulation by a 2D Gaussian fit. The cut is then placed at $3.5\sigma_i$ and events inside this ellipse pass the cuts and are used for analysis. Table 6.3 quotes the exact values of the Gaussian fit. Figure 6.7 shows the correlation combined with the red ellipse of the cut. The negative correlation and narrow band at $x = 0$ from background events can be nicely seen. Since this background correlation overlaps with the one from elastic scattering, the cut leaves some irreducible background inside the elastic-scattering ellipse. The cut is applied to the detectors on the right and left side of the spectrometer arm with a trigger signal in the event, but only the horizontal positions of the inner detectors are used.

6.1.4 Characteristics of elastic-scattering events

After the complete event selection about 800 000 elastic-scattering events remain for the cross-section analysis, which is about 12 % of all events in run 191373. In Table 6.4 the detailed numbers are listed. In arm 1368 1.06 times more events are observed than in arm 2457, which is related to the detectors not all being at the same distance, asymmetric beam screen positions and different background contributions.

The selected events contain a very small fraction of 0.23 % of pileup events, where two overlapping elastic-scattering events can be observed in both spectrometer arms, which individually pass the event selection cuts of the respective arm. In such a case both events are kept and used for the analysis. It is also possible for pileup to appear in the same arm, but because of the track matching explained in Section 3.4.2 only one of these events, the more elastic-scattering like, is taken for analysis. The amount of these kind of none observed

Table 6.4: Number of events after each event selection step. The number in a certain row includes all selections in the rows before.

Event selection	Number of events	
	Arm 1368	Arm 2457
Run 191373 physics stream	6 620 953	
BCId = 1	1 898 901	
Good LB list	1 822 128	
Elastic-scattering L1 trigger signal (OR)	1 106 855	
Elastic-scattering L1 trigger signal	585 570	553 585
Reconstructed	459 229	428 213
Fiducial cuts	437 859	404 680
x_A vs. x_C cuts	426 043	396 287
y_A vs. y_C cuts	421 292	393 012
x_{inner} vs. θ_x cuts	415 962	389 460
Total	805 422	
Included pileup	1060	

pileup events is assumed to be the same as for the observed different arm pileup events. A scaling factor of two is applied to the observed ones in order to correct for the not observed pileup events. In principle it is also possible to have pileup with more than two events, but because of the low average number of proton–proton interactions per bunch crossing of $\mu = 0.035$, this is only a very small fraction and can be neglected. Minimum bias pileup from inelastic scattering is also present but does not affect the elastic-scattering analysis as no veto is imposed on interactions measured with the ATLAS central detector. The events also contain a small fraction of 0.5 % of irreducible background mostly coming from beam-halo accidentals which is investigated in Section 6.2.

Elastic-scattering events appear in the detectors as part of a narrow elliptical pattern with its major axis in the vertical direction, with an aperture gap between the upper and lower detectors. The pattern can be seen in Figure 6.8 after event selection. The hitmaps in this figure show the horizontal versus vertical reconstructed track positions of all selected elastic-scattering events for an upper and lower detector. The red lines indicate the diamond shape of the actual sensitive detector volume consisting of tracking fibres. Most of the tracks are visible near the detector edge and at $x = 0$, which can also be seen in the projections of the track positions in x and y depicted in Figure 6.9 for RP3. The distribution of the horizontal track position has almost a Gaussian like shape and the vertical position has a maximum at the detector edge near the beam. These shapes are characteristic of elastic-scattering events and come from the exponential dependence of the differential elastic cross-section on t : $d\sigma/dt \sim \exp(-Bt)$. Because of the high- β^* beam optics with different effective lever arms, the distribution is much broader in the vertical plane, where the effective lever arms are larger.

With Equation (104) the local scattering angle θ_{ll} in two consecutive Roman Pots can be calculated in the horizontal and vertical plane. The distribution for θ_x has an almost Gaussian shape like the one for the horizontal position. The effect of beam optics can be nicely seen in the distribution for θ_y , where proton tracks in upper detectors have negative angles and in lower detectors positive ones. Both distributions are shown in Figure 6.10 for RP 3. For the vertical local angle in some bins around $|\theta_y| \approx 150 \mu\text{rad}$ and $|\theta_y| \approx 180 \mu\text{rad}$ an

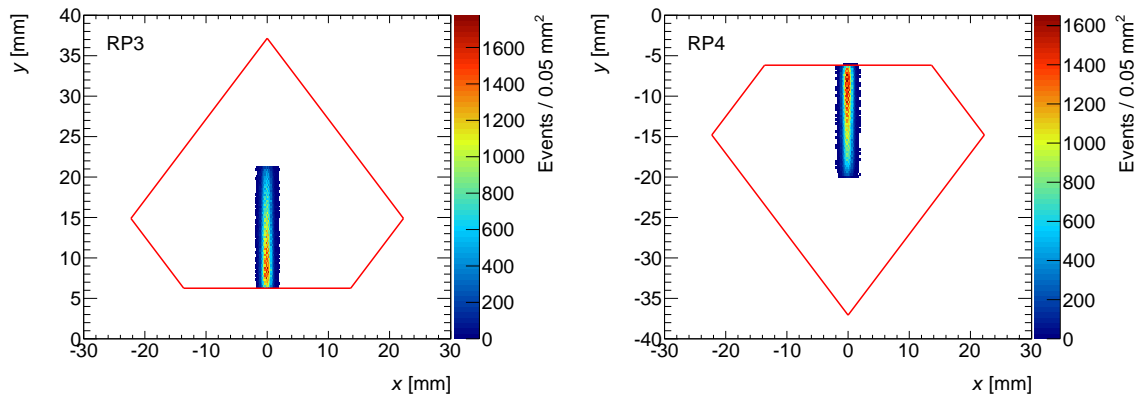


Figure 6.8: Hitmaps of upper detector RP3 (left) and lower detector RP4 (right) showing the reconstructed horizontal track position versus the vertical one for events after elastic-scattering event selection.

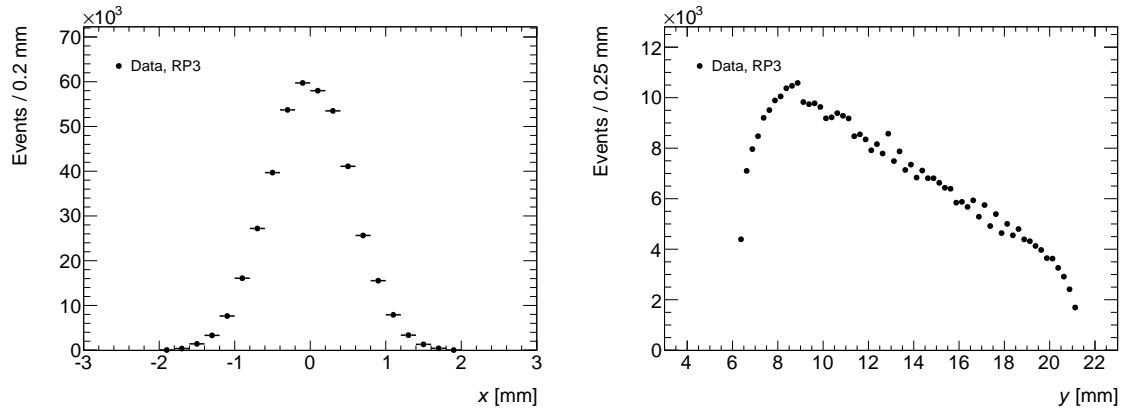


Figure 6.9: Horizontal and vertical position distribution of reconstructed tracks in RP3 after elastic-scattering event selection.

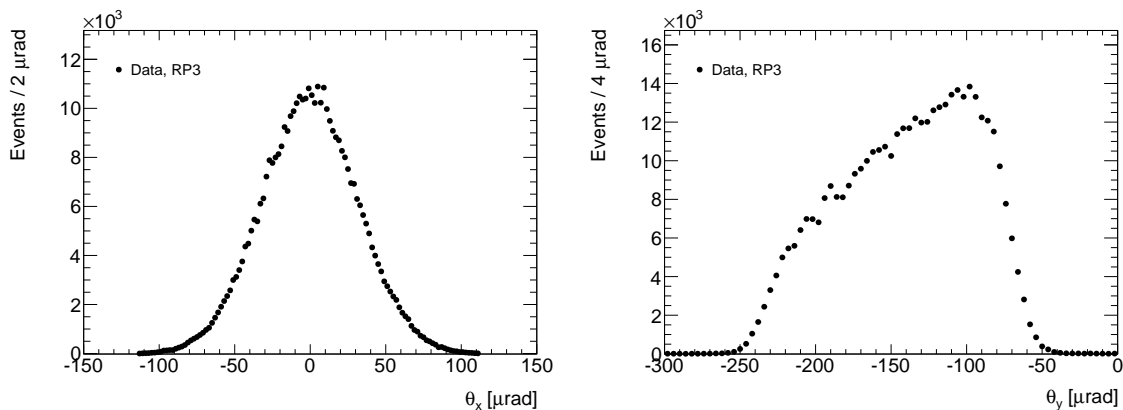


Figure 6.10: Horizontal and vertical local angle distribution of reconstructed tracks in RP3 after elastic-scattering event selection.

6 Data analysis

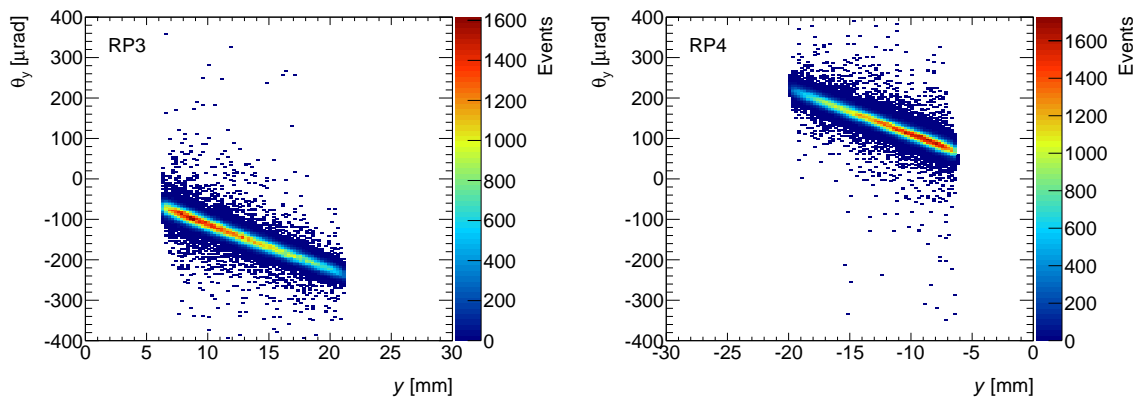


Figure 6.11: Correlation of reconstructed vertical track position versus vertical local angle for upper detector RP3 and lower one RP4 after elastic-scattering event selection.

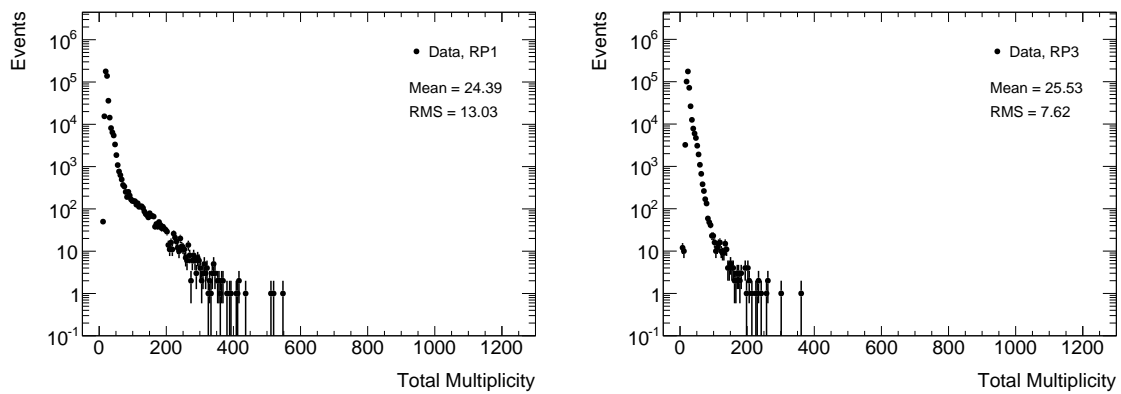


Figure 6.12: Total multiplicity in outer detector RP1 and inner one RP3 after elastic-scattering event selection.

irregular structure is observed, which is likely related to fibre metrology or mapping issues. However, this does not affect the t -reconstruction, which uses in the vertical plane for all four reconstruction methods only the position and not the local angle.

The correlation between the horizontal position x and local angle θ_x is used as an event selection cut to reduce background. In principle one could also look at the correlation for the vertical coordinates, which is shown in Figure 6.11 for an upper and lower detector. This correlation also shows a distinct pattern from elastic-scattering events, which appear as a diagonal band. Background tracks are outside of this pattern and could be reduced by a cut with two straight lines similar to the y_A vs. y_C cut. The figure shows the correlations after all elastic-scattering event selection cuts are applied and only a small fraction of background is left. Such a cut was investigated, but is not used in the end. This has two reasons: First the cut would reduce the number of elastic-scattering events in the sample used for total cross-section analysis and would not reduce the background much more than the already used cuts. Eventually this would only lead to a smaller acceptance. It would also not further reduce the remaining irreducible background contribution. Second the additional cut would not benefit the event reconstruction efficiency calculation described in Section 6.3, where the cuts are also used.

Additional observations are made for the total fibre multiplicity of reconstructed elastic-scattering events. These observations are not characteristics of such events per se, but are related to background and the detector structure. Most elastic-scattering events have a single clear track in the four detectors of a spectrometer arm. Since there are 20 fibre layers in the detectors this one track ideally would correspond to a total multiplicity $M_{\text{tot}} = 20$, if one fibre per layer would produce a signal. In practice this is not the case because on one hand the layer efficiency is only about 93 %, which would result in a smaller M_{tot} , but on the other hand because of cross-talk between the fibres, various beam-related backgrounds and electronic noise the total multiplicity would be larger (compare Section 3.4). The second effects dominate which results in an overall larger total multiplicity than 20. In Figure 6.12 the total multiplicity distribution of outer detector RP1 and inner detector RP3 are shown. One can see in both distributions a peak at $M_{\text{tot}} \approx 23$ which corresponds to a single track with cross-talk and/or electronic noise. Both distributions have a tail with larger multiplicity events that still get reconstructed. This tail goes up to $M_{\text{tot}} \approx 300$ for inner detectors and up to $M_{\text{tot}} \approx 500$ for outer ones, because of a higher fraction of background from hadronic showers. The probability for a shower in the outer detector is larger, because the proton has to pass more detector material. The hitmaps, position, angle and total multiplicity distributions for all eight detectors look very similar to the ones shown here as examples and are very characteristic for elastic-scattering events detected in ALFA. Some of them from spectrometer arm 1368 are in Appendix A.1.

6.2 Background estimation

After the event selection and background rejection cuts are applied, a small residual background component at small values of $|t|$ is still expected to be inside the elastic-scattering sample. The reason is, that the elliptical x_A vs. x_C and x_{inner} vs. θ_x cuts in Figures 6.6 and 6.7 (see pages 68 and 69) cannot reject background, which peaks at small values of x or θ_x . This irreducible background primarily originates from beam-halo particles which are in accidental coincidence with another halo particle or a single-diffractively scattered proton on the opposite side of the IP. The accidental coincidence leads to an elastic-scattering trigger signal and makes them look like an elastic-scattering event. Beam-halo particles are beam losses associated with a collection of particles of any origin and behaviour, e.g. beam-gas or beam-beam interactions, that lies in the low density region of the beam distribution surrounding the dense beam core far away from the centre. So these particles left the ordered beam structure but still circulate the beam pipe for some time. Because of the small distance of the tracking fibres to the beam centre, these particles are detected with the ALFA detectors. In a single diffraction event one of the protons dissociates and the other one remains intact, is scattered under a small angle and can also be seen in the detectors. To estimate the background two methods are used. The vertex method utilizes the reconstructed horizontal vertex position at the IP and the anti-golden method counts events in the so called anti-golden configuration, where tracks are reconstructed in all four lower or upper detectors.

The vertex method works similar to the lattice method for reconstructing t described in Section 4.3. But instead of using the second row of the inverted transport matrix M_u^{-1} to reconstruct the scattering angle the first row is now utilized to reconstruct the vertex position

$$u^* = M_{u,11}^{-1}u + M_{u,21}^{-1}\theta_u, \quad (125)$$

6 Data analysis

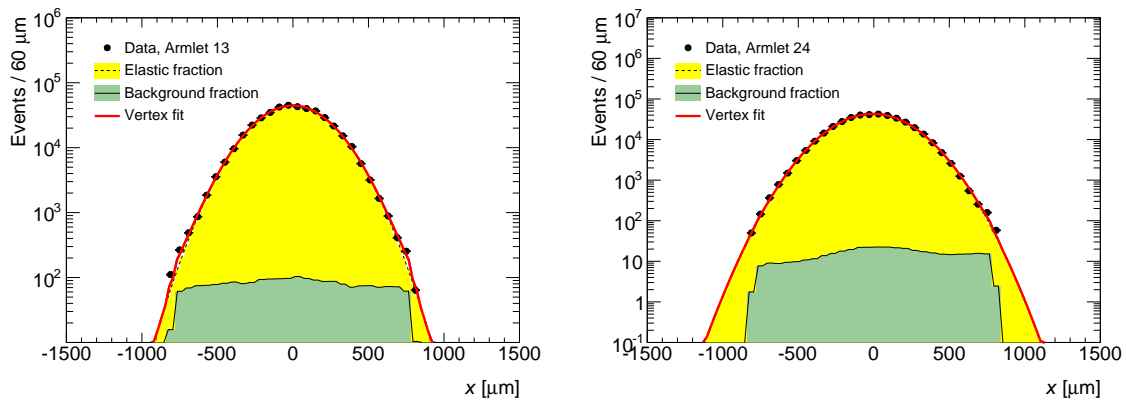


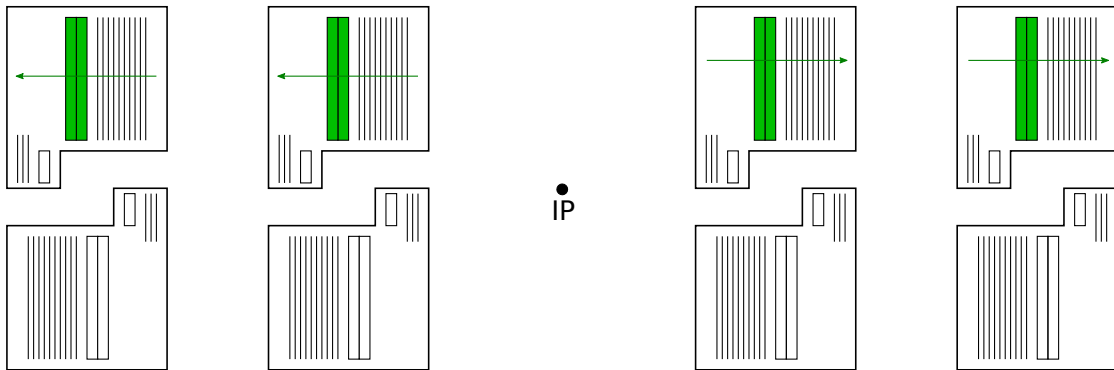
Figure 6.13: Reconstructed horizontal vertex position in armlet 13 (left) and armlet 24 (right) with a fit of a Gaussian distribution for the elastic-scattering signal and a template for the background.

where $u \in \{x, y\}$ is the measured position in the Roman Pots and θ_u the local angle reconstructed between two consecutive detectors (see Equation (104)). The reconstruction is only done for the horizontal vertex position, because in the vertical plane the obtained resolution is not very good. This is because of the parallel-to-point focusing optics, which causes the vertical position in the Roman Pot detectors to be largely independent of the vertical vertex position. Elastically scattered protons approximately have a Gaussian shaped vertex distribution, as it is shown in Figure 5.1 on page 55 for MC simulation; but the reconstructed vertex distribution of beam-halo particles has a broad and unspecific shape, since these particles do not originate from the IP. This can now be used to determine the background fraction in the vertex distribution of the selected elastic-scattering events, by using a parametrization of the background shape obtained from data. The calibration stream (see Section 3.3) in which un-prescaled L1_ALFA_Any trigger-signal information is available, is used to determine these background templates. Events are selected by requesting two consecutive detectors on one side of the IP with reconstructed tracks, but the remaining six are not allowed to have any tracks, to remove elastic-scattering contributions. The elastic-scattering event selection cuts from Section 6.1 are applied where possible. E.g. the left-right correlation cuts cannot be applied, because of missing tracks on the other side. Thereafter the horizontal vertex distribution is calculated from the reconstructed positions for the selected events, which results in separate background vertex templates for the four armlets 13, 24, 57 and 68 with 500k to 1M events per armlet. To determine the background fraction in the selected elastic-scattering events, the vertex distribution of these events is now fitted with the sum of a Gaussian distribution with three free parameters for the elastic-scattering signal and the background template with fixed shape and one free normalization parameter.

Two examples of this fit are shown in Figure 6.13, where the vertex position distributions obtained from armlet 13 and 24 are fitted. The number of background events is obtained from the integral of the fitted background template. From the background contribution in the two armlets, belonging to a spectrometer arm, an average contribution is calculated for the corresponding arm. Because no significant non-Gaussian tails are present in the selected elastic-scattering events, the background fraction is only about $f_{bg} < 0.002$. The statistical uncertainties of this method are large, because of the limited sensitivity. The fit is also rather poor, because the shape of the elastic-scattering vertex distribution is not truly Gaussian. Systematic uncertainties for the vertex method include the difference between the two armlets of one spectrometer arm and the choice of the background template. Alternative tem-

Table 6.5: Number of background events for both spectrometer arms estimated with the vertex method with statistical and systematic uncertainties.

	Arm 1368	Arm 2457
Background events	2428	231
Statistical uncertainty	256	218
Armlet difference	576	359
Unpaired bunches	355	150
L1_MinBias veto	120	12
SD enhanced	904	107

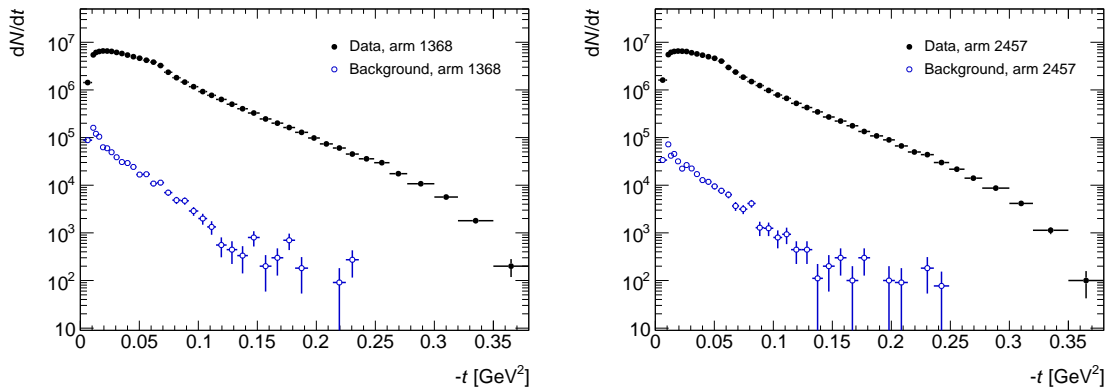
**Figure 6.14:** Diagram of an anti-golden ++ event. A trigger signal is present shown by green trigger tiles, but there is no interaction at the IP. In RP1, RP3, RP5 and RP7 tracks are reconstructed shown by green arrows.

plates are constructed by using unpaired bunches, by putting a veto on L1_MinBias trigger signals (L1_TE20, L1_ZDC, L1_LUCID and L1_MBTS2; see Section 3.3.2) to remove single diffraction contributions and on the other hand by requesting a L1_MinBias trigger signal to enhance the single diffraction and decrease the beam-halo contribution to the background. The number of background events and the uncertainties are summarized in Table 6.5.

The anti-golden method makes use of the anti-golden event topology, in which tracks are reconstructed in either all four upper or all four lower detectors. Compared to the elastic-scattering topology these anti-golden events are pure background from accidental coincidences, since they are not in the elastic-scattering back-to-back configuration. The background fraction in the selected elastic-scattering events can now be estimated by counting these anti-golden events. An illustration of such an anti-golden event in the upper detectors is shown in Figure 6.14. The configuration with the four upper detectors (1357) is called arm ++ and the one with lower detectors (2468) is called arm --. A huge benefit is, that with these events a differential t -spectrum can be reconstructed, by inverting the sign of the reconstructed proton track coordinates in the detectors on one side of the IP. By this inversion the anti-golden configuration is flipped artificially into the golden one of elastic-scattering events. This is done under the assumption, that the beam-halo contribution is the same in the upper and lower detectors and the assignment of the background t -spectra to the spectrometer arms is arbitrary. Like for the vertex method the calibration stream is used to select events with an L1_ALFA_ANY trigger signal, which have reconstructed tracks in arm ++ or -- and no tracks in the remaining four detectors. After the selection the events are flipped into the golden elastic-scattering configuration, by changing the sign of all track coordinates

Table 6.6: Number of background events for both spectrometer arms estimated with the anti-golden method with statistical and systematic uncertainties.

	Arm ++	Arm --
Background events	3329	1497
Statistical uncertainty	58	39
Systematic uncertainty	898	371

**Figure 6.15:** Comparison of the reconstructed raw differential t -spectrum with the background spectrum in arm 1368 (left) and 2457 (right). In both cases the nominal subtraction method is used.

on a randomly selected side. Finally the elastic-scattering event selection cuts are applied to obtain the background events in the two spectrometer arms. They are counted and the differential t -spectrum is determined.

Systematic uncertainties arise from the choice of the side on which the sign of the coordinates is flipped and from flipping only the sign in the vertical plane. In Table 6.6 the number of background events and uncertainties from the anti-golden method are summarized, and in Figure 6.15 the background t -spectra of both arms are shown in comparison with the raw differential t -spectra of golden elastic-scattering events. The shape of the background t -spectra is very different from the shape of elastic-scattering spectra. It is much more peaked at small $|t|$ values and falls off with a steeper slope in contrast to the one from elastic scattering. This difference is an acceptance effect and can be explained by the beam divergence, which translate into an angular smearing of the outgoing elastically scattered protons. At small $|t|$, close to the detector edge, the fraction of elastically scattered protons inside the acceptance on one side of the IP, but outside on the other side, increases. However, the accidental coincidences of the background are uncorrelated on the left and right side and have an almost flat acceptance up to the edges.

The anti-golden method yields about 1.8 times as much background as the vertex method and both predict an asymmetric background in the two spectrometer arms. Because of the huge advantage of an estimate of the shape of the background t -spectrum by the anti-golden method, it is used instead of the vertex method in the total cross-section analysis to subtract the background. In Figure 6.15 the background spectrum of arm ++ is arbitrarily assigned to the raw t -spectrum of arm 1368 and arm -- is assigned to arm 2457, but in the end this is irrelevant, since the two spectrometer arms are later combined to get the final differential cross-section. The raw t -spectrum is corrected by subtracting the background spectrum, before the unfolding procedure is applied (see Section 6.5).

6.3 Event reconstruction efficiency

The reconstruction algorithm described in Section 3.4 is used to reconstruct the x and y position of particle tracks in the eight RPs of the ALFA detector. The intrinsic reconstruction efficiency of ALFA for minimum ionizing particles inside the fiducial volume was determined in test beams to be close to 100 % [46–48]. This means a particle track is created and reconstructed in the MD almost every time, when a proton hits the detector without associated background. For elastic-scattering events with two protons in back-to-back configuration one would expect a reconstructed track in each of the four detectors of the corresponding spectrometer arm. The average total multiplicity of these kind of events is around $\bar{M}_{\text{tot}} = 23$ in each detector as described in Section 6.1.4. But due to several reasons it is possible to have more than one track in one or more detectors. A hadronic shower produced by a proton in the detector material leads to high multiplicity events because of multiple tracks caused by the shower particles. Other reasons are pileup events where protons of two or more elastic-scattering reactions are registered in a single event. Pileup can also happen if beam-halo particles cause tracks in the RPs in addition to the elastically scattered proton. Other background events coming e.g. from beam losses are further causes for events with higher multiplicity. To a certain amount these high multiplicity events are handled by the tracking algorithm (see Section 3.4), which reconstructs multiple tracks. But if the amount of tracks and the total multiplicity is too large, the event does not pass the reconstruction pre-selection criteria and no overlap maximum can be found. So the reconstruction fails and no track at all is reconstructed. This leads to a reconstruction inefficiency for elastic-scattering events, where a reconstructed proton track is expected. Figure 6.16 shows two example event displays for RP1. The left one shows a shower event where no track is reconstructed and the right one shows an elastic-scattering pileup event where two clear tracks can be recognized. The event reconstruction efficiency is most comprehensively described here, since it is the author's main contribution to the measurement of the total cross-section in Reference [45].

6.3.1 Definition

The event reconstruction efficiency for elastic-scattering events is in general a function of t and defined as

$$\varepsilon_{\text{rec}}(t) = \frac{N_{\text{reco}}(t)}{N_{\text{reco}}(t) + N_{\text{fail}}(t)}, \quad (126)$$

in which N_{reco} is the number of fully reconstructed elastic-scattering events, which have at least one reconstructed proton track in each of the four detectors of one spectrometer arm and N_{fail} is the number of partially and not fully reconstructed elastic-scattering events, which have reconstructed tracks in less than four detectors of one spectrometer arm or no track at all. Both numbers of events are determined only from data and therefore the calculation of the reconstruction efficiency in such a way does not make use of Monte Carlo simulations. Furthermore, the elastic-scattering events in arm 1368 and 2457 are independent of each other and therefore $\varepsilon_{\text{rec}}(t)$ is calculated separately for both arms.

The elastic-scattering events are divided into several reconstruction cases 'k/4' based on the number of detectors with at least one reconstructed track. The first digit 'k' depicts this number and the second one '4' stands for the number of detectors in one spectrometer arm, that should have a reconstructed track for a normal elastic-scattering event. Case 4/4 are all fully reconstructed golden elastic-scattering events, '3/4' are events with three detectors out of four which have at least one reconstructed track, '2/4' are events with two detectors on one side of the interaction point with at least one track, '1+1/4' are events with one detector

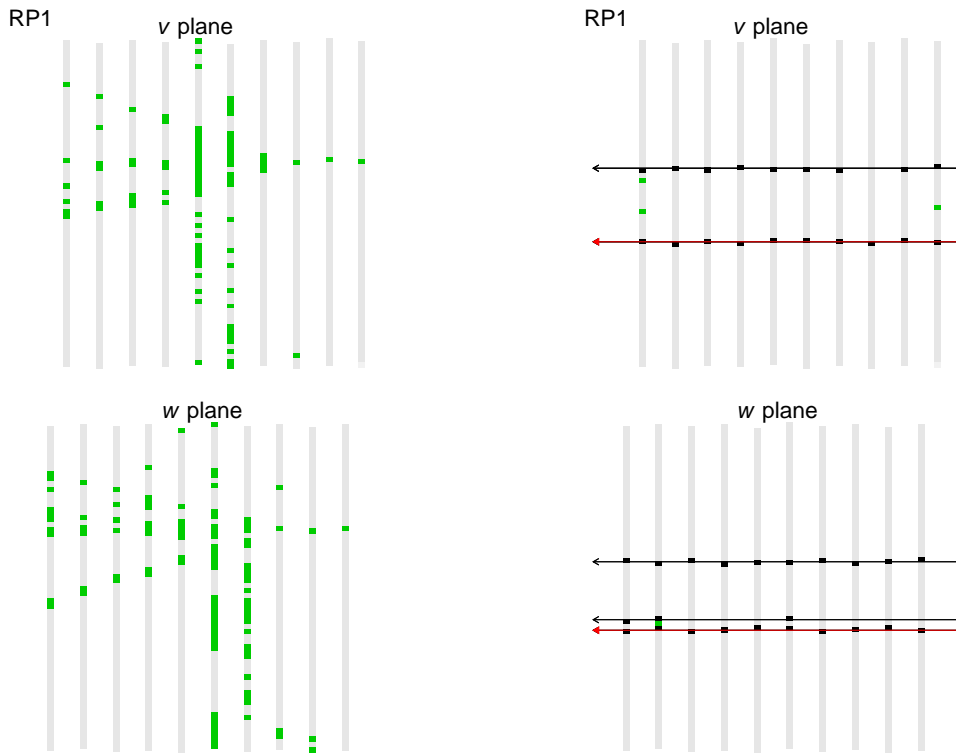


Figure 6.16: The left event display shows a shower in RP1 from a 3/4 event and the right display shows elastic-scattering pileup from a 4/4 event. The red arrows depict the reconstructed best track candidate and the black arrows the other reconstructed tracks.

on A-Side and one on C-Side with at least one track, ‘1/4’ are events with only one detector with at least one track and ‘0/4’ are elastic-scattering events with no reconstructed track in one of the four detectors of one arm. With this classification,

$$N_{\text{reco}}(t) = N_{4/4}(t), \quad (127)$$

$$N_{\text{fail}}(t) = N_{3/4}(t) + N_{2/4}(t) + N_{1+1/4}(t) + N_{1/4}(t) + N_{0/4}(t) \quad (128)$$

and under the assumption of a t -independent reconstruction efficiency, Equation (126) becomes

$$\epsilon_{\text{rec}} = \frac{N_{4/4}}{N_{4/4} + N_{3/4} + N_{2/4} + N_{1+1/4} + N_{1/4} + N_{0/4}}, \quad (129)$$

where $N_{k/4} = \int_{-\infty}^0 N_{k/4}(t) dt$ is the t -independent number of events with $4 - k$ detectors without any reconstructed track in one spectrometer arm. Here all numbers $N_{k/4}$ are assumed to be independent of t . This assumption needs to be verified and is addressed later in Section 6.3.3.1. In Figure 6.17 a diagram of a not fully reconstructed event is shown. In this example an elastic-scattering trigger signal is present in arm 1368 and in three out of the four detectors of this arm one or multiple tracks are reconstructed. Only in RP8 no track was reconstructed despite the elastic-scattering trigger signal. This example event would be classified as 3/4 and counted towards $N_{3/4}$.

In the following the different reconstruction cases and the methods how to select events and determine the number of events $N_{k/4}$ for these cases are described. For each case a proper

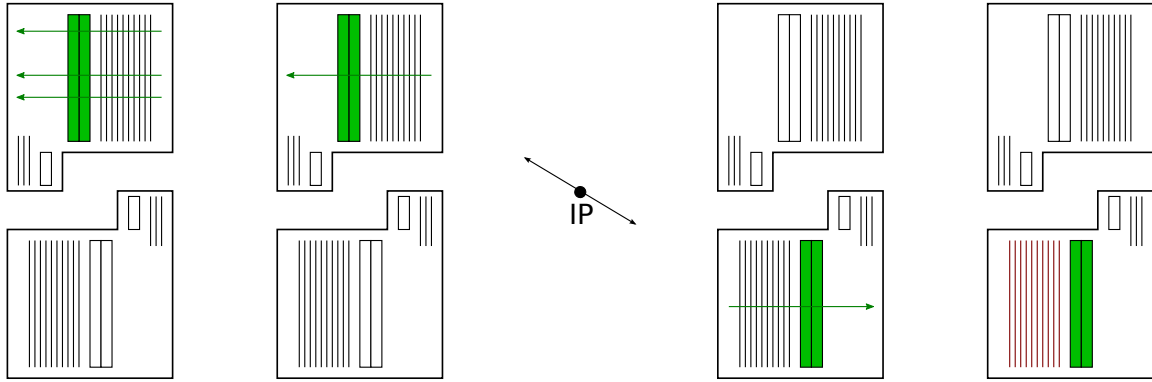


Figure 6.17: Diagram of a 3/4 event example. An elastic-scattering trigger signal is present in arm 1368 shown by green trigger tiles. In RP1, RP3 and RP6 tracks are reconstructed shown by green arrows. RP1 has also additional reconstructed tracks. RP8 has no reconstructed track which is shown by red fibre planes.

method is needed, because of different event topologies. With only about 5 % of N_{fail} coming from cases 1+1/4, 1/4 and 0/4, these events only play a minor role in the determination of the reconstruction efficiency, but nevertheless they are also included and described in the following.

6.3.2 Event selection and Tag-and-probe

Elastic-scattering events for all reconstruction cases need to be selected and separated from background. In order to do so, a tag-and-probe style method is utilized (see e.g. Reference [72]). Since an elastic-scattering event has two protons in back-to-back configuration, the proton with reconstructed tracks on one side of the interaction point is used as tag and the one on the other side as probe. Tag and probe have to pass several elastic-scattering event selection criteria to be considered as an elastic-scattering event and to be used for the reconstruction efficiency calculation.

The events are selected based as much as possible on the event selection for golden elastic-scattering 4/4 events described in Section 6.1. In particular one of the elastic-scattering Level 1 trigger signals L1_ALFA_ELAST15 or L1_ALFA_ELAST18 has to be present. The trigger efficiency of these is very high with 99.97 % [51], which ensures that some activity took place in an arm, if the corresponding trigger signal is present. Based on which trigger has fired the four RPs of the corresponding spectrometer arm are checked for reconstructed tracks and the event is classified into one of the reconstruction cases. To determine, if the event really is from elastic scattering and has to be counted for the efficiency, it has to pass the event selection cuts mentioned in Section 6.1. Not all cuts, that are applied to 4/4 events, can also be applied to not fully reconstructed ones. Because less than four RPs have reconstructed tracks, the left-right collinearity cuts can only be applied, if the corresponding RPs have tracks. This is also true for the rest of the cuts. For example for a 2/4 event only cuts for the two RPs with tracks can be applied. In this case these are fiducial cuts and one x vs. θ_x cut. Especially for 0/4 events no cut at all can be applied, because no track is reconstructed. This makes it very difficult to determine, if an event really is from elastic scattering. How these events are treated is described in Section 6.3.7 in detail.

There are two possibilities to have a detector without any reconstructed track in an elastic-scattering event at the LHC because the reconstruction algorithm failed :

6 Data analysis

- (a) Too many background tracks from showers, beam-halo accidentals, elastic-scattering pile-up or others,
- (b) not enough fibre hits because the proton only scratched the edge of the detector.

Possibility (a) is the one that leads to reconstruction inefficiency, but (b) is an acceptance effect and therefore these events need to be excluded from the efficiency determination, since they are corrected with the acceptance (see Section 6.4). This is done with an additional cut on the total fibre multiplicity M_{tot} (fibres hit per layer summed over all layers of a detector) of all detectors without a reconstructed track in an event. The total multiplicity of every detector without a track in the same arm has to be $M_{\text{tot}} > 5$ to pass this cut, which ensures that some activity is present in the detector. Furthermore, in order to not lose good elastic-scattering events, that e.g. pass the cuts on one side but not on the other one, the cuts for 4/4 events are a little modified compared to the nominal selection. Not every RP has to fulfil the fiducial cuts, but only the detectors on one side of the IP need to. Furthermore, the limits of the local x vs. θ_x cut have been extended to accept more events (looser cut).

In the following sections the cuts, that are applied to a certain reconstruction case, are explained. Some cuts are changed compared to the nominal 4/4 selection and to some cases additional cuts are applied. A further look is taken at the horizontal and vertical position distributions in all RPs of all reconstruction cases. This is done to check, if these cuts actually only select elastic-scattering events. The distributions are compared to the ones of golden elastic-scattering 4/4 events, to decide, if the cuts are appropriate.

6.3.3 3/4

Case 3/4 is the most important one, because only one detector out of four in a spectrometer arm has no reconstructed track. In most cases this is an outer one, because a shower was started in the inner detector, spread to the outer and could not be reconstructed there. Sometimes there are also not reconstructed tracks in inner detectors and reconstructed ones in the subsequent outer detector. The case consists of eight sub-cases, each corresponding to one RP without reconstructed tracks. For example sub-case 136 has reconstructed tracks in RP1, RP3 and RP6 but none in RP8. This sub-case is illustrated in Figure 6.17, where an elastic-scattering trigger signal is present in all four RPs of arm 1368 (green tiles), but no track reconstructed in RP8 (red fibres).

With three detectors with reconstructed tracks it is still possible to apply most of the event selection cuts. The fiducial cuts (beam screen and detector edge) are applied to the three RPs with reconstructed tracks. On the side with two reconstructed RPs the x vs. θ_x cut is applied. Left-right collinearity cuts in x and y are also applied to either the inner or outer detectors, depending on which of the two detectors has reconstructed tracks on the side with only one reconstructed RP. The multiplicity cut is only applied to the single detector without tracks.

The distributions of the x and y positions in the eight Roman Pot detectors for this case agree very well with the distributions for fully reconstructed elastic-scattering events of case 4/4. This means with the applied elastic-scattering event selection cuts, real elastic-scattering events are selected for 3/4, that are comparable to not fully reconstructed golden elastic-scattering events but not background events.

Some distributions are shown in Figure 6.18 for sub-case 136 where RP 8 has no reconstructed track. One can see, that the x and y track positions of both inner detectors agree very well with the ones of 4/4 events in these RPs. The distribution from 4/4 is scaled to the one from 3/4. The ratios between the distributions in the bottom parts of the plots also confirm the

6.3 Event reconstruction efficiency

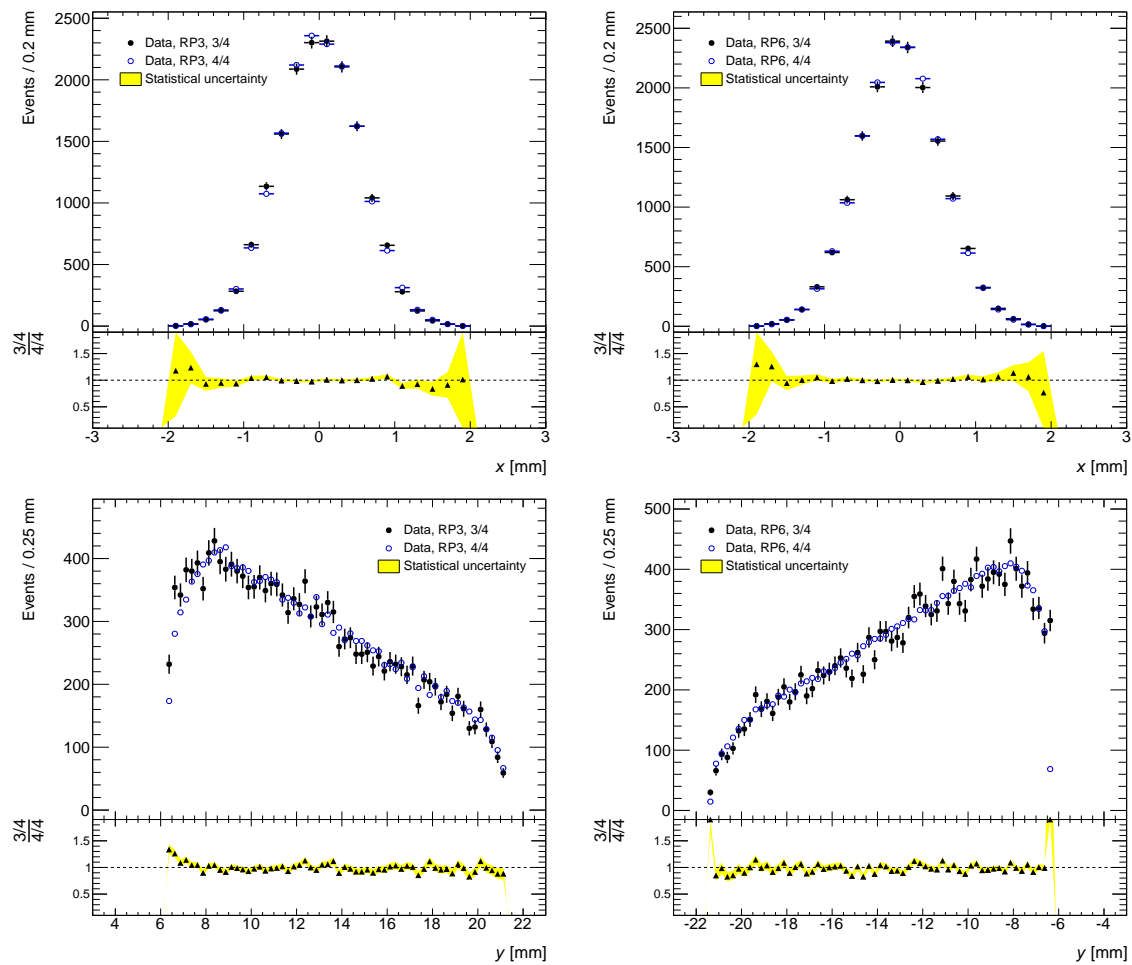


Figure 6.18: Position distributions in x at the top and y at the bottom of case 3/4, sub-case 136 for RP3 and RP6 where no track was reconstructed in RP8. The distributions of case 4/4 in blue are normalized to the ones of 3/4 for comparison. In the bottom part of the plots the ratio of both distributions is shown with the statistical uncertainty as yellow band.

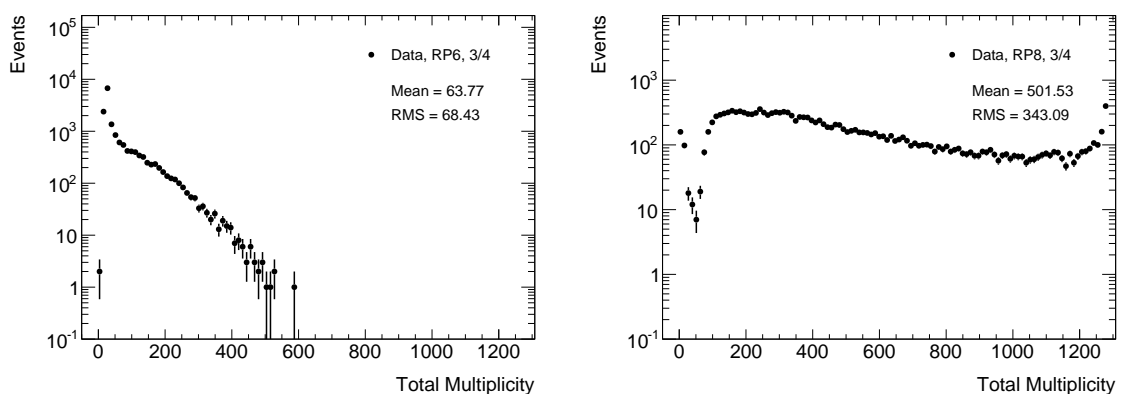


Figure 6.19: Total multiplicity distributions of case 3/4, sub-case 136 for RP6 and RP8, where no track was reconstructed in RP8.

good agreement. The distributions of the other Roman Pot detectors and seven sub-cases look similar and agree with elastic-scattering events, too. The complete set of distributions can be found in Appendix A.2.

The total multiplicity distributions of sub-case 136 in RP6 and RP8 are shown in Figure 6.19. The distribution of the reconstructed detector RP6 looks similar to the ones of 4/4 events. It has a maximum at $M_{\text{tot}} \approx 23$ corresponding to events with a single reconstructed track but a larger high multiplicity tail. The events in this tail are of course events with one or multiple reconstructed tracks. Since RP8 has no reconstructed track the total multiplicity distribution looks different. It has a minimum at $M_{\text{tot}} \approx 23$ instead, because events with this value would be reconstructed in most cases. The high multiplicity tail is very large and goes up to the maximum number of available fibres of 1280. At this maximum value the multiplicity is saturated and every fibre of the detector produces a signal. Therefore, one can assume, that the 3/4 case is dominated by high multiplicity shower events with a lot of fibre cross-talk in the not reconstructed RP. Figure 6.20 shows an event display of such a high multiplicity 3/4 event. In RP1 no track is reconstructed because nearly every fibre shows a signal. In RP3 a single track could be reconstructed despite the shower that just started inside the detector. The first layers are clear enough for the algorithm to reconstruct the track. The not shown RPs on the other side of the IP are clear and look similar to displays of 4/4 events.

With the event selection for 3/4 events described above one gets $N_{3/4}(\text{Arm 1368}) = 33\,264$ and $N_{3/4}(\text{Arm 2457}) = 33\,554$ events. This corresponds to a fraction of $N_{3/4}/N_{\text{fail}} \approx 0.66$ and shows that this case is the most important one of the not fully reconstructed cases. In Table 6.7 the number of events of the eight different sub-cases is shown in detail. The numbers are shown after reconstruction and after the event selection is applied.

6.3.3.1 t -independence

Until now it was assumed, that the event reconstruction efficiency is independent of t . With data it is not possible to determine the efficiency as a function of t for all reconstruction cases, because the t reconstruction methods don't perform very well with less than four reconstructed detectors in an spectrometer arm. Furthermore, for case 0/4 it is not possible at all to reconstruct t because of no reconstructed tracks. Only for events of case 3/4 it is possible to calculate t reasonably well, although one reconstructed detector is missing. The subtraction method can still be used here and provides a nice reconstructed t value. Furthermore, the good agreement of 3/4 position distributions with 4/4 events and the ability to apply most of the event selection cuts shows, that 3/4 events contain the least amount of background. Therefore, events of case 3/4 are used to assess the t stability of the event reconstruction efficiency. It is assumed that the efficiency is flat in t as test beam studies revealed a homogeneous efficiency across the detection area. One can now define a partial reconstruction efficiency

$$\varepsilon_{3/4}(t) = \frac{N_{4/4}(t)}{N_{4/4}(t) + N_{3/4}(t)} \quad (130)$$

from the t -dependent number $N_{3/4}(t)$ of 3/4 events, without considering the other 'fail' cases. Assuming the position distributions of all reconstruction cases agree with elastic-scattering events, $\varepsilon_{3/4}(t)$ is used to verify the t -independence of $\varepsilon_{\text{rec}}(t)$. In order to get $N_{3/4}(t)$, elastic-scattering events with only three detectors with reconstructed tracks are taken and reconstructed for t with the subtraction method. The use of the local angle method is not possible here, because a reconstructed track in one detector is missing and therefore the local

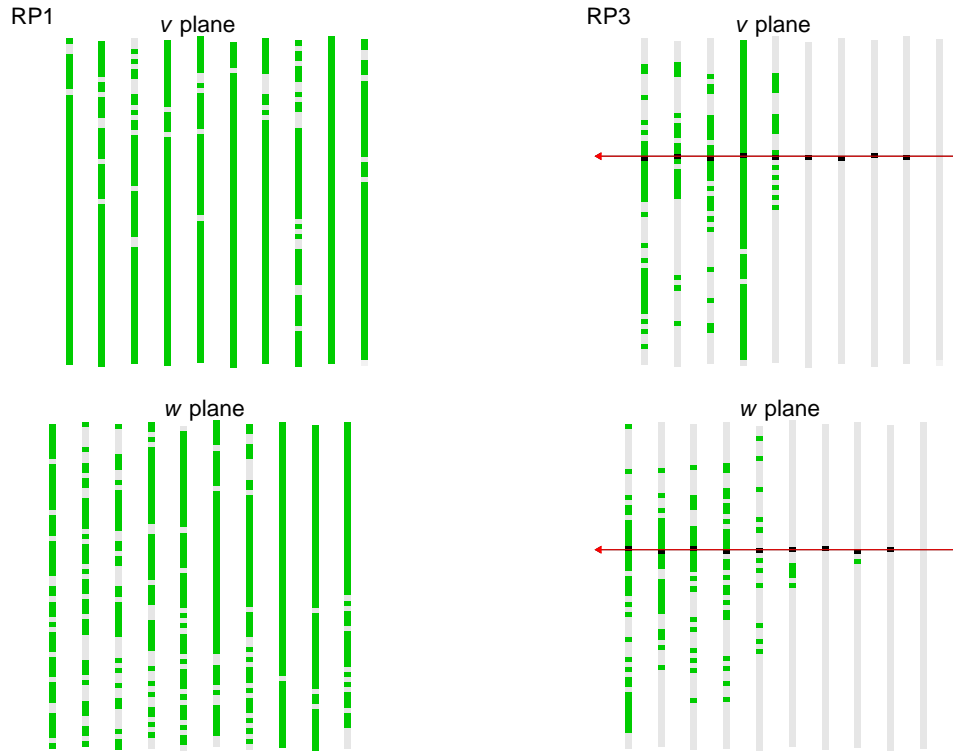


Figure 6.20: Event displays of event 10236 (3/4, sub-case 368). The arrows indicate a reconstructed track. In RP1 no track at all is reconstructed. The not shown RPs on the other side of the IP look similar to displays of 4/4 events.

Table 6.7: Number of events for all 3/4 sub-cases in both spectrometer arms after reconstruction and elastic-scattering event selection.

	Reconstructed	Event selection
$N_{3/4}(136)$	24 081	16 421
$N_{3/4}(138)$	2400	490
$N_{3/4}(168)$	3627	631
$N_{3/4}(368)$	19 209	15 719
$N_{3/4}(245)$	20 208	16 168
$N_{3/4}(247)$	2931	763
$N_{3/4}(257)$	2701	781
$N_{3/4}(457)$	21 380	15 842
$N_{3/4}(1368)$	49 317	33 264
$N_{3/4}(2457)$	47 220	33 554

6 Data analysis

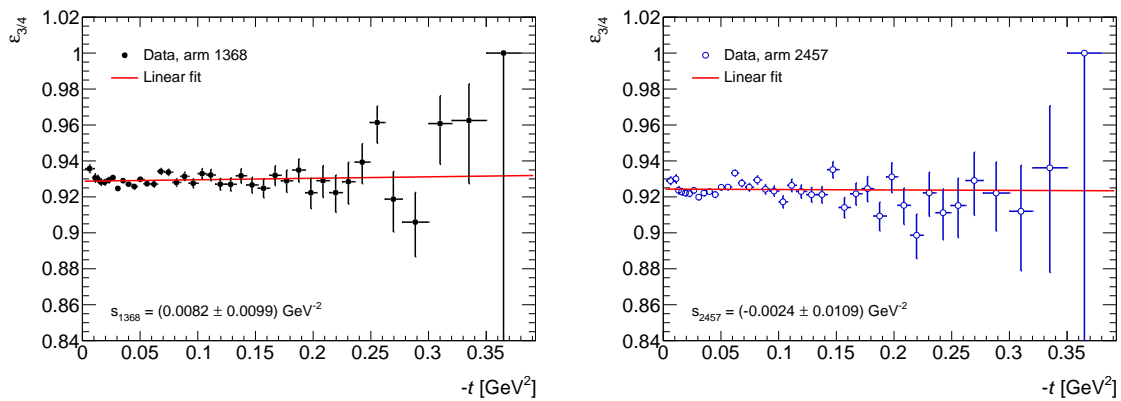


Figure 6.21: Partial reconstruction efficiency $\varepsilon_{3/4}$ as a function of $-t$ for spectrometer arms 1368 and 2457. The red lines are linear fits to the partial efficiency of both arms.

angle can only be reconstructed on one side of the IP. The same is true for the local subtraction method. In principle the lattice method could also be used, but the nominal subtraction method is preferred in this case. The number $N_{4/4}(t)$ of fully reconstructed events is also determined by reconstructing the corresponding events for t with the subtraction method, similar to the rest of the analysis.

Figure 6.21 shows $\varepsilon_{3/4}(t)$ for both arms separately. A linear regression function is fitted to both efficiency distributions and shows a small residual t -dependence with a slope of $s_{1368} = (0.0082 \pm 0.0099) \text{ GeV}^{-2}$ for arm 1368 and $s_{2457} = (-0.0024 \pm 0.0109) \text{ GeV}^{-2}$ for arm 2457. Because of the large statistical uncertainty this is consistent with a t -independent function and based on this result the assumption of a t -independent reconstruction efficiency ε_{rec} in Equation (129) is confirmed. Only the last few bins with less statistics show a small difference to the fit. But since the t -range, that is used for the final fit of the differential elastic cross-section, excludes these bins, this difference does not effect the total cross-section. In addition, the impact of a residual t -dependence on the total cross-section and nuclear slope is probed in terms of a stability check in Section 7.2.3.

6.3.4 2/4

This case covers events where both detectors on one side of the IP in one arm do not contain any reconstructed track despite an elastic-scattering trigger signal. Events of this case are found mainly because of showers, that were created by the elastically scattered proton before or in the inner detector on one side of the IP, spread to the subsequent outer one and could not be reconstructed in both due to high multiplicity. Case 2/4 consists of four sub-cases, corresponding to the two subsequent detectors in both arms and sides. Arm 1368 is divided into two armlets 13 and 68 and an 2/4 event has tracks only in one of these armlets. Arm 2457 is divided into armlet 24 and 57, respectively. Sub-case 13 is illustrated in Figure 6.22, where tracks are only reconstructed in RP1 and RP3. No tracks can be found in RP6 and RP8, but a trigger signal is present.

Due to this configuration the event selection cuts, that can be used, are limited. Fiducial cuts are only applied to the two detectors with reconstructed tracks. The x vs. θ_x cut is applied on the side with the two reconstructed detectors. Left-right collinearity cuts cannot be used, because there are no tracks on the other side of the IP. And of course the total multiplicity cut is applied to the two detectors without reconstructed tracks.

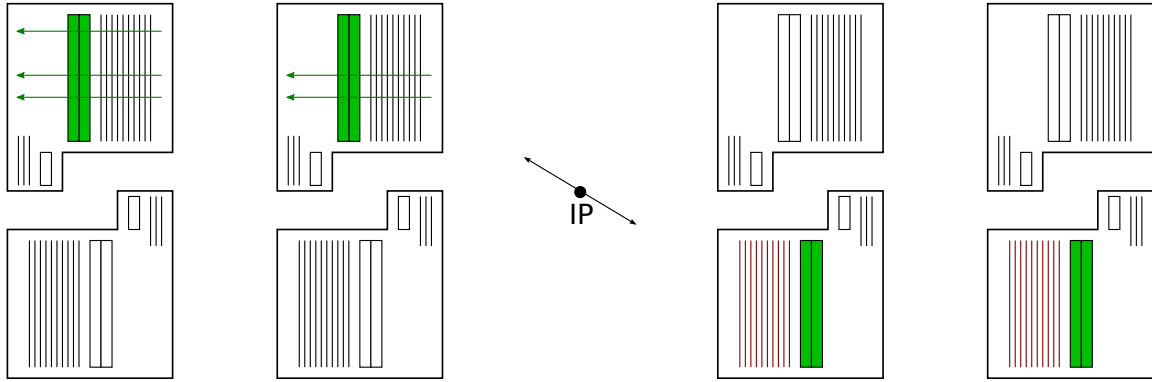


Figure 6.22: Diagram of a 2/4 event. An elastic-scattering trigger signal is present in arm 1368 shown by green trigger tiles. In RP1 and RP3 tracks are reconstructed shown by green arrows. RP6 and RP8 have no reconstructed tracks which is shown by red fibre planes.

Single diffraction events are a potential background of this case, because of their similar configuration with only two detectors on one side containing reconstructed tracks. In a single diffraction event one of the protons remains intact and is scattered under a small angle. Therefore, it can be seen and reconstructed in the ALFA detector. The other proton dissociates and its components are typically visible in the ATLAS central detector and other forward detectors like LUCID or ZDC. Fragments of the dissociation or beam-halo particles can hit ALFA on the other side and create a coincidence with a fake elastic-scattering trigger signal, which make the single diffraction look like a 2/4 event in ALFA. To suppress this background additional vetoes are imposed on L1 trigger signals related to minimum-bias and forward events. These trigger signals are ‘L1_TE20’ which is based on total energy ($\sum E_T$) in the central detector and has a threshold of 20 GeV; ‘L1_ZDC’ which requires at least one hit in ZDC on either A- or C-side; ‘L1_LUCID’ which requires at least one hit in LUCID on either A- or C-side and ‘L1_MBTS2’ which requires at least two hits in the MBTS detector on either A- or C-side. An event is only counted as 2/4, if none of these trigger signals is present.

The track position distributions for sub-case 13 are shown in Figure 6.23 for x and y coordinates of both reconstructed pots. The x distributions agree very well with elastic-scattering 4/4 events both for the inner and outer detector. There is only a minor disagreement at the edges, because of small statistics. This agreement is important, because thus the statement about a t -independent efficiency can also be used here. Admittedly it is completely different for the y coordinate, where the distributions do not agree at the edges, because of large peaks at the beam screen and detector edge in 2/4 events. However, the central part of the distributions agree very well. The 4/4 distributions in the plots are normalized to the one of 2/4 events, but only the central part is used to determine the normalization. The limits for these parts are the same as in Table 6.9. The rest of the distributions for the other sub-cases can be found in Appendix A.3. In x they all agree with 4/4 events, but in every y distribution edge peaks are visible.

Since there are no left-right correlation cuts applied, this case contains many elastic-scattering events, that hit the beam screen or the thin Roman Pot window and produce showers on one side of the IP. On the other side the tracks of these kind of events produce enhancements in the y distribution of reconstructed tracks in the two detectors, given the back-to-back topology of elastic scattering. The comparison with the y distribution for fully reconstructed elastic-scattering 4/4 events clearly shows these peaks at both edges of the distribution. Similar to events with low total multiplicity these are actually outside of the fiducial

6 Data analysis

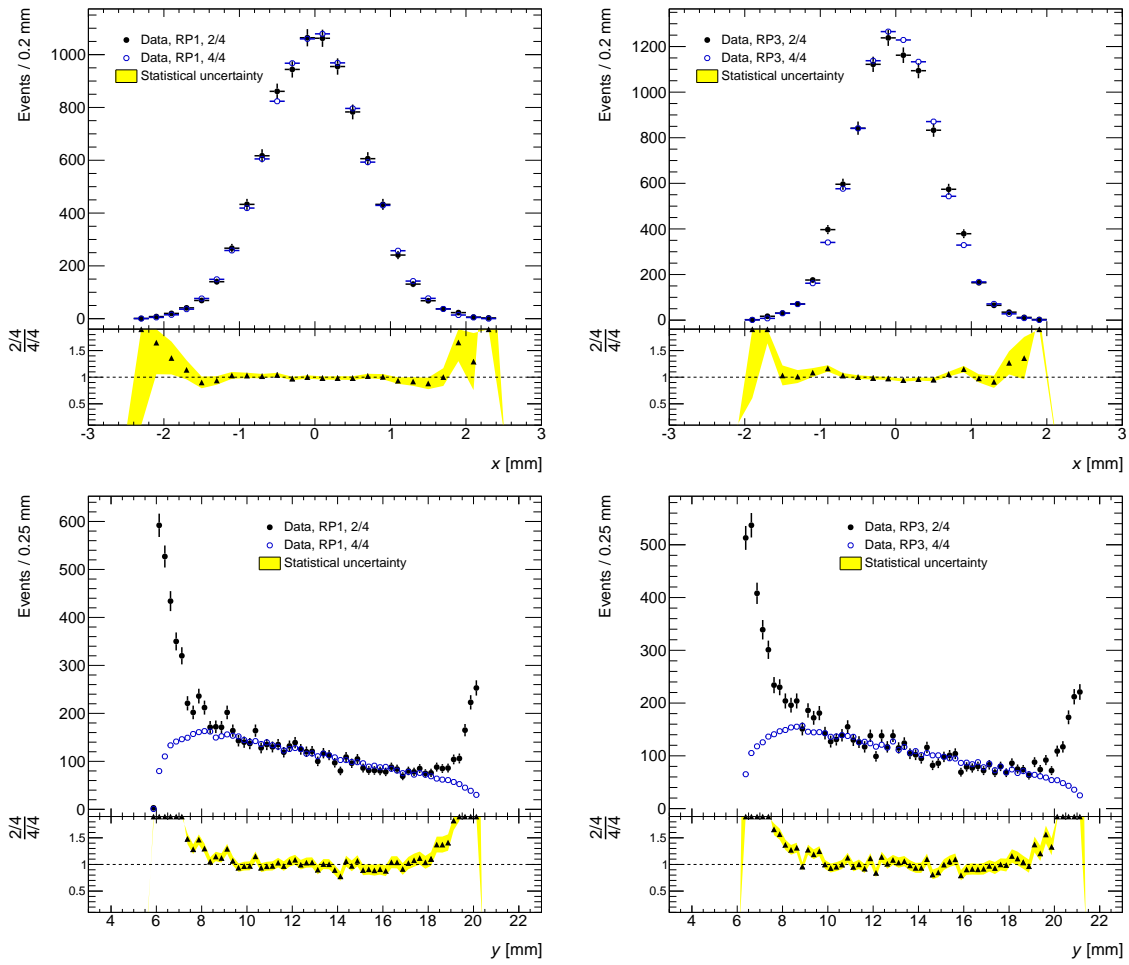


Figure 6.23: Position distributions in x at the top and y at the bottom of case 2/4, sub-case 13 for RP1 and RP3 where no track was reconstructed in RP6 and RP8. The distributions of case 4/4 in blue are normalized to the ones of 2/4 for comparison. In the bottom part of the plots the ratio of both distributions is shown with the statistical uncertainty as yellow band.

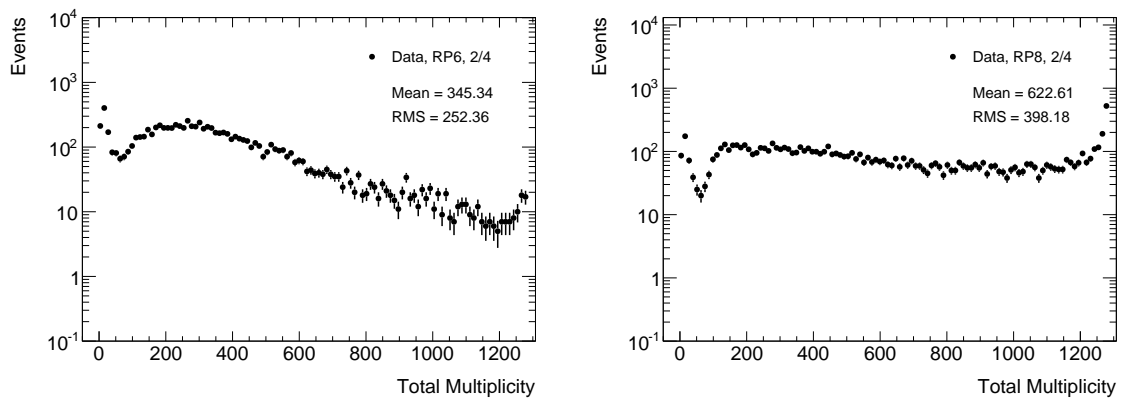


Figure 6.24: Total multiplicity distributions of case 2/4, sub-case 13 for RP6 and RP8, in which no tracks were reconstructed.

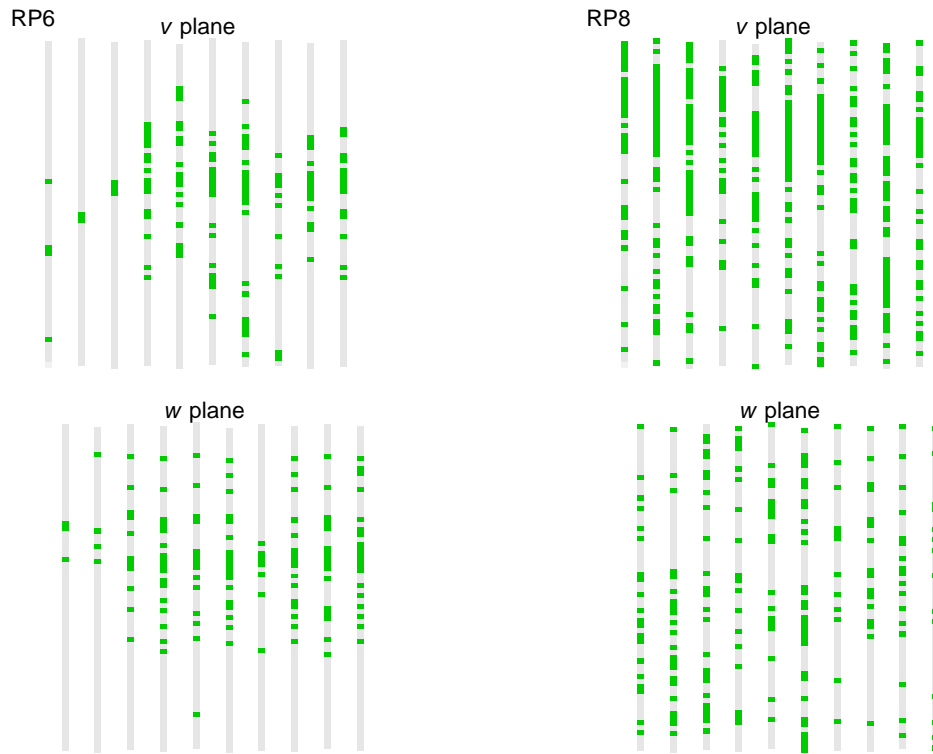


Figure 6.25: Event displays of event 40537 (2/4, sub-case 12). In RP6 and RP8 no track at all is reconstructed. The not shown RPs on the other side of the IP look similar to displays of 4/4 events.

volume, related to acceptance and therefore have to be excluded from the efficiency determination.

As mentioned before, in this case mainly single-diffraction events occur as background, because of the similar event topology as for the 2/4 case. After suppressing this background with the veto on L1_MinBias trigger signals, still some residual background can be found in the 2/4 events. Because of this residual background and the edge peaks in the y distributions two corrections need to be applied to get the correct number of 2/4 events for the reconstruction efficiency. They are needed to really make sure, that only elastic-scattering events are selected and that the efficiency is disentangled from acceptance. Otherwise the reconstruction efficiency would be overestimated. These corrections are described in the next section in detail.

The total multiplicity distributions for the not reconstructed detectors (RP6 and RP8) of sub-case 13 are shown in Figure 6.24. They look similar to the not reconstructed ones of the 3/4 case, where large high multiplicity tails are visible. This implies also a major contribution from showers to the 2/4 case. The distributions for reconstructed detectors are comparable with the ones from 4/4 events, where a maximum can be found at $M_{\text{tot}} \approx 23$ together with a small high multiplicity tail. The complete set of distributions for all sub-cases can be found in the appendix. Figure 6.25 shows an event display of a 2/4 event with a small shower in RP6 and RP8. In both RPs no track is reconstructed, because there are not enough clean fibre layers for the tracking algorithm to work. The not shown pots have a clean track pattern that is nicely reconstructed like for 4/4 events.

Table 6.8: Number of events for all 2/4 sub-cases in both spectrometer arms after reconstruction, elastic-scattering event selection and final selection with corrections.

	Reconstructed	Event selection	Final selection
$N_{2/4}(13)$	20 245	8813	5725
$N_{2/4}(68)$	16 991	8239	6177
$N_{2/4}(24)$	22 742	12 157	8736
$N_{2/4}(57)$	18 955	10 832	7783
$N_{2/4}(1368)$	37 236	17 052	11 902
$N_{2/4}(2457)$	41 697	22 989	16 519

Table 6.9: Lower and upper limits of the central normalization region ('extrapolation limits').

RP	$y_{\text{lower limit}}$ [mm]	$y_{\text{upper limit}}$ [mm]
1	8.934	17.721
2	-8.942	-16.410
3	9.255	18.747
4	-9.173	-17.385
5	9.036	17.028
6	-9.273	-18.879
7	8.830	16.109
8	-9.121	-17.843

With the described event selection for 2/4 events and after the corrections specified in Section 6.3.4.1 one gets $N_{2/4}(\text{Arm } 1368) = 11\,902$ and $N_{2/4}(\text{Arm } 2457) = 16\,519$ elastic-scattering events. This corresponds to a fraction of $N_{2/4}/N_{\text{fail}} \approx 0.28$, which makes this the second most import case. In Table 6.8 the number of events of the four different sub-cases is shown in detail. The numbers are shown after reconstruction and the event selection is applied and after the final selection with the corrections is done. It is important to notice, that arm 2457 has about 1.4 times as many 2/4 events as arm 1368. This eventually leads to a smaller efficiency in arm 2457 and is further explained in Section 6.3.9.

6.3.4.1 Corrections

Because of residual background and edge peaks in the y distributions two corrections need to be applied to get the correct final number of 2/4 events. First the distributions need to be corrected for the edge peaks. This is done by applying an additional cut on the y position of reconstructed tracks, that removes these peaks. Since the peaks also contain events relevant for efficiency and not coming from these kind of edge showers, the distributions obtained with the additional cut need to be corrected and extrapolated to the real shape of the y distributions. This is done by normalizing the distribution of 4/4 events, which provides the real shape, to the one of 2/4 events in the central region, where the peaks are not present. In Table 6.9 the values for the lower and upper limits of the central regions are summarized for all eight Roman Pots. The extrapolated number $N_{2/4}^{\text{ext}}$ of 2/4 events is then obtained from the integral of the normalized 4/4 distribution in the complete y range. In Figure 6.23 on page 86 this normalization is shown for two RPs. Here the integrals are taken of the blue

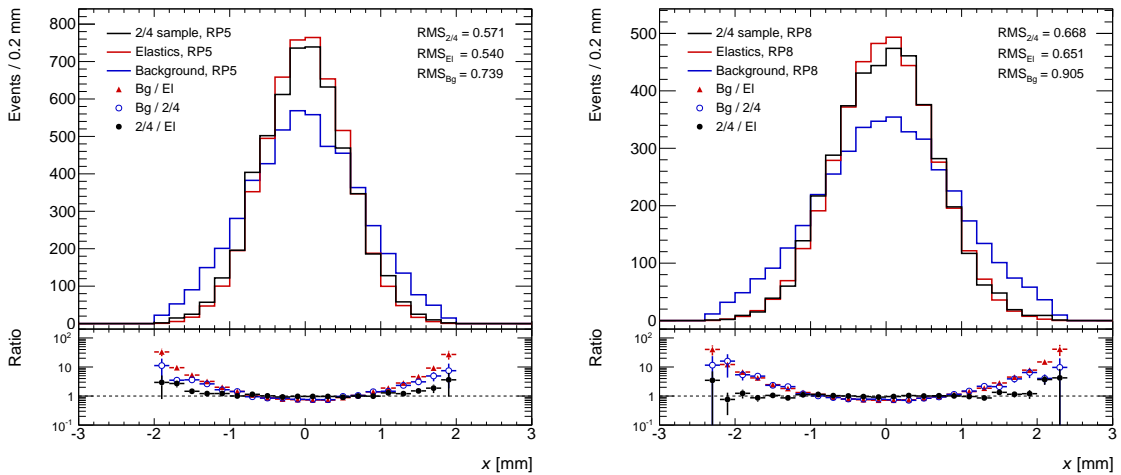


Figure 6.26: Templates and 2/4 sample for the elastic-scattering fraction fit of RP5 (left) and RP8 (right).

4/4 vertical position distributions. Every distribution of the four sub-cases has these edge peaks and needs to be extrapolated with the described method.

And second the number of 2/4 events needs to be corrected for residual background. This background includes primarily single diffraction events, but also other tracks coming from accidental beam-halo particles. The beam-halo background can have a fake elastic-scattering L1 trigger signal and can look like 2/4 events. In principle any other background that looks like 2/4 events is also possible. Because of the missing left-right collinearity cuts, background is much more pronounced in the 2/4 case and needs to be treated with a special correction.

The fact that the x distribution of this background is broader than of elastic-scattering events is now used to estimate the fraction f_{bg} of this background in every RP of the 2/4 sample. This is done with a fraction fit, that fits the sum of two templates for background and elastic-scattering events to the x distributions of the 2/4 sample. These templates have a fixed shape and one free normalization parameter for the fit and only data is used to obtain their shape. The elastic-scattering template uses fully reconstructed 4/4 events with the nominal event selection and in addition the same cut as for the edge peak correction is applied to the y distributions. In a first stage events with an un-prescaled L1_ALFA_Any trigger signal are selected for the background templates. This un-prescaled trigger-signal information is only available in the calibration stream of run 191373 (compare Section 3.3.2). And thus this stream is used for the generation of the background templates as opposed to the rest of the analysis, where the physics stream is used. The background events selected in this way have a signal in any of the eight Roman Pot detectors. In the second stage the selected events need to have reconstructed tracks in two consecutive detectors on the same side of the IP and no tracks in all other six detectors. In addition the same L1_MinBias trigger signals, that are used as veto for the 2/4 sample, are required now, since they indicate the presence of the dissociative component of the single diffraction. The same event selection cuts are applied as for the 2/4 case, but without the requirement to have a total multiplicity of more than five in the detectors without reconstructed tracks. And also the same additional cut on the y distribution for edge peak correction is applied. Because of this selection the background template includes mainly single-diffraction events that look like 2/4 events and is therefore called ‘single-diffraction-enhanced’.

6 Data analysis

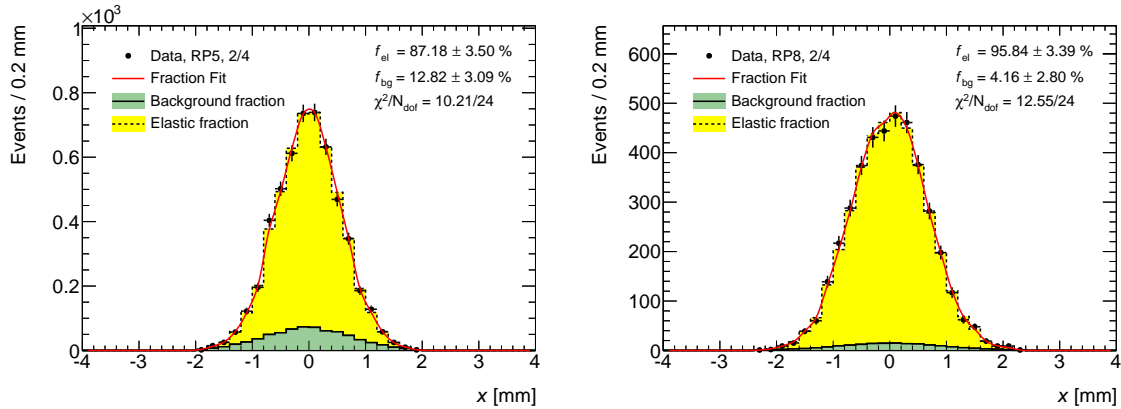


Figure 6.27: Result of the elastic-scattering fraction fit for RP5 (left) and RP8 (right).

Table 6.10: Elastic-scattering fraction of 2/4 events obtained with the fraction fit.

	Armlet 13	Armlet 68	Armlet 24	Armlet 57
Elastic-scattering fraction f_{el}	0.9267	0.9518	0.9618	0.8836
Statistical uncertainty	0.0369	0.0365	0.0281	0.0348
Systematic uncertainty	+0.0733 −0.1607	+0.0482 −0.1680	+0.0382 −0.1679	+0.1164 −0.1686
Total uncertainty	+0.0733 −0.1649	+0.0482 −0.1720	+0.0382 −0.1702	+0.1164 −0.1722

Figure 6.26 shows the templates for background and 4/4 events together with the 2/4 sample that is fitted for RP5 and RP8. The 2/4 sample of the inner detector RP5 has an $RMS_{2/4} = 0.571$ which is between the elastic-scattering template ($RMS_{El} = 0.540$) and background template ($RMS_{Bg} = 0.739$) and therefore they can be used for the fraction fit. The templates for the outer detector RP8 are broader, but they have the same order $RMS_{El} < RMS_{2/4} < RMS_{Bg}$ and are also good for the fit. The templates for the rest of the RPs can be found in Appendix A.3 and they are all consistent with the two detectors shown here, where the distributions of the four outer detectors are broader than of the inner ones.

The distributions of the eight detectors are fitted separately. Since there are four 2/4 sub-cases, consisting of the four armlets 13, 24, 57 and 68, the fits of two detectors are averaged to get the elastic-scattering fraction f_{el} and background fraction f_{bg} in these armlets. Figure 6.27 shows two fraction fits for RP5 and RP8. In RP5 the 2/4 sample consists of 87.18 % elastic-scattering (yellow template) and 12.82 % background events (green template). In RP8 the elastic-scattering fraction is a little bigger with $f_{el} = 95.84 \%$. Table 6.10 shows the averaged fraction fit results in all four armlets with statistical and systematic uncertainty. The statistical uncertainty is rather large, because of the small 2/4 sample statistics compared to both template statistics. Furthermore, the used template fit is optimized for templates with very large statistics from MC simulation, which is not used here. The procedure to obtain the systematic uncertainties is described in detail in Section 6.3.8. Since the elastic-scattering fraction can at most be one ($0 \leq f_{el} \leq 1$) the systematic and total uncertainty are asymmetric to not get a fraction greater than one.

The elastic-scattering fraction f_{el} in the upper detectors is about 90 % and somewhat smaller than in the lower ones with about 96 %. The average elastic-scattering fraction in the four

armlets is about 93 %. This means only this 93 % of the 2/4 events are from elastic scattering and need to be included in the reconstruction efficiency calculation. In armlet 57 the elastic-scattering fraction is relatively small, compared to the other three armlets. A comparison can be seen in Figure 6.37 on page 101 for example. In this armlet the x distribution of the 2/4 sample is broader than in the other armlets, but the background and elastic-scattering templates are similar to the other ones. In the end this yields a smaller elastic-scattering fraction in armlet 57. But everything is consistent and no error could be found in the determination of the templates.

The final numbers $N_{2/4}$ (Arm 1368) and $N_{2/4}$ (Arm 2457) of 2/4 events in the two arms is than simply the sum of the number of 2/4 events in all sub-cases of the respective arm after applying the two steps of the correction procedure described above. Because the two corrections have several steps, that need to be done in a specific order, the steps are summarized here again:

- 1.) Selection of reconstructed 2/4 events requiring a veto on L1_MinBias trigger signals. Events have to fulfill all applicable event selection cuts.
- 2.) Applying additional cuts on vertical position to get sub sample of 2/4 events without peak region at detector and beam screen edges.
- 3.) Generation of templates from x -distributions of elastic-scattering 4/4 and background events with calibration stream. In both cases all applicable event selection cuts and the additional cuts to exclude the peak regions are applied.
- 4.) Fit of the elastic-scattering fraction in the 2/4 sample without peak region via template fit.
- 5.) Extrapolation of 2/4 sample to full region using vertical position distribution of elastic-scattering 4/4 events.
- 6.) Correction of extrapolated sample with elastic-scattering fraction to get the final number of 2/4 events.

6.3.5 1+1/4

This case consists of events with only two reconstructed detectors out of four in an spectrometer arm. In contrast to 2/4 events, where both reconstructed and not reconstructed detectors are on the same side of the IP, in 1+1/4 events the two detectors with reconstructed tracks are on opposite sides of the IP. One of the main differences is the absence of single diffraction background in this case. Therefore, a correction like the elastic-scattering fraction fit is not needed here.

There are eight sub-cases with different configurations of the detectors with reconstructed tracks. Basically they are classified into three groups, according to whether the inner or outer detectors have the reconstructed tracks:

- (a) Both inner detectors with reconstructed tracks.
- (b) Both outer detectors with reconstructed tracks.
- (c) On one side an inner detector and on the other side an outer detector with reconstructed tracks.

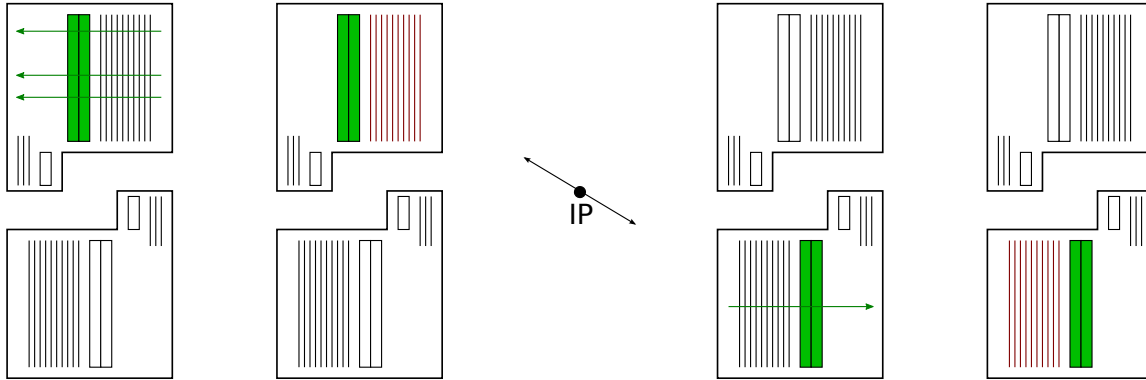


Figure 6.28: Diagram of a 1+1/4 event. An elastic-scattering trigger signal is present in arm 1368 shown by green trigger tiles. In RP1 and RP6 tracks are reconstructed shown by green arrows. RP1 and RP8 have no reconstructed tracks which is shown by red fibre planes.

Sub-case 16, which is illustrated in Figure 6.28, is classified into group (c), for example. Here RP1 and RP6 have reconstructed tracks, they are on opposite sides of the IP and one of them is an inner and one an outer detector. Again an elastic-scattering trigger signal is present in arm 1368, depicted by the green trigger tiles, but reconstructed tracks cannot be found in RP3 and RP8. Typically group (a) events can be found, when on both sides of the IP too many hits are produced in the outer detectors. This is the case, if a shower creates a high multiplicity event, which is similar to the 3/4 sub-cases, where no track is reconstructed in the outer detectors. Such a configuration is fairly common, so that this group of events yields the largest number in the 1+1/4 case. One possible explanation for the occurrence of group (b) events are showers started before or in both inner detectors, spreading to the outer ones and producing not too much hits there, so that the tracking algorithm can reconstruct tracks. Not many events in this group can be found and they only play a minor role in the overall number of 1+1/4 events. Group (c) is probably a mixture of the showers found in (a) and (b). The number of events in this group is also very small compared to group (a).

Only a few event selection cuts can be used to decide whether or not an event is from elastic scattering. In all groups the fiducial cuts are applied to the two detectors with reconstructed tracks. Additionally left-right collinearity cuts in x and y are applied in group (a) and (b), because of the configuration with two inner or outer detectors with reconstructed tracks. In group (c) one normally could not apply the collinearity cuts. But now the track position extrapolation described in Section 3.4.2 is used to extrapolate the position in coordinates $u \in \{x, y\}$ of the outer detector on one side to the position of the inner one on the same side by using the effective lever arms given by

$$u_{\text{inner}} = u_{\text{outer}} \frac{L_{u,\text{inner}}^{\text{eff}}}{L_{u,\text{outer}}^{\text{eff}}}. \quad (131)$$

The extrapolated position is then used together with the measured one in the inner detector on the other side to apply the collinearity cuts. Since there are not two detectors reconstructed on one side, the local angle θ_x cannot be reconstructed, which also means the x vs. θ_x cut cannot be applied in any of the three groups. Finally the total multiplicity cut is applied to the two detectors without reconstructed tracks.

To further reduce background and enhance the elastic-scattering pattern especially in group (b) and (c) an additional event selection cut on the horizontal coordinate is applied. The x position of tracks in inner detectors have to fulfil $|x| < 2.2$ mm and in outer ones $|x| < 2.5$ mm.

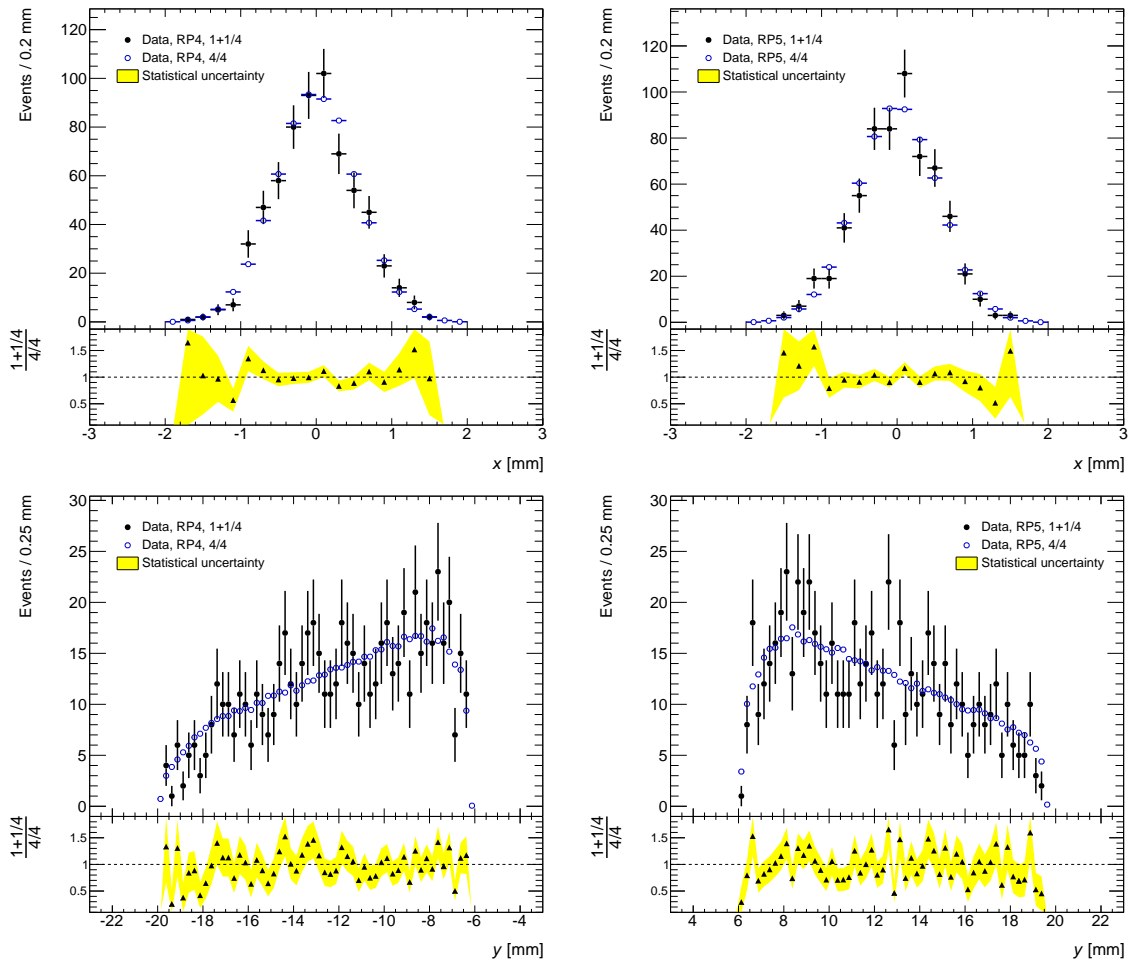


Figure 6.29: Position distributions in x at the top and y at the bottom of case 1+1/4, sub-case 45 for RP4 and RP5 where no track was reconstructed in RP2 and RP7. The distributions of case 4/4 in blue are normalized to the ones of 1+1/4 for comparison. In the bottom part of the plots the ratio of both distributions is shown with the statistical uncertainty as yellow band.

This cut limits the horizontal position distribution to events with small x , which corresponds to the pattern of the distribution in 4/4 events.

In Figure 6.29 the x - and y -position distributions for sub-case 45 of group (a) are shown after all event selection cuts. They agree very well with the distributions of fully reconstructed elastic-scattering 4/4 events. Because of the small statistics, larger fluctuations than in the aforementioned cases can be observed. The complete set of distribution, especially of group (b) and (c), is shown in Appendix A.4. In (b) and (c) the distributions barely agree, but this is not that important. Because the statistics in these sub-cases are even smaller, they only play a minor role in the overall number of 1+1/4 events. In summary one can say, that with the described cuts really elastic-scattering events are selected in this reconstruction case.

The total multiplicity distributions of not reconstructed detectors shown in Figure 6.30 for sub-case 45 confirms the mentioned showers as reason for the inefficiency. Both distributions are comparable with the ones of 3/4 events, where a high multiplicity tail from showers can be found. The distributions of group (b) and (c) in Appendix A.4 have also very small statistics and no conclusion can be made about them. All distributions of detectors with re-

6 Data analysis

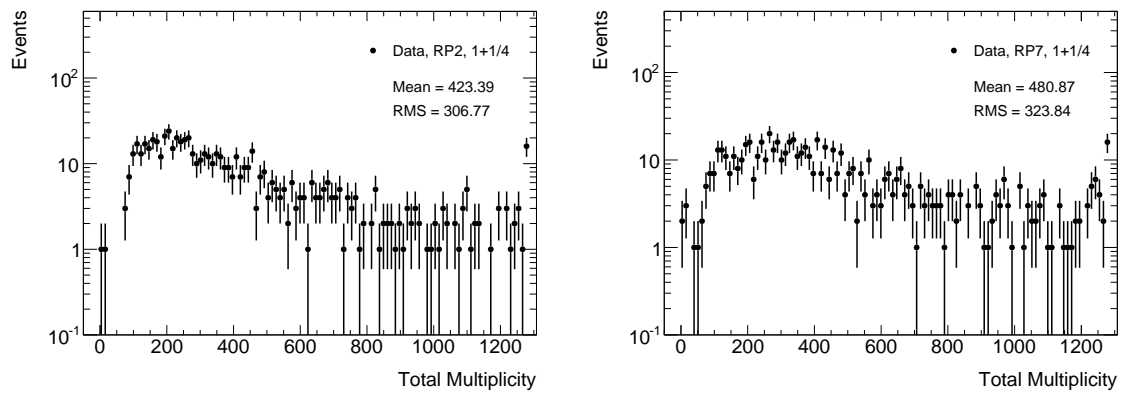


Figure 6.30: Total multiplicity distributions of case 1+1/4, sub-case 45 for RP2 and RP7, in which no tracks were reconstructed.

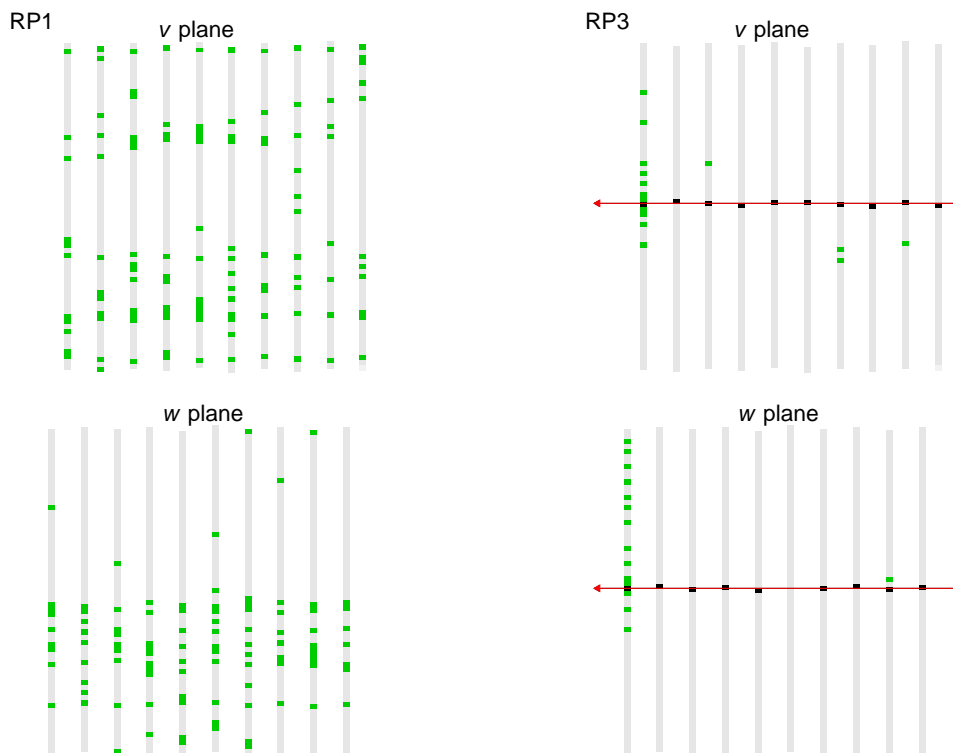


Figure 6.31: Event displays of event 509298 (1+1/4, sub-case 36). A track is reconstructed in RP3 but not in RP1.

Table 6.11: Number of events for all 1+1/4 sub-cases in both spectrometer arms after reconstruction and elastic-scattering event selection.

	Reconstructed	Event selection
$N_{1+1/4}(16)$	1186	56
$N_{1+1/4}(18)$	784	17
$N_{1+1/4}(36)$	1818	617
$N_{1+1/4}(38)$	816	39
$N_{1+1/4}(25)$	941	62
$N_{1+1/4}(27)$	761	10
$N_{1+1/4}(45)$	1943	642
$N_{1+1/4}(47)$	898	55
$N_{1+1/4}(1368)$	4604	729
$N_{1+1/4}(2457)$	4543	769

constructed tracks are similar to the ones of 4/4 events, but with a small high multiplicity tail. An event display of sub-case 36 is shown in Figure 6.31. Here the pattern with a reconstructed track in the inner detector RP3 and a shower in the outer one RP1 can be seen. This is again similar to such shower events in the 3/4 case. The complete display can be found in the appendix in Figure A.50 on page 182. Another display of sub-case 38 is also shown there in Figure A.51, which clearly shows a high multiplicity event in the inner detector RP6, but a nicely reconstructed track in the outer RP8. Because not all shower fragments propagate to the outer detector, only a fraction with lower total multiplicity is detected and tracks are reconstructed. These tracks are not necessarily from the original elastically-scattered proton, but can be from its shower fragments. The probability for such an event is very low, which can also be seen in the small number of events in group (b) and (c).

After the described event selection for 1+1/4 events and no further corrections one gets $N_{1+1/4}(\text{Arm } 1368) = 729$ and $N_{1+1/4}(\text{Arm } 2457) = 769$ elastic-scattering events. This corresponds to a fraction of $N_{1+1/4}/N_{\text{fail}} \approx 0.015$, where most of the event are from group (a). In Table 6.11 the number of events of the eight different sub-cases is shown in detail. The numbers are shown after reconstruction and the event selection is applied. A large difference between events after reconstruction and event selection can be seen in the table. This means that many of the rejected reconstructed tracks do not correspond to an elastically scattered proton, but rather to shower tracks or other background.

6.3.6 1/4

In this case only one detector in the spectrometer arm with a trigger signal has reconstructed tracks. There are only two possibilities: either the detector with reconstructed tracks is an inner one or an outer one. Therefore, this case is also divided into eight sub-cases, which represent the eight RPs. Because only one detector has reconstructed tracks, these events are dominated by background coming from showers and beam-halo events. The illustration in Figure 6.32 shows an event of sub-case 1, where tracks are reconstructed only in RP1.

Because of the limited number of detectors with reconstructed tracks only the fiducial cuts are applied to the single reconstructed detector. Neither the left-right collinearity cuts nor the x vs. θ_x cuts can be applied. For the collinearity cuts a reconstructed track is missing on the other side of the IP and for the other cut a second detector with reconstructed tracks

6 Data analysis

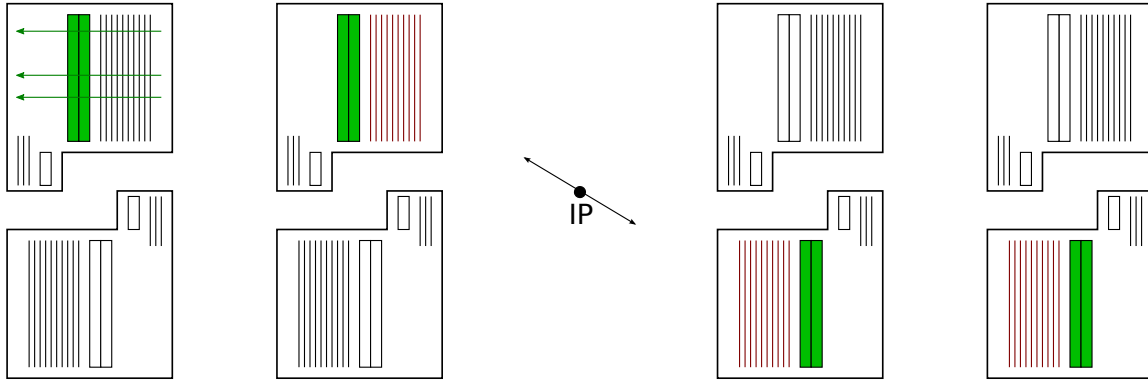


Figure 6.32: Diagram of a $1/4$ event. An elastic-scattering trigger signal is present in arm 1368 shown by green trigger tiles. In RP1 tracks are reconstructed shown by green arrows. RP3, RP6 and RP8 have no reconstructed tracks which is shown by red fibre planes.

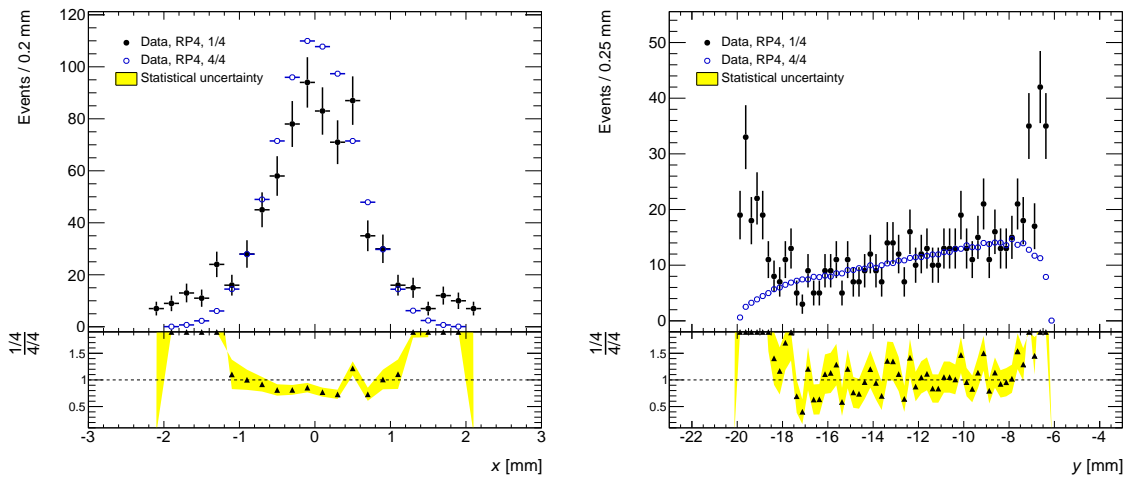


Figure 6.33: Position distribution in x and y of case $1/4$ for RP4 where tracks were reconstructed only in RP4 and of the fully reconstructed elastic-scattering case $4/4$. The y distribution of case $4/4$ in blue is normalized to the one of $1/4$ in the central part without the peaks and x is normalized in the whole range. In the bottom part the ratios of both distributions are shown with the statistical uncertainty as yellow band.

on the same side is missing to reconstruct the local angle. The total multiplicity cut is of course applied to the three not reconstructed detectors of the arm with a trigger signal. To suppress the mentioned background and enhance the elastic-scattering event pattern the same additional cut on the horizontal coordinate as for $1+1/4$ events is applied.

Figure 6.33 shows the position distributions in RP 6 after all event selection cuts, where this RP is the only one with reconstructed tracks. At larger x the position distributions of $1/4$ events and fully reconstructed elastic-scattering $4/4$ events do not agree very well, because of the mentioned background. The additional cut does not take care of this difference completely, but this can be neglected, because of the low impact of the case on the efficiency. Furthermore, in the y -position distribution peaks are visible at the edges like in the $2/4$ case. The inner detectors do agree a little bit better with elastic-scattering events than the outer ones, which can be seen in the complete set of distributions in Appendix A.5.

Table 6.12: Number of events for all 1/4 sub-cases in both spectrometer arms after reconstruction, elastic-scattering event selection and final selection with extrapolation correction.

	Reconstructed	Event selection	Final selection
$N_{1/4}(1)$	4115	317	271
$N_{1/4}(3)$	3986	582	412
$N_{1/4}(6)$	4719	540	432
$N_{1/4}(8)$	3383	233	222
$N_{1/4}(2)$	3947	303	260
$N_{1/4}(4)$	4791	756	540
$N_{1/4}(5)$	3983	707	557
$N_{1/4}(7)$	2862	227	199
$N_{1/4}(1368)$	16 203	1672	1337
$N_{1/4}(2457)$	15 583	1993	1556

To correct for the edge peaks, the same extrapolation procedure as for 2/4 events described in Section 6.3.4.1 is applied. The limits for the extrapolation are also the same as summarized in Table 6.9. But a template fit to determine the elastic-scattering fraction is not done, because no single diffraction background is expected here.

Total multiplicity distributions can be found in the appendix. They show the same structure as for the other cases. In the reconstructed detector a peak at $M_{\text{tot}} \approx 23$ can be seen with a small high multiplicity tail. The not reconstructed detectors all show a larger high multiplicity tail up to the maximum value.

The described event selection for 1/4 events yields $N_{1/4}(\text{Arm 1368}) = 1337$ and for the other arm $N_{1/4}(\text{Arm 2457}) = 1556$ elastic-scattering events. This corresponds to a fraction of $N_{1/4}/N_{\text{fail}} \approx 0.03$, which is slightly more than the 1+1/4 case. In Table 6.12 the number of events of the eight different sub-cases is shown in detail. The numbers are shown after reconstruction and the event selection is applied and after the final selection where the extrapolation correction is done. There is also a large difference between reconstructed and finally selected events, which confirms the existence of showers, where random tracks are reconstructed.

6.3.7 0/4

In this case no detector has any reconstructed tracks in the spectrometer arm where a L1 trigger signal is present. This is illustrated in Figure 6.34 where only the green trigger tiles provide signals. There are only two sub-cases for the two arms.

Because there is no track coordinate reconstructed, the elastic-scattering event selection cuts cannot be applied. Only the cut on total multiplicity in all four detectors of the arm with a trigger signal is used to reduce the background and disentangle acceptance. There is no possibility to check if these events are really from elastic scattering and could not be reconstructed because of e.g. showers.

The total multiplicity distributions of arm 1368 is shown in Figure 6.35. All of them show the large high multiplicity tail corresponding to showers where nearly every fibre is hit and provides a signal. The other arm is shown in Figure A.64 in the appendix and basically shows the same distributions. A typical event display for two RPs is shown in Figure 6.36. Nearly every fibre is hit or provides a signal because of cross-talk, thus no track can be reconstructed.

6 Data analysis

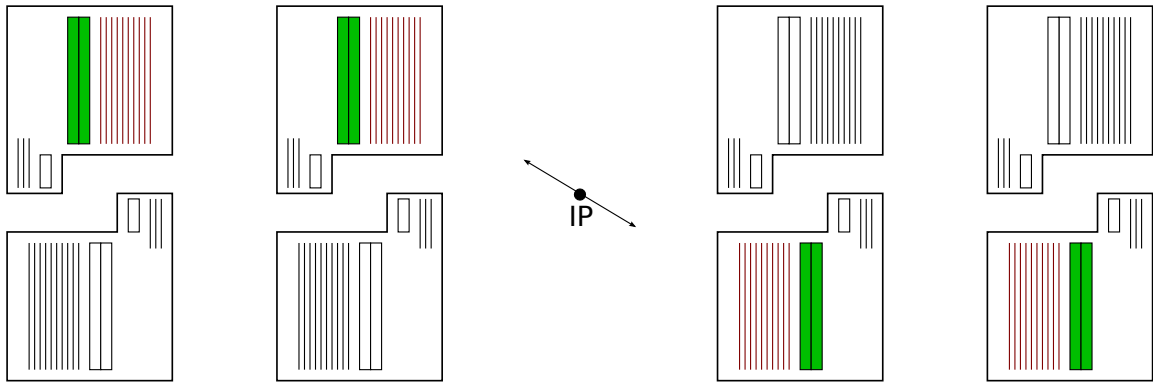


Figure 6.34: Diagram of a 0/4 event. An elastic-scattering trigger signal is present in arm 1368 shown by green trigger tiles, but none of the RPs has reconstructed tracks which is shown by red fibre planes.

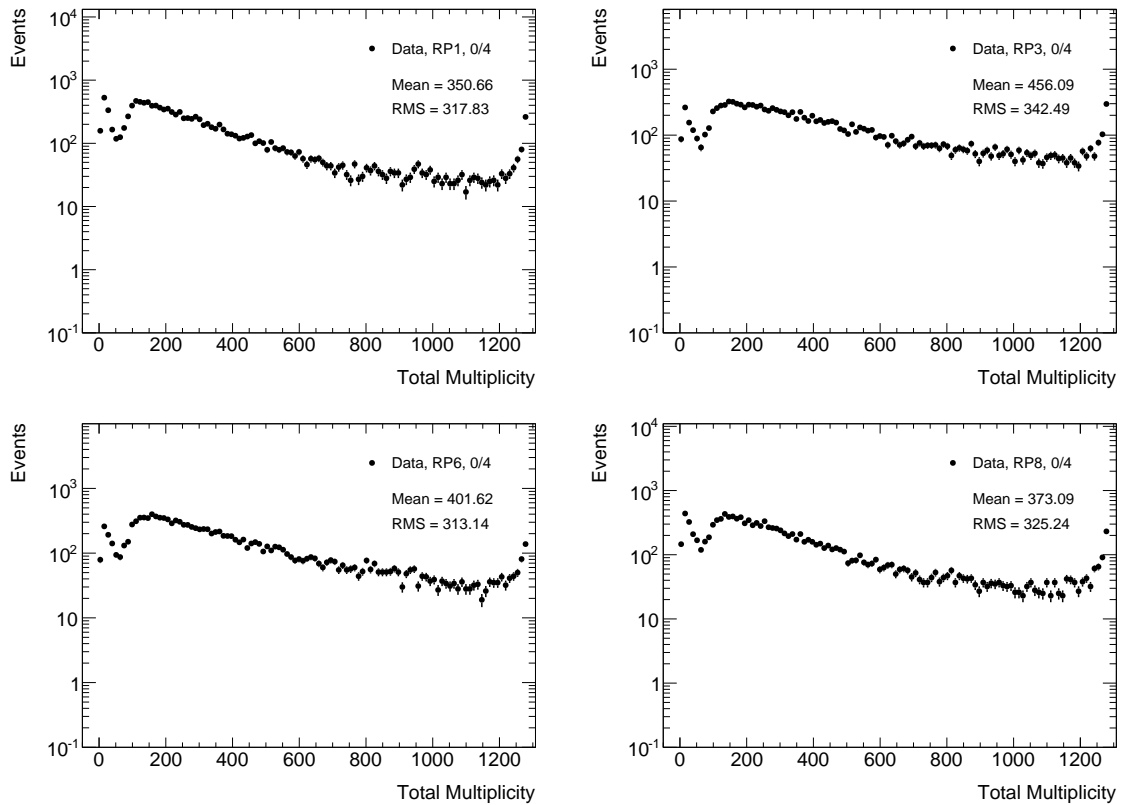


Figure 6.35: Total multiplicity distributions of case 0/4, sub-case 1368 for all RPs, in which no tracks were reconstructed.

Table 6.13: Number of events for both 0/4 sub-cases after reconstruction, total multiplicity cut and estimation via 2/4 events.

	Reconstructed	Multiplicity cut	Estimated
$N_{1/4}(1368)$	17 751	13 383	340
$N_{1/4}(2457)$	15 395	11 954	700

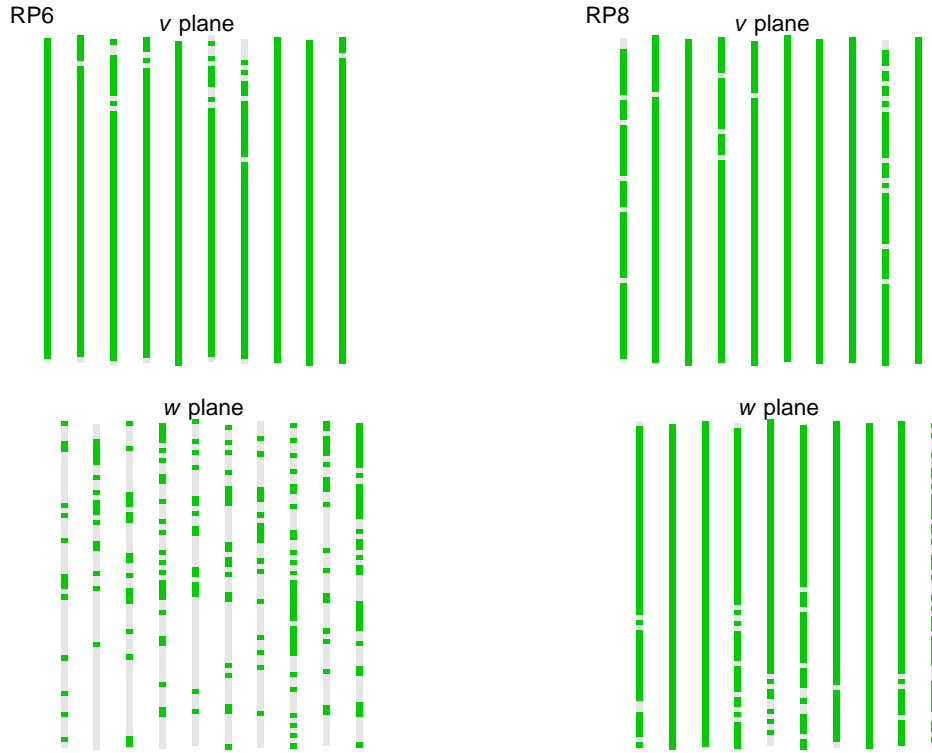


Figure 6.36: Event displays of event 1002541 (0/4, sub-case 1368). No track is reconstructed.

With the normal method from the previous sections one can only determine a raw number of 0/4 events $N_{2/4}^{\text{raw}}$. This number is dominated by background events and shower tracks. It is not used for the efficiency calculation, since the exact number of real elastic-scattering events cannot be determined. Thus the number $N_{0/4}$ of events in this case is estimated from the number $N_{2/4}$ of elastic-scattering 2/4 events, that was determined in Section 6.3.4. In principle a 0/4 event is a double 2/4 event, where the not reconstructed detectors appear on both sides of the IP. Given that the probability $P(2/4)$ to get an 2/4 event in one spectrometer arm is

$$P(2/4) = \frac{N_{2/4}}{N_{4/4}}, \quad (132)$$

the probability to get an 0/4 event in the same arm is then

$$P(0/4) = P(2/4)^2 = \frac{N_{2/4}^2}{N_{4/4}^2}. \quad (133)$$

And the number $N_{0/4}$ of 0/4 events is estimated to

$$N_{0/4} = P(0/4) \cdot N_{4/4} = \frac{N_{2/4}^2}{N_{4/4}}. \quad (134)$$

The described estimation of 0/4 events yields separately for both arms $N_{0/4}(\text{Arm 1368}) = 340$ and $N_{0/4}(\text{Arm 2457}) = 700$ elastic-scattering events. This corresponds to a fraction of $N_{0/4}/N_{\text{fail}} \approx 0.01$, which is the smallest one of all reconstruction cases. In Table 6.13 the number of events is shown in detail for both sub-cases after reconstruction, with the multiplicity

cut and the estimated values. There is of course a large difference between reconstructed events and the estimated number, because of the background domination. Here it would be preferable to have an estimate of 0/4 events from MC simulation, but unfortunately this is not possible in a satisfying way. In Section 6.3.10 the efficiency is determined from simulation and it is shown why it ultimately is not used.

6.3.8 Systematic uncertainties

The calculation of reconstruction efficiency is based on the selection of not fully reconstructed events. As described in the previous sections, event selection cuts are used to determine, if an event really is from elastic scattering and has to be considered for the efficiency calculation. Therefore, systematic uncertainties are also based on these selection cuts. In general a variation of the cuts over a large range is done to test their influence on the efficiency. Each cut is varied individually in this range and the efficiency ϵ_{rec} is calculated via Equation (129) for each cut value. Half of the spread between maximum and minimum of the efficiency in a reasonable range is taken as systematic uncertainty for each cut:

$$\Delta\epsilon_{\text{rec}}^{\text{cut}} = \frac{1}{2} (\max \epsilon_{\text{rec}}^{\text{cut}} - \min \epsilon_{\text{rec}}^{\text{cut}}). \quad (135)$$

The half of the spread is taken, because of the large number of variation values. Another important uncertainty comes from the template fit of the elastic-scattering fraction in the 2/4 case. Furthermore, this fraction fit depends on the choice of templates, which is also based on elastic-scattering event selection cuts. Hence a variation of these cuts is also done for the template fit in the same way as described above. For each variation value of the cuts the template fit is done and the elastic-scattering fraction is calculated. The systematic uncertainty is again taken from the half spread in a reasonable variation range. The following sub-sections describe the systematic uncertainty determination for the fraction fit and efficiency in detail. The choice of the reasonable range for every cut is also depicted there.

6.3.8.1 Elastic-scattering fraction fit

The systematic uncertainty of the elastic-scattering fraction fit has several sources that are involved in the choice of the 2/4 sample and 4/4 template. First this are the event selection cuts: the fiducial cuts on the beam screen and detector edge, the left-right collinearity cuts in x and y , the x vs. θ_x cut and the total multiplicity cut. Additional sources are the limits of the extrapolation range, the binning for the horizontal position distribution and the range of the template fit. All of these sources are varied over a large range and the template fit is done for every variation value to get the elastic-scattering fraction. This is shown in Figure 6.37 and 6.38 for all involved quantities. The systematic uncertainty for these quantities is obtained from half of the spread of the fraction fit results in the range depicted by the two red dotted vertical lines in the plots. Indicated by the black line is the value of the cut used for nominal event selection (see also Section 6.1). Not the whole range is taken, because especially too tight cuts would throw away most of the elastic-scattering events and result in large fluctuations. For example this can be seen for the x vs. θ_x cut, where the elastic-scattering fraction drops significantly for a tight cut with 2σ . Such tight cuts are not reasonable and therefore excluded from the final variation range. The same is true for too loose cuts, which are also excluded from the range. For most of the cuts a final $\pm 1\sigma$ range around the nominal value is chosen.

6.3 Event reconstruction efficiency

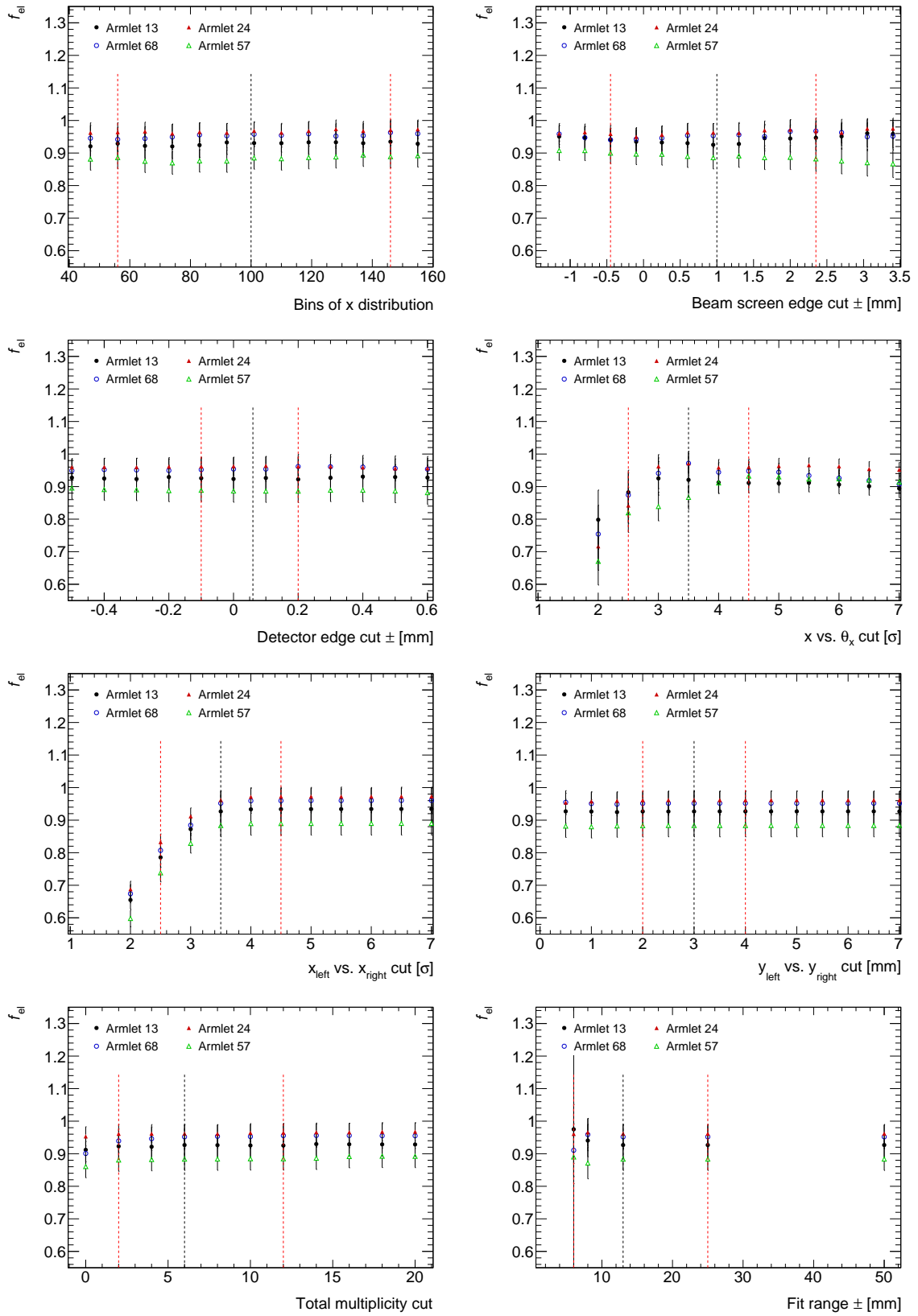


Figure 6.37: Elastic-scattering fraction of 2/4 events from template fit as a function of the variation of event selection cuts for four armlets. The shown cuts are: binning horizontal coordinate, vertical coordinate beam screen edge, vertical coordinate detector edge, x vs. θ_x , horizontal collinearity, vertical collinearity, total multiplicity and fit range.

6 Data analysis

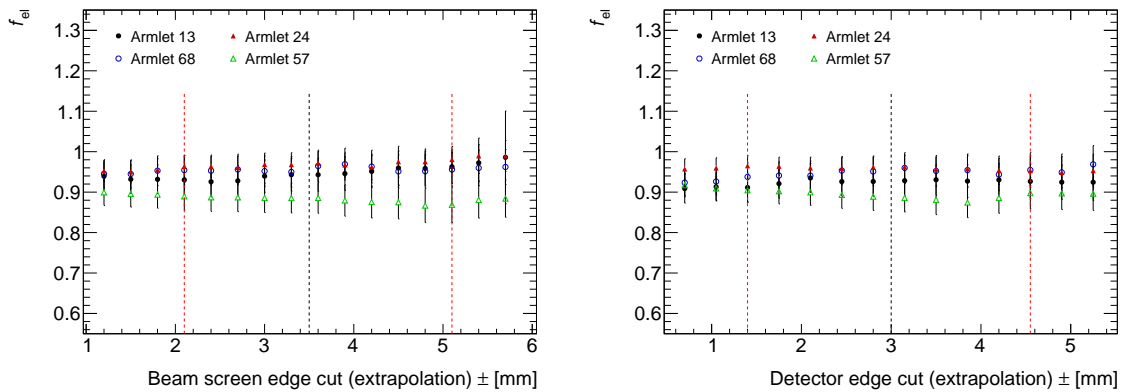


Figure 6.38: Elastic-scattering fraction of 2/4 events from template fit as a function of the variation of event selection cuts for four armlets. The shown cuts are: extrapolation limit beam screen edge and extrapolation limit detector edge.

Table 6.14: Elastic-scattering fraction f_{el} of 2/4 events obtained from halo-enhanced and mixed template with statistical uncertainty.

	Armlet 13	Armlet 68	Armlet 24	Armlet 57
f_{el} (halo)	0.9876	0.9743	0.9743	0.9709
Statistical uncertainty (halo)	0.3544	0.1276	0.0975	0.0637
f_{el} (mixed)	0.8355	0.8706	0.9190	0.7331
Statistical uncertainty (mixed)	0.0699	0.0724	0.0484	0.0661

Another systematic uncertainty source is the choice of the background template. In Section 6.3.4.1 a single-diffraction enhanced template is used to determine the elastic-scattering fraction, but it is also possible to use a halo-enhanced or mixed template. In order to get the systematic uncertainty of this choice, the fraction fit was performed with these two additional templates. The halo-enhanced template is produced from events in unpaired bunches of run 191373, where no collisions occurred. To get the beam-halo events, that look like 2/4, the same event selection cuts as for the single-diffraction enhanced template are applied. The mixed template uses the same bunches, trigger signals and event selection cuts as the single-diffraction enhanced one, except for the requirement of L1_MinBias trigger signals. The trigger signals are not required but they are also not vetoed.

The first template leads to a higher and the second one to a lower elastic-scattering fraction as shown in Table 6.14. The full spread between these two is taken as systematic uncertainty of the background template. In contrast to the half of the spread, which is taken for the variation, here the full one is used, because only values from two templates are available. Furthermore, the average of the two detectors comprising the four armlets is taken as uncertainty for each armlet. The total systematic uncertainty of the elastic-scattering fraction fit consists then of the individual contributions from the varied quantities and the background template choice. It is calculated by summing up the uncertainties quadratically:

$$\Delta f_{el} = \sqrt{\sum_i (\Delta f_{el,i})^2} \quad (136)$$

The contributions to the total systematic uncertainty are listed in Table 6.15. It can be seen, that the uncertainty from the background template is the dominating part. The second

Table 6.15: Contributions to statistical, systematic and total uncertainty of elastic-scattering fraction f_{el} . The uncertainty from the background template is the average of the four armlets.

Source	Armlet 13	Armlet 68	Armlet 24	Armlet 57
f_{el}	0.9267	0.9518	0.9618	0.8836
Statistical uncertainty	0.0369	0.0365	0.0281	0.0348
Beam screen edge cut	0.0108	0.0134	0.0112	0.0088
Detector edge cut	0.0021	0.0048	0.0009	0.0014
x vs. θ_x cut	0.0214	0.0487	0.0647	0.0564
x_A vs. x_C cut	0.0738	0.0761	0.0695	0.0756
y_A vs. y_C cut	0.0001	0.0003	0.0002	0.0003
Multiplicity cut	0.0027	0.0082	0.0019	0.0019
Extrapolation limit BS	0.0128	0.0121	0.0105	0.0119
Extrapolation limit DE	0.0118	0.0111	0.0061	0.0152
Fit range	0.0242	0.0242	0.0024	0.0094
Horizontal binning	0.0072	0.0107	0.0066	0.0121
Background template	0.1373	0.1373	0.1373	0.1373
Total systematic uncertainty	0.1607	0.1680	0.1679	0.1686
Total uncertainty	+0.0733 −0.1649	+0.0482 −0.1720	+0.0382 −0.1702	+0.1164 −0.1722

largest uncertainty comes from the left-right collinearity cut in x . The systematic uncertainty along with the statistical uncertainty is then propagated to the reconstruction efficiency by recalculating the efficiency with the maximum and minimum elastic-scattering fraction values. Since the elastic-scattering fraction can at most be one ($0 \leq f_{\text{el}} \leq 1$) the total uncertainty is asymmetric to not get a fraction greater than one.

6.3.8.2 Efficiency

Likewise, for the systematic uncertainty of the reconstruction efficiency several sources are considered. This are the event selection cuts in particular the fiducial cuts on the beam screen and detector edge, the left-right collinearity cuts in x and y , the x vs. θ_x cut, the additional event selection cut on the horizontal coordinate for 1+1/4 and 1/4 events and the total multiplicity cut. More sources are the limits of the extrapolation range and the elastic-scattering fraction.

Except for the uncertainty from elastic-scattering fraction these sources are varied over a large range and the reconstruction efficiency is calculated for every variation value. This is shown in Figure 6.39 and 6.40 for all involved quantities. Again the systematic uncertainty for these quantities is obtained from half of the spread of reconstruction efficiency in the range depicted by the two red dotted lines in the plots. Indicated by the black line is the value of the cut used for nominal event selection. As for the fraction fit uncertainty not the whole range is taken, because especially too tight cuts would throw away most of the elastic-scattering events. This would lead to unreasonable results that manifest in efficiency drops and large fluctuations. Such drops can be seen e.g. for the x vs. θ_x and the left-right collinearity cut in x . Looser cuts would also result in unreasonable efficiencies, because too much background would be allowed in the number of elastic-scattering events. However, for most of the cuts ε_{rec} does not fluctuate very much, and a $\pm 1\sigma$ range around the nominal value is chosen.

6 Data analysis

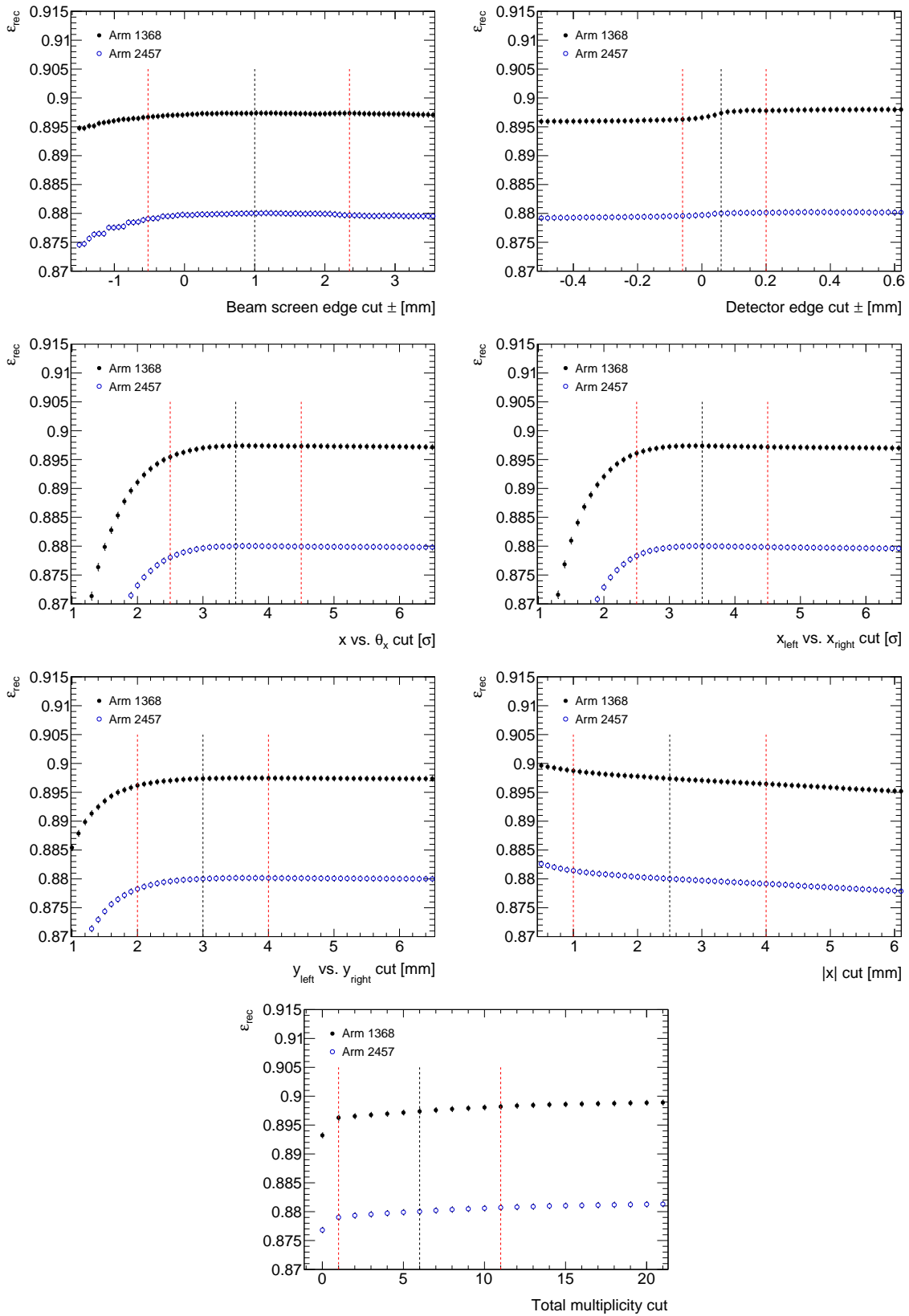


Figure 6.39: Reconstruction efficiency as a function of the variation of event selection cuts for both spectrometer arms. The shown cuts are: total multiplicity, vertical coordinate beam screen edge, vertical coordinate detector edge, x vs. θ_x , horizontal collinearity, vertical collinearity and additional horizontal coordinate.

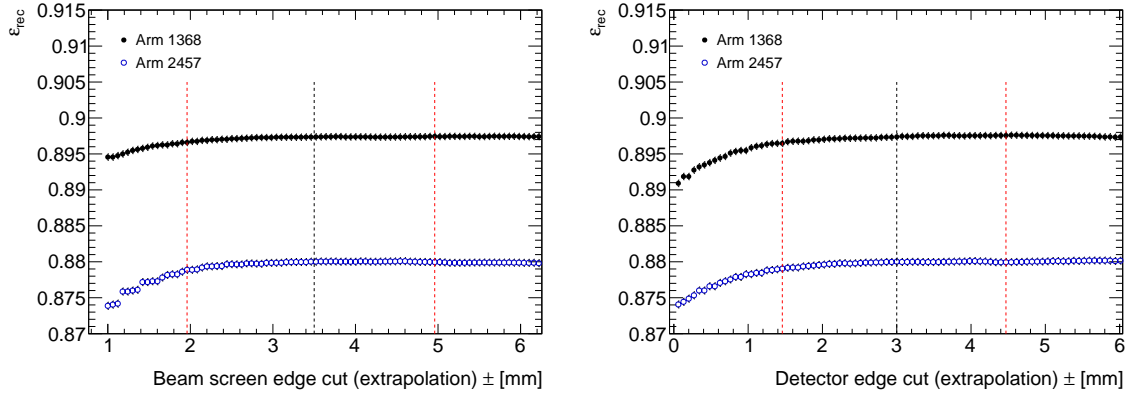


Figure 6.40: Reconstruction efficiency as a function of the variation of event selection cuts for both spectrometer arms. The shown cuts are: extrapolation limit beam screen edge and extrapolation limit detector edge.

Table 6.16: Contributions to statistical, systematic and total uncertainty of reconstruction efficiency ε_{rec} .

Source	Arm 1368	Arm 2457
ε_{rec}	0.8974	0.8800
Statistical uncertainty	0.0004	0.0005
Beam screen edge cut	0.0003	0.0005
Detector edge cut	0.0008	0.0003
Multiplicity cut	0.0010	0.0008
$ x $ cut	0.0011	0.0011
x vs. θ_x cut	0.0010	0.0010
x_A vs. x_C cut	0.0006	0.0009
y_A vs. y_C cut	0.0006	0.0010
Extrapolation limit BS	0.0004	0.0006
Extrapolation limit DE	0.0006	0.0005
Fraction fit	0.0056	0.0089
Total systematic uncertainty	0.0061	0.0092
Total uncertainty	0.0061	0.0092

The only source that is not varied is the elastic-scattering fraction, whose uncertainty is determined in the previous sub-section. It is propagated to the efficiency, which results in a maximum and minimum value. The full spread of these values is taken as systematic uncertainty from the elastic-scattering fraction fit on the efficiency. Like for the template this is done, because only two values are available.

The total systematic uncertainty is determined by quadratically summing up the individual uncertainties from the sources. Table 6.16 summarizes the different contributions to the systematic uncertainty of ε_{rec} . The dominant one is the elastic-scattering fraction fit followed by the total multiplicity cut, the x vs. θ_x cut and the additional cut on the horizontal coordinate for 1+1/4 and 1/4 events.

6 Data analysis

Table 6.17: Number of events $N_{k/4}$ for all reconstruction cases after reconstruction, event selection cuts and the final elastic-scattering selection for efficiency calculation.

	Reconstructed		Event selection		Final elastic selection	
	Arm 1368	Arm 2457	Arm 1368	Arm 2457	Arm 1368	Arm 2457
$N_{4/4}$	459 229	428 213	415 965	389 463	415 965	389 463
$N_{3/4}$	49 317	47 220	33 264	33 554	33 264	33 554
$N_{2/4}$	37 236	41 697	17 052	22 989	11 902	16 519
$N_{1+1/4}$	4604	4543	729	769	729	769
$N_{1/4}$	16 203	15 583	1672	1993	1337	1556
$N_{0/4}$	17 751	15 395	13 383	11 954	340	700
N_{total}	584 340	552 651	482 065	460 722	463 537	442 561
N_{fail}	125 111	124 438	66 100	71 259	47 572	53 098

6.3.9 Result

In Table 6.17 the number of events $N_{k/4}$ for all reconstruction cases are summarized, along with the total number of events N_{total} and the number of all not fully reconstructed events $N_{\text{fail}} = N_{\text{total}} - N_{4/4}$. The numbers are quoted after reconstruction, after event selection cuts and after the special corrections mentioned in the description of the cases before (denoted as ‘final elastic selection’). From these numbers one can see that 69 % of all reconstructed 3/4 events are selected as coming from elastic scattering and are used for the determination of the reconstruction efficiency. The fraction of used elastic-scattering events for 2/4 is about 36 %, for 1+1/4 about 16 %, for 1/4 about 9 % and for 0/4 about 3 %. With the ‘final’ elastic-scattering numbers and Equation (129) one gets the reconstruction efficiencies for both spectrometer arms with statistical and systematic uncertainties to be

$$\varepsilon_{\text{rec}}(\text{Arm 1368}) = 0.8974 \pm 0.0005 (\text{stat.}) \pm 0.0061 (\text{syst.}), \quad (137)$$

$$\varepsilon_{\text{rec}}(\text{Arm 2457}) = 0.8800 \pm 0.0005 (\text{stat.}) \pm 0.0092 (\text{syst.}), \quad (138)$$

also listed in Table 6.18 in detail. The statistical uncertainties are determined from simple Poisson statistics of the number of events $N_{k/4}$ and uncertainty propagation, and the systematic uncertainties are described in the sub-section before.

The reconstruction efficiency in arm 1368 is about 2 % larger than in the other one because of different detector configurations. In arm 1368 the trigger tiles are positioned after the scintillating tracking fibres and in arm 2457 they are positioned before them. This can be seen e.g. in the illustration in Figure 6.34, where the green trigger tiles are positioned after the tracking fibres. This ultimately leads to a higher shower probability, more not fully reconstructed events and a lower reconstruction efficiency in arm 2457. The largest contribution to the number of not fully reconstructed events N_{fail} comes from the 3/4 and 2/4 cases with 66 % and 28 % respectively.

Because of the large number of elastic-scattering events the statistical uncertainty is very small. The systematic uncertainty is dominated by the uncertainty from the elastic-scattering fraction fit and larger in arm 2457 than in 1368.

Table 6.18: Results of reconstruction efficiency for both spectrometer arms.

	Arm 1368	Arm 2457
Efficiency ε_{rec}	0.897 37	0.880 02
Statistical uncertainty	0.000 45	0.000 49
Systematic uncertainty	0.006 07	0.009 16
Total uncertainty	0.006 09	0.009 17

6.3.10 Comparison with simulation

The fully data-driven method is compared to MC simulation using the full simulation described in Section 5. This MC includes a full GEANT4 simulation of the interactions in the ALFA detector system and provides the true generated t value, referred to as \hat{t} , for every elastic-scattering event. With the simulation the event reconstruction efficiency can be determined in two different ways. First using the same method as for data, where the events are classified into reconstruction cases and the efficiency is calculated from the number of these events according to Equation (129). And a second possibility is to make use of the fact that the true \hat{t} of every elastic-scattering event is known in the simulation. With this knowledge one can calculate the efficiency as a function of \hat{t} for every reconstruction case, even for 0/4 events where no information is available in the measured data. In the following both methods are used to determine the efficiency in simulation and to compare it to the data-driven method.

For both methods an elastic-scattering trigger signal is needed, but this information is not available in the simulation. However, there is also no background and every generated event is from elastic scattering. Therefore, an elastic-scattering trigger signal is simulated by simply requesting two protons on opposite sides of the IP, which have both reached the Roman Pot stations and which are inside of the trigger acceptance.

For the first method events with an simulated elastic-scattering trigger signal are classified into the reconstruction cases based on the number of detectors with reconstructed tracks in the corresponding spectrometer arm, like it is done for data. All applicable event selection cuts are applied with the same parameters as for data, to decide if an event really is from elastic scattering and has to be counted for the reconstruction calculation. Since every event in the full simulation is from elastic scattering and no single-diffraction or beam-halo background is included, the elastic-scattering fraction fit for 2/4 events is not performed and the fraction is assumed to be $f_{\text{el}} = 1$. Therefore, a correction of the number of 2/4 events for the fraction is not done. Edge peaks in the vertical position distributions are present in fully simulation, but only at the detector edge near the beam. The interactions of protons with the beam-screens are not simulated and hence no hadronic showers from them are detected, which results in the absence of peaks at the beam-screen edge. But in contrast to data, peaks are visible at the detector edge for every reconstruction case and not only for 2/4 and 1/4 events. This can be seen in Figure 6.41 where the vertical position distribution in a detector with reconstructed tracks for 3/4 events is shown. A large peak is clearly visible at the detector edge and this peak is even larger than the ones in the data. Therefore, in simulation the extrapolation procedure is done for all cases except 0/4 and the range only excludes the peak on the detector edge. The number of 0/4 events is again estimated from the number of 2/4 events. After the extrapolation correction the events in every case are counted independently of t and the efficiency is calculated by Equation (129) to get the result for this method.

6 Data analysis

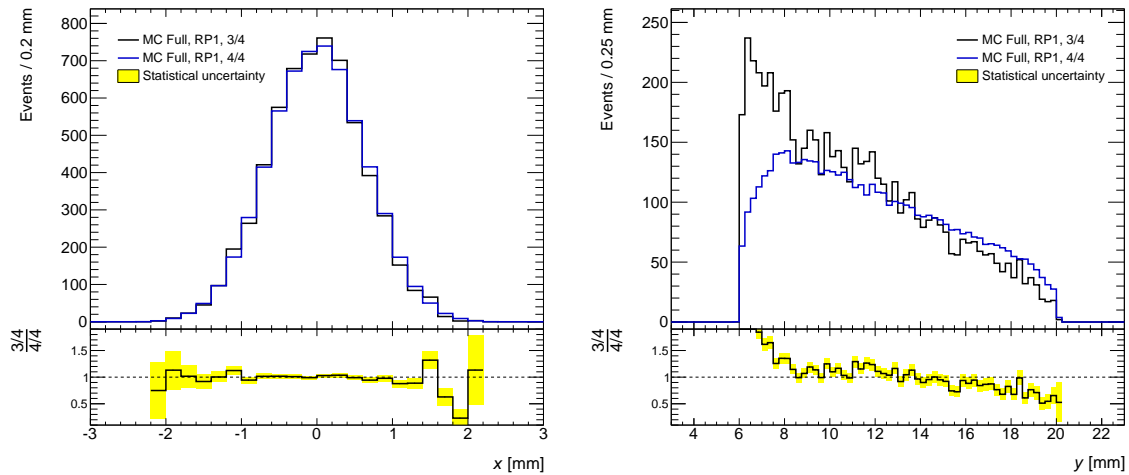


Figure 6.41: Position distribution in x and y of case 3/4, sub-case 138 for RP1 where no tracks were reconstructed in RP6 and of the fully reconstructed elastic-scattering case 4/4. The y distribution of case 4/4 in blue is normalized to the one of 3/4 in the part without the peak and x is normalized in the whole range.

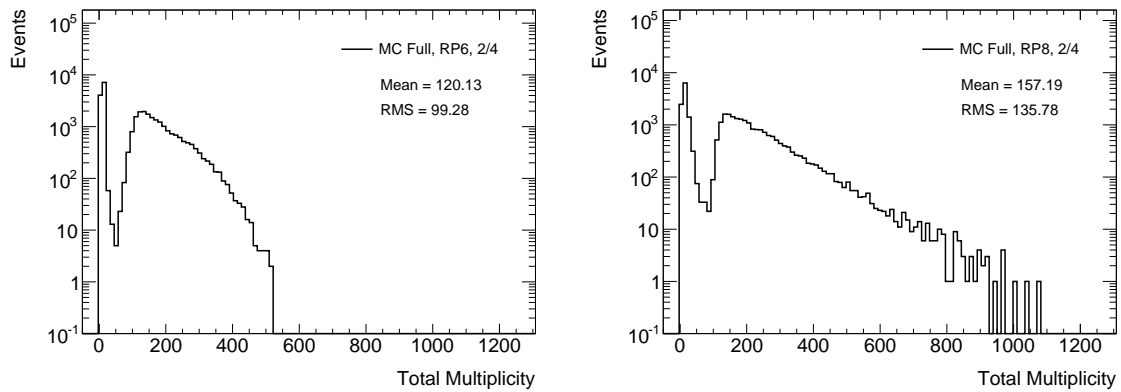


Figure 6.42: Total multiplicity distributions of case 2/4, sub-case 13 for RP6 and RP8, in which no tracks were reconstructed.

The event reconstruction efficiency from full simulation with the data method is for the two spectrometer arms $\varepsilon_{\text{rec}, 1368}^{\text{MC}} = 0.94330 \pm 0.00011$ (stat.) and $\varepsilon_{\text{rec}, 2457}^{\text{MC}} = 0.92890 \pm 0.00013$ (stat.). The efficiency in arm 1368 is about 1.6 % larger than in the other one, which is comparable with the same difference in data. This means the position of the trigger tiles is the most probable cause for this difference, since the tiles are also present in the full simulation and give rise to different shower probabilities in the arms. Compared to data the efficiency is about 5 % larger in both arms. This is mainly due to the absence of background e.g. from elastic-scattering and beam-halo pileup and the missing cross-talk in the simulation. Figure 6.42 shows the total multiplicity distributions for the two detectors without reconstructed tracks in a 2/4 case. In comparison with the same distributions for data (see Figure 6.24) the long tail with high multiplicity events up to the saturation at the maximum value can not be observed. Therefore, the full simulation does not describe showers, noise, cross-talk and the total multiplicity distributions like they are observed in data. All that makes the full simulation much cleaner with less background than data and as a result the event reconstruction

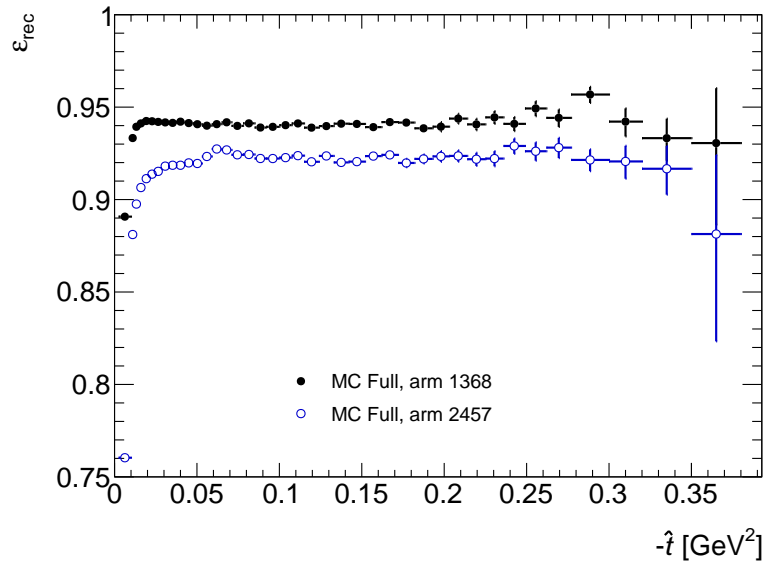


Figure 6.43: Event reconstruction efficiency as a function of the true \hat{t} for both spectrometer arms from full simulation.

efficiency is larger, because more events can be fully reconstructed. This insufficient description of the data is the main reason why the full simulation is not used for the determination of the reconstruction efficiency and why instead the fully data-driven method was developed.

For the second method the event selection and grouping into cases is the same as for the first method. But since the true \hat{t} is known for every event at the generator stage, a \hat{t} -dependent reconstruction efficiency $\varepsilon_{\text{rec}}(\hat{t})$ is calculated according to Equation (126). Here the number of not fully reconstructed events $N_{\text{fail}}(\hat{t})$ includes all cases from 3/4 to 0/4. The result for both arms is shown in Figure 6.43. A drop in efficiency is visible at small $|\hat{t}|$, because of the detector edge peaks which are present in all cases at small $|y|$ in the vertical distributions and are not removed here. An extrapolation procedure, like for the data method, cannot be applied for the \hat{t} -dependent method, so that a disproportionately large number of not fully reconstructed events with small $|y|$ and therefore small $|\hat{t}|$ are included in the efficiency calculation. Apart from this drop the efficiency is similar to the partial reconstruction efficiency of 3/4 events. Both distributions are flat (excluding the drop at small $|\hat{t}|$) and only small statistical fluctuations are visible. Hence this is another indication, that the event reconstruction efficiency is really t -independent, like it is shown in Section 6.3.3.1. The average efficiency is comparable with the values obtained with the first method and the difference between the arms is the same, too. Because of the reasons mentioned before this result from full simulation is also not used for the total cross-section analysis and the data-driven method is preferred.

6.4 Acceptance

The acceptance of the ALFA detector system for elastic-scattering events is determined from MC simulation. For this purpose the tuned fast simulation with PYTHIA 8.1 as generator and MAD-X for the beam transport is used. The produced MC sample contains several million elastic-scattering events, and further details can be found in Section 5.1. The total acceptance ε_{acc} is split into two parts. One is the geometrical acceptance ε_{geo} and the other one the elastic-

6 Data analysis

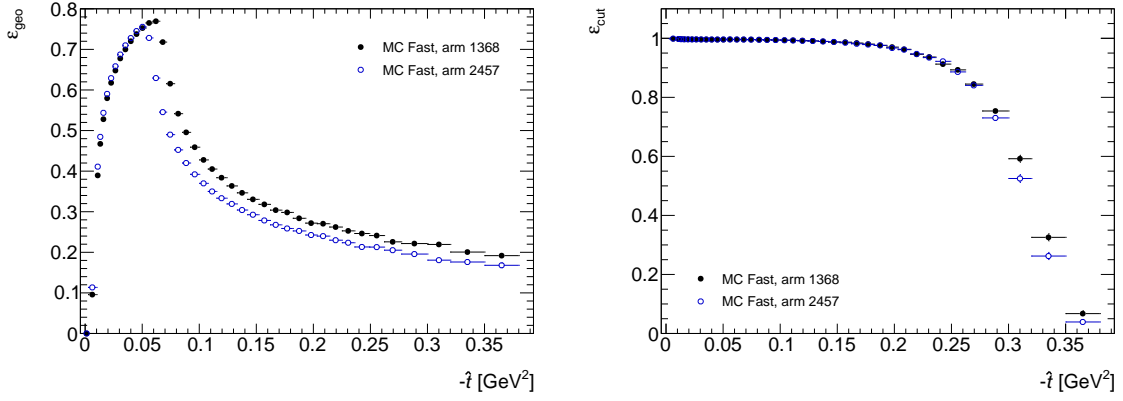


Figure 6.44: Geometrical (left) and event selection cut acceptance (right) as a function of the true generated $-\hat{t}$ for both spectrometer arms.

scattering event selection cut acceptance ε_{cut} . The geometrical acceptance is the ratio between elastic-scattering events inside the fiducial volume of the ALFA detectors and all generated elastic-scattering events. The volume is defined by the vertical fiducial cuts depicted in Table 6.1. The event selection cut acceptance is the ratio between events passing the selection cuts in Tables 6.2 and 6.3 and the events inside the fiducial volume. All cuts are applied to the positions and local angles in the simulation, which are smeared like it is described in Section 5.1. Both acceptances are determined as a function of the true generated \hat{t} value and the product of both yields the total acceptance $\varepsilon_{\text{acc}}(\hat{t}) = \varepsilon_{\text{geo}}(\hat{t})\varepsilon_{\text{cut}}(\hat{t})$.

The geometrical acceptance for both spectrometer arms is shown in Figure 6.44 in the left histogram. Because of different contributions of the horizontal and vertical scattering angle to t , the acceptance has a distinctive shape. At small $|\hat{t}|$ the acceptance is very low because of losses from beam divergence near the beam at small y positions, where on one side of the IP the elastically scattered proton is inside the fiducial cuts but on the other side the proton is outside of the cuts. At this small y positions the horizontal scattering angle has the largest contribution to t , but with larger y the divergence losses decrease and the contribution of both planes become nearly equal, which manifests in the steep rise of the acceptance up to $-\hat{t} \approx 0.07 \text{ GeV}^2$. Beyond this point events with larger y and vertical scattering angle cannot be detected anymore, because of the beam screen cuts. Therefore, only events with larger x position contribute to t and for a given $-\hat{t}$ value the fraction of lost events with large y position increases. As a result the acceptance decreases steadily up to the maximum detectable $|\hat{t}|$ value. There is also a difference in the starting point of this decrease (maximum of the geometrical acceptance) between the two arms because of different positions of the beam screen cuts. This means in arm 1368 events with larger y can be detected than in arm 2457.

The second part of the total acceptance the event selection cut acceptance is shown in Figure 6.44 in the right histogram. At small values of $|\hat{t}|$ up to $-\hat{t} \approx 0.2 \text{ GeV}^2$ one can basically see no losses associated with the elastic-scattering event selection cuts, because most events in this t range lie way inside of the cut limits depicted in Figures 6.6 and 6.7 on pages 68 and 69. At larger $|\hat{t}|$ a rapid decrease of the acceptance down to $\varepsilon_{\text{cut}} = 0$ can be seen. In this range basically no events with large y are available because of the fiducial cuts. Furthermore, the x_{inner} vs. θ_x cut also limits the amount of available events with larger x in this region and therefore events with larger $|\hat{t}|$.

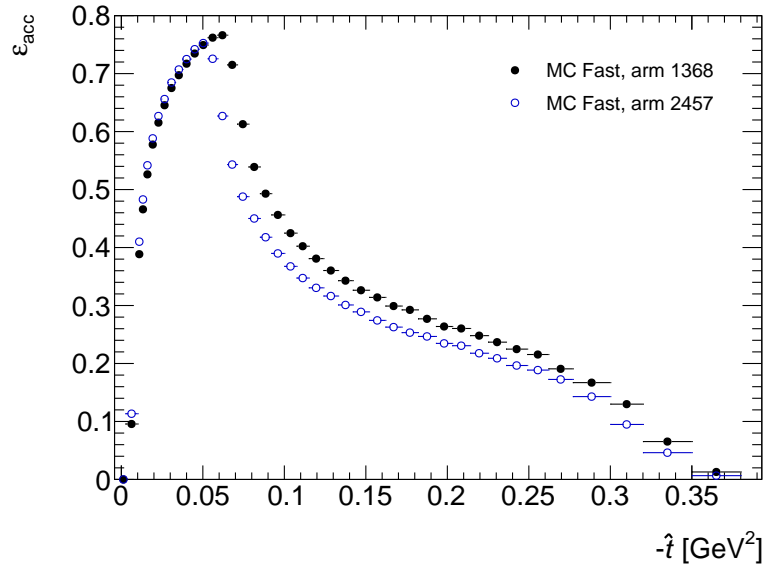


Figure 6.45: Total acceptance as a function of the true generated $-\hat{t}$ for both spectrometer arms with statistical uncertainties.

Finally the total acceptance $\varepsilon_{\text{acc}}(\hat{t})$ is shown in Figure 6.45 as a function of $-\hat{t}$ for both arms with statistical uncertainties only. This combination shows characteristics of both acceptances described before. The acceptance is later used to correct the raw differential t -spectrum and also as a guideline for the maximum fit range of the cross-section. Only points with an acceptance of $\varepsilon_{\text{acc}}(\hat{t}) > 0.1$ in the maximum range $0.01 \text{ GeV}^2 < -\hat{t} < 0.3 \text{ GeV}^2$ are considered for the fit to avoid too large acceptance corrections of bins with low statistics. Especially the first bin has to be excluded because of an acceptance of $\varepsilon_{\text{acc}}(\hat{t}) \approx 0$.

Three sources are taken into account for systematic uncertainties. First the parameters of the physics model used in the elastic-scattering event generation by PYTHIA 8.1 (see Table 5.1). The nuclear slope B is varied by $\pm 1 \text{ GeV}^{-2}$ to change the form of the differential t -spectrum. This variation has little impact on the acceptance, since it is dominated by geometrical cuts and the ratio of detected and non-detected particles inside the fiducial volume is not changed. Other generator parameters like σ_{tot} and ρ are not varied and have negligible impact. Second the beam parameters and in particular the divergence of the beams, since the divergence has an impact on the fraction of events inside the fiducial volume. The horizontal and vertical vertex spread and divergence are varied in the elastic-scattering event generation by the uncertainty, that is coming from the limited knowledge of the beam emittance. And third the beam optics whose systematic uncertainties, described in Section 6.7, are also propagated to the acceptance.

6.5 Unfolding

The measured differential t -spectrum is distorted by detector resolution and beam smearing effects. These migration effects include the angular divergence, the intrinsic energy uncertainty and the vertex spread at the IP of the beams. They are visible in the t -resolution and the purity of the spectrum.

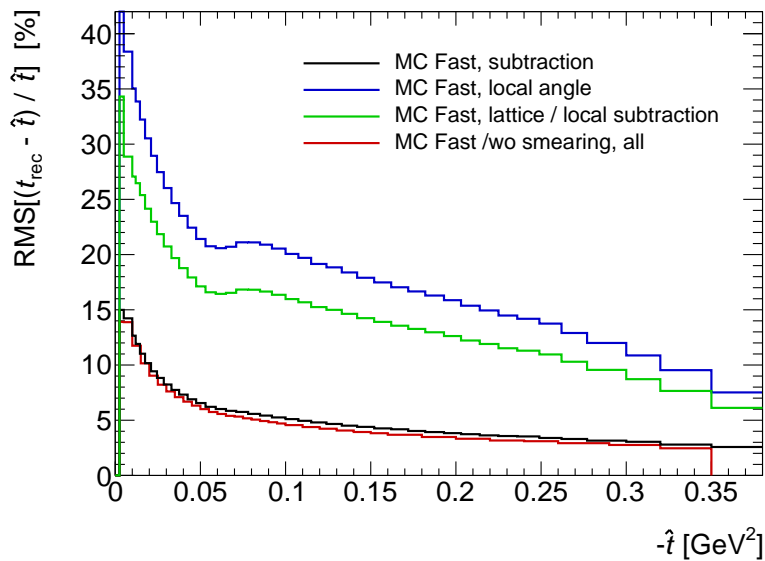


Figure 6.46: Resolution of the differential t -spectrum for the four reconstruction methods as a function of $-\hat{t}$ determined from fast simulation.

The fast simulation is used to determine the resolution of the differential t -spectrum by comparing the true \hat{t} with the reconstructed value t_{rec} , which has been calculated with the four reconstruction methods. The t -resolution is defined as

$$r_t(\hat{t}) = \frac{t_{\text{rec}} - \hat{t}}{\hat{t}}. \quad (139)$$

The detector resolution in the fast simulation is taken into account by applying a Gaussian smearing to the reconstructed track positions. All the beam smearing effects are parameters of the MC simulation described in Section 5. Figure 6.46 shows the resolution of the t -spectrum as a function of $-\hat{t}$ for the four reconstruction methods. The red histogram only includes beam effects and is the same for all methods. The t -resolution for the lattice and local subtraction method is also the same so that only one histogram is shown for both. By looking at the resolution without position smearing a deterioration of the spectrum can be seen, coming from the beam effects, especially at small $|\hat{t}|$. When comparing the t -resolutions, which include the position smearing, with the one without smearing, a strong dependence of detector resolution effects on the reconstruction method can be observed. The subtraction method only has a small contribution from the position smearing, because it only uses space coordinate measurements. In contrast the other three methods use the badly measured local angle in the horizontal plane, which results in a considerable degradation of the t -resolution. The distance between two stations is with about four meters too small to obtain a better performance in the local angle measurement. Except for a small bump at $-\hat{t} \approx 0.085 \text{ GeV}^2$ the form of the t -resolution function is not changed very much by including the detector resolution.

The purity is another quantity that reflects the migration effects and can be used to gauge the performance of the four reconstruction methods. It is the ratio of reconstructed to all events generated in a particular bin. Because of the mentioned effects the reconstructed value of t is smeared, which leads to a limited migration in the binned differential t -spectrum from the bin corresponding to the true value of t to the bin of the reconstructed value. To deter-

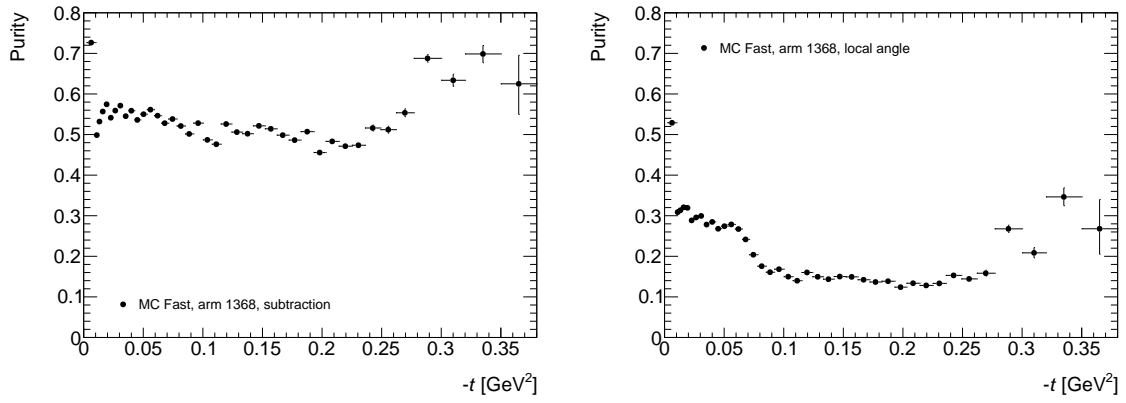


Figure 6.47: Purity as a function of $-t$ for subtraction (left) and local angle method (right) of arm 1368.

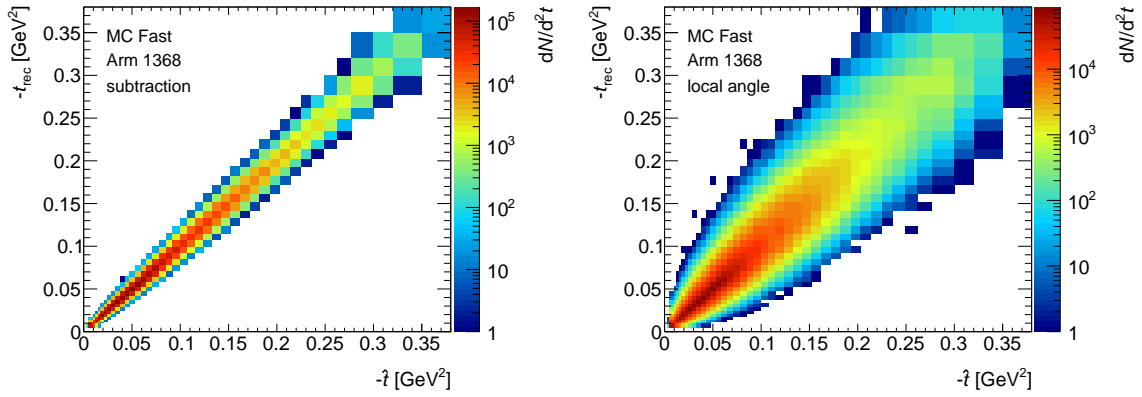


Figure 6.48: Migration matrix for subtraction (left) and local angle method (right) of arm 1368. The true value $-\hat{t}$ is plotted against the reconstructed one $-t_{\text{rec}}$.

mine the purity the fast simulation is used, in which the true value \hat{t} at the stage of generation is available. The purity for the subtraction method, which has the highest t -resolution, is about twice as high as for the local angle method, which has the worst t -resolution. Both can be seen in Figure 6.47 for arm 1368. A lower resolution entails a larger migration into neighbouring bins, leads to a lower purity and needs to be corrected. The binning of the t -spectrum is adjusted for the subtraction method to have an approximately constant purity of about 60 %. This binning is used for all four reconstruction methods for the ease of analysis uniformity. It is shown in Table A.1, in which for the 41 bins the lower and upper limits $-t_{\text{lower}}$ and $-t_{\text{upper}}$ are listed. By increasing the bin width the purity of the lower resolution methods can be improved, but the information on the shape of the differential cross-section is lost in doing so.

The correction of the migration effects in the raw t -spectrum is performed by an unfolding procedure [56]. From the fast simulation an migration matrix is obtained for each reconstruction method and both spectrometer arms. In this matrix the detector response is encoded, which describes the migration of events from the true value \hat{t} to the reconstructed one. The matrices for subtraction and local angle method of arm 1368 are shown in Figure 6.48.

As shown by the purity before, the reconstruction methods with lower t -resolution, which use the local angle, suffer more from migration effects. This can also be seen in the migration

6 Data analysis

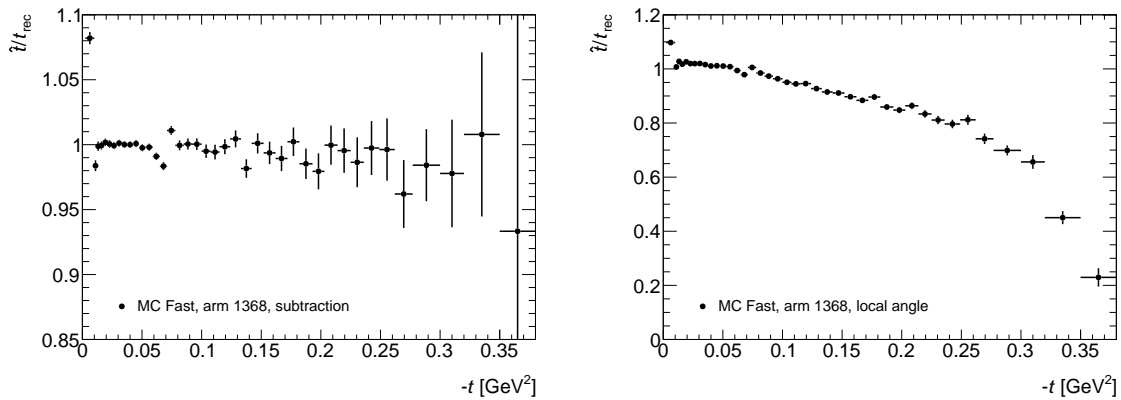


Figure 6.49: Correction used for the simple bin-by-bin unfolding as a function of $-t$ for subtraction (left) and local angle method (right) of arm 1368.

matrices of the two methods with the best and worst resolution. For the subtraction method only a small spread in the matrix is visible, whereas for the local angle method a large spread can be seen coming from larger bin-to-bin migration effects. This also means the unfolding corrections for the methods using the local angle are much larger than for the subtraction method. As baseline method for the unfolding an Iterative Dynamically Stabilized (IDS) method [73] is applied, which uses the migration matrices to correct the raw but background subtracted t -spectra (see Section 6.2). For the purpose of systematic stability checks two other unfolding methods are investigated: one based on Singular Value Decomposition (SVD) [74] and another simple bin-by-bin correction. The SVD method also uses the migration matrices and the simple bin-by-bin correction uses the one dimensional ratio between the true and reconstructed t value \hat{t}/t_{rec} . This ratio is shown in Figure 6.49 for subtraction and local angle method of arm 1368. The corrections for the subtraction method are of the order of a few percent, but the methods using the local angle suffer again from the poor t -resolution and the corrections are large and get even larger with increasing $|t|$.

Statistical uncertainties are evaluated and propagated through the unfolding procedure by using toy models. These toy models for the measured data are obtained by applying a Gaussian smearing in each bin of the raw t -spectrum with a width equal to the statistical uncertainty in this bin, which is obtained by means of Poisson statistics. Additional toy models are built for the t -spectra in the fast simulation and for the migration matrices. From the average of 1000 data and migration matrix toy models the mean unfolded differential t -spectrum is obtained along with its corresponding covariance matrix. In this matrix all the information needed for statistical uncertainty propagation is included, taking into account the bin-to-bin correlations. The IDS and SVD methods unfold the migration between bins and introduce statistical correlations which cannot be neglected. In contrast to the bin-by-bin unfolding which applies a simple correction factor to the differential t -spectrum. Therefore, the covariance matrix is included in the fits of the total cross-section performed in Section 7.2.

The estimation of systematic uncertainties in the unfolded data t -spectrum shape, due to mismodelling of the reconstruction-level spectrum shape in the simulation, is based on the difference between the spectrum in data and fast MC simulation. The ratio between data and simulation is close to one and shows deviations up to +30 % at larger values of $|t|$ for all reconstruction methods and both arms. This ratio is parametrized by a fourth order polynomial function, which is used to re-weight and bias the differential t -spectrum in the MC

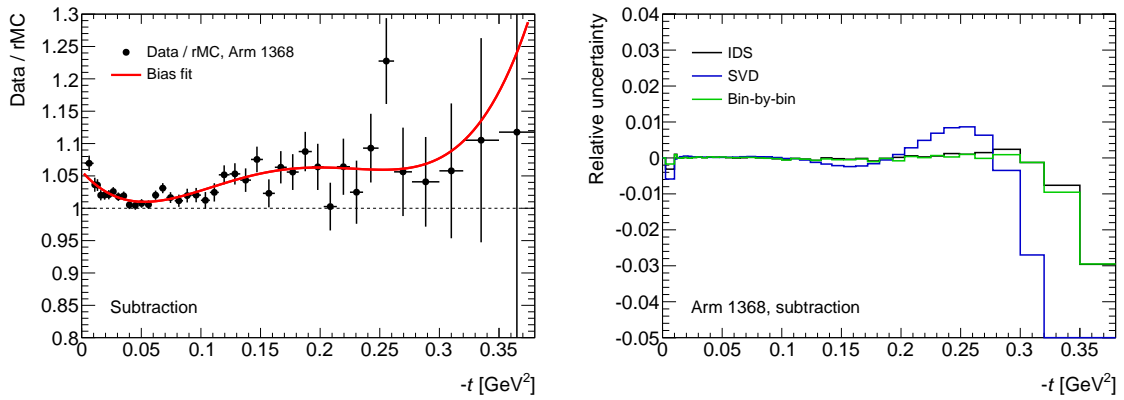


Figure 6.50: Parametrization of the unfolding bias with a 4th order polynomial function (left) and relative systematic uncertainty for the three different unfolding methods (right). Both are shown for arm 1368 and the subtraction method. The re-weighted MC is called ‘rMC’ here.

simulation on particle level such that the reconstructed simulation matches the data. In Figure 6.50 (left) such a ratio parametrization is shown for the subtraction method in arm 1368. Under the assumption that this re-weighted spectrum correctly describes the data after unfolding, it is used to assess the systematic uncertainties by investigating the difference between the unfolded data and the biased simulated spectrum. Up to a value of $-t \approx 0.2 \text{ GeV}^2$ the uncertainty is on a level of 0.5 % and negligible for all reconstruction methods and both arms. At large values of $|t|$ the uncertainty suffers from large fluctuations and goes up to 8 % depending on the reconstruction method. The relative systematic uncertainty of the three unfolding methods for the subtraction method in arm 1368 is shown in Figure 6.50 (right).

6.6 Luminosity

An accurate measurement of the luminosity \mathcal{L} is a key component of the total cross-section analysis as described in Section 2.3. The luminosity and its uncertainties are determined by ATLAS in the luminosity task-force for all data taking periods from 2010 to 2013. This includes also the ALFA $\beta^* = 90 \text{ m}$ run which is used to measure the differential elastic cross-section in this thesis. In this section the determination of the total integrated luminosity and the associated uncertainties by ATLAS is described for the ALFA run [45]. A complete and detailed description of the measurement and calibration procedures, results and systematic uncertainty sources can be found in Reference [75], in which the luminosity determination for nominal optics ($\beta^* = 0.5 \text{ m}$) and running conditions is described. The high- β^* run has a low average number of proton–proton interactions per bunch crossing $\mu = 0.035$ compared to normal running conditions with $\mu \approx 5$ to 10 which makes the luminosity determination challenging and different in several aspects due to lack of sensitivity.

In general the luminosity of a proton–proton collider can be expressed as

$$\mathcal{L} = \frac{R_{\text{inel}}}{\sigma_{\text{inel}}} = \frac{\mu n_b f_r}{\sigma_{\text{inel}}} = \frac{\mu_{\text{vis}} n_b f_r}{\sigma_{\text{vis}}} \quad (140)$$

with units of $(\text{area})^{-1} \times (\text{time})^{-1}$, and where R_{inel} is the inelastic collision rate and σ_{inel} the inelastic cross-section. This is equal to the second expression for a storage ring like LHC, which operates at a revolution frequency f_r and with n_b bunch pairs colliding per revolution. The luminosity is monitored by measuring the observed interaction rate per crossing

μ_{vis} independently with several detectors using different algorithms. By measuring the visible cross-section σ_{vis} for a particular detector and algorithm the absolute luminosity scale is calibrated. This calibration is performed with dedicated beam-separation scans, also known as van-der-Meer scans, where the absolute luminosity can be inferred from direct measurements of the beam parameters [76], given by

$$\mathcal{L} = \frac{n_b f_r n_1 n_2}{2\pi \Sigma_x \Sigma_y}, \quad (141)$$

where $n_1 n_2$ is the bunch population product (protons per bunch) of beam 1 and 2, and Σ_x and Σ_y characterize the horizontal and vertical convolved beam widths.

A strategy which compares measurements by various detectors and algorithms is used by ATLAS to assess the systematic uncertainties. These include LUCID and BCMs which both measure the luminosity bunch-by-bunch and the Tile and forward calorimeter FCal which only measure an integrated luminosity over all bunches. The Inner Detector system is also used to measure luminosity based on a vertex-counting method. The absolute luminosity scale of all used detectors and algorithms was calibrated in a van-der-Meer scan performed in May 2011.

In normal physics running the BCM is used as main luminosity detector. There are two BCMs, a horizontal and vertical one, consisting both of two stations on the A- and C-side respectively. An event for luminosity determination is defined by two algorithms: an inclusive OR between the two sides called BCMX_EventOR and the coincidence between the sides called BCMX_EventAND ($X \in \{H, V\}$ depending on whether the horizontal or vertical BCMs are used). Only the EventOR measurements of the vertical and horizontal BCMs are used, because for the EventAND measurement no sufficiently sensitive and internally consistent drift- and background correction procedure is currently available for the high- β^* running conditions.

LUCID also consists of two sub-detectors on the A- and C-side for which EventOR and EventAND algorithms are defined. In addition a hit counting algorithm called LUCID_HitOR is exploited, in which the number of hits is counted rather than just the number of events. In contrast to most of the normal running in 2011 the LUCID vessel was filled with radiator gas during the $\beta^* = 90$ m run and the van-der-Meer scans. The stability of the calibration is checked by comparing LUCID with the BCMs and Tile calorimeter and a discrepancy in the luminosity measurements is found, caused by a change in PMT gain over time. Thus, LUCID is recalibrated using the Tile calorimeter as a reference, which is described in detail in Reference [75].

The Tile and FCal calorimeters are not used in the luminosity measurement of the $\beta^* = 90$ m run, due to sensitivity reasons with the very low instantaneous luminosity conditions. Nevertheless the short- and long-term stability of both calorimeters is used to assess systematic uncertainties of the BCMs and LUCID.

Another independent method of luminosity measurement is provided by the Inner Detector, which counts the number of primary vertices per event. This number is proportional to the luminosity and allows for statistically meaningful bunch-by-bunch measurements. A minimum number of tracks with a transverse momentum of $p_T = 400$ MeV forming a common vertex and additional quality requirements are needed in order for a vertex to be selected. Values of 5, 7 and 10 are used for the minimum number of required tracks to reconstruct a vertex, to get a handle on the difference for varying selection criteria. The statistical uncertainty for up to 7 tracks per vertex is only about 20 % larger than for the BCM algorithms. Therefore, the vertex-counting method is essential for understanding and quan-

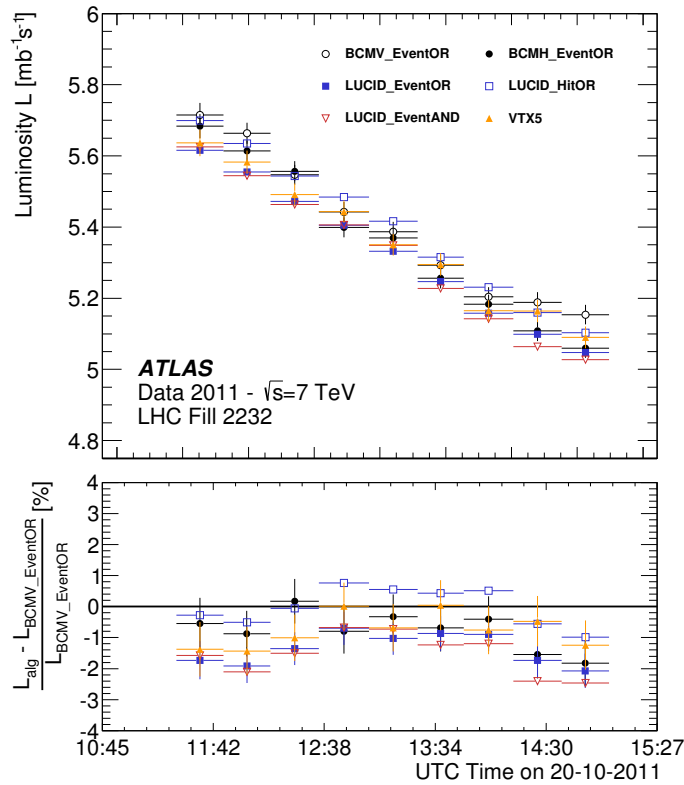


Figure 6.51: Luminosity measured by the various detectors and algorithms as a function of time during the run (fill 2232) [45]. The bottom panel shows the deviations from the reference BCMV_EventOR algorithm.

tifying the overall consistency of the different methods used during the $\beta^* = 90$ m run and to assess their systematic uncertainties.

Compared to normal physics running the background conditions in the high- β^* run are quite different, and background subtraction becomes a delicate procedure. In principle two sources of background are considered, as for normal running conditions, namely the afterglow and beam-gas interactions, which are extensively evaluated in Reference [75]. The afterglow effect is caused by photons from nuclear de-excitation, induced by the hadronic cascades initiated by pp collision products. The beam-gas interactions are related to activity induced by the passage of a single beam through the detector and includes also halo particles in time with the beam. For a large number of colliding bunches and a high average number of interactions per bunch crossing, as in normal running conditions, the dominating background contribution comes from the afterglow, while the beam-gas interactions are negligible with respect to the luminosity from pp collision. However, for the special case of only one colliding bunch pair with very small μ , as for the high- β^* run, the contribution from afterglow is reduced, while the beam-gas contribution becomes comparable or larger than the afterglow effect. The random nature of the beam-gas interactions make this type of background well manageable by the used background subtraction method.

As reference algorithm BCMV_EventOR is selected and the redundancy of the other detectors and algorithms is only used to assess the systematic uncertainties and to solve initial inconsistencies. This choice is made because of several reasons: the systematic uncertainties of the absolute luminosity calibration are studied more extensively for the BCM algorithms;

Table 6.19: Systematic uncertainties sources affecting the luminosity determination in the $\beta^* = 90$ m run [45] compared to normal running conditions at instantaneous high luminosity [75].

Source	$\beta^* = 90$ m [%]	high luminosity [%]
Calibration (vdM)	1.53	1.53
BCM drift	0.25	0.25
Consistency	1.60	
Background	0.20	0.20
Time stability	0.70	0.70
μ -dependence		0.5
Total	2.34	1.80

the vertex-method was not available during parts of the run; the recalibration of LUCID results in substantial corrections with additional uncertainties; the net drift correction is zero for BCMV_EventOR; and the choice is consistent with the one for normal high luminosity physics running.

Systematic uncertainties affecting the luminosity measurement arise from the detector calibration through van-der-Meer scans, the consistency among the various detectors and algorithms, the BCM drift, the background subtraction procedure and the Tile long-term stability. The contribution of each source is listed in Table 6.19, and a complete discussion of all sources can be found in Reference [75]. After summing up all sources a systematic uncertainty of 2.34 % is obtained. In Figure 6.51 the luminosity as measured by the various algorithms is shown as a function of time during the $\beta^* = 90$ m run. And in the bottom part the deviations from the reference BCMV_EventOR algorithm are shown in percent. Most of the algorithms show a non-flat ratio with respect to the reference as a function of time. The reason for that is not known and this behaviour is not visible for other reference choices. Nevertheless, the choice of BCMV_EventOR is the most solid, based on the reasons mentioned above.

The result of the luminosity measurement [45] for the list of good LBs selected for the cross-section analysis (see Section 6.1) is therefore an integrated luminosity of

$$\mathcal{L}_{\text{int}} = 78.72 \pm 0.13 \text{ (stat.)} \pm 1.85 \text{ (syst.) } \mu\text{b}^{-1}. \quad (142)$$

6.7 Effective beam optics

From the initial design optics described in Section 4.2, along with the alignment parameters, magnet currents and field calibrations, all elements of the transport matrix $M_{ij}(s)$ can be calculated. However, the precision of the t -reconstruction depends on the knowledge of these elements. Small corrections are allowed within the range of the systematic uncertainties, which need to be applied to the design optics for the measurement of the total cross-section. These corrections are especially needed in the horizontal plane, where the phase advance Ψ is close to 180° and the effective lever arm L_{eff} is rather sensitive to the exact Ψ value. Therefore, an ‘effective’ $\beta^* = 90$ m optics is obtained from a global fit, which uses constraints derived from ALFA data, supplemented by machine constraints, and the design optics as a starting point [45]. This fit procedure and the constraints are described in the following.

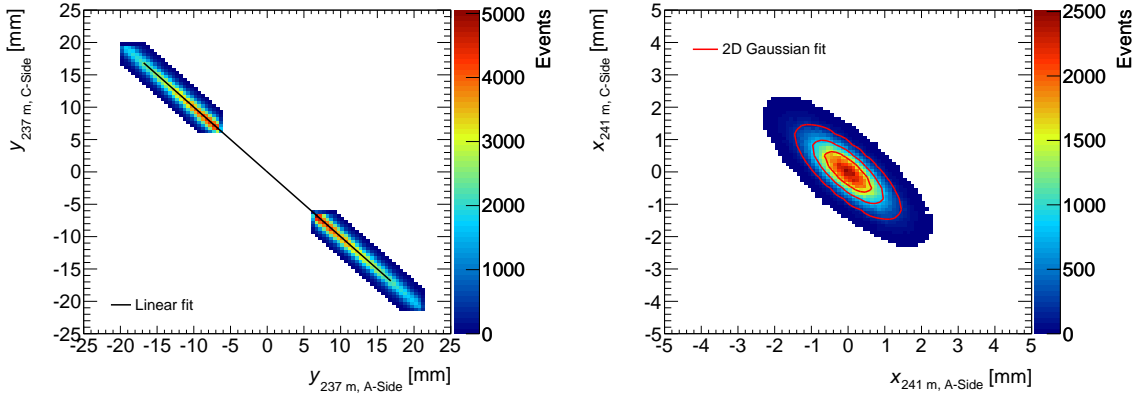


Figure 6.52: Correlation in the vertical plane between measured positions in the inner detectors on the A- and C-Side with linear fit in black (left). And correlation in the horizontal plane between measured positions in the inner detectors on the A- and C-Side with 2D Gaussian fit in red (right).

6.7.1 ALFA constraints

Elastic data from the same run, that is used for the cross-section analysis, is also used to directly derive two classes of constraints on the beam optics:

1. The ratio of transport matrix elements is derived from correlations between measured positions or angles at either A- and C-Side or at inner and outer stations. The resulting constraints are fully independent from any optics input.
2. Rescaling factor constraints on transport matrix elements are derived from correlations between the reconstructed scattering angle at the IP determined using different reconstruction methods. These rescaling factors indicate the amount of scaling, which has to be applied to a given transport matrix element ratio to equalize the scattering angle measurements from the different methods. The resulting constraints depend on the reference optics model ('design optics' described in Section 4.2).

To determine these constraints the complete elastic-scattering dataset of the $\beta^* = 90$ m run is used and all standard selection cuts are applied, as for the cross-section analysis.

From the first class several transport matrix element ratios are derived. With parallel-to-point focusing the measured position in the horizontal and vertical plane in the Roman Pot detectors is in first approximation related to the scattering angle at the IP by Equation (93), neglecting a small contribution from the vertex position term in $M_{x,11}$. Hence, the ratio of measured positions on the A- and C-Side is in average equal to the lever arm ratio

$$\frac{u(A)}{u(C)} = \frac{M_{u,12}(A)}{M_{u,12}(C)}. \quad (143)$$

In practice this ratio is determined from a fit to a 2D-histogram representing the position at the A-Side versus the C-Side for the inner and outer station pair. This is shown in Figure 6.52 for the inner stations in the vertical and horizontal plane, which reveals negative correlations, that are expected for elastically scattered protons. In y the correlation is much clearer, but a gap is visible, whose width is driven by the vertical approach of the detectors to the beam. The slope of a linear regression fit to the y correlation yields the transport matrix element ratio (here $M_{y,12}(+237) / M_{y,12}(-237)$), which is very close to one, and in agreement

6 Data analysis

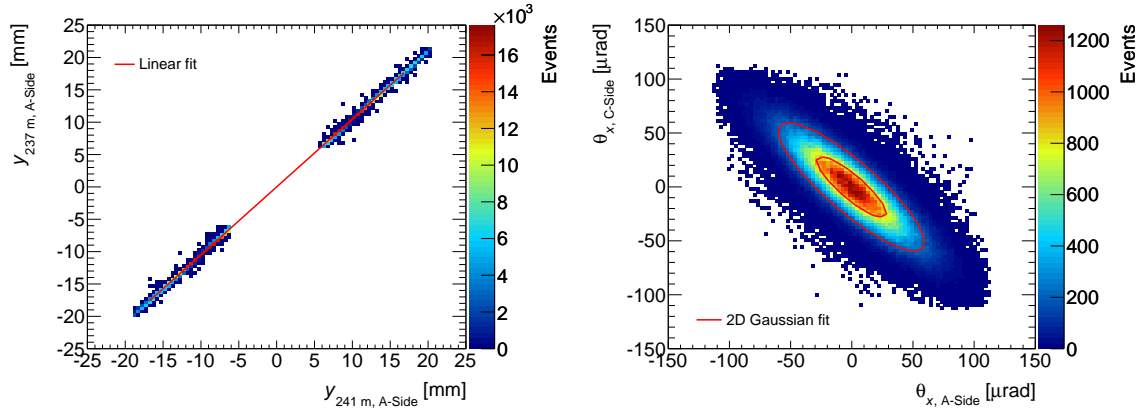


Figure 6.53: Correlation in the vertical plane between measured positions between the inner and outer detectors on the A-Side with linear fit in red (left). And correlation in the horizontal plane between the measured local angle on the A- and C-Side with 2D Gaussian fit in red (right).

with the expectation from design optics. In x the measurements are peaked around zero and distributed over a small range, which induces a larger smearing in the correlation patterns. Therefore, instead of the linear fit a 2D Gaussian distribution function with six free parameters (σ and offset in each dimension, normalization and rotation angle) is used for the fit. The rotation angle defines the major axis of the ellipse representing the contour lines of constant density of the 2D Gaussian, and yields the matrix element ratio. The same fits are done for the outer stations in x and y .

From the correlation between inner and outer detectors on either A- or C-Side another transport matrix element ratio is derived. As shown in Figure 6.53 on the left, a positive correlation appears in the vertical plane as the coordinates are from the same proton track. Again the pattern is very clear, and only smeared by detector resolution and multiple scattering, compared to the correlation between the A- and C-Side, where the divergence introduces an additional smearing. A linear fit yields once more the matrix element ratio (here $M_{y,12}(+237)/M_{y,12}(+241)$), and is also performed on the other side. Although the correlation is also measured in the horizontal plane, it is not used to derive a transport matrix element ratio. Simulations show that the measurement does not correspond to the matrix element ratio, since the contribution of the vertex position term in $M_{x,11}$ introduces a sizeable bias of about 3 %.

Finally the correlation between the measured local angle on A- and C-Side is used to derive two more transport matrix element ratios. Similar to the position the measured local angle between two consecutive Roman Pot detectors is in first approximation related to the scattering angle by

$$\theta_u \approx M_{u,22}\theta_u^*, \quad (144)$$

which can be deduced from Equation (90) by neglecting a small contribution from the vertex position term in $M_{u,21}$. Therefore, a measurement of the local angle on A-Side versus C-Side yields the transport matrix element ratio

$$\frac{\theta_u(A)}{\theta_u(C)} = \frac{M_{u,22}(A)}{M_{u,22}(C)}. \quad (145)$$

However, the local angle is measured less well than the position, because the distance between two consecutive stations $d = 4.1$ m is relatively short. For the vertical plain a negative

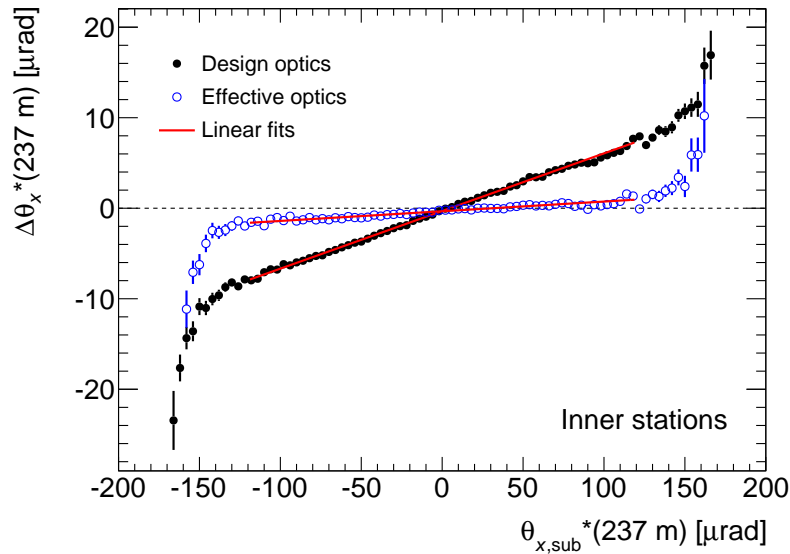


Figure 6.54: Difference in scattering angle reconstructed with the subtraction and local angle method $\Delta\theta_x^*$ as a function of the scattering angle reconstructed with the subtraction method from inner detectors. In each bin the mean value of $\Delta\theta_x^*$ is recorded and the error bar represents the RMS (profile histogram). Shown are the distribution for the initial design optics (see Section 4.2) in black and effective optics after the optics fit is performed in blue. The red lines represent linear fits to both distributions.

correlation with larger spread is observed, which is related to the back-to-back topology of elastically scattered protons. It is fitted with a linear regression line to yield the matrix element ratio. In Figure 6.53 on the right the correlation in the horizontal plane is shown. Again the correlation pattern shows a large smearing, and is therefore fitted with a 2D Gaussian to yield the matrix element ratio. Since only one local angle can be measured on each side, only one ratio is derived for each plane.

From the second class of constraints rescaling factors for transport matrix element ratios are derived, by assuming that the reconstructed scattering angle must be the same for different reconstruction methods (see Section 4.3) for a consistent beam optics model. These constraints are obtained for a given reference optics, which is the design optics. Figure 6.54 shows a profile histogram for design optics in black with the horizontal scattering angle reconstructed with the subtraction method on the horizontal axis and the difference between the horizontal scattering angle reconstructed with the subtraction and the local angle method $\Delta\theta_x^*$ on the vertical axis. If the design optics used for the reconstruction was identical to the real optics, an essentially flat shape would be observed, with a small residual slope of about 1 % induced by limited resolution of the local angle measurement. However, the histogram shows a slope of about 6 %, and reveals a difference in the scattering angle from the two methods, which can be explained by a difference in the transport matrix elements used for the reconstruction. The histogram is fitted with a linear function, and the slope is a measure of the ratio of the true matrix element ratio to the design ratio. The result of the fit is corrected for the mentioned bias of 1 % for the inner detectors determined from MC simulation, while for the outer detectors a slightly smaller bias with opposite sign of -0.8% is determined. Since the subtraction method uses the effective lever arm $M_{u,12}$ and the local angle method

6 Data analysis

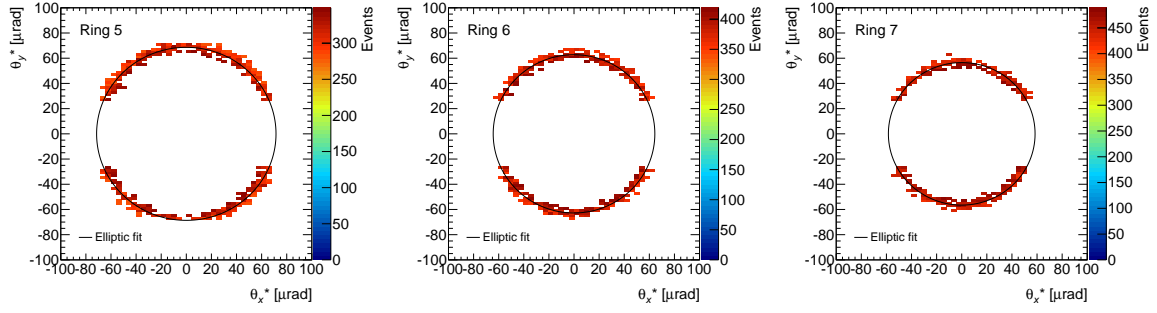


Figure 6.55: Three central rings of constant density in the scattering angle plane with elliptical fits determining their contour in black. The scattering angle is reconstructed with the inner detectors only.

the transport matrix element $M_{u,22}$ for the reconstruction, the constraint extracted from the linear fit is defined as

$$R \left(\frac{M_{u,12}}{M_{u,22}} \right) = \frac{(M_{u,12}/M_{u,22})_{\text{true}}}{(M_{u,12}/M_{u,22})_{\text{design}}}. \quad (146)$$

The equality between the methods cannot be used to infer any absolute value for the transport matrix elements themselves, however it imposes a strong constraint on the model for the true optics by fixing its matrix elements ratio with respect to the reference design optics. Furthermore, the measurement is striking evidence that the design optics suffers from inaccuracies of the order of 5 %. The measurement is also done in the vertical plane, and separately for inner and outer detector pairs.

The last constraints are derived from the azimuthal isotropy of the scattering angle in elastic scattering with unpolarized beams. This implicates that the azimuthal angle distribution ϕ of elastic scattering events is flat, or equivalent that the distribution of the vertical and horizontal scattering angle θ_y^* and θ_x^* are the same. By looking at the two-dimensional distribution of the scattering angle, the ϕ -isotropy implies that at a given distance from the origin r_{θ^*} the density of events must be the same at every point fulfilling

$$r_{\theta^*}^2 = \theta_x^{*2} + \theta_y^{*2}. \quad (147)$$

If the design optics used to reconstruct the scattering angle is not equal to the true optics, the contours of equal density will be of elliptical shape, showing a deviation from an ideal circle. In practice the entire two-dimensional distribution is split into ten rings of about constant density. The rings are fit with an ellipse, which minimizes the distance of each pixel of the ring to said ellipse. However, the rings are interrupted in the centre, because of the vertical detector gap for the beam, and the inner- and outermost rings are affected by acceptance cuts. Therefore, only the three central rings are used for the fit, which are shown in Figure 6.55 for the inner stations. Four free parameters are fitted (two offsets and the major and minor axis), and the ratio of the major and minor axes of the ellipses are then a measure of the rescaling factors

$$R \left(\frac{M_{y,12}}{M_{x,12}} \right) = \frac{(M_{y,12}/M_{x,12})_{\text{true}}}{(M_{y,12}/M_{x,12})_{\text{design}}}. \quad (148)$$

The average of the three rings is taken as final result. The measurement is done separately for the inner and outer stations and gives deviations of the order of 2 – 3 % from unity, however with larger statistical uncertainties since only the fraction of events in the three

Table 6.20: ALFA constraints obtained from elastic-scattering data with statistical and systematic uncertainties [45]. The systematic uncertainties are averaged for similar constraints to suppress statistical fluctuations in the case of $M_{i,12}(A)/M_{i,12}(A)$ for inner and outer stations and for $M_{y,12}(\pm 237)/M_{y,12}(\pm 241)$ for A- and C-Side.

Constraint	Value	Stat. uncert.	Syst. uncert.	Total uncert.
$M_{x,12}(+237)/M_{x,12}(-237)$	1.0063	0.0015	0.0041	0.0044
$M_{x,12}(+241)/M_{x,12}(-241)$	1.0034	0.0010	0.0041	0.0042
$M_{x,22}(A)/M_{x,12}(C)$	0.9932	0.0007	0.0041	0.0042
$M_{y,12}(+237)/M_{y,12}(-237)$	0.9951	0.0001	0.0026	0.0026
$M_{y,12}(+241)/M_{y,12}(-241)$	0.9972	0.0001	0.0026	0.0026
$M_{y,12}(+237)/M_{y,12}(+241)$	1.0491	0.0001	0.0007	0.0008
$M_{y,12}(-237)/M_{y,12}(-241)$	1.0481	0.0001	0.0007	0.0008
$M_{y,22}(A)/M_{y,22}(C)$	0.9830	0.0002	0.0180	0.0180
$R[M_{x,12}(\pm 237)/M_{x,22}(\pm 237)]$	1.0551	0.0003	0.0022	0.0023
$R[M_{x,12}(\pm 241)/M_{x,22}(\pm 241)]$	1.0453	0.0002	0.0013	0.0014
$R[M_{y,12}(\pm 237)/M_{y,22}(\pm 237)]$	1.0045	0.0001	0.0061	0.0061
$R[M_{y,12}(\pm 241)/M_{y,22}(\pm 241)]$	1.0046	0.0001	0.0065	0.0065
$R[M_{y,12}(\pm 237)/M_{x,12}(\pm 237)]$	0.9736	0.0052	0.0104	0.0116
$R[M_{y,12}(\pm 241)/M_{x,12}(\pm 241)]$	0.9886	0.0057	0.0072	0.0092

selected rings is used. Furthermore, the ellipses can only be determined reliably if the upper and lower hemispheres of the rings are fit simultaneously, which means that the two arms are fit simultaneously.

In total 14 constraints are obtained from elastic-scattering data for the two classes, which are listed in Table 6.20 with statistical and systematic uncertainties. The statistical uncertainty of the constraints is determined from Monte Carlo simulation. With $< 0.1\%$ it is in general negligible, except for $M_{x,12}(A)/M_{x,12}(C)$, where many parameters are fit with the 2D Gaussian function, and for $R(M_{y,12}/M_{x,12})$, where only a subset of the data is used for the fit. The systematic uncertainties are evaluated from several sources: the difference between the two arms, except for the ϕ -isotropy; variation of the selection criteria to probe an impact of background; variation of the fit ranges to probe acceptance effects; the vertical alignment uncertainty; the dependence on the physics model in simulation by varying the value of the nuclear slope B ; and the dependence on detector resolution. In general the systematic uncertainty is dominated by the difference in the two spectrometer arms, and ranges from 0.004 to 2%. Some uncertainties are highly correlated, e.g. in the cases where measurements from inner and outer detectors are used.

The eight lever arm ratios determined from elastic-scattering data in the first class of constraints are furthermore used as input for the track matching in Section 3.4.2.

6.7.2 Beam optics fit

The 14 ALFA constraints are now combined, and used in a global fit to determine corrected beam optics from the design optics as starting point [45]. In principle the number of free optics parameters is large: strengths of six quadrupoles in each beam between the ATLAS IP and the Roman Pots, and several alignment constants per quadrupole. However, the number of constraints is limited, and therefore the phase space of free parameters has to be reduced. So only the strength of a limited number of quadrupoles is varied. Since the ALFA constraints

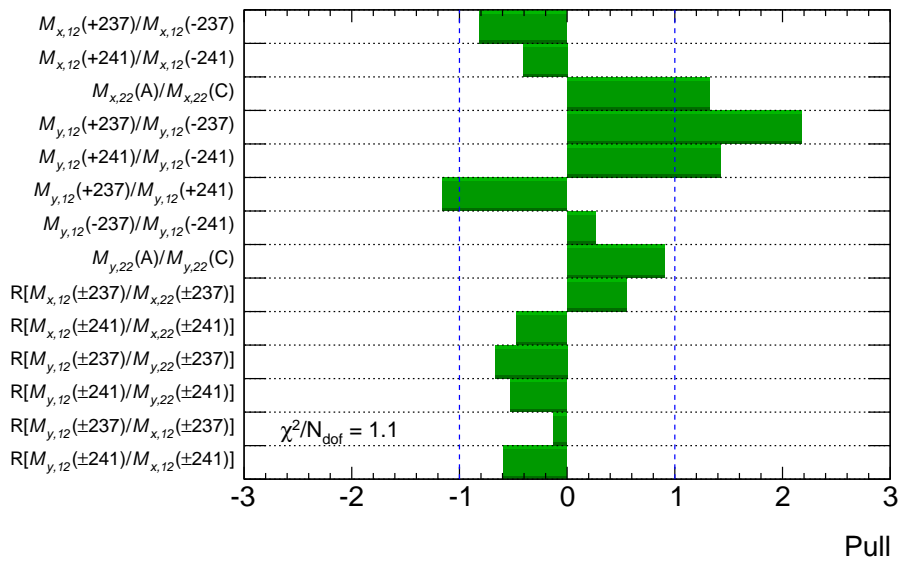


Figure 6.56: Pulls of the optics fit (effective optics) with respect to the ALFA constraints.

only provide precise information about the transport matrix element ratios, but not the deviation of single magnets, several combinations of quadrupole strengths exist that minimize the χ^2 used in the fit. The inner triplet magnets Q1 and Q3 are chosen to be varied coherently from their nominal strength, and the obtained solution is called the ‘effective beam optics’. This choice is motivated by the maximum sensitivity of the total cross-section on the inner triplet and possible relative calibration offsets between these quadrupoles, because Q1 and Q3 were manufactured at a different site than Q2 (Fermilab and KEK). However, the choice is somewhat arbitrary in the sense that another varied magnet strength combination could lead to the same effective optics and transport matrix elements. In the fit all 14 ALFA constraints are included with their systematic uncertainties and treated as uncorrelated. The effect of the longitudinal quadrupole position is negligible when varied by its uncertainty, though this is considered in the systematic uncertainties. The only two free parameters are inter-calibration offsets of Q1 and Q3 $\Delta kQ1Q3$ for beam 1 and 2. All other parameters are fixed to their design values. In the minimization procedure MAD-X is used to extract the Twiss parameters for a given set of quadrupole strengths in the beam-line between the IP and Roman Pots. The transport matrix element ratios are calculated from these parameters and compared to the experimental constraints and their total uncertainties to obtain a χ^2 , which is minimized with MINUIT [77]. The fit results in $\Delta kQ1Q3(\text{A-Side}) = 0.00313 \pm 0.00012$ and $\Delta kQ1Q3(\text{C-Side}) = 0.00288 \pm 0.00015$, which lies in the anticipated range for the possible calibration offset. The pulls of the fit with respect to the ALFA constraints are shown in Figure 6.56. Here the pull is defined by the matrix element ratios after the fit C_{fit} and the ALFA constraints $C_{\text{ALFA}} \pm \sigma_{\text{ALFA}}$ as $\text{pull} = (C_{\text{fit}} - C_{\text{ALFA}}) / \sigma_{\text{ALFA}}$. The effective beam optics obtained with this fit is used for the MC simulation described in Section 5 and to reconstruct the differential t -spectrum from the elastic-scattering data. The transport matrix elements for the effective optics are summarized in Table 4.3.

Several systematic effects are considered for the effective optics. The resulting uncertainties affect the differential t -spectrum as well as the total cross-section. Therefore, variations of the effective optics are obtained for these uncertainties and the maximum impact on the

t -spectrum and total cross section is evaluated (compare Section 7.1.1): the uncertainties from the optics fit on Δk_{Q1Q3} are used to shift the central value up and down; a possible mis-alignment of the longitudinal position of the quadrupoles as determined from a survey; systematic uncertainties of k -values of the fixed magnets Q2, Q4, Q5 and Q6 in the order of 0.1 %; the systematic uncertainties of the ALFA constraints as described before; and a two-stage fit approach where the value of Δk_{Q2} is released in a second minimization with Δk_{Q1Q3} fixed to the value at the minimum of the first stage.

7 Results

7.1 Differential elastic cross-section

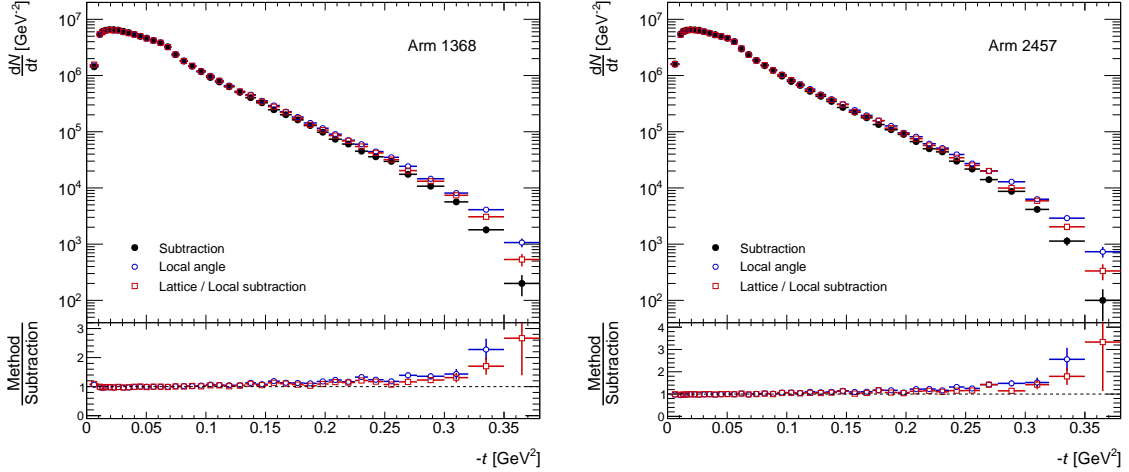


Figure 7.1: Raw differential t -spectrum dN/dt without any corrections as a function of $-t$ for both spectrometer arms and three reconstruction methods. Only the statistical uncertainty is shown, and since the local subtraction method is indistinguishable from the lattice method only the later one is shown. The bottom panels show the ratio of the local angle and lattice to the subtraction method.

After applying the event selection (Section 6.1) and reconstructing the four-momentum transfer squared t for every selected event with the four reconstruction methods (Section 4.3) using the effective optics (Section 6.7) a raw and uncorrected differential t -spectrum dN/dt is obtained for spectrometer arm 1368 and 2457 separately. Both spectra are shown in Figure 7.1 for three reconstruction methods, with the binning listed in Table A.1. Since the local subtraction method is indistinguishable from the lattice method only the latter one is shown. The spectra in the two arms are somewhat different, because of different acceptances, which originate from asymmetric vertical cuts at the beam-screen. At larger $|t|$ differences between the methods are visible, which are related to detector resolution effects inducing a bias on all methods using the local angle measurement.

In order to obtain the differential elastic cross-section $d\sigma/dt$ several corrections, described in Section 6, are applied to the raw t -spectra. The corrections are applied individually in each arm, since most of them are different for the two arms. Afterwards the spectra are combined and divided by the integrated luminosity \mathcal{L}_{int} for the selected LBs to yield $d\sigma/dt$. This operation is described for a given bin i in t by

$$\left(\frac{d\sigma}{dt}\right)_i = \frac{1}{\Delta t_i} \frac{\mathbf{U}^{-1}(N_i - B_i)}{\varepsilon_{\text{acc},i} \varepsilon_{\text{rec}} \varepsilon_{\text{trig}} \varepsilon_{\text{DAQ}} \mathcal{L}_{\text{int}}}, \quad (149)$$

where Δt_i is the bin width, \mathbf{U}^{-1} represents the unfolding procedure applied to the background-subtracted number of events $N_i - B_i$, $\varepsilon_{\text{acc},i}$ is the total acceptance, ε_{rec} is the event reconstruction efficiency, $\varepsilon_{\text{trig}}$ is the trigger efficiency and ε_{DAQ} is the dead-time correction (life fraction). The binning of $d\sigma/dt$ in t is listed in Table A.1, and is chosen appropriately for the experimental resolution and statistics, based on the purity of the subtraction method (see Section 6.5). At small $|t|$ the selected bin width is 1.5 times the resolution, where at larger $|t|$

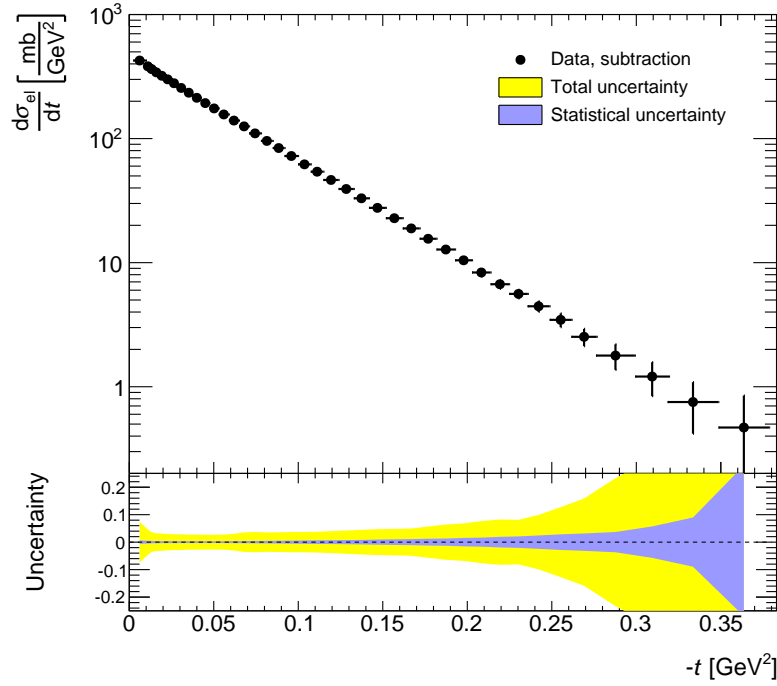


Figure 7.2: Differential elastic cross-section $d\sigma_{el}/dt$ for pp scattering at $\sqrt{s} = 7$ TeV obtained with the subtraction method. The error bars represent the total uncertainty. In the bottom part the relative total and statistical uncertainties are shown.

the bin width is increased to compensate for the lower number of events, due to the exponential decrease of the distribution. The final differential elastic cross-section $d\sigma_{el}/dt$ for pp scattering at $\sqrt{s} = 7$ TeV is shown in Figure 7.2 with statistical and systematic uncertainties, where the nominal subtraction method is used. The values for each bin are listed in Table A.1 in Appendix A.7.

7.1.1 Systematic uncertainties

Systematic uncertainties for the differential elastic cross-section are obtained by the so-called ‘offset method’. This means, that the nominal value of a certain parameter in the analysis chain, like e.g. the event reconstruction efficiency, is varied according to the assigned uncertainty. In case of the event reconstruction efficiency the central value is shifted up- and downward by its systematic uncertainty, and for both cases a new alternative differential cross-section is calculated. The shift $\delta_k(i)$ of these alternative differential cross-sections in each bin i for a systematic uncertainty source k corresponding to a $\pm 1\sigma$ variation

$$\delta_k(i) = \frac{d\sigma_k}{dt}(i) - \frac{d\sigma_{\text{nominal}}}{dt}(i) \quad (150)$$

is recorded with the sign, to account for correlations across the t range. The positive and negative variations are largely symmetric up to statistical fluctuations, and therefore symmetrised in the shifts.

Some of the systematic shifts are constructed from several individual variations contributing in different regions of $-t$. In these cases the single variation closest to the full envelope (most extreme case in each bin of $-t$) is selected to build the shift. In total 24 uncertainty sources are considered [45], and propagated to the differential elastic cross-section:

- The amount of subtracted background is varied according to its systematic uncertainty obtained from the difference between the anti-golden and the vertex method as described in Section 6.2. Furthermore the background shape is varied, by inverting the sign of the vertical coordinate in a different anti-golden armlet, and by inverting the sign in the horizontal coordinate as well.
- The alignment parameters are varied corresponding to the uncertainties on the horizontal offset, the rotation in the transverse plane, the vertical distance measurement, the optics lever arm used in the extrapolation from one to another detector, the vertical offset and the choice of the reference station, as described in Section 3.4.3. A large number of alignment parameter sets is used for the variation and the sets with maximum impact in the differential cross-section are retained as systematic shifts.
- The effective optics, as described in Section 6.7, are varied by changing the constraints of the optics fit, the strength of the quadrupoles Q2, Q4, Q5 and Q6 by their uncertainty of $\pm 0.1\%$ and changing only Q5 and Q6 by -0.2% , as suggested by LHC constraints on the phase advance Ψ . Furthermore, the longitudinal position of the quadrupoles are varied according to their alignment uncertainty, the fit uncertainties for the strength of Q1 and Q3 Δk_{Q1Q3} is propagated to the resulting optics and the difference between the transport matrix based transport used in the optics fit and the MAD-X beam transport is taken. These variations effect the differential cross-section directly through the reconstruction methods and indirectly through the MC simulation, which uses the effective optics. Therefore, the acceptance- and unfolding-corrections are also re-calculated for each variation of the optics to obtain the systematic shifts of the differential cross-section.
- The event reconstruction efficiency ε_{rec} is varied by its uncertainty of $\pm 0.6\%$ for arm 1368 and $\pm 0.9\%$ for arm 2457, as determined in Section 6.3.
- The intrinsic unfolding uncertainty, as determined in Section 6.5, based on the difference between the true bias fast MC simulation and data (data-driven closure test) is propagated to the differential cross-section as systematic shift.
- The luminosity is varied by its uncertainty of 2.34% , as described in Section 6.6, and propagated to the differential cross-section as systematic shift.
- The pre-selection criterion for good candidate events in the tracking algorithm, that at least three layers with one to three hits each are required, is varied up to at least six layers (see Section 3.4).
- The value of the nuclear slope B used in the MC simulations, as described in Section 5, is varied conservatively by $\pm 1 \text{ GeV}^{-2}$.
- The tuned spatial detector resolution $\sigma_{x,y}^{\text{tuned}}$, as discussed in Section 5.3, is varied by its systematic uncertainty. The resolution is replaced by the values from full simulation $\sigma_{x,y}^{\text{Full}}$, which underestimate the tuned ones by 3 to 4 μm , and by the values from test beams $\sigma_{x,y}^{\text{TB}}$, which overestimate the tuned ones by 4 to 5 μm . In addition the constant tuned resolution is replaced by a y -dependent one.
- The emittance ϵ , as described in Section 3.3.1, which is used to calculate the angular divergence as input for the MC simulation, is varied by $\pm 10\%$.

- The vanishing crossing angle at the IP, used as input for MC, is varied in the horizontal plane by $\pm 10 \mu\text{rad}$, as derived from the precision of the BPMs.
- The nominal beam momentum of 3.5 TeV used in the t -reconstruction in Equation (94) is varied by $\pm 0.65 \%$ as determined in Reference [53].

In addition two stability checks are performed, whose resulting systematic shifts are smaller than the statistical uncertainty and therefore not included in the systematic uncertainty of the differential cross-section:

- The event selection cuts (vertical acceptance, elastic selection and background rejection), as described in Section 6.1, are varied.
- The IDS unfolding is exchanged with the SVD unfolding (see Section 6.5).

The contributions of the most important uncertainties to the relative total uncertainty as a function of $-t$ are shown in Figure 7.3. The fit range used in the next Section to extract the total cross-section, is indicated as vertical lines. The dominant contribution comes from the constant luminosity uncertainty, followed by the energy uncertainty, which goes to zero at $-t \approx 0.05 \text{ GeV}^2$ because of a sign flip. The statistical uncertainty contributes only with a small fraction, and the other experimental uncertainty contains the rest of the list given above (as quadratic sum).

7.2 Total cross-section and nuclear slope

The differential elastic cross-section is fitted with two free parameters to obtain the total cross-section σ_{tot} and the nuclear slope B . The fit is performed with the theoretical form

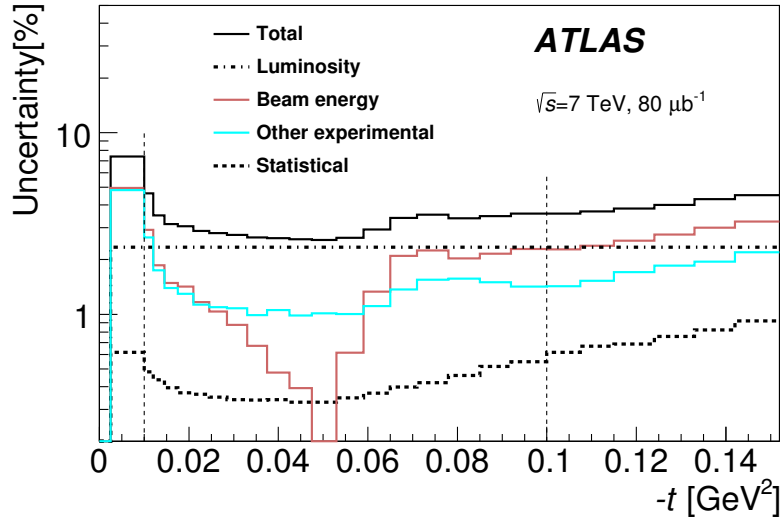


Figure 7.3: Relative systematic uncertainties of the differential elastic cross-section for the sources luminosity, beam energy and other experimental, and the relative statistical uncertainty in the $|t|$ region relevant for the total cross-section determination [45]. The other experimental uncertainty includes all sources except luminosity and beam energy. The total uncertainty is the quadratic sum of statistical and systematic uncertainties. The fit range for the total cross-section determination is indicated with two vertical dashed lines.

of $d\sigma_{\text{el}}/dt$ given by Equation (28) including the Coulomb and CNI terms, with the dipole parametrization of the proton electromagnetic form factor $G(t)$, the Coulomb phase $\phi(t)$ parametrization by West and Yennie and a fixed ρ value of $\rho = 0.140 \pm 0.008$ as described in Section 2.2. In this fit correlations between different bins induced by statistical and systematic uncertainties are taken into account. For statistically induced correlations the covariance matrix, calculated in the unfolding procedure in Section 6.5 with toy MCs, is used. However, for correlations induced by systematic uncertainties a profile minimization procedure [78] is applied. In this procedure the systematic shifts $\delta_k(i)$ for every of the 24 sources of uncertainty explained in the previous section are used as input for the fit. The sources of the 24 systematic shifts are listed in Table 7.1 with a description and abbreviation.

The theoretical prediction is now fitted to the measured differential elastic cross-section with a χ^2 minimization using MINUIT [77] which includes statistical and systematic uncertainties. The χ^2 is given by

$$\chi^2 = \sum_i^{\Delta t_f} \sum_j^{\Delta t_f} \left\{ \left[D(i) - \left(1 + \sum_{l=23}^{24} n_l \right) T(i) - \sum_{k=1}^{22} n_k \delta_k(i) \right] V^{-1}(i, j) \right. \\ \left. \times \left[D(j) - \left(1 + \sum_{l=23}^{24} n_l \right) T(j) - \sum_{k=1}^{22} n_k \delta_k(j) \right] \right\} + \sum_{k=1}^{22} n_k^2 + \sum_{l=23}^{24} \frac{n_l^2}{\Delta n_l^2}, \quad (151)$$

where $D(i)$ is the measured value of $d\sigma_{\text{el}}/dt$ in bin i , $T(i)$ the theoretical prediction in the same bin and $V(i, j)$ the statistical covariance matrix from the unfolding. For each t -dependent systematic uncertainty k , which changes the shape of $d\sigma_{\text{el}}/dt$, a nuisance parameter n_k scaling the corresponding systematic shift $\delta_k(i)$ is fitted as a free parameter, and added to the χ^2 as a penalty term $\sum_{k=1}^{22} n_k^2$ outside of the sums. Since the luminosity and event reconstruction efficiency are t -independent and only change the normalisation of the data, two corresponding scale parameters n_l are used to describe the rescaling of the normalization of the theoretical prediction due to these two uncertainties. Consequently, a second penalty term $\sum_{l=23}^{24} n_l^2 / \Delta n_l^2$ is added, which corresponds to the quadratic sum of these two scale factors divided by their uncertainties. The first two sums in j and k run over all bins in the fit range $\Delta t_f = [-0.01 \text{ GeV}^2; -0.1 \text{ GeV}^2]$, the sum in k runs over the t -dependent systematic uncertainties and the sum in l runs over the two t -independent uncertainties, where the values of k and l correspond to the number in the first column in Table 7.1.

The lower limit of the fit range in $-t$ is chosen to be as close as possible to $t = 0$ to reduce the extrapolation uncertainty, described in the following, while having an acceptance of more than 10 %. On the other hand, the choice of the upper limit is motivated by theoretical considerations not to extend the fit into a region where deviations from the simple exponential parametrization of the nuclear term are expected [79].

Including the 24 nuisance parameters, the total cross-section σ_{tot} and the nuclear slope B in total 26 free parameters are determined in the minimization. However, the nuisance parameters are expected to have a distribution with a mean of zero and a width of one. In Figure 7.4 these parameters are shown after the fit for the subtraction and local angle method, and confirm the expectation. The results of the fit for all four reconstruction methods are shown in Figures 7.5 and 7.6.

For the differential elastic cross-section reconstructed by the subtraction method the fit yields

$$\sigma_{\text{tot}} = 95.35 \pm 1.30 \text{ mb}, \quad (152)$$

$$B = 19.73 \pm 0.24 \text{ GeV}^{-2}, \quad (153)$$

Table 7.1: Systematic shift sources of uncertainties.

No.	Source (abbr.)	Description
1	ALFA constraints	1σ variations of the ALFA constraints (256 variations)
2	Q scan	0.1 % variations of the k -values of all quadrupoles (256 variations)
3	MAD-X	replace transport matrix beam transport by MAD-X tracking
4	$kQ2$ re-fit	at the optimum for $kQ1Q3$ relax and re-fit $kQ2$
5	$kQ5Q6$	set $kQ5Q6$ to -0.2% as indicated by machine constraints
6	Q misalignment	set longitudinal quadrupole position to survey values
7	$kQ1Q3$ fit	propagate 1σ optics fit error to effective optics
8	Station 2	replace nominal station 1 as reference by station 2
9	Distance	1σ variation of overlap distance measurement
10	Lever arm	1σ variation of the optics lever arm used in alignment
11	Vertical offset	1σ variation of the vertical offset
12	Horizontal offset	extreme variation of the horizontal offset (4 variations)
13	Rotation	extreme variation of the x - y rotation (4 variations)
14	BG norm	vary background normalisation by vertex-anti-golden difference
15	BG shape	alternative symmetry assumptions to turn anti-goldens in goldens (4 variations)
16	MC resolution	variation of the inner-to-outer resolution scaling factor (3 variations)
17	Physics model	variation the nuclear slope $B = 19.5 \pm \text{GeV}^{-2}$ in the simulation
18	Emittance	1σ variation of the emittance in simulation
19	Unfolding	uncertainty from data-driven closure test
20	Tracking algo	variation of track reconstruction criterion
21	Crossing angle	variation by $\pm 10 \mu\text{rad}$
22	Beam energy	nominal beam energy uncertainty $\pm 0.65\%$
23	Reco eff	1σ variation of the event reconstruction efficiency
24	Lumi	luminosity uncertainty $\pm 2.34\%$

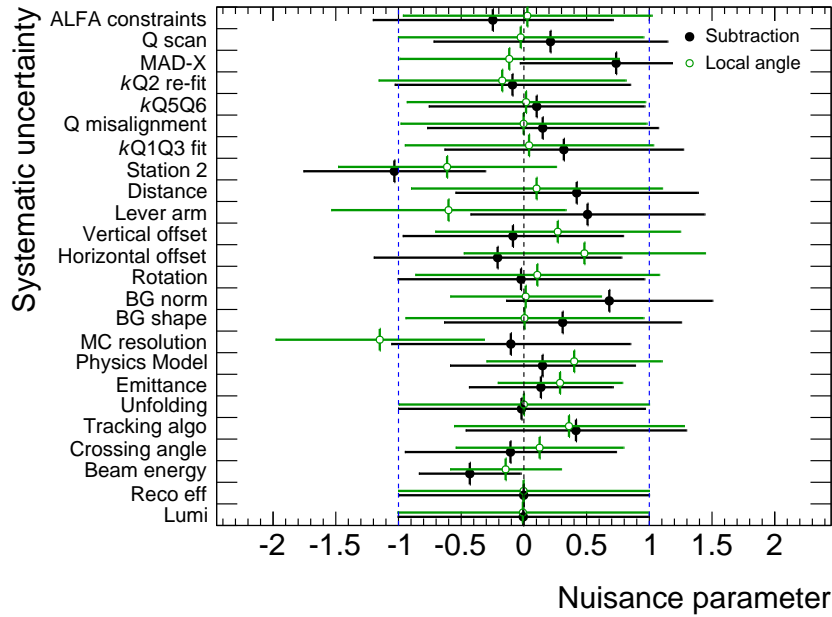


Figure 7.4: Nuisance parameters from the profile minimization procedure for the subtraction and local angle method [45].

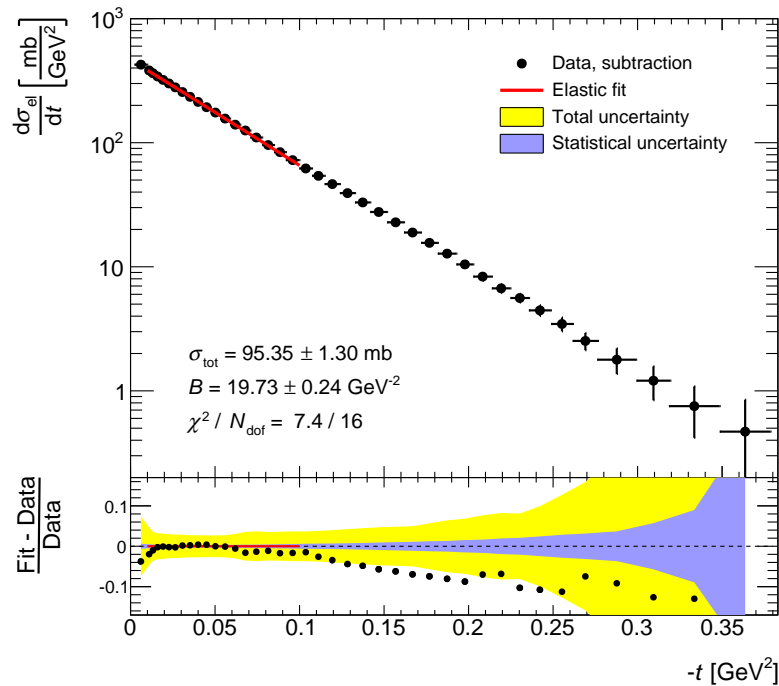


Figure 7.5: Fit to the differential elastic cross-section $d\sigma_{el}/dt$, reconstructed with the subtraction method, of the theoretical prediction with σ_{tot} , B and 24 nuisance parameters as free parameters [45]. The bottom part shows the normalized residuals with statistical and total uncertainty. The red line indicates the fit range, and the fit result is extrapolated in the bottom part outside the fit range.

7 Results

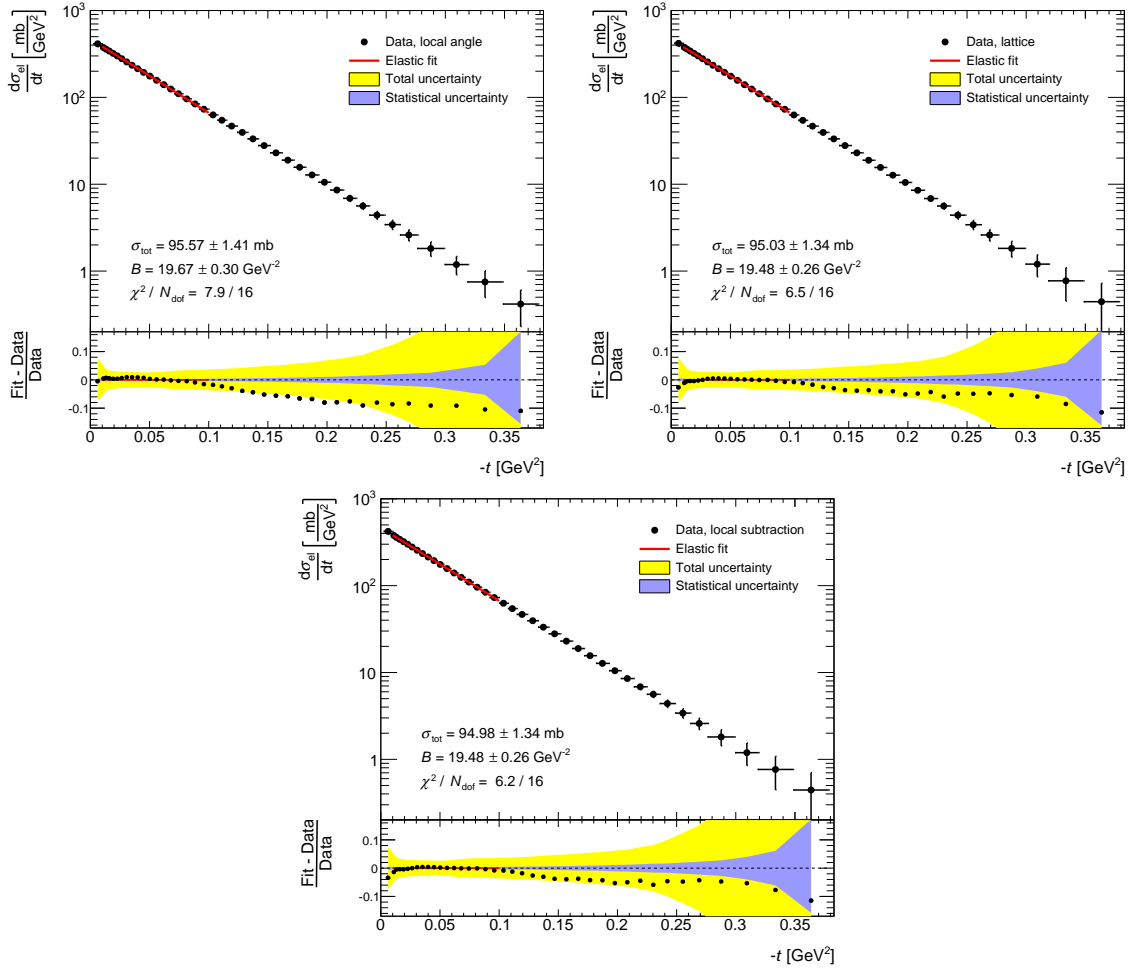


Figure 7.6: Fit to the differential elastic cross-section $d\sigma_{el}/dt$, reconstructed with the local angle, lattice and local subtraction method, of the theoretical prediction with σ_{tot} , B and 24 nuisance parameters as free parameters. The bottom part shows the normalized residuals with statistical and total uncertainty. The red line indicates the fit range, and the fit result is extrapolated in the bottom part outside the fit range.

where the uncertainty comes directly from the fit and includes statistical and experimental systematic uncertainties from the sources listed in Table 7.1. The total uncertainty is dominated by the systematic uncertainty, where the statistical uncertainty is only $\Delta_{\text{stat.}}\sigma_{\text{tot}} = 0.38 \text{ mb}$ and $\Delta_{\text{stat.}}B = 0.14 \text{ GeV}^{-2}$, respectively. The inclusion of these large systematic uncertainties in the fit also explains the rather good $\chi^2/N_{\text{dof}} = 7.4/16$, where N_{dof} does not include the nuisance parameters. For all four reconstruction methods a range of $\sigma_{\text{tot}} = 94.98$ to 95.57 mb and $B = 19.48$ to 19.73 GeV^{-2} is obtained, which is well compatible with the uncorrelated systematic uncertainties. The total uncertainty of all reconstruction meth-

Table 7.2: Results of the total cross-section σ_{tot} for four reconstruction methods with statistical and systematic uncertainties [45].

	Subtraction	Local angle	Lattice	Local subtraction
σ_{tot} [mb]	95.35	95.57	95.03	94.98
Statistical uncert.	0.38	0.38	0.33	0.31
Experimental uncert.	1.25	1.36	1.30	1.30
Extrapolation uncert.	0.37	0.27	0.50	0.33
Total uncert.	1.36	1.44	1.43	1.38

Table 7.3: Results of the nuclear slope B for four reconstruction methods with statistical and systematic uncertainties [45].

	Subtraction	Local angle	Lattice	Local subtraction
B [GeV^{-2}]	19.73	19.67	19.48	19.48
Statistical uncert.	0.14	0.15	0.14	0.15
Experimental uncert.	0.19	0.26	0.22	0.21
Extrapolation uncert.	0.17	0.17	0.26	0.18
Total uncert.	0.29	0.35	0.37	0.31

ods for both parameters are very similar and range from $\Delta_{\text{tot.}}\sigma_{\text{tot}} = 1.30$ to 1.41 mb and $\Delta_{\text{tot.}}B = 0.24$ to 0.30 GeV^{-2} , respectively. Here the subtraction method has slightly larger uncertainties from the beam optics, where the other methods are more sensitive to the detector resolution. Because of the best t -resolution, as discussed in Section 6.5, the subtraction method is chosen as nominal method and yields the nominal values for σ_{tot} and B . Additional systematic uncertainties related to the theoretical parameters and the extrapolation to $-t \rightarrow 0$ are discussed in the following. A summary of all results is given in Tables 7.2 and 7.3 including the additional systematic uncertainties.

7.2.1 Experimental systematic uncertainties

Since the experimental systematic uncertainties of the differential elastic cross-section are included in the fit through the nuisance parameters and the statistical uncertainty of data and MC through the covariance matrix, the total uncertainty of σ_{tot} and B is directly calculated with the fit.

The statistical uncertainties of σ_{tot} and B quoted in Tables 7.2 and 7.3 are determined from 200 toy MC samples, each with the same number of elastic-scattering events as the data. These MC events are reconstructed and analysed with the same chain as the data, and the RMS of the resulting fit parameters is taken as statistical uncertainty.

Individual systematic uncertainty sources are roughly estimated by excluding the corresponding systematic shift and nuisance parameter from the fit, and quadratically subtracting the fitted total uncertainty from the nominal total uncertainty which includes all systematic sources [45]. However, this procedure is of limited precision, especially for small uncertainties, and only the total uncertainty from the fit is really trustworthy. The individual uncertainties of σ_{tot} and B determined in this way are listed in Table A.2 and A.3 in Appendix A.7. For the total cross-section the main contribution to the experimental systematic uncertainty comes from the luminosity, the beam energy and the event reconstruction efficiency uncer-

tainties. For reconstruction methods using the local angle (not subtraction) also the detector resolution uncertainty is important. For the nuclear slope the main contribution comes from the beam energy uncertainty. The detector resolution uncertainty is again only important for reconstruction methods using the local angle. Here the important uncertainties for the total cross-section like the luminosity and event reconstruction efficiency uncertainties have no impact, since they only change the normalization and not the slope.

7.2.2 Extrapolation uncertainties

In addition to the experimental systematic uncertainties from the differential cross-section further uncertainties arise from the extrapolation to $-t \rightarrow 0$ [45]. One contribution comes from the dependence on the fit range, which is related to possible deviations of the differential elastic cross-section from the simple exponential slope at larger $|t|$. And indeed, a curvature is present in the data, as can be seen in the bottom residual histogram in Figures 7.5 and 7.6. The uncertainty from the fit-range dependence is estimated by varying the upper limit six bins from $-t = 0.1 \text{ GeV}^2$ to $-t = 0.15 \text{ GeV}^2$. This variation limit is chosen in order to remain in a range where a simple exponential is still a reasonable assumption for the nuclear slope [79]. Furthermore, the upper edge is symmetrically varied down to $-t = 0.059 \text{ GeV}^2$ by the same number of bins, and the symmetrised change is taken as a systematic uncertainty from the fit-range dependence of $\Delta\sigma_{\text{tot}} = 0.3 \text{ mb}$ and $\Delta B = 0.17 \text{ GeV}^{-2}$.

The other contributions come from the choice of parameters and parametrizations in the theoretical form of the differential cross-section in Equation (28). These values are varied to estimate the uncertainties:

- The choice of $\rho = 0.14$ is varied by its uncertainty of ± 0.008 , as discussed in Section 2.2.1.
- The dipole parametrization of the proton electromagnetic form factor $G(t)$ is replaced by a double-dipole form, as described in Section 2.2.2.
- The Coulomb phase parametrization $\phi(t)$ from West and Yennie [19] is replaced by the parametrizations from Cahn [15] and KFK [27], as discussed in Section 2.2.3.

The contributions of these additional systematic extrapolation uncertainties to the total uncertainty of σ_{tot} and B are listed in Tables A.2 and A.3 in Appendix A.7, and the summaries of the results with combined statistical, experimental, extrapolation and total uncertainties are given in Tables 7.2 and 7.3. The by far dominating contribution comes for both parameters from the fit-range dependence uncertainty. In contrast to recent TOTEM measurements [28, 80], the Coulomb and CNI terms are included in the theoretical form of $d\sigma_{\text{el}}/dt$, that is used for the fit. A fit without these term using only the nuclear term yields a significantly lower total cross-section by 0.6 mb for all four reconstruction methods, and a small change of 0.09 GeV^{-2} for the nuclear slope. However, the contribution from the Coulomb and CNI terms is small, since the accessible t -range is still too large to observe the rise of the differential elastic cross-section, induced by the Coulomb scattering amplitude. Thus the uncertainties from the Coulomb phase and form factor only yield a negligible contribution to the total uncertainty.

7.2.3 Stability checks

Several supplemental stability checks [45] for the measurement of the total cross-section are performed, which are not included as additional systematic uncertainties but intended to corroborate the nominal result, the uncertainties and the profile fit procedure.

In addition to varying the upper limit of the fit range, as described above, this is also done for the lower limit. Here the subtraction method is more stable than the other methods, but an overall smaller dependence compared to the upper limit is observed. This very small change in the total cross-section measurement can be related to uncertainties in the background and for methods other than subtraction to resolution issues. Since the extrapolation uncertainty is not probed in the low $|t|$ -region, this check is not included as systematic uncertainty.

The fit of the total cross-section and nuclear slope is repeated only with the statistical covariance matrix, to cross-check the profile fit procedure including nuisance parameters and to evaluate the impact of the systematic uncertainties on the nominal result. This fit shows an excellent agreement with the profile fit procedure for all methods except the local angle method, where a difference of about 0.6 mb for σ_{tot} is observed. However, since the systematic uncertainties are not included in the fit, the fit quality in terms of χ^2/N_{dof} is poor, in particular for the subtraction method.

In contrast to the nominal fit, where the measured differential elastic cross-section in both spectrometer arms is combined, the fit is performed individually per arm, for the sub-sample collected in that arm, which involves however a reduced acceptance. Here the same fit range is used as for the combined differential cross-section, although the acceptance in the first bin is smaller than 10 %. The fit is carried out including only statistical uncertainties, and an excellent consistency is observed between the two spectrometer arms. Furthermore the differential elastic cross-sections of the arms are directly compared with a χ^2 -test, which also shows a very good agreement of $\chi^2/N_{\text{dof}} = 0.65$.

A MC-based (fast simulation) closure test is performed, by feeding simulated pseudo-data at reconstruction level through the whole analysis chain. The profile fit procedure is performed to yield the total cross-section and the nuclear slope, but only central values and statistical uncertainties are taken from the pseudo-data whereas the systematic shifts from measured data are used. First the same physics model with $\sigma_{\text{tot}} = 95$ mb and $B = 19.5$ GeV⁻² is used to generate the pseudo-data and to calculate the migration matrix for the unfolding, however with independent seeds. As shown in Section 6.3.10, the event reconstruction efficiency is not correctly calculated with MC and anyhow determined by the data-driven method, so that the pseudo-data is only normalized to the number of events reconstructed in the measured data sample. Secondly, a different physics model with $B = 19.5 \pm 1$ GeV⁻² is used to generate pseudo-data, while keeping the nominal model for MC-corrections in acceptance and unfolding. The closure test is successful for subtraction, lattice and local subtraction methods, which pass the test with small deviations on the level of statistical fluctuations. However, for the local angle method the deviations are somewhat larger, and the nuclear slope is determined with a shift of about 2σ of the statistical uncertainty with respect to the generated value. This indicates a potential but small bias in the unfolding procedure arising from the poor local angle resolution.

In the nominal analysis approach an unfolding procedure is used to correct for resolution and beam smearing effects, and to yield a fully corrected differential elastic cross-section. However, a different approach for the fit of the total cross-section and nuclear slope is possible, where the measured data are not unfolded, but instead all t -dependent corrections and migrations are applied to the theoretical form of the differential cross-section, which is fit

Table 7.4: Results for the total cross-section σ_{tot} using the subtraction method for different parametrizations of the nuclear amplitude $F_{\text{N}}(t)$ given in Section 2.2.4. The uncertainties comprise only the statistical and experimental systematic uncertainties [45].

Parametrization	σ_{tot} [mb]
Simple exponential [Equation (23)]	95.35 ± 1.30
Ct^2 [19, 31]	95.49 ± 1.27
$c\sqrt{4\mu - t} - 2\mu$ [32]	96.03 ± 1.31
Kohara, Ferreira and Kodama [27]	94.90 ± 1.23
Phillips and Barger [33]	95.49 ± 1.54
Bourrely, Soffer and Wu [35]	95.53 ± 1.38

to the raw and uncorrected t -spectrum. The advantage of this approach is that no correlations between the bins in the data are introduced and that no covariance matrix needs to be included in the fit. The statistical uncertainty is obtained without any toy MCs from simple error propagation and the migration matrix is used as-is without any iterative procedure. Such a folded fit is performed without including systematic uncertainties and yields results very close to the nominal ones for all four reconstruction methods except the local angle method, where a deviation of about 0.6 mb is found for σ_{tot} .

To probe the time stability of the total cross-section measurement the data are sub-divided into ten groups of about 25 LBs containing each about 80 000 selected elastic-scattering events. The entire analysis steps are carried out for each sub-sample as for the complete sample, and in the end the profile fit procedure is performed for each one. Only at the very beginning and end of the data taking period of about 4 hours deviations are visible of up to 2σ of the statistical uncertainty with respect to the nominal result.

In Section 6.3.3.1 the event reconstruction efficiency is shown to be t -independent. To probe the effect of a possible residual t -dependence on the total cross-section, the reconstruction efficiency $\varepsilon_{\text{rec}}(t)$ as a function of t is parametrized by assuming that it follows the shape of the partial efficiency of the 3/4 case $\varepsilon_{3/4}(t)$ in the two spectrometer arms (see Equation (130) and Figure 6.21 on page 84). The value in each bin is given by the overall t -independent total efficiency value ε_{rec} modulated by the ratio $\varepsilon_{3/4}(t)/\varepsilon_{3/4}^{\text{mean}}$. A fit of the differential elastic-cross section, constructed with this t -dependent reconstruction efficiency, yields a total cross-section very close to the nominal value, with a difference smaller than the statistical uncertainty. The impact on the nuclear slope is a little larger but the difference is still within the statistical uncertainty.

Traditionally, the nuclear amplitude $F_{\text{N}}(t)$ is parametrized at small $|t|$ with a single exponential function with constant slope B , as shown in Equation (23) in Section 2.2, which was used by many experiments before to extract σ_{tot} and is also used in this analysis. At larger $|t|$, approaching the diffractive minimum at $-t = 0.5 \text{ GeV}^2$, deviations from this simple exponential form are expected. Hence, several alternative model-independent parametrizations of the nuclear amplitude have been proposed predicting a t -dependent slope, as described in Section 2.2.4, which are used now to assess the impact of a different parametrization on the extrapolation to $-t \rightarrow 0$. Since all alternative forms have at least one more free parameter and are intended to describe the region at larger $|t|$, the fit range is enlarged up to $-t = 0.3 \text{ GeV}^2$, to increase the sensitivity for these additional parameters. The profile fit procedure is performed for all forms, and yields results in the range of $\sigma_{\text{tot}} = 94.90$ to 96.03 mb for the subtraction method shown in Table 7.4, which is in good agreement with

the extrapolation uncertainty for the simple exponential obtained from the fit-range variation of 0.37 mb. The alternative parametrizations have at least one more free parameter, which improves the fit quality at larger $|t|$, where best sensitivity for additional parameters is obtained. However, parametrizations with only one more free parameter give only a good description of the measured differential elastic cross-section up to $-t = 0.2 \text{ GeV}^2$, whereas models with more parameters are able to describe the entire range. The results for all four reconstruction methods are similar.

7.3 Elastic and inelastic cross-section

As shown in Section 2.3 several other derived quantities can be determined from the differential elastic cross-section and the total cross-section [45]. From the fitted parametrisation of Equation (28) by using only the nuclear term the intersection at $-t \rightarrow 0$ the optical point is determined to be

$$\left(\frac{d\sigma_{\text{el}}}{dt}\right)_{t \rightarrow 0} = 474 \pm 4 \text{ (stat.)} \pm 13 \text{ (syst.)} \frac{\text{mb}}{\text{GeV}^2}, \quad (154)$$

where the systematic uncertainty includes all experimental and extrapolation uncertainties.

By integrating the same parametrization with only the nuclear term over the full t -range, as given by Equation (49), the total elastic cross-section is obtained with

$$\sigma_{\text{el}} = 24.00 \pm 0.19 \text{ (stat.)} \pm 0.58 \text{ (syst.)} \text{ mb}, \quad (155)$$

where in the uncertainty calculation the correlation between σ_{tot} and B are taken into account, which is determined from the fit to be about 42 %.

By integrating only over the fiducial range from $-t = 0.0025 \text{ GeV}^2$ to 0.38 GeV^2 this yields a measured total elastic cross-section of

$$\sigma_{\text{el}}^{\text{fiducial}} = 21.66 \pm 0.02 \text{ (stat.)} \pm 0.58 \text{ (syst.)} \text{ mb}, \quad (156)$$

which corresponds to 90 % of σ_{el} . This determination does not involve any fit, hence the uncertainties are integrated from the differential elastic cross-section uncertainties without any profiling procedure. Furthermore, the fact that 90 % of σ_{el} is directly measured, substantiates the use of only the nuclear term in Equation (49).

The total elastic cross-section is used to determine the total inelastic cross-section by subtraction from the total cross-section as shown in Equation (51) as

$$\sigma_{\text{inel}} = 71.34 \pm 0.36 \text{ (stat.)} \pm 0.83 \text{ (syst.)} \text{ mb}, \quad (157)$$

where again the correlation between σ_{tot} and B is taken into account.

And finally the ratio of the total elastic cross-section to the total cross-section can be calculated to

$$\frac{\sigma_{\text{el}}}{\sigma_{\text{tot}}} = 0.2517 \pm 0.0022 \text{ (stat.)} \pm 0.0070 \text{ (syst.)}. \quad (158)$$

All derived quantities are summarized in Table 7.5 with their uncertainties. Since they all depend on σ_{tot} and B they are highly correlated.

Table 7.5: Results of the derived quantities optical point, total elastic cross-section, fiducial elastic cross-section and total inelastic cross-section with statistical and systematic uncertainties [45].

	$(\frac{d\sigma_{el}}{dt})_{t \rightarrow 0} \left[\frac{\text{mb}}{\text{GeV}^2} \right]$	σ_{el} [mb]	$\sigma_{el}^{\text{fiducial}}$ [mb]	σ_{inel} [mb]
Result	474	24.00	21.66	71.34
Statistical uncert.	4	0.19	0.02	0.36
Experimental uncert.	12	0.57	0.58	0.72
Extrapolation uncert.	4	0.03		0.40
Total uncert.	13	0.60	0.58	0.90

7.4 Discussion

The result of $\sigma_{\text{tot}} = 95.35 \pm 1.36$ mb, obtained here with the luminosity-dependent method, can now be compared to measurements performed by the TOTEM experiment, which use data from the same $\beta^* = 90$ m LHC fill. In their first measurement TOTEM also uses a luminosity-dependent analysis [28] and quotes a value of $\sigma_{\text{tot}}^{\text{TOTEM}} = 98.6 \pm 2.2$ mb, which is about 3.3 mb larger than the result reported in this thesis. Assuming fully uncorrelated uncertainties this corresponds to a difference of 1.3σ . However, the uncertainty of the TOTEM measurement is dominated by a luminosity uncertainty of 4 %, which corresponds to a ± 2 mb contribution to σ_{tot} , because of a square root dependence of σ_{tot} on the luminosity. On the other hand, the measurement reported here profits from a smaller luminosity uncertainty of 2.3 %, which gives rise to a smaller total uncertainty than in TOTEM's result. Later TOTEM also measured $\sigma_{\text{tot}}^{\text{TOTEM}} = 98.1 \pm 2.4$ mb with a luminosity-independent method [80], by using a simultaneous determination of elastic- and inelastic-scattering event yields (compare Equation (45)). In addition, they also made a ρ -independent measurement [81] of $\sigma_{\text{tot}}^{\text{TOTEM}} = 98.1 \pm 4.4$ mb without using the optical theorem by summing directly the elastic and inelastic cross-sections.

All three results, which are obtained from data taken in the same $\beta^* = 90$ m LHC fill, are consistent with each other, and differ only by 0.5 mb. This can be seen in Figure 7.7, where the measurement reported here is compared with the TOTEM results. A difference of about 0.5 mb between the luminosity-dependent and -independent TOTEM results indicates, that potential offsets between the ATLAS and CMS luminosity scales cannot be the only explanation for the total cross-section difference. The recently discovered beam-beam effects lowering the luminosity scale by 1.41 % in ATLAS [75] were not yet known at the time of the TOTEM publication [28]. It is claimed by TOTEM, that the contribution of the CNI term is beyond their experimental sensitivity and thus not included in their fits, but the measurement shown here reveals in contrast, that omitting this term lowers the total cross-section by as much as 0.6 mb. Another source for the difference between the result presented here and by TOTEM could be the beam optics. Where TOTEM uses only the local angle method for t -reconstruction, this would give without further tuning an about 2 mb larger value for the total cross-section than for the effective optics in this measurement. The different reconstruction methods are carefully compared, and consistency at the level of 0.4 mb supports the correctness of the effective optics.

Another possibility is to compare the result for σ_{tot} obtained here with results from experiments at lower energies [23], from TOTEM (combination of all three measurements) and from cosmic ray experiments [83–86]. This is displayed in Figure 7.8, where the total cross-section as a function of the c.m. energy \sqrt{s} is shown. In this figure also the best fit to the

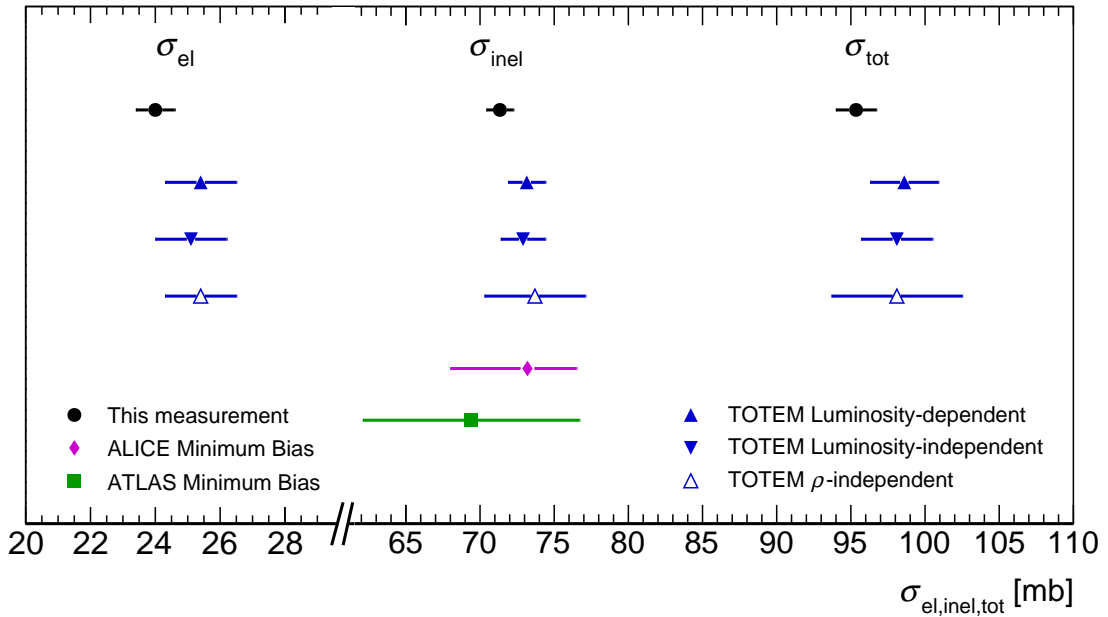


Figure 7.7: Comparison of the measurement of the elastic cross-section σ_{el} , the inelastic cross-section σ_{inel} and the total cross-section σ_{tot} presented here [45] with results from TOTEM [28, 80, 81], ALICE [82] and an early ATLAS measurement [11].

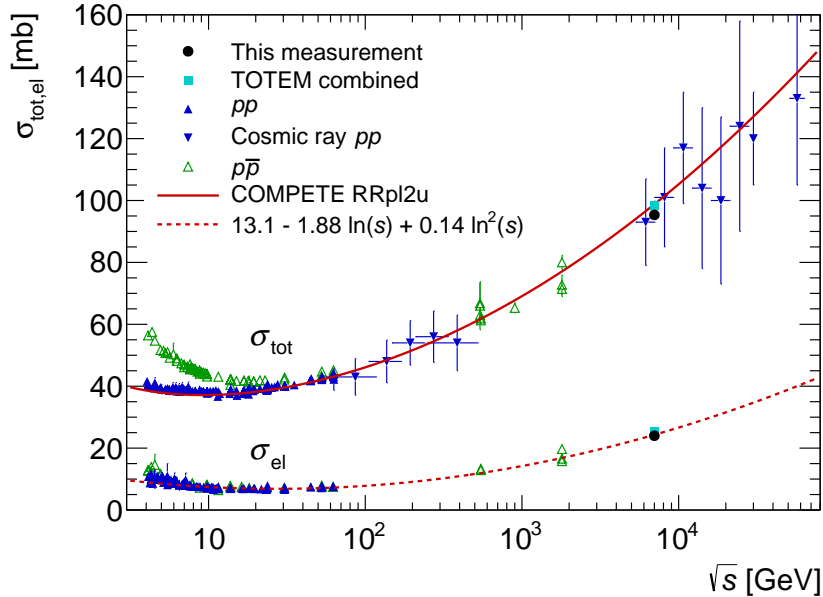


Figure 7.8: Comparison of the measurements of the total cross-section σ_{tot} and the elastic cross-section σ_{el} presented here [45] with other measurements for pp and $p\bar{p}$ from experiments at lower energies [23], from TOTEM [28, 80, 81] at the LHC and from cosmic ray experiments [83–86] as a function of the centre-of-mass energy. The solid red line is a the best fit to the energy evolution of σ_{tot} from the COMPETE Collaboration [20], and the dashed red line is a simple parametrization of the energy evolution of σ_{el} .

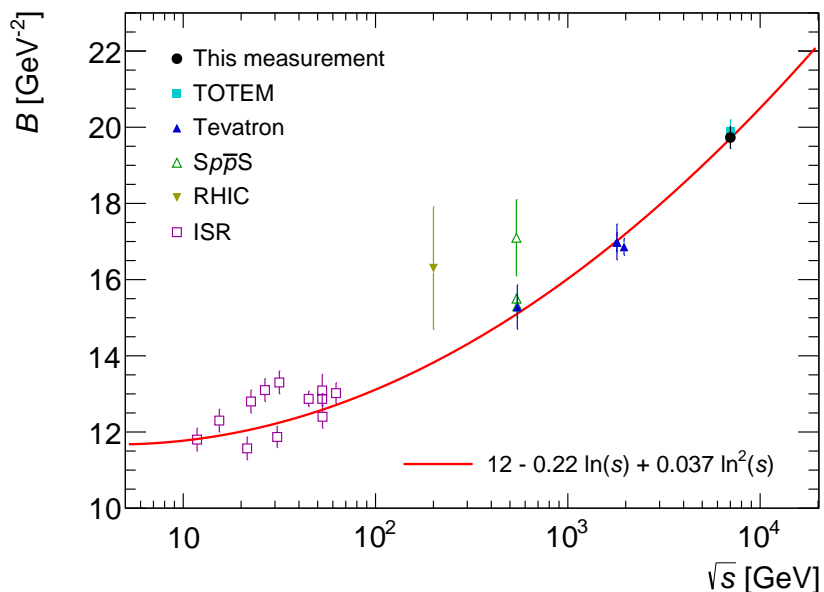


Figure 7.9: Comparison of the measurement of the nuclear slope B presented here [45] with other measurements at the ISR [91–94], the Sp \bar{p} S [95–97], RHIC [98], the Tevatron [16, 99, 100], and from TOTEM [28] at the LHC as a function of the centre-of-mass energy. The red line shows the calculation from Reference [101] with a linear and quadratic term in $\ln s$.

energy evolution of σ_{tot} from the COMPETE Collaboration [20] is shown, which assumes a dependence on s of $\ln^2 s$. The result for σ_{tot} is about 2σ below the COMPETE parametrization, but other models [87–89] prefer a somewhat slower increase of the total cross-section with energy, predicting values below $\sigma_{\text{tot}} = 95$ mb at $\sqrt{s} = 7$ TeV, and hence agree slightly better. Especially the model by Block and Halzen [90], based on a revised version of the eikonal formulation, predicts $\sigma_{\text{tot}} = 95.4 \pm 1.1$ mb, which agrees very well with the measurement. Admittedly, for the time being this cannot answer the question, if the Froissart–Martin bound [9, 10] is saturated by an energy dependence proportional to $\ln^2 s$ or rather $\ln s$.

The result of $B = 19.73 \pm 0.29$ GeV $^{-2}$ reported here is in good agreement with the TOTEM measurement [28] of $B^{\text{TOTEM}} = 19.89 \pm 0.27$ GeV $^{-2}$, which is only about 0.16 GeV $^{-2}$ larger. For both results the total uncertainties are similar, where the beam energy is the dominant contribution, and an offset of the nominal beam energy would only change the slope for ATLAS and TOTEM in the same way. These large values of the nuclear slope confirm, that elastically scattered protons continue to be confined to a gradually narrowing cone as the centre-of-mass energy increases. This can be seen in Figure 7.9, where the nuclear slope B as a function of the c.m. energy \sqrt{s} is shown. The slope is related to the proton radius and as for the total cross-section an increase can be expected at higher energies (compare Section 2.3). However, as outlined in Reference [101] and shown in Figure 7.9 the dependence of B on s as $s \rightarrow \infty$ from ISR to LHC energies is more compatible with a quadratic than a linear term in $\ln s$.

The measured total elastic cross-section of $\sigma_{\text{el}} = 24.0 \pm 0.6$ mb is also in agreement with the TOTEM result from the luminosity-dependent method of $\sigma_{\text{el}}^{\text{TOTEM}} = 25.4 \pm 1.1$ mb within 1.1σ . This is shown in Figure 7.7, where also the TOTEM results from the other two measurements are depicted. The differences in the total cross-section and nuclear slope described above, propagate to the extrapolated elastic cross-section, which results once more in

a smaller value than TOTEM's results. In Figure 7.8 the measured value is compared to measurements from other experiments at lower energies and a simple second order polynomial fit in $\ln s$.

As described in Section 2.3, the ratio $\sigma_{\text{el}}/\sigma_{\text{tot}}$ is a measure of the opacity of the proton, and asymptotically approaches the black disk limit at $\sigma_{\text{el}}/\sigma_{\text{tot}} = 1/2$. The measured value of $\sigma_{\text{el}}/\sigma_{\text{tot}} = 0.252 \pm 0.007$ is clearly below $1/2$ and indicates, that the black disk limit is not yet reached at the LHC. In addition, the result from TOTEM of $\sigma_{\text{el}}/\sigma_{\text{tot}}^{\text{TOTEM}} = 0.257 \pm 0.005$ [28, 81] is very similar to the measurement reported here, despite small differences in the total and elastic cross-sections.

Finally, the result for the inelastic cross-section of $\sigma_{\text{inel}} = 71.34 \pm 0.90$ mb is again smaller than the best TOTEM measurement of $\sigma_{\text{inel}}^{\text{TOTEM}} = 73.15 \pm 1.26$ mb measured via elastic scattering with the luminosity-dependent method, which corresponds to a difference of about 1.2σ . The TOTEM result again does not include the beam energy uncertainty not known at the time of the TOTEM publication. Furthermore, the result can also be compared to direct measurements of the inelastic rate by TOTEM [81], ALICE [82] and an early ATLAS result [11], both based on an analysis of minimum-bias events. The result presented here is comparable with all three values of $\sigma_{\text{inel}}^{\text{TOTEM}} = 73.7 \pm 3.4$ mb, $\sigma_{\text{inel}}^{\text{ALICE}} = 73.2^{+3.3}_{-5.2}$ mb and $\sigma_{\text{inel}}^{\text{ATLAS}} = 69.4 \pm 7.3$ mb. The direct measurements have in general a larger uncertainty because of the model dependence when extrapolating to the unobservable cross-section at low diffractive invariant masses, and therefore the measurement presented here improves considerably the previous ATLAS result. The comparison of these measurements is also shown in Figure 7.7.

8 Summary

In this thesis the measurement of elastic pp scattering $p + p \rightarrow p + p$ at $\sqrt{s} = 7$ TeV at the LHC with the ALFA detector system, one of the ATLAS sub-detectors, is presented. By using the optical theorem the total hadronic cross-section σ_{tot} , the nuclear slope B and several other derived quantities are determined from the measured differential elastic cross-section $d\sigma_{\text{el}}/dt$. The data were taken in 2011 during a special LHC fill with $\beta^* = 90$ m beam optics, where an integrated luminosity of $\mathcal{L} = 80 \mu\text{b}^{-1}$ were accumulated. The analysis uses data-driven methods to determine the event reconstruction efficiency, the background and beam optics parameters, and to tune MC simulations.

A key element of the analysis is a newly developed data-driven method based on a tag-and-probe approach to determine the event reconstruction efficiency directly from the elastic-scattering data without the use of MC simulations. Contributions from different reconstruction cases, where elastic-scattering events are not completely reconstructed in the ALFA detector system, are carefully determined. An important part is the selection of proper elastic-scattering events, and the suppression of different background contributions in the reconstruction cases. A dedicated effort is made for events of the reconstruction case '2/4', where only two out of four detectors contain reconstructed tracks, to evaluate the fraction of elastic-scattering events and to correct for background induced by showers at the thin Roman Pot window and beam screen. Moreover, the event reconstruction efficiency is shown to be independent of the four-momentum transfer squared t . For the two spectrometer arms 1368 and 2457 the event reconstruction efficiency is determined to be

$$\varepsilon_{\text{rec}}(\text{Arm 1368}) = 0.8974 \pm 0.0005 (\text{stat.}) \pm 0.0061 (\text{syst.}), \quad (159)$$

$$\varepsilon_{\text{rec}}(\text{Arm 2457}) = 0.8800 \pm 0.0005 (\text{stat.}) \pm 0.0092 (\text{syst.}), \quad (160)$$

with statistical and systematic uncertainties. The systematic uncertainty is dominated by uncertainties on the determination of the elastic-scattering fraction for the 2/4 case and on different event selection cuts. A small difference between the two spectrometer arms of about 2 % is coming from different detector and trigger tile configurations. Furthermore, a comparison of the data-driven method with a method using MC simulations shows, that the MC approach is insufficient because of a not accurately modelled simulation, and the data-driven method is therefore preferred.

Other important elements are the determination of effective beam optics, which takes into account measurements from the ALFA detector, that are sensitive to ratios of transport matrix elements and calibration uncertainties of the LHC quadrupoles, and a dedicated effort by ATLAS to determine the absolute luminosity and its systematic uncertainties while taking into account the special conditions with a very low average number of interactions per bunch crossing. Further parts of the analysis are the track-based alignment, selection of elastic-scattering events, background determination, acceptance and unfolding corrections determined from MC simulations.

From a fit of the yielded differential elastic cross-section $d\sigma_{\text{el}}/dt$ with the theoretical form using a profile method the total hadronic cross-section is determined to be

$$\sigma_{\text{tot}} = 95.35 \pm 0.38 (\text{stat.}) \pm 1.25 (\text{exp.}) \pm 0.37 (\text{extr.}) \text{ mb}, \quad (161)$$

with statistical, experimental systematic and extrapolation uncertainties related to $-t \rightarrow 0$. The experimental systematic uncertainty is dominated by the uncertainty on the luminosity and the nominal beam energy, where uncertainties associated to beam optics and detector

8 Summary

modelling are less important. At small $|t|$ where the differential elastic-cross section is dominated by the nuclear-scattering amplitude the constant nuclear slope is determined to be

$$B = 19.73 \pm 0.14 \text{ (stat.)} \pm 0.26 \text{ (syst.) GeV}^{-2}, \quad (162)$$

where the dominating systematic uncertainty is the beam energy uncertainty. Among other derived quantities, the elastic cross-section is determined by integrating the fitted parametrization of the nuclear term to be $\sigma_{\text{el}} = 24.00 \pm 0.60 \text{ mb}$, and by subtracting the elastic from the total cross-section the inelastic cross-section is derived to be $\sigma_{\text{inel}} = 71.34 \pm 0.90 \text{ mb}$.

All results are in good agreement with previous measurements from the TOTEM Collaboration, and in addition the result of the inelastic cross-section is a significant improvement of an early ATLAS measurement. The total cross-section and elastic cross-section also agree well with predictions from various models, that favour a dependence of the total cross-section on the centre-of-mass energy squared s of $\ln^2 s$.

Acknowledgement

I would like to thank my supervisor Michael Düren for the opportunity to work in his group as a graduate student. I am thankful for the chances to go to international conferences and different meetings in Germany and Europe.

I would also like to thank my direct supervisor Hasko Stenzel for the help and support on my thesis work, and for always having an open door for questions. The feedback and corrections for this thesis are also highly appreciated.

I enjoyed the work with the ALFA community and especially the help and input on different parts of the analysis from Matthieu, Samah, Tom, Petr, Karl-Heinz, Maciej, Per . . .

The working environment in the AG Düren was constantly very pleasant, and I always enjoyed the casual conversations at lunch or during coffee breaks. I am especially thankful to Avetik for sharing the office with me and for the discussions about football.

I would like to thank the ATLAS Collaboration for the opportunity to experience and work with such a huge experiment at the frontier of particle physics. I learned very much about the operation of ATLAS during the time doing shift work in the control room, which let me even more appreciate the dedication and effort behind this large endeavour. It was an honour to be part of one of the experiments, that found the Higgs boson, even if I did not directly work on any of the analyses connected to it. I also enjoyed the yearly ATLAS-D meetings, which gave me a glimpse of the vast potential of searches and measurements in ATLAS, and the lunches and discussions with the PhD representatives.

Außerdem möchte ich meiner Familie für die Unterstützung während all den Jahren vom Beginn meines Studiums bis heute danken.

Bibliography

- [1] G. Aad et al. (ATLAS Collaboration). “The ATLAS Experiment at the CERN Large Hadron Collider”. *Journal of Instrumentation* 3.08 (2008), S08003. DOI: 10.1088/1748-0221/3/08/S08003 (cit. on pp. 1, 17).
- [2] ATLAS Collaboration. *ATLAS Forward Detectors for Measurement of Elastic Scattering and Luminosity*. Technical Design Report. CERN-LHCC-2008-004. CERN, 2008. URL: <http://cds.cern.ch/record/1095847> (cit. on pp. 1, 22).
- [3] S.R. Amendolia et al. “Measurement of the total proton-proton cross-section at the ISR”. *Phys. Lett. B* 44.1 (1973), pp. 119–124. DOI: 10.1016/0370-2693(73)90316-X (cit. on p. 1).
- [4] U. Amaldi et al. “The energy dependence of the proton-proton total cross-section for centre-of-mass energies between 23 and 53 GeV”. *Phys. Lett. B* 44.1 (1973), pp. 112–118. DOI: 10.1016/0370-2693(73)90315-8 (cit. on p. 1).
- [5] M. Bozzo (UA4 Collaboration). “Measurement of the proton-antiproton total and elastic cross sections at the CERN SPS collider”. *Phys. Lett. B* 147.4-5 (1984), pp. 392–398. DOI: 10.1016/0370-2693(84)90139-4 (cit. on p. 1).
- [6] C. Augier (UA4/2 Collaboration). “Measurement of the proton-antiproton total cross section at the SppS collider by a luminosity dependent method”. *Phys. Lett. B* 344.1-4 (1995), pp. 451–454. DOI: 10.1016/0370-2693(94)01485-U (cit. on p. 1).
- [7] N.A. Amos et al. (E710 Collaboration). “Antiproton–proton elastic scattering at $\sqrt{s} = 1.8$ TeV from $|t| = 0.034$ to 0.65 (GeV/c)²”. *Phys. Lett. B* 247.1 (1990), pp. 127–130. DOI: 10.1016/0370-2693(90)91060-0 (cit. on pp. 1, 10).
- [8] C. Avila et al. (E811 Collaboration). “A measurement of the proton-antiproton total cross section at $\sqrt{s} = 1.8$ TeV”. *Phys. Lett. B* 445.3-4 (1999), pp. 419–422. DOI: 10.1016/S0370-2693(98)01421-X (cit. on pp. 1, 5).
- [9] M. Froissart. “Asymptotic Behavior and Subtractions in the Mandelstam Representation”. *Phys. Rev.* 123.3 (Aug. 1961), pp. 1053–1057. DOI: 10.1103/PhysRev.123.1053 (cit. on pp. 1, 142).
- [10] A. Martin. “Extension of the axiomatic analyticity domain of scattering amplitudes by unitarity-I”. *Il Nuovo Cimento A Series 10* 42.4 (1966), pp. 930–953. DOI: 10.1007/BF02720568 (cit. on pp. 1, 142).
- [11] G. Aad et al. (ATLAS Collaboration). “Measurement of the Inelastic Proton-Proton Cross-Section at $\sqrt{s} = 7$ TeV with the ATLAS Detector”. *Nature Commun.* 2 (2011), p. 463. DOI: 10.1038/ncomms1472 (cit. on pp. 1, 141, 143).
- [12] G. Anelli et al. (TOTEM Collaboration). “The TOTEM Experiment at the CERN Large Hadron Collider”. *Journal of Instrumentation* 3.08 (2008), S08007. DOI: 10.1088/1748-0221/3/08/S08007 (cit. on pp. 1, 14).
- [13] V. Barone and E. Predazzi. *High-Energy Particle Diffraction*. Berlin Heidelberg: Springer, 2002. DOI: 10.1007/978-3-662-04724-8 (cit. on p. 4).
- [14] M. M. Block and R. N. Cahn. “High-energy $p\bar{p}$ and pp forward elastic scattering and total cross sections”. *Rev. Mod. Phys.* 57.2 (Apr. 1985), pp. 563–598. DOI: 10.1103/RevModPhys.57.563 (cit. on pp. 4, 12).

Bibliography

- [15] R. Cahn. “Coulombic-hadronic interference in an eikonal model”. *Z. Phys. C* 15.3 (1982), pp. 253–260. DOI: 10.1007/BF01475009 (cit. on pp. 5, 8, 136).
- [16] F. Abe et al (CDF Collaboration). “Measurement of small angle antiproton-proton elastic scattering at $\sqrt{s} = 546$ and 1800 GeV”. *Phys. Rev. D* 50.9 (Nov. 1994), pp. 5518–5534. DOI: 10.1103/PhysRevD.50.5518 (cit. on pp. 5, 142).
- [17] G. Antchev et al. (TOTEM Collaboration). “First measurement of the total proton-proton cross-section at the LHC energy of $\sqrt{s} = 7$ TeV”. *Europhys. Lett.* 96.2 (2011), p. 21002. DOI: 10.1209/0295-5075/96/21002 (cit. on pp. 5, 7, 8).
- [18] H. A. Bethe. *Ann. Phys.* 3.190 (1958) (cit. on p. 6).
- [19] G. B. West and D. R Yennie. “Coulomb Interference in High-Energy Scattering”. *Phys. Rev.* 172.5 (Aug. 1968), pp. 1413–1422. DOI: 10.1103/PhysRev.172.1413 (cit. on pp. 6, 10, 136, 138).
- [20] J. R. Cudell et al. (COMPETE Collaboration). “Benchmarks for the Forward Observables at RHIC, the Tevatron-Run II, and the LHC”. *Phys. Rev. Lett.* 89.20 (Oct. 2002), p. 201801. DOI: 10.1103/PhysRevLett.89.201801 (cit. on pp. 7, 8, 141, 142).
- [21] W. M. Yao et al. “Review of Particle Physics”. *J. Phys. G: Nucl. Part. Phys.* 33.1 (2006), p. 1. DOI: 10.1088/0954-3899/33/1/001 (cit. on pp. 7, 8).
- [22] A. Alkin, J.R. Cudell, and E. Martynov. “Dispersion Relations for Meson–Proton and Proton–Proton Forward Elastic Scattering”. *Few-Body Systems* 53.1-2 (2012), pp. 87–98. DOI: 10.1007/s00601-012-0306-5 (cit. on pp. 7, 8).
- [23] J. Beringer et al. (Particle Data Group). “Review of Particle Physics”. *Phys. Rev. D* 86.1 (July 2012), p. 010001 (cit. on pp. 7, 8, 140, 141).
- [24] M. J. Menon and P. V. R. G. Silva. “A study on analytic parametrizations for proton–proton cross-sections and asymptotia”. *J. Phys. G: Nucl. Part. Phys.* 40.12 (2013), p. 125001. DOI: 10.1088/0954-3899/40/12/125001 (cit. on pp. 7, 8).
- [25] G.G. Simon et al. “Absolute electron-proton cross sections at low momentum transfer measured with a high pressure gas target system”. *Nucl. Phys. A* 333.3 (1980), pp. 381–391. DOI: 10.1016/0375-9474(80)90104-9 (cit. on p. 8).
- [26] J.C. Bernauer et al. (A1 Collaboration). “Electric and magnetic form factors of the proton”. *Phys. Rev. C* 90.1 (July 2014), p. 015206. DOI: 10.1103/PhysRevC.90.015206 (cit. on pp. 8, 9).
- [27] A.K. Kohara, E. Ferreira, and T. Kodama. “Amplitudes and observables in pp elastic scattering at $\sqrt{s} = 7$ TeV”. *Eur. Phys. J. C* 73.2 (2013), p. 2326. DOI: 10.1140/epjc/s10052-013-2326-9 (cit. on pp. 8, 10, 136, 138).
- [28] G. Antchev et al. (TOTEM Collaboration). “Measurement of proton-proton elastic scattering and total cross-section at $\sqrt{s} = 7$ TeV”. *Europhys. Lett.* 101.2 (2013), p. 21002. DOI: 10.1209/0295-5075/101/21002 (cit. on pp. 8, 136, 140–143).
- [29] M. Abramowitz and I. A. Stegun, eds. *Handbook of Mathematical Functions*. Dover Publications, 1965. URL: <http://people.math.sfu.ca/~cbm/aands/> (cit. on p. 9).
- [30] G. Antchev et al. (TOTEM Collaboration). “Proton-proton elastic scattering at the LHC energy of $\sqrt{s} = 7$ TeV”. *Europhys. Lett.* 95.4 (2011), p. 41001. DOI: 10.1209/0295-5075/95/41001 (cit. on pp. 9, 10).

- [31] M.M. Block and R.N. Cahn. “High-energy predictions for $\bar{p}p$ and pp elastic scattering and total cross-sections”. *Czech. J. Phys.* 40 (1990), pp. 164–175. DOI: 10.1007/BF01597729 (cit. on pp. 10, 138).
- [32] O.V. Selyugin. “Problems of determination of σ_{tot} at the LHC”. *Proceedings of EDS Blois 2013*. 2013. arXiv: 1310.0928v2 (cit. on pp. 10, 138).
- [33] R.J.N. Phillips and V. Barger. “Model independent analysis of the structure in pp scattering”. *Phys. Lett. B* 46.3 (1973), pp. 412–414. DOI: 10.1016/0370-2693(73)90154-8 (cit. on pp. 10, 138).
- [34] D. A. Fagundes et al. “Modeling the elastic differential cross-section at LHC”. *Proceedings of DIS2013*. 2013. arXiv: 1307.0298 (cit. on p. 10).
- [35] C. Bourrely, J. Soffer, and T. Wu. “Determination of the forward slope in pp and $\bar{p}p$ elastic scattering up to LHC energy”. *Eur. Phys. J. C* 71.3 (2011), p. 1601. DOI: 10.1140/epjc/s10052-011-1601-x (cit. on pp. 11, 138).
- [36] J. Haffner. *The CERN accelerator complex*. CERN. 2013. URL: <https://cds.cern.ch/record/1621894> (visited on 06/06/2014) (cit. on p. 13).
- [37] *CERN Website*. 2014. URL: <http://home.web.cern.ch/> (visited on 07/02/2014) (cit. on p. 13).
- [38] J. Caron. *LHC Layout*. CERN. 1997. URL: <https://cds.cern.ch/record/841573> (visited on 06/06/2014) (cit. on p. 14).
- [39] J. Pequeno. *Computer generated image of the whole ATLAS detector*. CERN. 2008. URL: <https://cds.cern.ch/record/1095924> (visited on 06/06/2014) (cit. on p. 16).
- [40] J. Pequeno and P. Schaffner. *An computer generated image representing how ATLAS detects particles*. CERN. 2013. URL: <https://cds.cern.ch/record/1505342> (visited on 06/06/2014) (cit. on p. 16).
- [41] ATLAS Collaboration. *Detector and physics performance: Technical Design Report*. CERN-LHCC-99-014, CERN-LHCC-99-015. CERN, 1999. URL: <http://cdsweb.cern.ch/record/391176>; <http://cds.cern.ch/record/391177> (cit. on p. 17).
- [42] G. Aad et al. (ATLAS Collaboration). “Observation of a new particle in the search for the Standard Model Higgs boson with the ATLAS detector at the LHC”. *Phys. Lett. B* 716.1 (2012), pp. 1–29. DOI: 10.1016/j.physletb.2012.08.020. arXiv: 1207.7214 (cit. on p. 17).
- [43] V. Cindro et al. “The ATLAS Beam Conditions Monitor”. *Journal of Instrumentation* 3.02 (2008), P02004. DOI: 10.1016/0370-2693(90)91060-0 (cit. on p. 22).
- [44] D. Berge et al. *Luminosity Measurement using the ATLAS Minimum Bias Trigger Scintillator System*. Internal ATLAS Note ATL-LUM-INT-2010-004. CERN, Mar. 2010. URL: <https://cds.cern.ch/record/1256521> (cit. on p. 22).
- [45] G. Aad et al. (ATLAS Collaboration). “Measurement of the total cross section from elastic scattering in pp collisions at $\sqrt{s} = 7$ TeV with the ATLAS detector”. *Nucl. Phys. B* 889 (2014), pp. 486–548. DOI: 10.1016/j.nuclphysb.2014.10.019 (cit. on pp. 23, 32, 37, 77, 115, 117, 118, 123, 128, 130, 133, 135–142).
- [46] B. Allongue. *Results from the ALFA test beam campaign in 2009*. Internal ATLAS Note ATL-COM-LUM-2010-031. CERN, Oct. 2010. URL: <https://cds.cern.ch/record/1303329> (cit. on pp. 24, 39, 58, 77).

Bibliography

- [47] F. Anghinolfi et al. “Hadron beam test of a scintillating fibre tracker system for elastic scattering and luminosity measurement in ATLAS”. *Journal of Instrumentation* 07.2 (2007), P07004. arXiv: 0706.3316 (cit. on pp. 24, 39, 77).
- [48] S. Ask et al. “Luminosity measurement at ATLAS—Development, construction and test of scintillating fibre prototype detectors”. *Nucl. Instr. and Meth. A* 568.2 (2006), pp. 588–600. doi: 10.1016/j.nima.2006.07.008 (cit. on pp. 24, 25, 39, 77).
- [49] F. Pfeiffer. “Simulation of the ATLAS ALFA detector in comparison with testbeam data”. Diplomarbeit. Gießen: JLU Gießen, 2010 (cit. on pp. 24, 39, 58).
- [50] C. Joram, H. Stenzel, and A. Braem. *Basic Considerations on the Overlap Detectors of the ATLAS ALFA system*. ATLAS Note ATL-LUM-PUB-2007-002; ATL-COM-LUM-2006-009; CERN-ATL-LUM-PUB-2007-002. CERN, June 2006. URL: <https://cds.cern.ch/record/1002695> (cit. on p. 25).
- [51] M. Medici and S. Jakobsen. *Trigger efficiency for the ALFA detector in 2011*. Internal ATLAS Note ATL-DAPR-INT-2013-001. CERN, Nov. 2013. URL: <https://cds.cern.ch/record/1631718> (cit. on pp. 25, 31, 79).
- [52] S. Jakobsen. “Commissioning of the Absolute Luminosity For ATLAS detector at the LHC”. PhD thesis. Niels Bohr Institut, University of Copenhagen, Dec. 2013. URL: <https://cds.cern.ch/record/1637195> (cit. on pp. 26, 28, 30).
- [53] J. Wenninger. *Energy Calibration of the LHC Beams at 4 TeV*. Accelerators and Technology Sector Report CERN-ATS-2013-040. CERN, May 2013. URL: <http://cds.cern.ch/record/1546734> (cit. on pp. 28, 130).
- [54] G. Baud et al. “Performance Assessment of Wire-Scanners at CERN”. *Proceedings of IBIC2013*. CERN-ACC-2013-0308. Sept. 2013. URL: <http://cds.cern.ch/record/1638354/> (cit. on p. 29).
- [55] S. Jakobsen. *ALFA trigger in 2011*. Internal ATLAS Note ATL-COM-LUM-2012-016. CERN, Dec. 2012. URL: <https://cds.cern.ch/record/1500484> (cit. on p. 30).
- [56] S. Abdel Khalek. “Mesure de la section efficace totale proton-proton avec le détecteur ATLAS au LHC”. PhD thesis. Orsay: Université Paris Sud, 2013. URL: <http://tinyurl.com/m1h7k78> (cit. on pp. 39, 113).
- [57] H. Wiedemann. *Particle Accelerator Physics*. Berlin Heidelberg: Springer, 2007. doi: 10.1007/978-3-540-49045-6 (cit. on p. 43).
- [58] F. Hinterberger. *Physik der Teilchenbeschleuniger und Ionenoptik*. Berlin: Springer, 2008. doi: 10.1007/978-3-540-75282-0 (cit. on p. 43).
- [59] H. Burkhardt et al. “90 m β^* Optics for ATLAS/ALFA”. *Proceedings of IPAC2011*. Vol. C110904. IPAC-2011-TUPZ002. 2011, pp. 1798–1800. URL: <https://accelconf.web.cern.ch/accelconf/IPAC2011/papers/tupz002.pdf> (cit. on pp. 48, 49).
- [60] H. Burkhardt et al. “90 m Optics Studies and Operation in the LHC”. *Proceedings of IPAC2012*. Vol. C1205201. IPAC-2012-MOPPC006. 2012, pp. 130–132. URL: <http://accelconf.web.cern.ch/AccelConf/IPAC2012/papers/MOPPC006.PDF> (cit. on p. 48).
- [61] S. Agostinelli et al. “Geant4 - a simulation toolkit”. *Nucl. Instr. and Meth. A* 506.3 (2003), pp. 250–303. doi: 10.1016/S0168-9002(03)01368-8 (cit. on p. 55).
- [62] J. Allison et al. “Geant4 developments and applications”. *IEEE Trans. Nucl. Sci.* 53.1 (2006), pp. 270–278. doi: 10.1109/TNS.2006.869826 (cit. on p. 55).

- [63] T. Sjostrand, S. Mrenna, and P. Z. Skands. “A Brief Introduction to PYTHIA 8.1”. *Comput. Phys. Commun.* 178 (2008), pp. 852–867. DOI: 10.1016/j.cpc.2008.01.036 (cit. on p. 55).
- [64] T. Sjostrand, S. Mrenna, and P. Z. Skands. “PYTHIA 6.4 Physics and Manual”. *J. High Energy Phys.* 2006.05 (2006), p. 026. DOI: 10.1088/1126-6708/2006/05/026 (cit. on p. 55).
- [65] G. Aad et al. (ATLAS Collaboration). “Performance of the ATLAS Trigger System in 2010”. *Eur. Phys. J. C* 72.1 (2012), p. 1849. DOI: 10.1140/epjc/s10052-011-1849-1 (cit. on p. 55).
- [66] MAD Team. *MAD-X User’s Guide*. BE/ABP Accelerator Beam Physics Group. 2002. URL: <http://mad.web.cern.ch/mad/> (visited on 04/16/2014) (cit. on p. 56).
- [67] F. Schmidt, E. Forest, and E. McIntosh. *Introduction to the polymorphic tracking code: Fibre bundles, polymorphic Taylor types and “Exact tracking”*. CERN-SL-2002-044-AP. KEK-REPORT-2002-3. Geneva: CERN, July 2002. URL: <http://cds.cern.ch/record/573082> (cit. on p. 56).
- [68] P. Calafiura et al. “The athena control framework in production, new developments and lessons learned”. *Computing in High Energy Physics and Nuclear Physics 2004*. 2005, pp. 456–458. URL: <http://cds.cern.ch/record/865624> (cit. on p. 57).
- [69] G. Aad et al. (ATLAS Collaboration). “The ATLAS Simulation Infrastructure”. *Eur. Phys. J.* 70.3 (2010), pp. 823–874. DOI: 10.1140/epjc/s10052-010-1429-9 (cit. on p. 57).
- [70] P. Bussey. *FPTrack Program*. 2012. URL: <http://ppewww.physics.gla.ac.uk/~bussey/FPTRACK/> (visited on 04/16/2014) (cit. on p. 57).
- [71] D. Pelikan, F. Pfeiffer, and H. Stenzel. *Beam transport simulation of elastically scattered protons in Athena*. Internal ATLAS Note ATL-LUM-INT-2010-003. Geneva: CERN, Mar. 2010. URL: <https://cds.cern.ch/record/1248428> (cit. on p. 57).
- [72] G. Aad et al. (ATLAS Collaboration). “Measurement of the muon reconstruction performance of the ATLAS detector using 2011 and 2012 LHC proton-proton collision data”. *Eur. Phys. J. C (submitted)* (2014). arXiv: 1407.3935 (cit. on p. 79).
- [73] B. Malaescu. “An Iterative, Dynamically Stabilized (IDS) Method of Data Unfolding”. *PHYSTAT 2011 Workshop on Statistical Issues Related to Discovery Claims in Search Experiments and Unfolding*. Ed. by H. B. Prosper and L. Lyons. 2011. DOI: 10.5170/CERN-2011-006.271 (cit. on p. 114).
- [74] A. Höcker and V. Kartvelishvili. “SVD approach to data unfolding”. *Nucl. Instrum. Methods A* 372.3 (1996), pp. 469–481. DOI: 10.1016/0168-9002(95)01478-0 (cit. on p. 114).
- [75] G. Aad et al. (ATLAS Collaboration). “Improved luminosity determination in pp collisions at $\sqrt{s} = 7$ TeV using the ATLAS detector at the LHC”. *Eur. Phys. J. C* 73.8, 2518 (2013). DOI: 10.1140/epjc/s10052-013-2518-3 (cit. on pp. 115–118, 140).
- [76] S. van der Meer. *Calibration of the effective beam height in the ISR*. CERN-ISR-PO-68-31; ISR-PO-68-31. CERN, 1968. URL: <http://cds.cern.ch/record/296752> (cit. on p. 116).
- [77] F. James and M. Roos. “Minuit: A System for Function Minimization and Analysis of the Parameter Errors and Correlations”. *Comput. Phys. Commun.* 10 (1975), pp. 343–367. DOI: 10.1016/0010-4655(75)90039-9 (cit. on pp. 124, 131).

- [78] V. Blobel. “Some Comments on χ^2 Minimization Applications”. *Proceedings of PHY-STAT2003*. Vol. eConf C030908. 2003, MOET002. URL: <http://www.slac.stanford.edu/econf/C030908/papers/MOET002.pdf> (cit. on p. 131).
- [79] V.A. Khoze, A.D. Martin, and M.G. Ryskin. “Soft diffraction and the elastic slope at Tevatron and LHC energies: a multi-Pomeron approach”. *Eur. Phys. J. C* 18.1 (2000), pp. 167–179. DOI: 10.1007/s100520000494 (cit. on pp. 131, 136).
- [80] G. Antchev et al. (TOTEM Collaboration). “Luminosity-independent measurements of total, elastic and inelastic cross-sections at $\sqrt{s} = 7$ TeV”. *Europhys. Lett.* 101.2 (2013), p. 21004. DOI: 10.1209/0295-5075/101/21004 (cit. on pp. 136, 140, 141).
- [81] G. Antchev et al. (TOTEM Collaboration). “Measurement of proton-proton inelastic scattering cross-section at $\sqrt{s} = 7$ TeV”. *Europhys. Lett.* 101.2 (2013), p. 21003. DOI: 10.1209/0295-5075/101/21003 (cit. on pp. 140, 141, 143).
- [82] B. Abelev (ALICE Collaboration). “Measurement of inelastic, single- and double-diffraction cross sections in proton–proton collisions at the LHC with ALICE”. *Eur. Phys. J. C* 73.6 (2013), p. 2456. DOI: 10.1140/epjc/s10052-013-2456-0 (cit. on pp. 141, 143).
- [83] R. M. Baltrusaitis et al. “Total Proton-Proton Cross Section at $s^{\frac{1}{2}} = 30$ TeV”. *Phys. Rev. Lett.* 52.16 (1984), pp. 1380–1383. DOI: 10.1103/PhysRevLett.52.1380 (cit. on pp. 140, 141).
- [84] M. Honda et al. “Inelastic cross section for p -air collisions from air shower experiments and total cross section for p - p collisions up to $\sqrt{s} = 24$ TeV”. *Phys. Rev. Lett.* 70.5 (1993), pp. 525–528. DOI: 10.1103/PhysRevLett.70.525 (cit. on pp. 140, 141).
- [85] G. Aielli et al. (ARGO-YBJ Collaboration). “Proton-air cross section measurement with the ARGO-YBJ cosmic ray experiment”. *Phys. Rev. D* 80.9 (2009), p. 092004. DOI: 10.1103/PhysRevD.80.092004 (cit. on pp. 140, 141).
- [86] P. Abreu et al. (Pierre Auger Collaboration). “Measurement of the Proton-Air Cross Section at $\sqrt{s} = 57$ TeV with the Pierre Auger Observatory”. *Phys. Rev. Lett.* 109.6 (2012), p. 062002. DOI: 10.1103/PhysRevLett.109.062002 (cit. on pp. 140, 141).
- [87] M.G. Ryskin, A.D. Martin, and V.A. Khoze. “High-energy strong interactions: from ‘hard’ to ‘soft’”. *Eur. Phys. J. C* 71.4 (2011), p. 1617. DOI: 10.1140/epjc/s10052-011-1617-2 (cit. on p. 142).
- [88] M. M. Block and F. Halzen. “New experimental evidence that the proton develops asymptotically into a black disk”. *Phys. Rev. D* 86.5 (2012), p. 051504. DOI: 10.1103/PhysRevD.86.051504 (cit. on p. 142).
- [89] J. Soffer. “Do we understand elastic scattering up to LHC energies?” *AIP Conference Proceedings*. Vol. 1523. 1. 2013, pp. 115–118. DOI: 10.1063/1.4802130 (cit. on p. 142).
- [90] M. M. Block and F. Halzen. “Forward hadronic scattering at 7 TeV: An update on predictions for the LHC”. *Phys. Rev. D* 83.7 (2011), p. 077901. DOI: 10.1103/PhysRevD.83.077901 (cit. on p. 142).
- [91] G. Barbiellini et al. “Small-angle proton-proton elastic scattering at very high energies ($460 \text{ GeV} < s < 2900 \text{ GeV}^2$)”. *Phys. Lett. B* 39.5 (1972), pp. 663–667. DOI: 10.1016/0370-2693(72)90025-1 (cit. on p. 142).

- [92] U. Amaldi et al. (CERN-Pisa-Rome-Stony Brook Collaboration). “New measurements of proton-proton total cross section at the CERN intersecting storage rings”. *Phys. Lett. B* 62.4 (1976), pp. 460–466. doi: 10.1016/0370-2693(76)90685-7 (cit. on p. 142).
- [93] M. Ambrosio et al. (CERN-Naples-Pisa-Stony Brook Collaboration). “Measurement of elastic scattering in antiproton-proton collisions at 52.8 GeV centre-of-mass energy”. *Phys. Lett. B* 115.6 (1982), pp. 495–502. doi: 10.1016/0370-2693(82)90400-2 (cit. on p. 142).
- [94] N. Amos et al. “Measurement of small-angle antiproton-proton and proton-proton elastic scattering at the CERN intersecting storage rings”. *Nucl. Phys. B* 262.4 (1985), pp. 689–714. doi: 10.1016/0550-3213(85)90511-5 (cit. on p. 142).
- [95] G. Arnison et al. (UA1 Collaboration). “Elastic and total cross section measurement at the CERN proton-antiproton collider”. *Phys. Lett. B* 128.5 (1983), pp. 336–342. doi: 10.1016/0370-2693(83)90271-X (cit. on p. 142).
- [96] M. Bozzo et al. (UA4 Collaboration). “Low momentum transfer elastic scattering at the CERN proton-antiproton collider”. *Phys. Lett. B* 147.4-5 (1984), pp. 385–391. doi: 10.1016/0370-2693(84)90138-2 (cit. on p. 142).
- [97] C. Augier et al. (UA4/2 Collaboration). “A precise measurement of the real part of the elastic scattering amplitude at the $S\bar{p}pS$ ”. *Phys. Lett. B* 316.2-3 (1993), pp. 448–454. doi: 10.1016/0370-2693(93)90350-Q (cit. on p. 142).
- [98] S. Bültmann et al. (PP2PP Collaboration). “First measurement of proton-proton elastic scattering at RHIC”. *Phys. Lett. B* 579.3-4 (2004), pp. 2453–250. doi: 10.1016/j.physletb.2003.11.023 (cit. on p. 142).
- [99] N. A. Amos et al. (E710 Collaboration). “Measurement of ρ , the ratio of the real to the imaginary part of the $\bar{p}p$ forward elastic-scattering amplitude, at $\sqrt{s} = 1.8$ TeV”. *Phys. Rev. Lett.* 68.16 (1992), pp. 2433–2436. doi: 10.1103/PhysRevLett.68.2433 (cit. on p. 142).
- [100] V. M. Abazov et al. (D0 Collaboration). “Measurement of the differential cross section $d\sigma/dt$ in elastic $p\bar{p}$ scattering at $\sqrt{s} = 1.96$ TeV”. *Phys. Rev. D* 86.1 (2012), p. 012009. doi: 10.1103/PhysRevD.86.012009 (cit. on p. 142).
- [101] V. A. Schegelsky and M. G. Ryskin. “Diffraction cone shrinkage speed up with the collision energy”. *Phys. Rev. D* 85.9 (May 2012), p. 094024. doi: 10.1103/PhysRevD.85.094024 (cit. on p. 142).

A Appendix

This appendix includes some additional histograms and tables mainly for the event reconstruction efficiency, that complete the figures and results shown in the respective sections. In appendix A.1 additional distributions of spectrometer arm 1368 for the characteristics of elastic-scattering events described in Section 6.1.4 are shown. In appendices A.2, A.3, A.4, A.5 and A.6 the complete set of position and total multiplicity distributions for the event reconstruction efficiency described in Section 6.3 are shown. And in appendix A.7 tables with detailed results for the differential and total cross-section and nuclear slope, referred to in Section 7, are shown.

A.1 Additional plots for golden elastic-scattering events

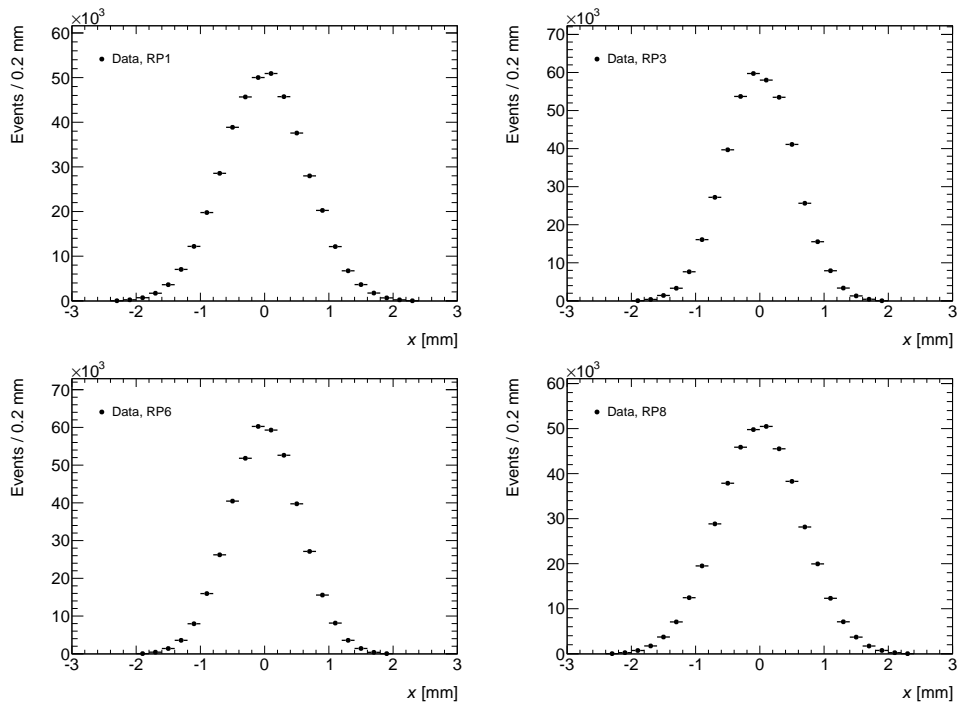


Figure A.1: Horizontal position distributions for elastic-scattering events after cuts in spectrometer arm 1368 on A-Side (top row) and C-Side (bottom row).

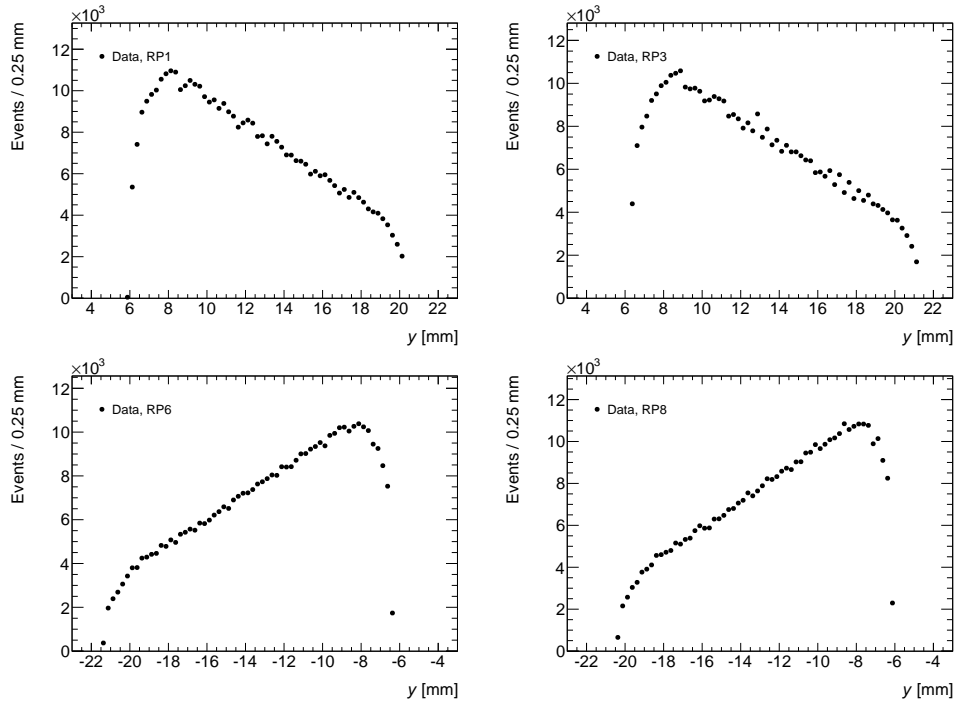


Figure A.2: Vertical position distributions for elastic-scattering events after cuts in spectrometer arm 1368 on A-Side (top row) and C-Side (bottom row).

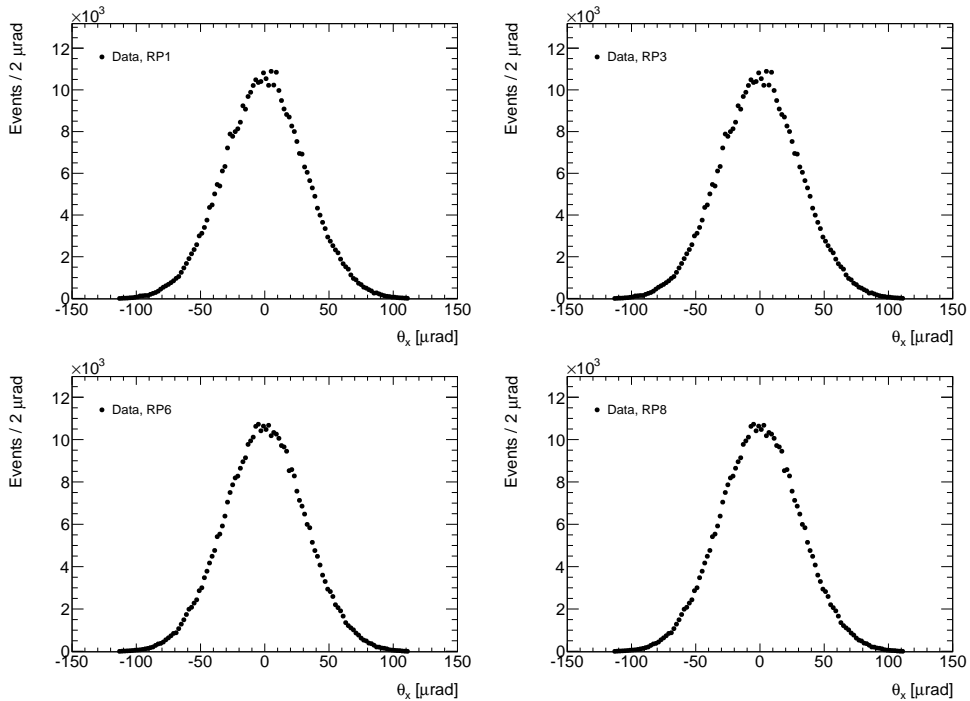


Figure A.3: Horizontal local angle distributions for elastic-scattering events after cuts in spectrometer arm 1368 on A-Side (top row) and C-Side (bottom row).

A.1 Additional plots for golden elastic-scattering events

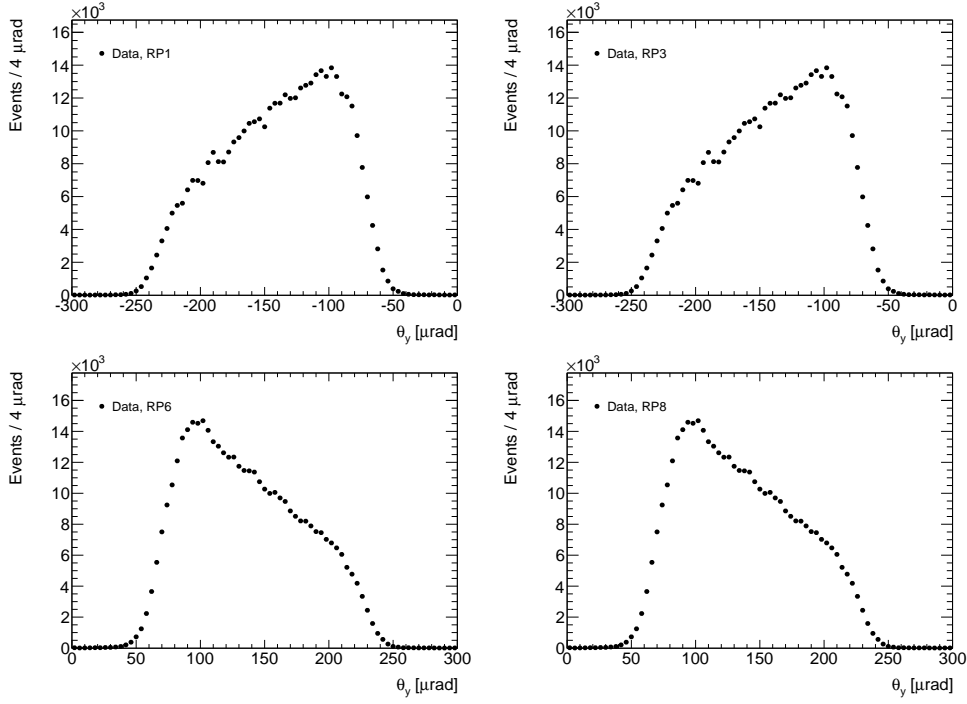


Figure A.4: Vertical local angle distributions for elastic-scattering events after cuts in spectrometer arm 1368 on A-Side (top row) and C-Side (bottom row).

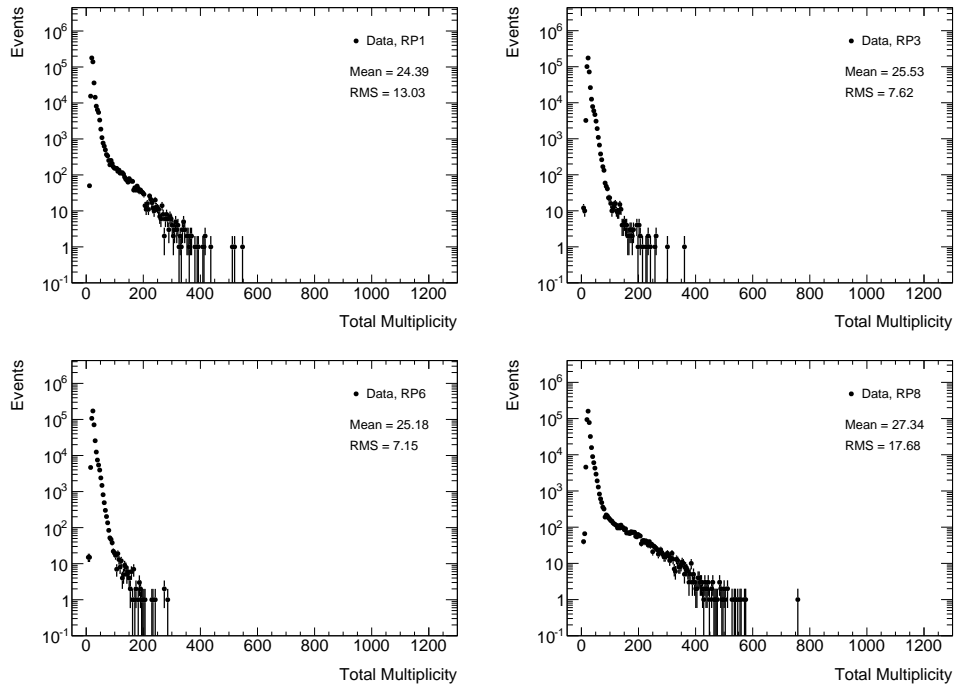


Figure A.5: Total multiplicity distributions for elastic-scattering events after cuts in spectrometer arm 1368 on A-Side (top row) and C-Side (bottom row).

A.2 Additional plots for reconstruction case 3/4

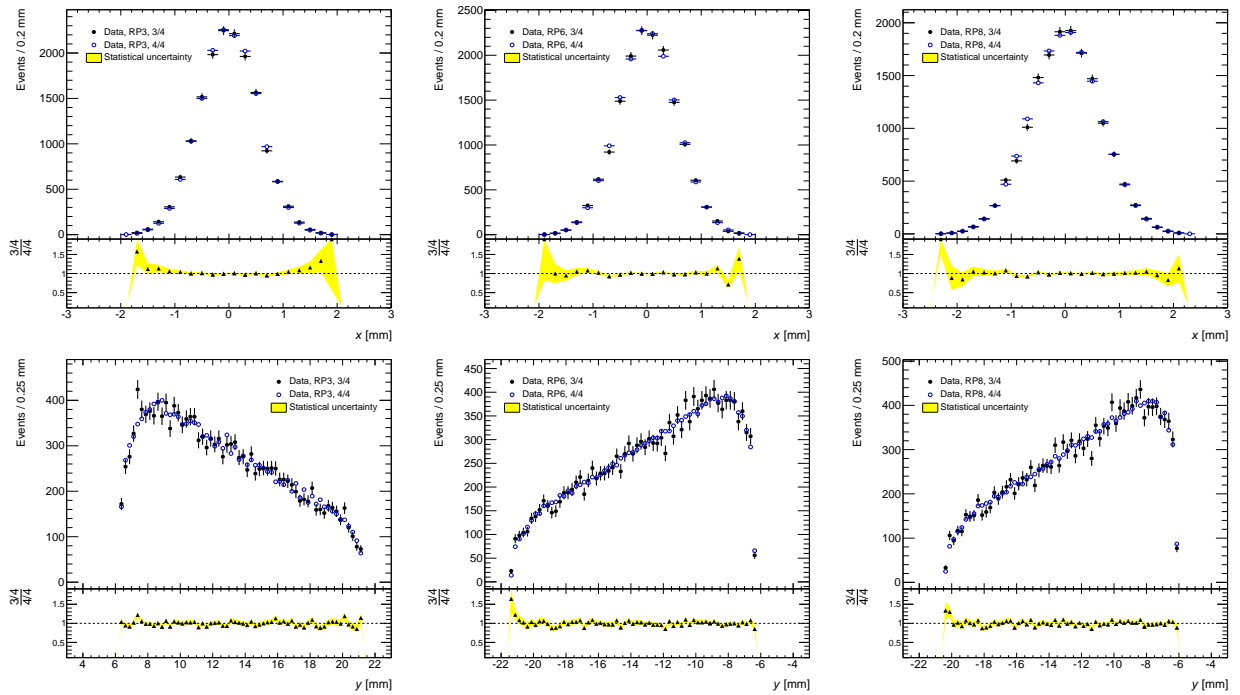


Figure A.6: Position distributions of case 3/4, sub-case 368 where no track was reconstructed in RP1.

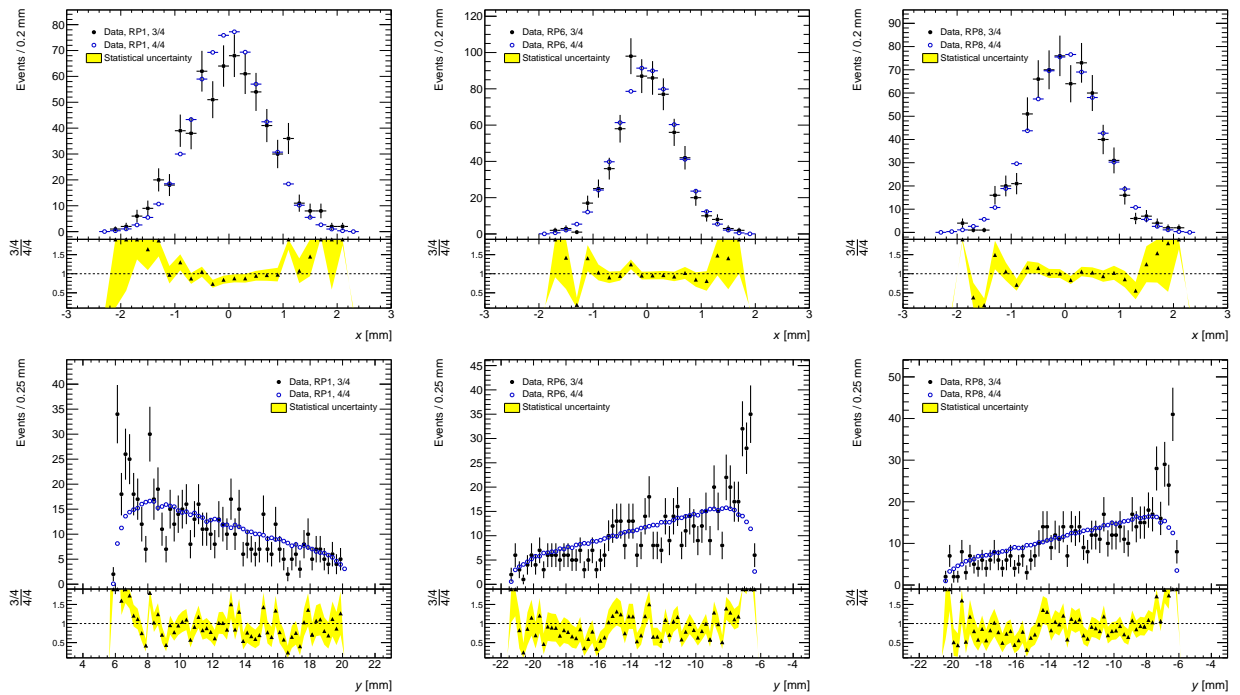


Figure A.7: Position distributions of case 3/4, sub-case 168 where no track was reconstructed in RP3.

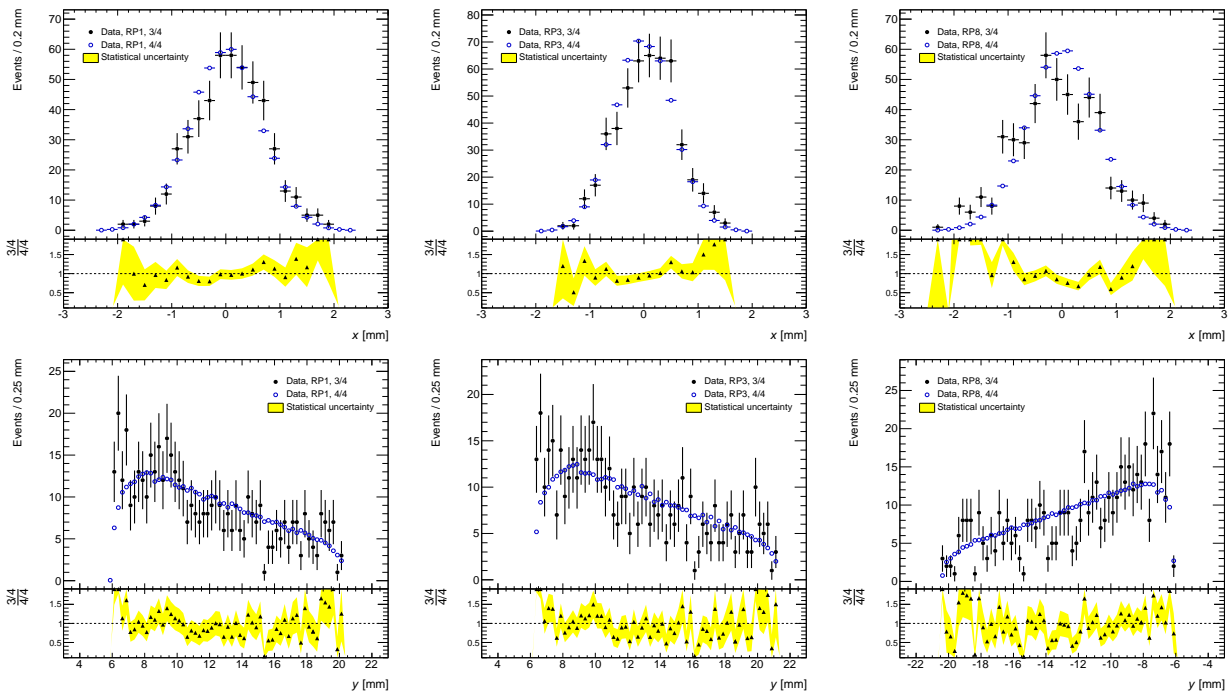


Figure A.8: Position distributions of case 3/4, sub-case 138 where no track was reconstructed in RP6.

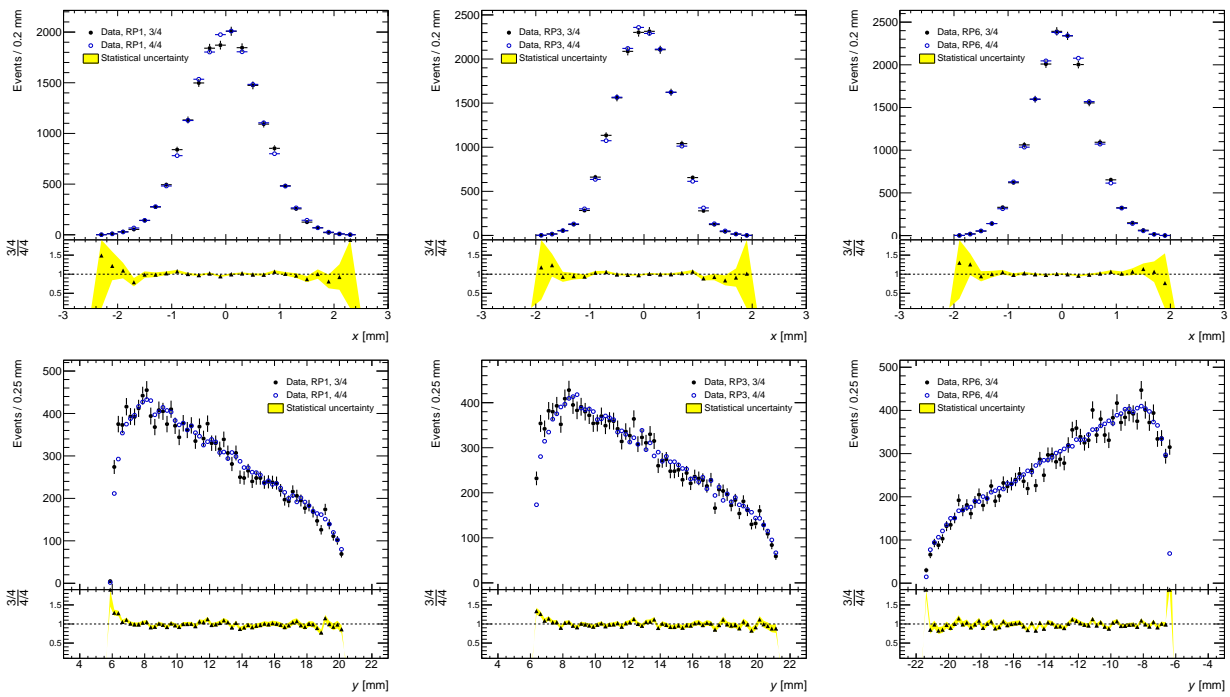


Figure A.9: Position distributions of case 3/4, sub-case 136 where no track was reconstructed in RP8.

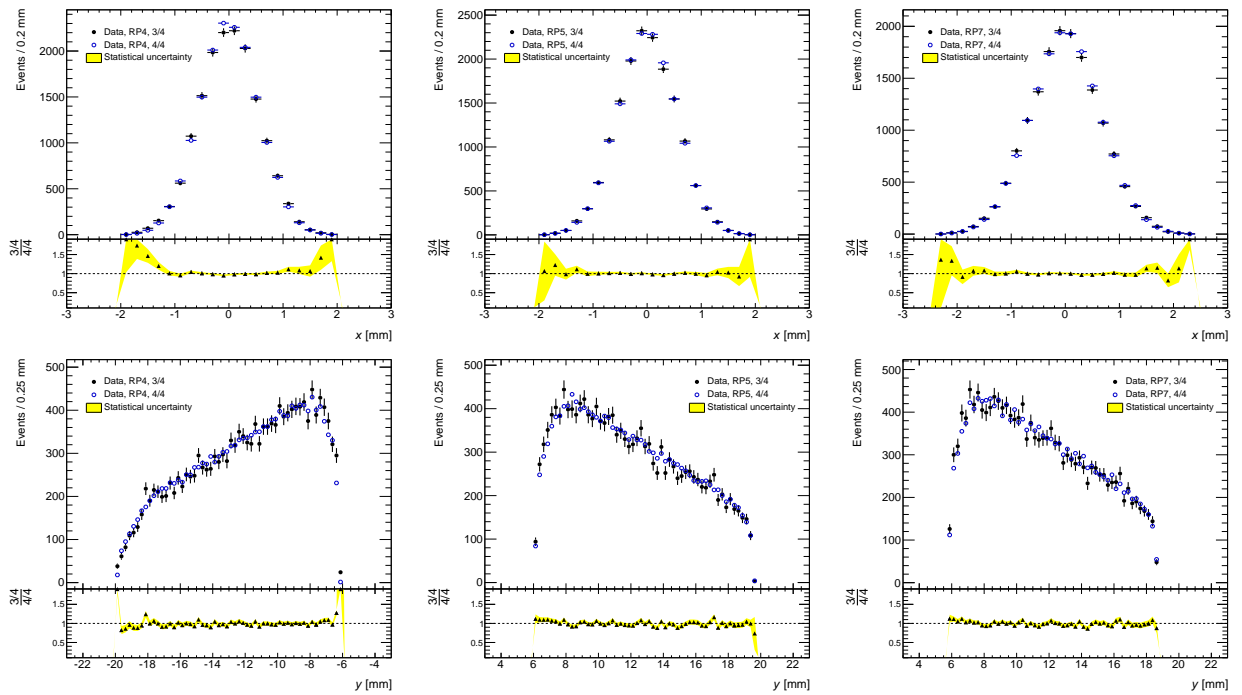


Figure A.10: Position distributions of case 3/4, sub-case 457 where no track was reconstructed in RP2.

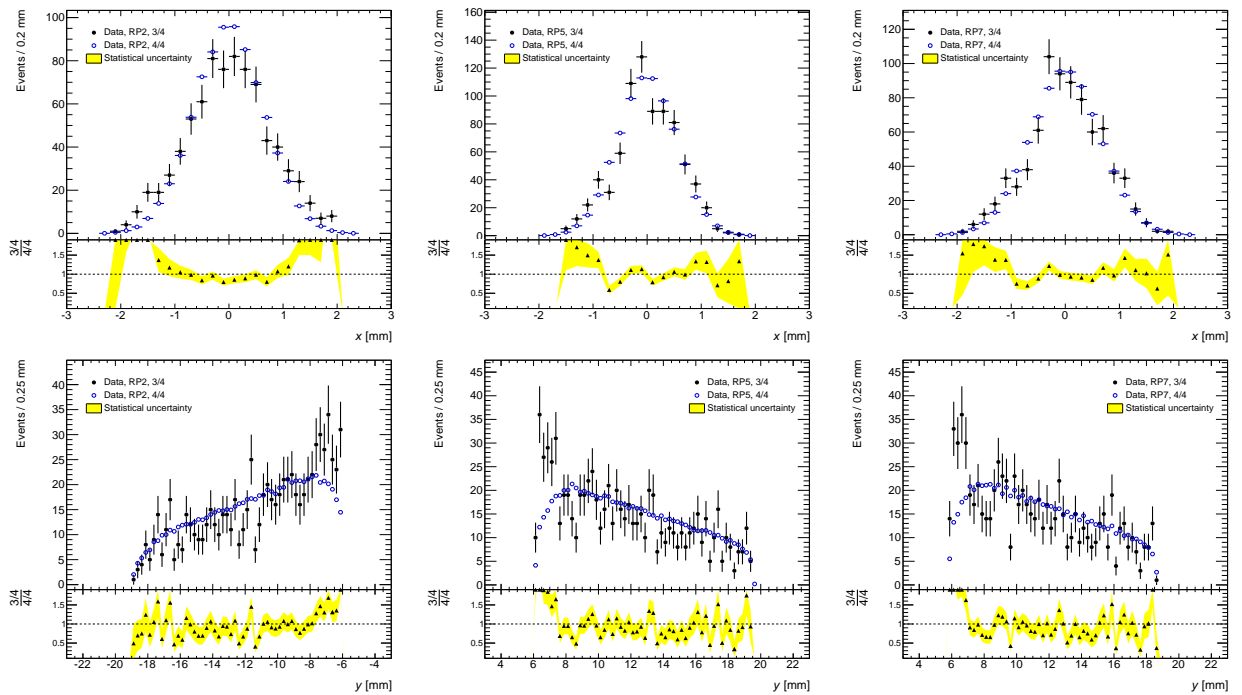


Figure A.11: Position distributions of case 3/4, sub-case 257 where no track was reconstructed in RP4.

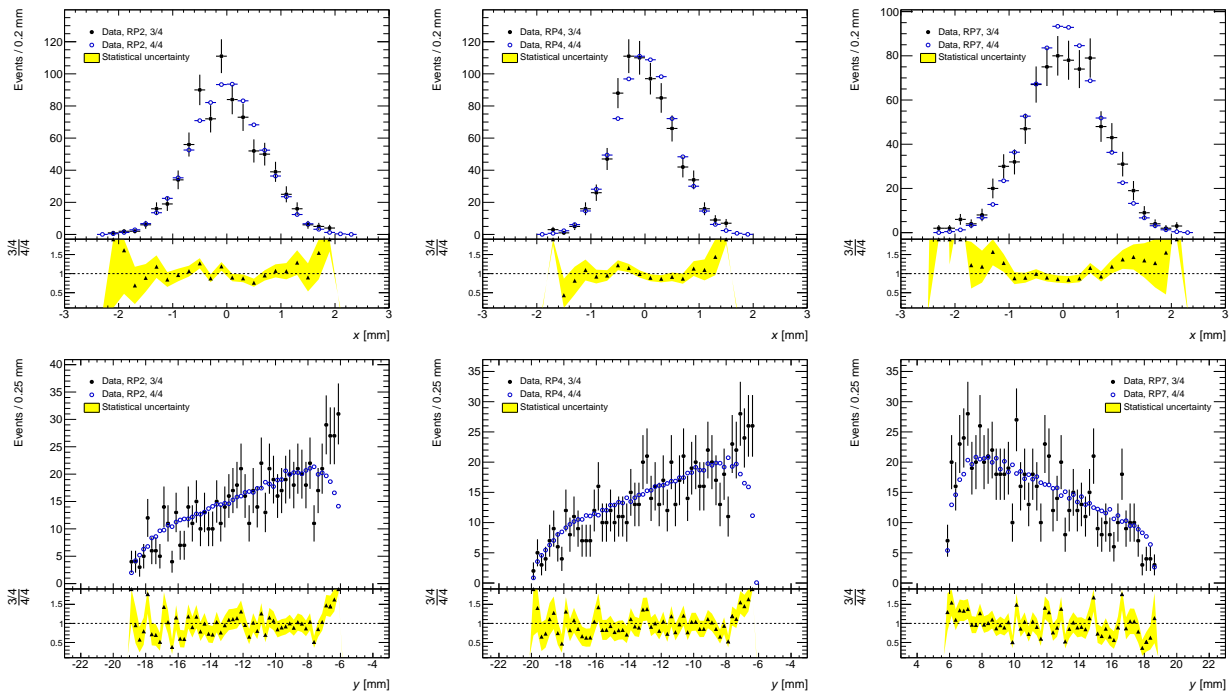


Figure A.12: Position distributions of case 3/4, sub-case 247 where no track was reconstructed in RP5.

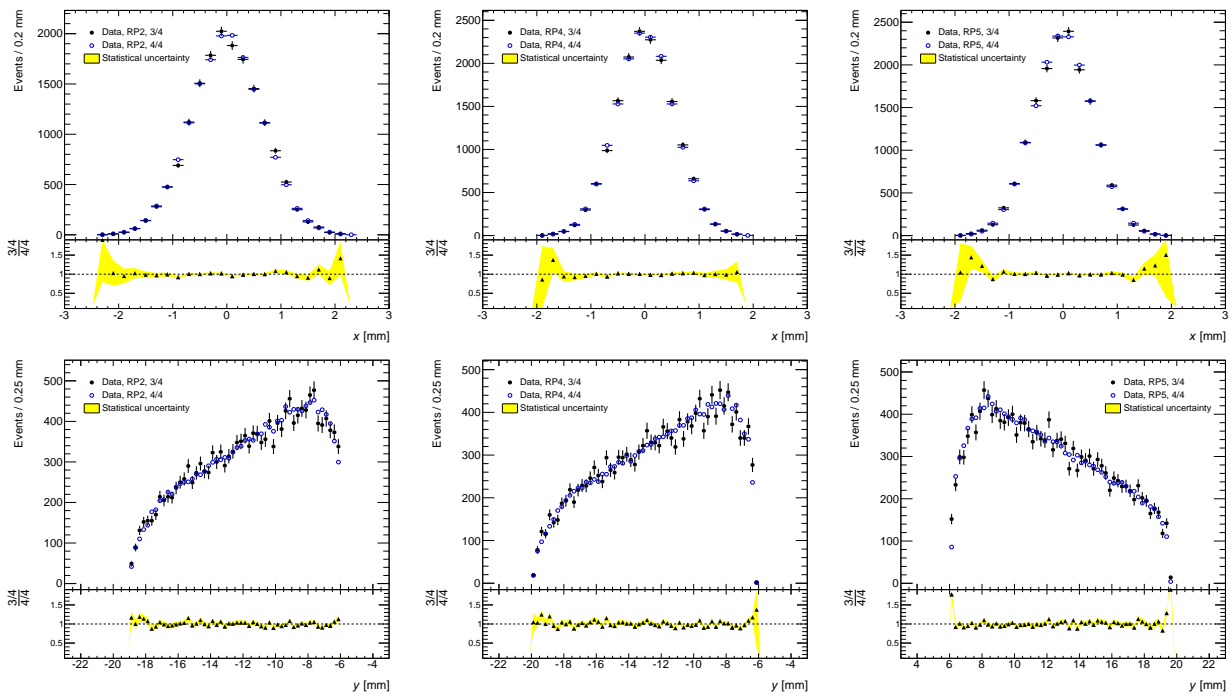


Figure A.13: Position distributions of case 3/4, sub-case 245 where no track was reconstructed in RP7.

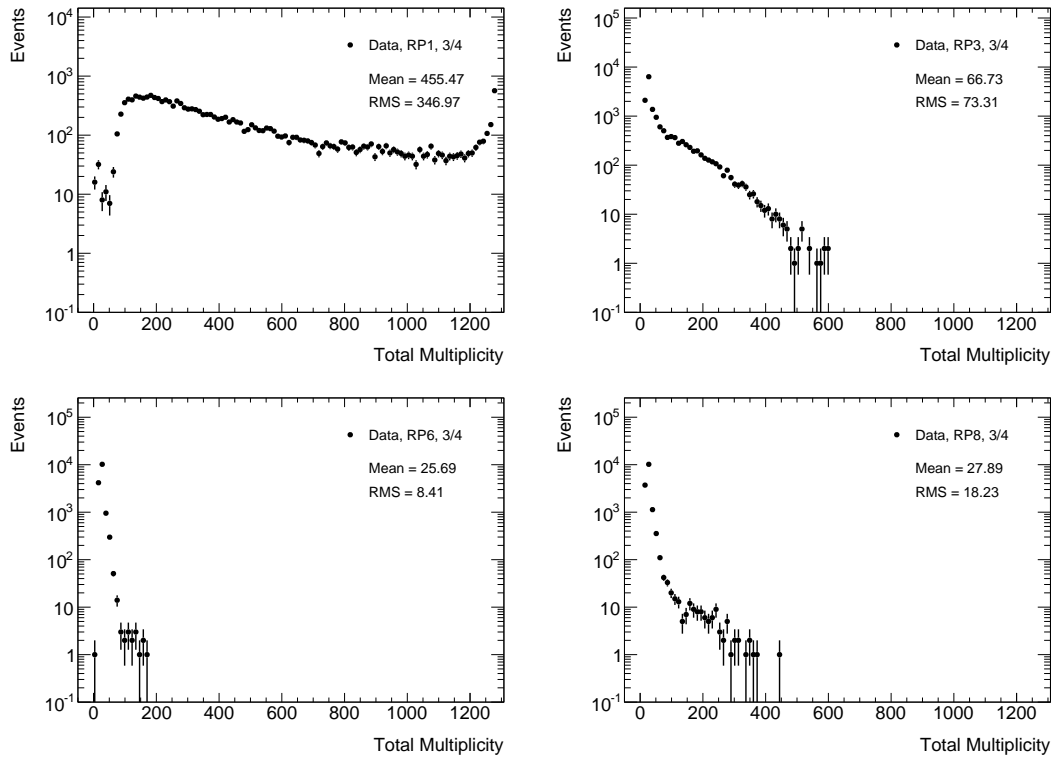


Figure A.14: Total multiplicity distributions of case 3/4, sub-case 368 where no track was reconstructed in RP1.

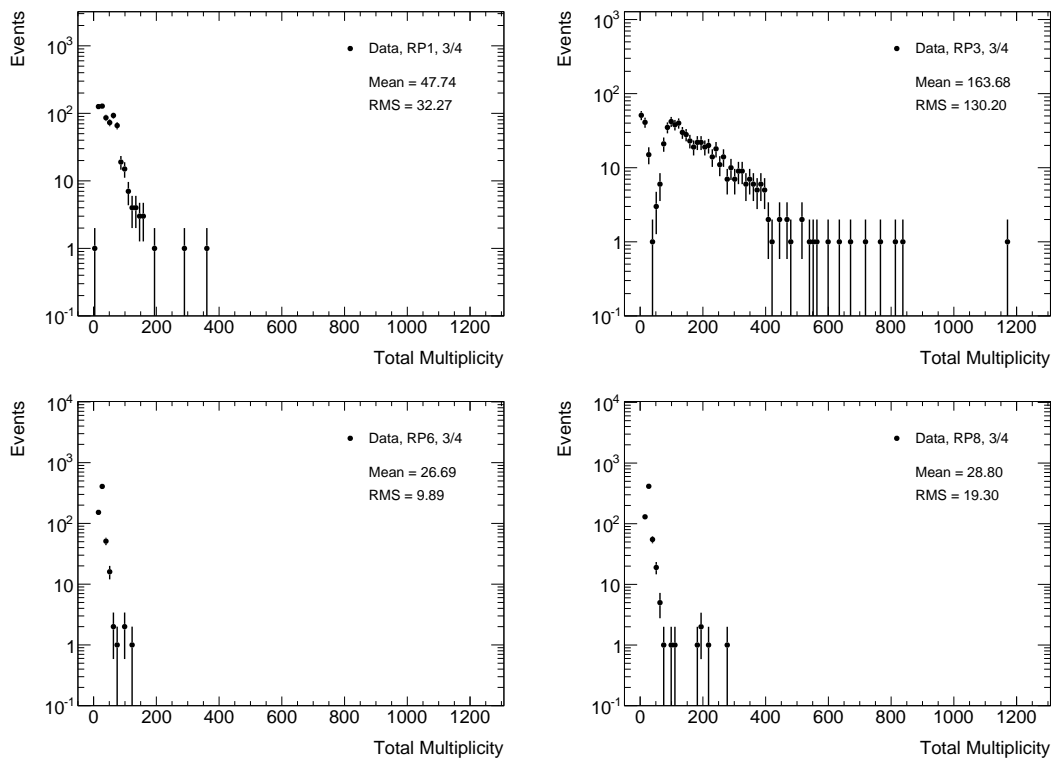


Figure A.15: Total multiplicity distributions of case 3/4, sub-case 168 where no track was reconstructed in RP3.

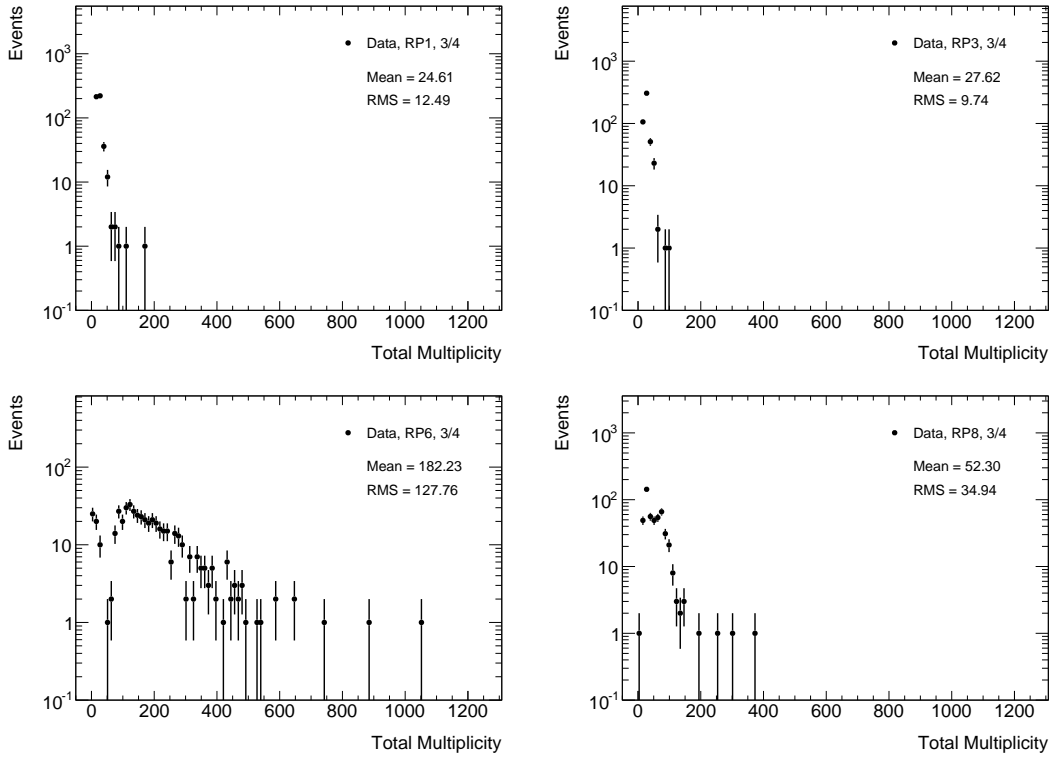


Figure A.16: Total multiplicity distributions of case 3/4, sub-case 138 where no track was reconstructed in RP6.

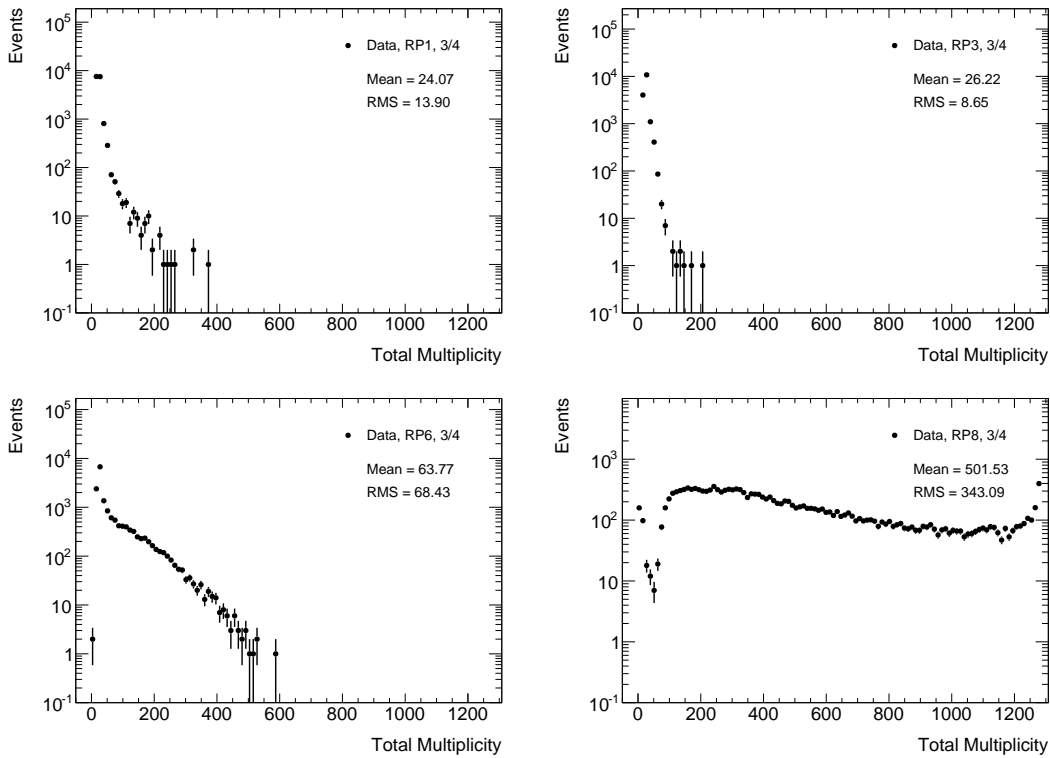


Figure A.17: Total multiplicity distributions of case 3/4, sub-case 136 where no track was reconstructed in RP8.

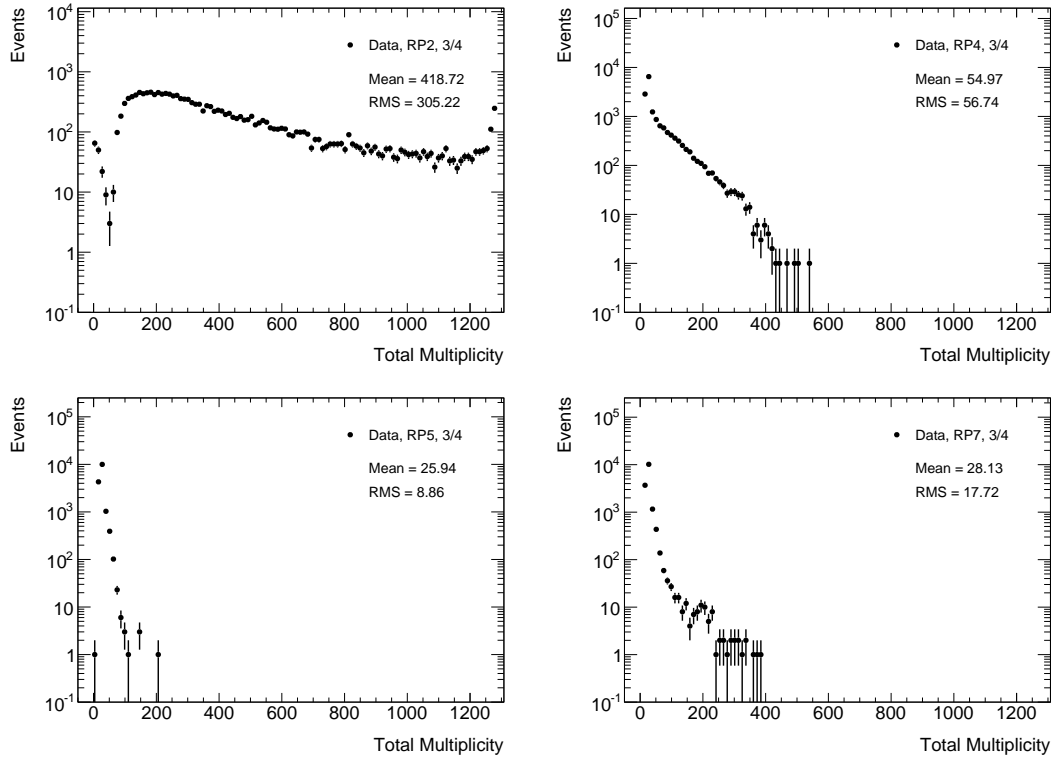


Figure A.18: Total multiplicity distributions of case 3/4, sub-case 457 where no track was reconstructed in RP2.

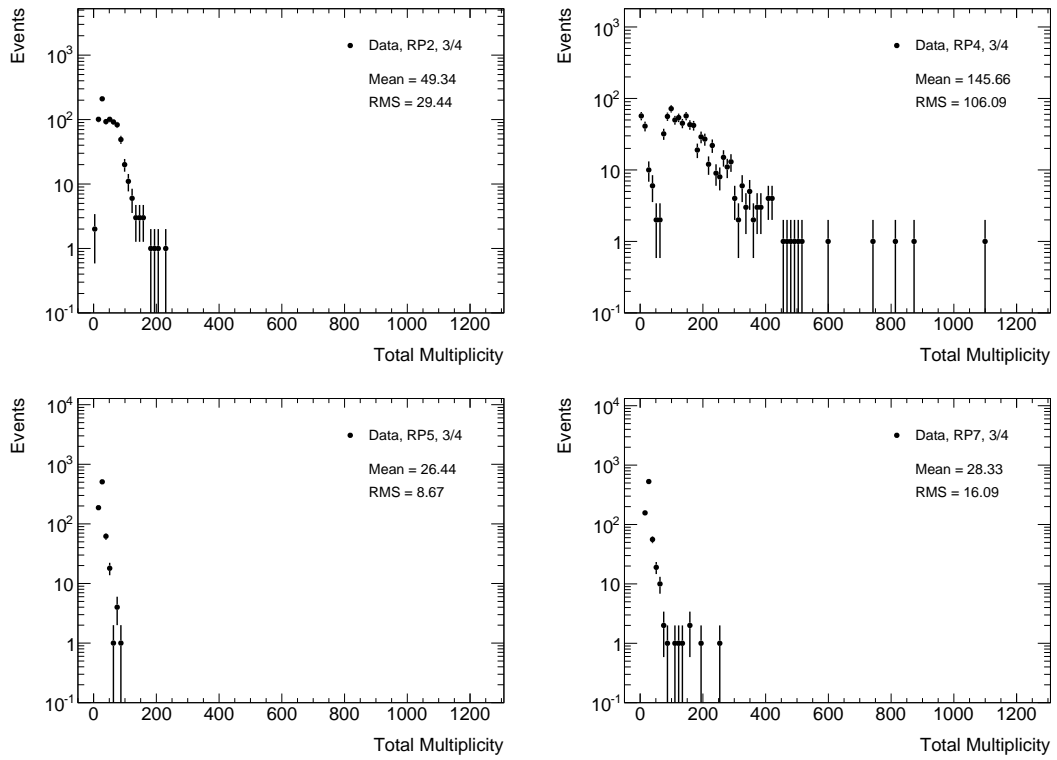


Figure A.19: Total multiplicity distributions of case 3/4, sub-case 257 where no track was reconstructed in RP4.

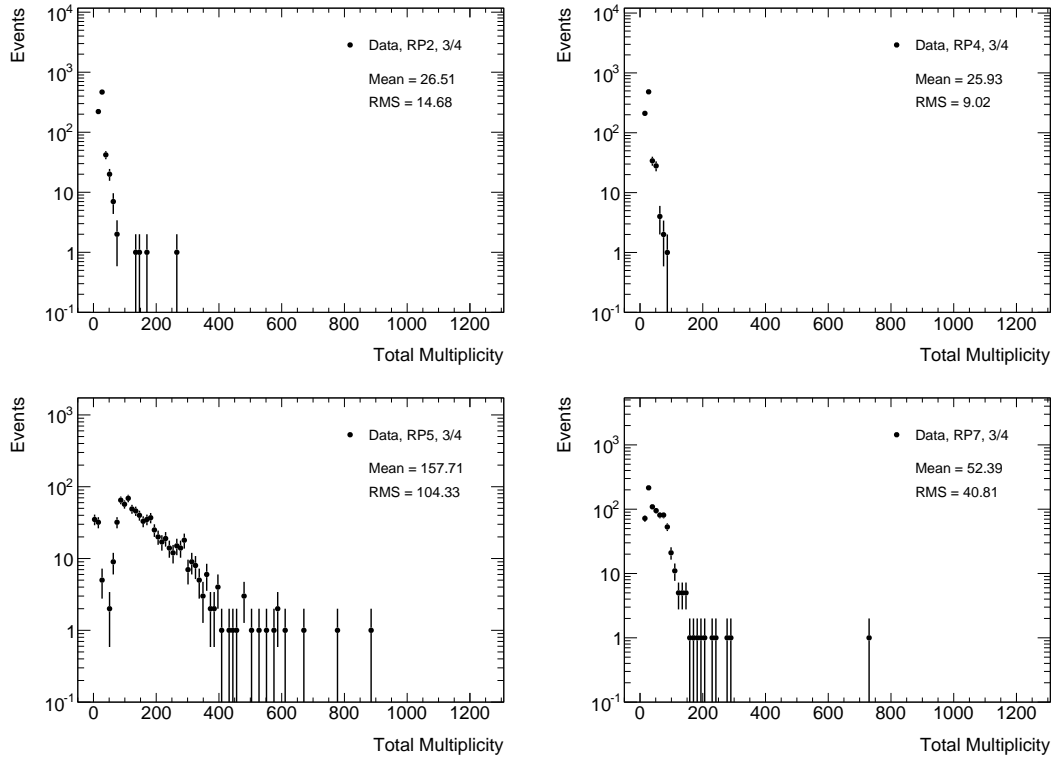


Figure A.20: Total multiplicity distributions of case 3/4, sub-case 247 where no track was reconstructed in RP5.

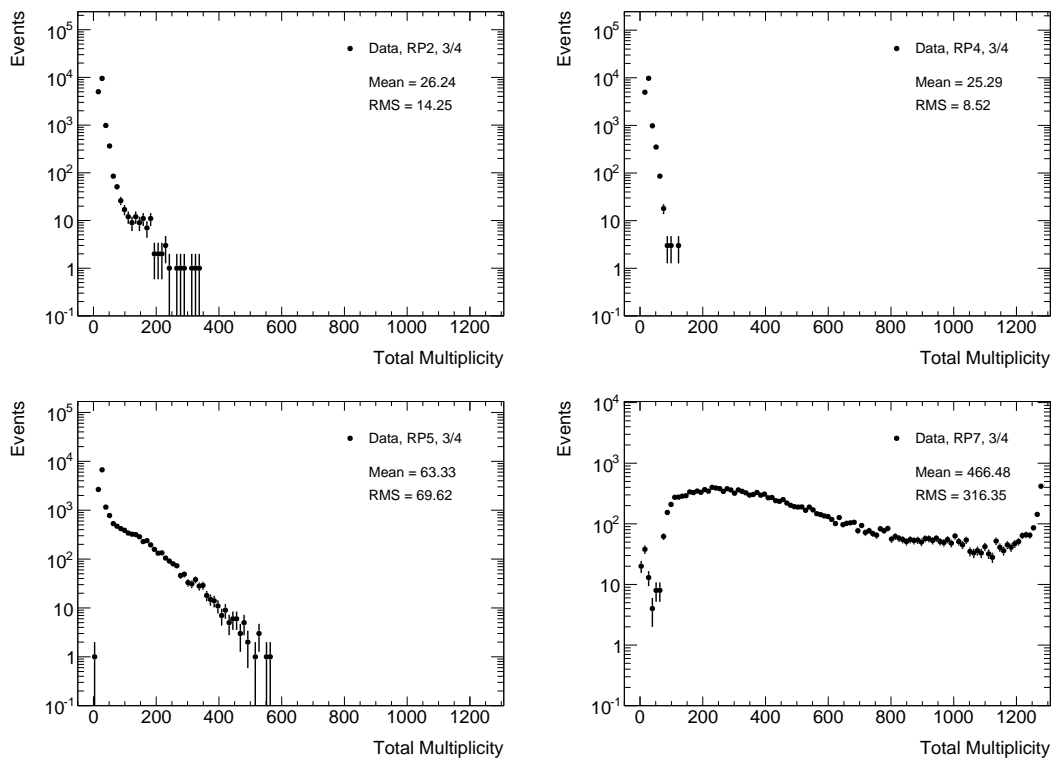


Figure A.21: Total multiplicity distributions of case 3/4, sub-case 245 where no track was reconstructed in RP7.

A.3 Additional plots for reconstruction case 2/4

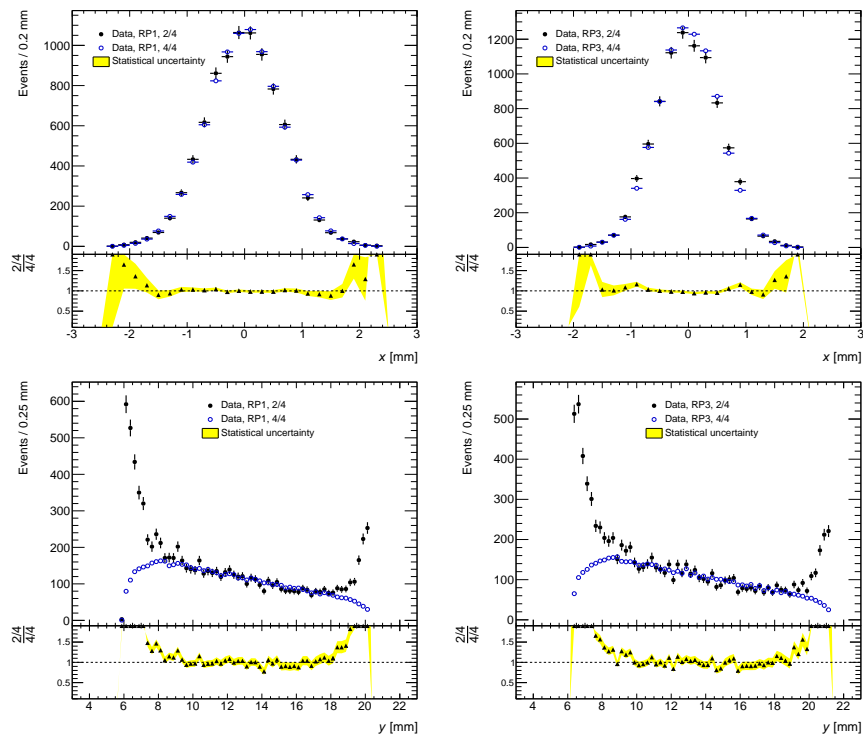


Figure A.22: Position distributions of case 2/4, sub-case 13.

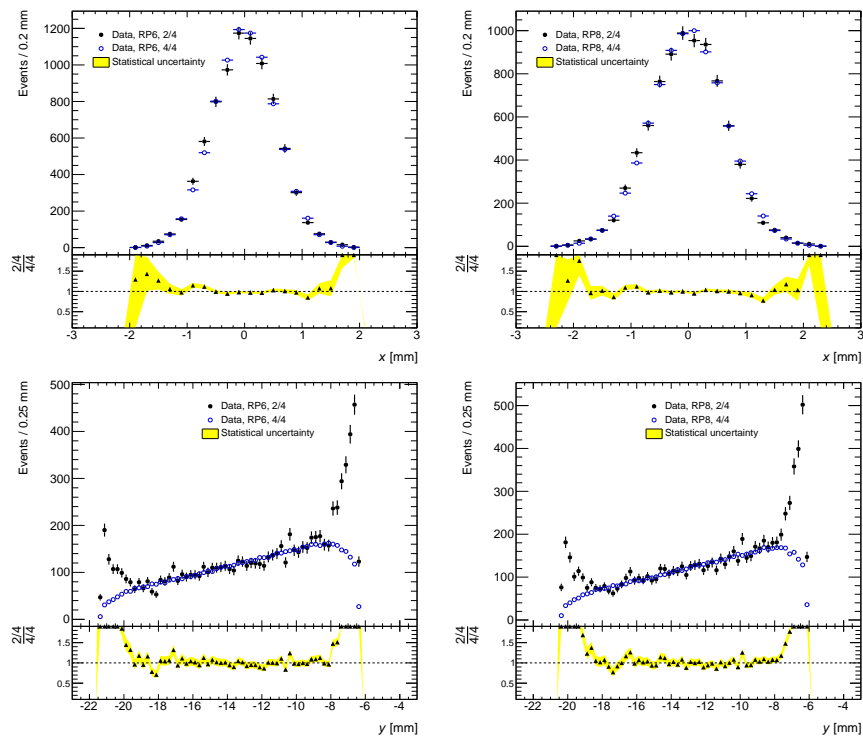


Figure A.23: Position distributions of case 2/4, sub-case 68.

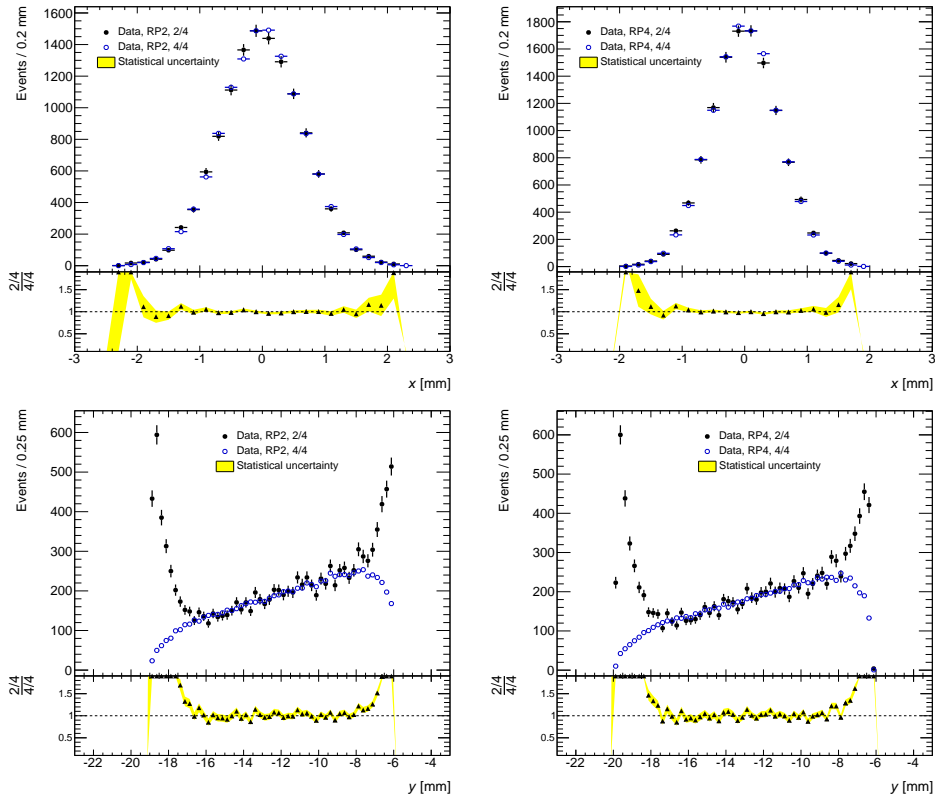


Figure A.24: Position distributions of case 2/4, sub-case 24.

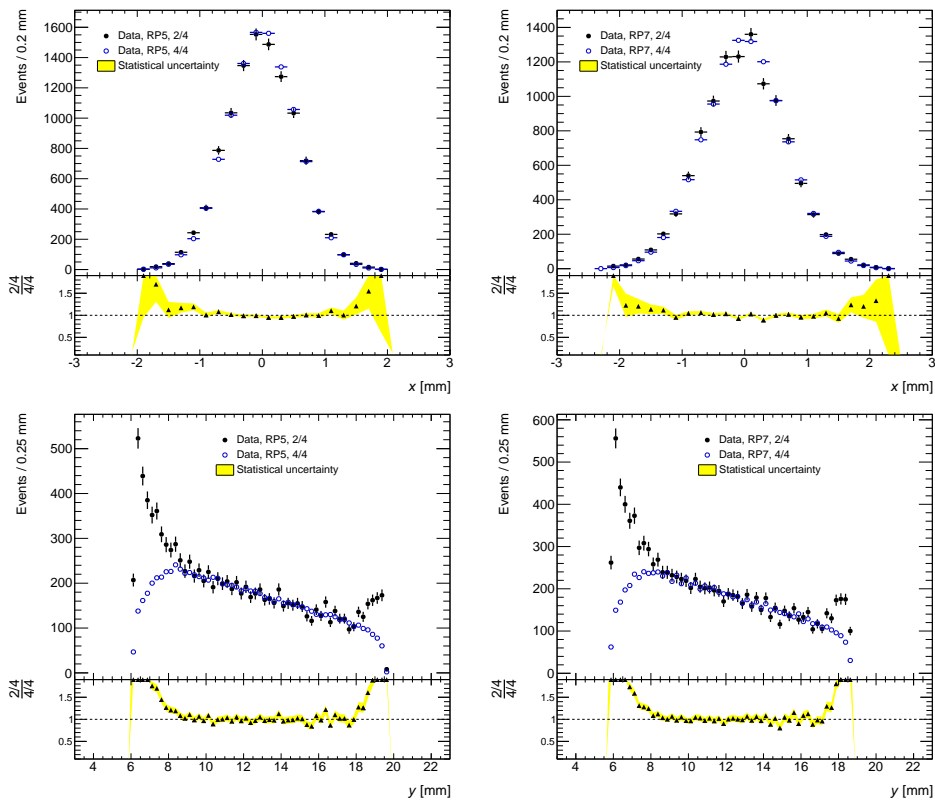


Figure A.25: Position distributions of case 2/4, sub-case 68.

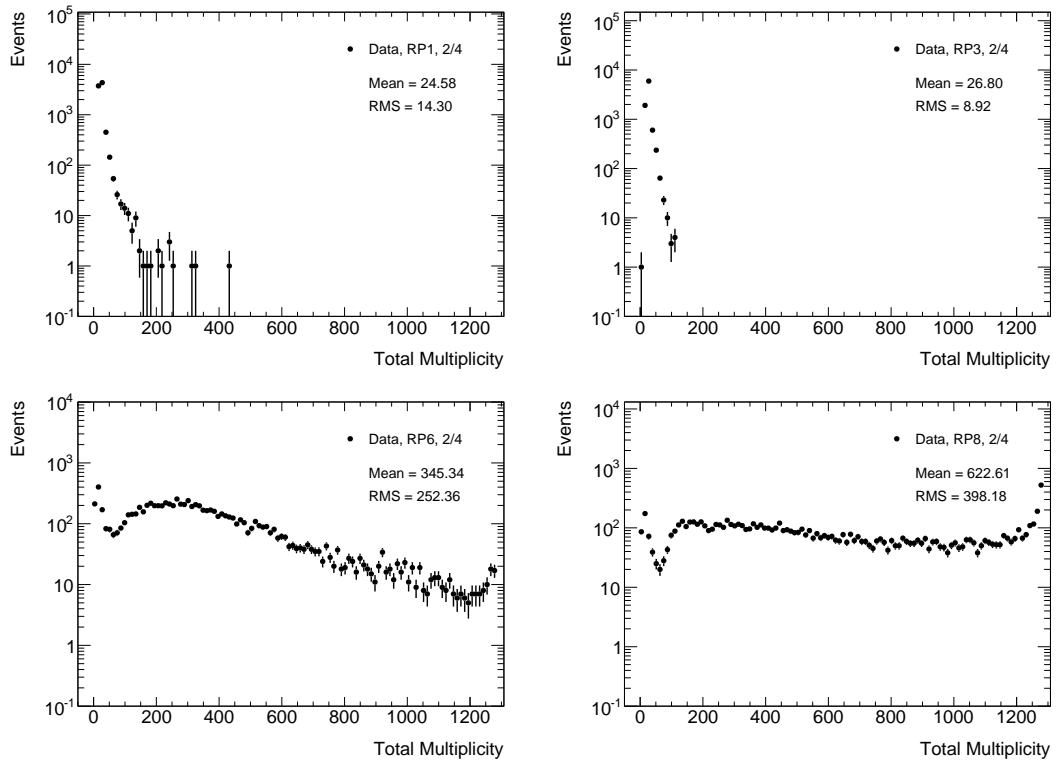


Figure A.26: Total multiplicity distributions of case 2/4, sub-case 13 where no track was reconstructed in RP6 and RP8.

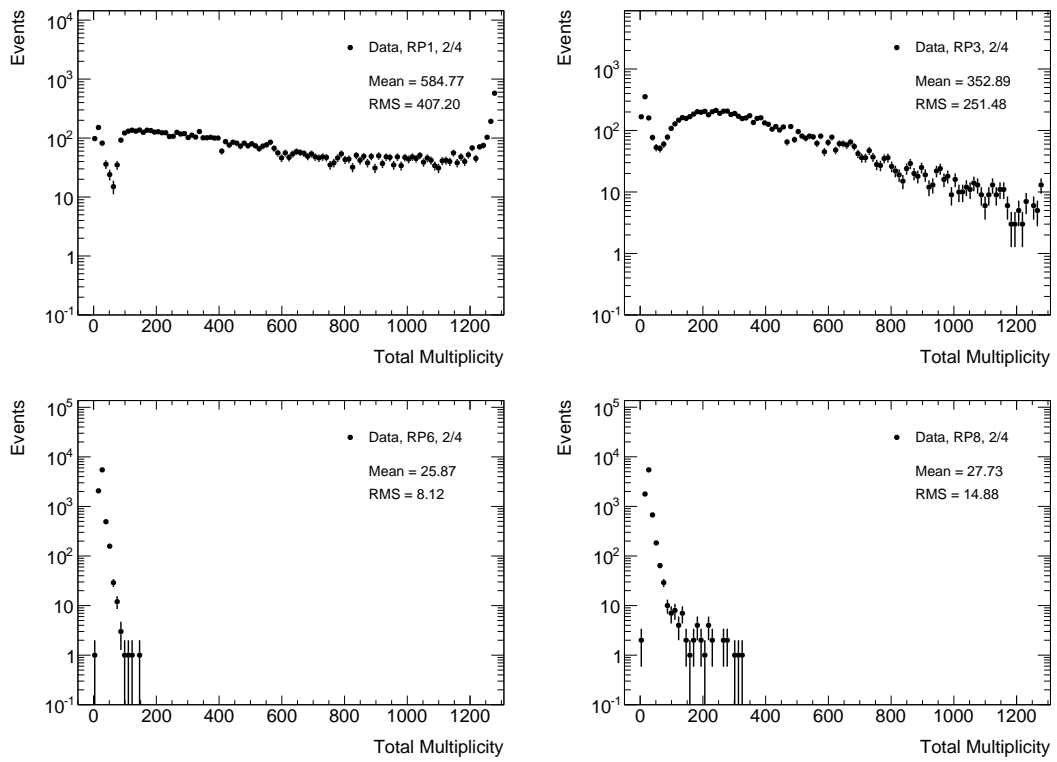


Figure A.27: Total multiplicity distributions of case 2/4, sub-case 68 where no track was reconstructed in RP1 and RP3.

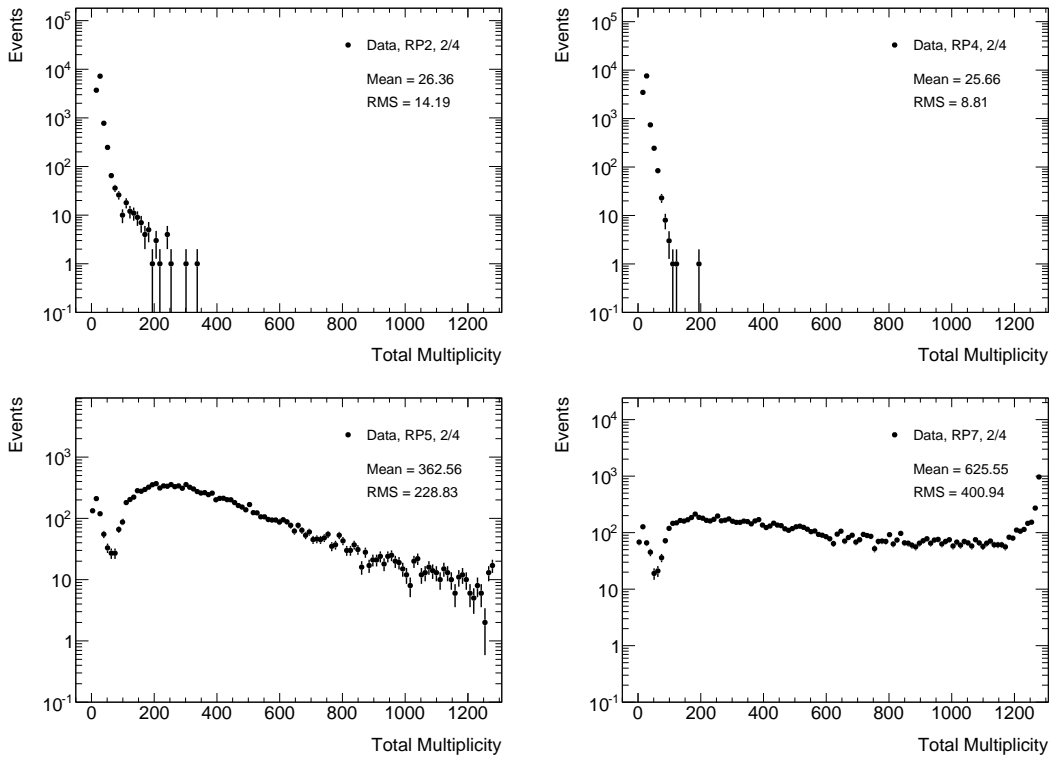


Figure A.28: Total multiplicity distributions of case 2/4, sub-case 24 where no track was reconstructed in RP5 and RP7.

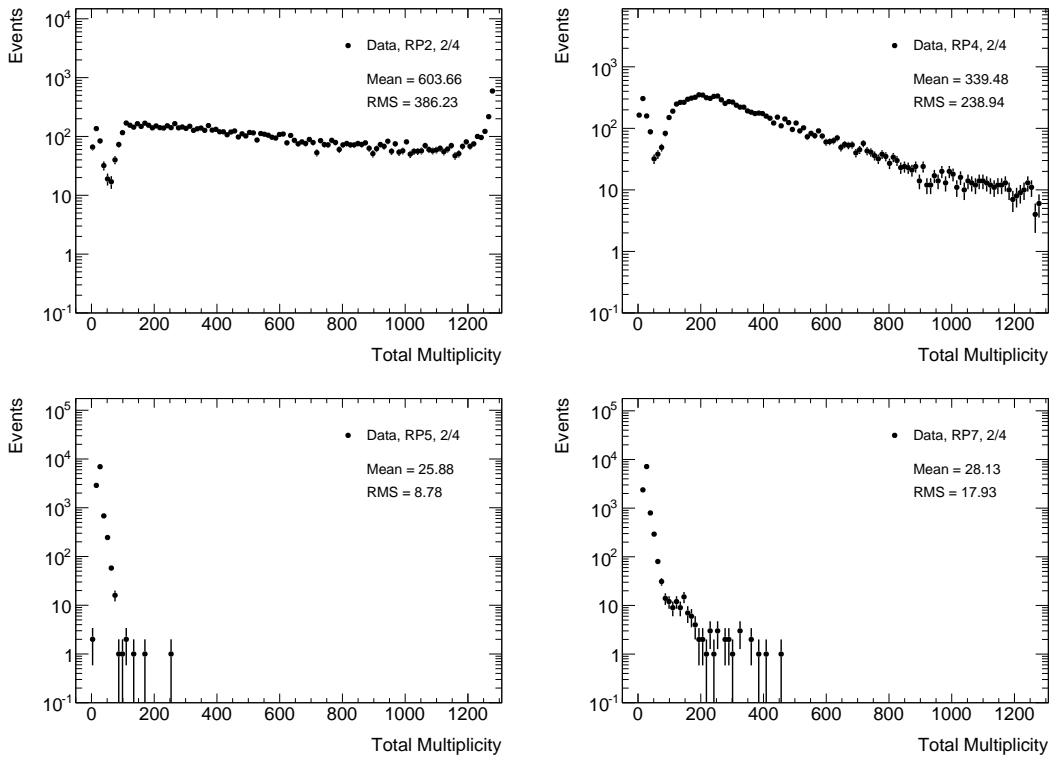


Figure A.29: Total multiplicity distributions of case 2/4, sub-case 57 where no track was reconstructed in RP2 and RP4.

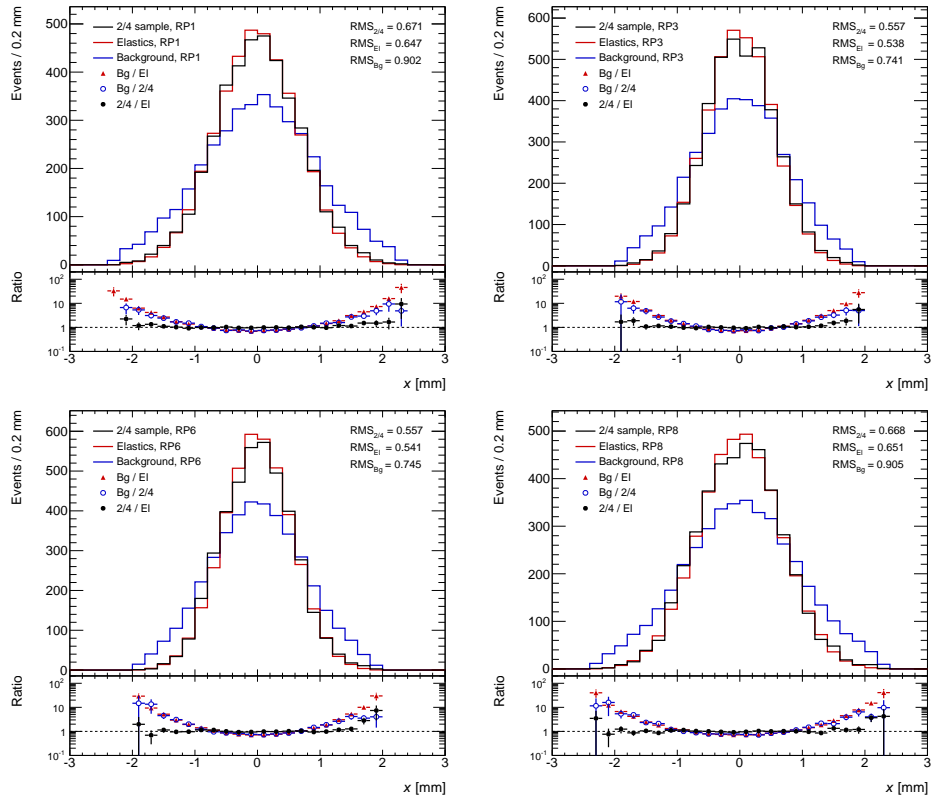


Figure A.30: Elastic-scattering and background templates of armlet 13 and 68.

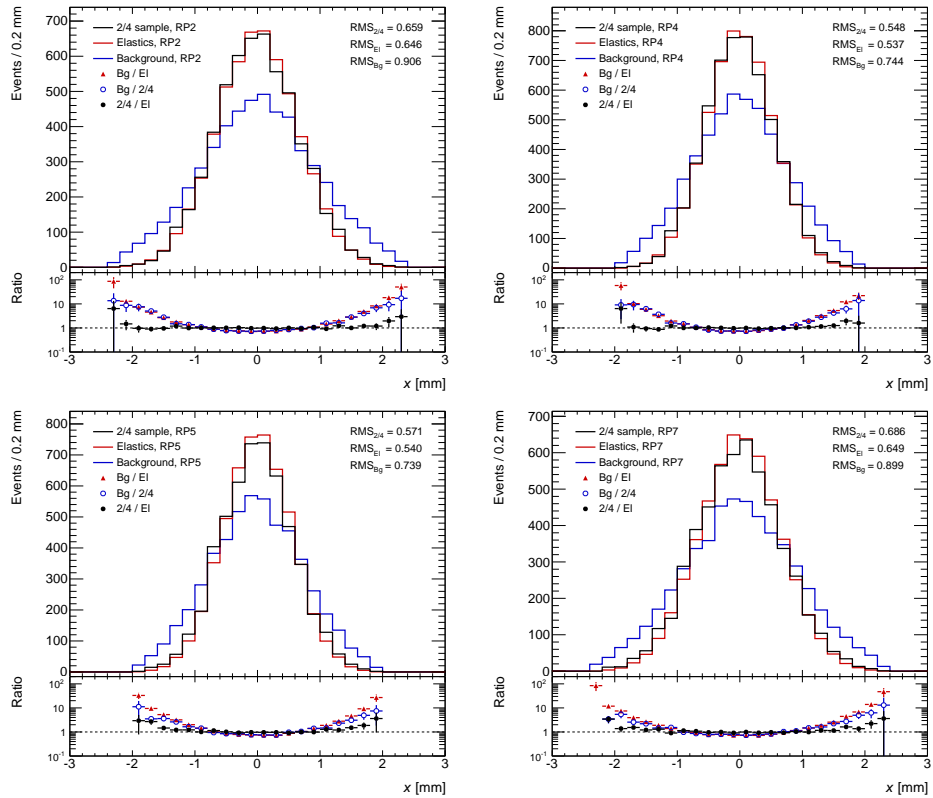


Figure A.31: Elastic-scattering and background templates of armlet 24 and 57.

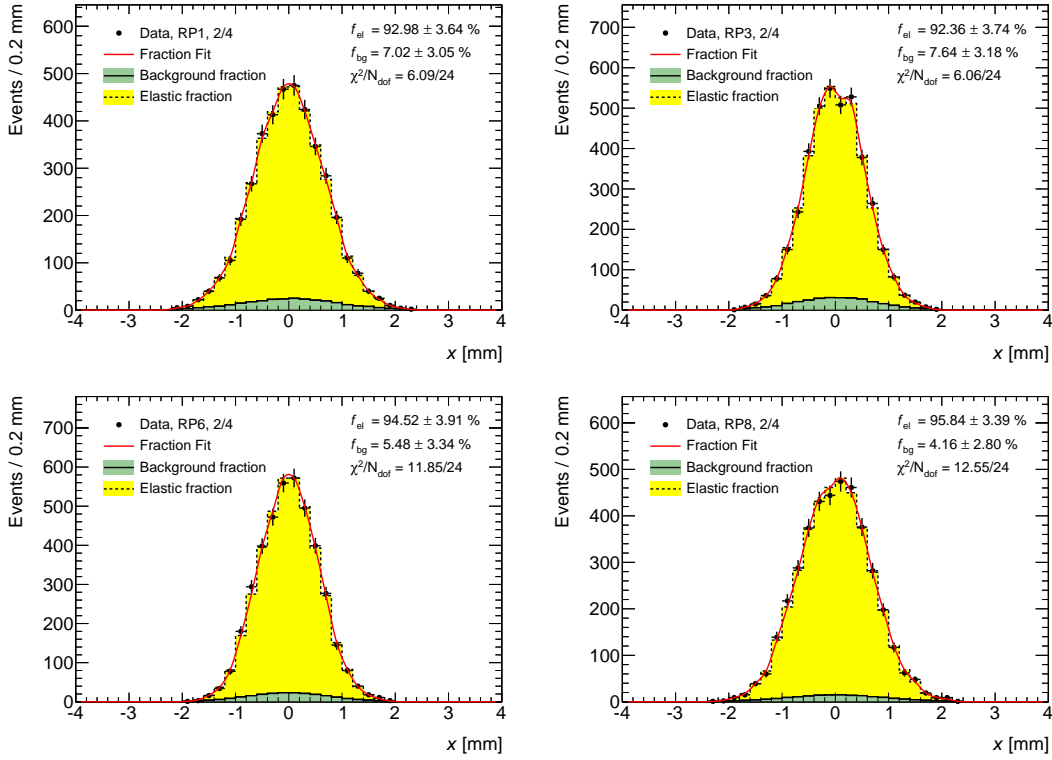


Figure A.32: Template fit of elastic-scattering fraction in armlet 13 and 68.

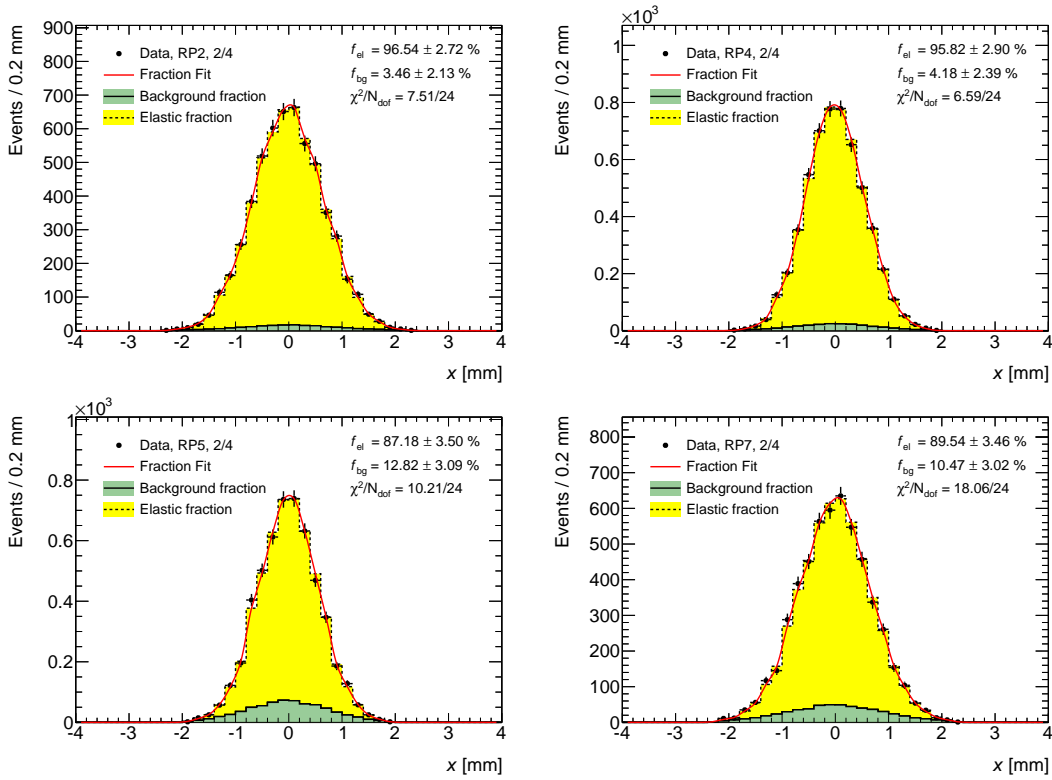


Figure A.33: Template fit of elastic-scattering fraction in armlet 24 and 57.

A.4 Additional plots for reconstruction case 1+1/4

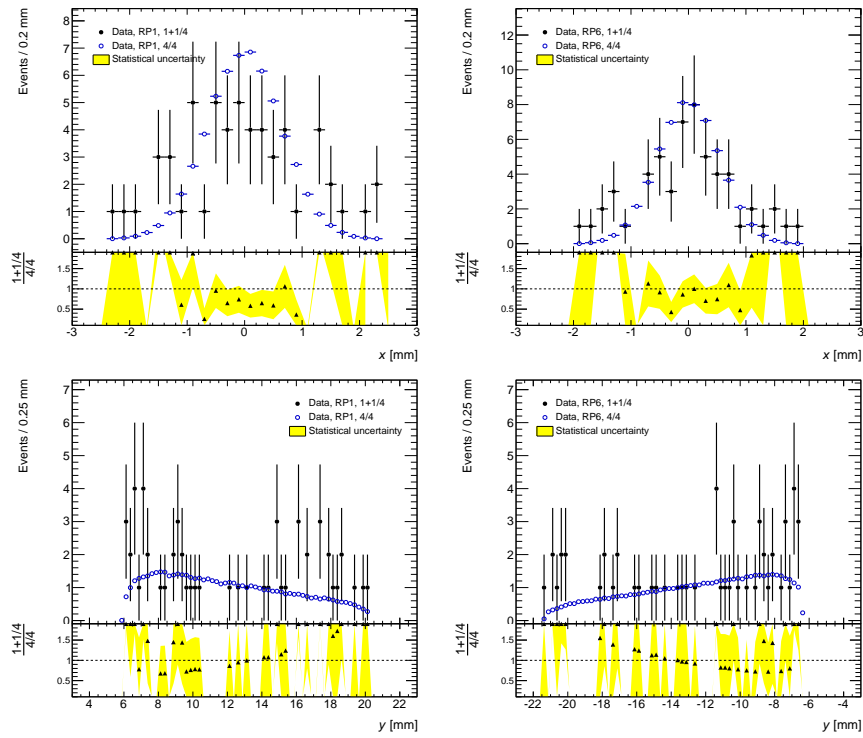


Figure A.34: Position distributions of case 1+1/4, sub-case 16.

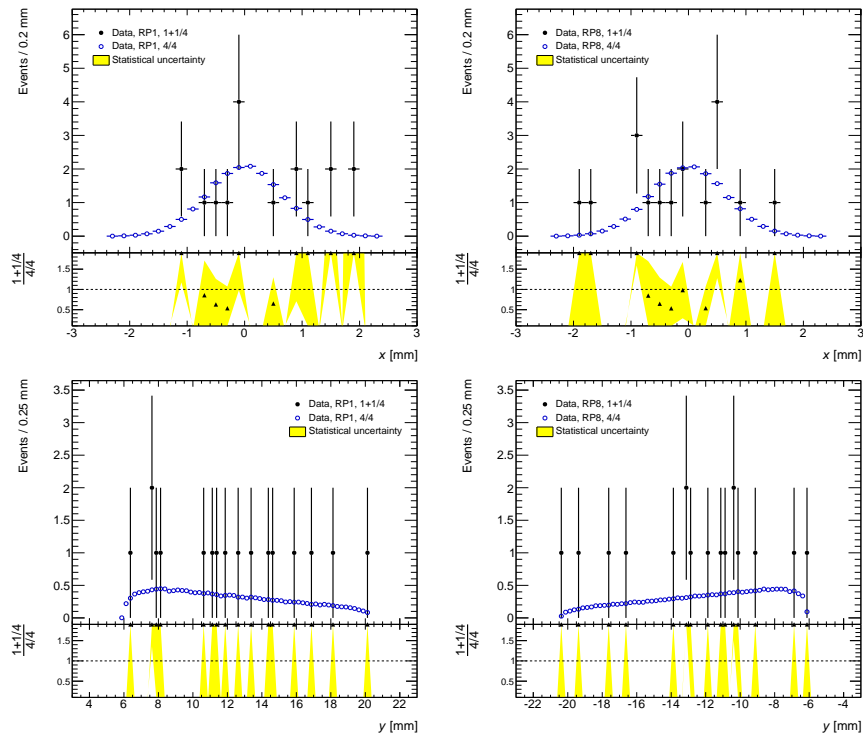


Figure A.35: Position distributions of case 1+1/4, sub-case 18.

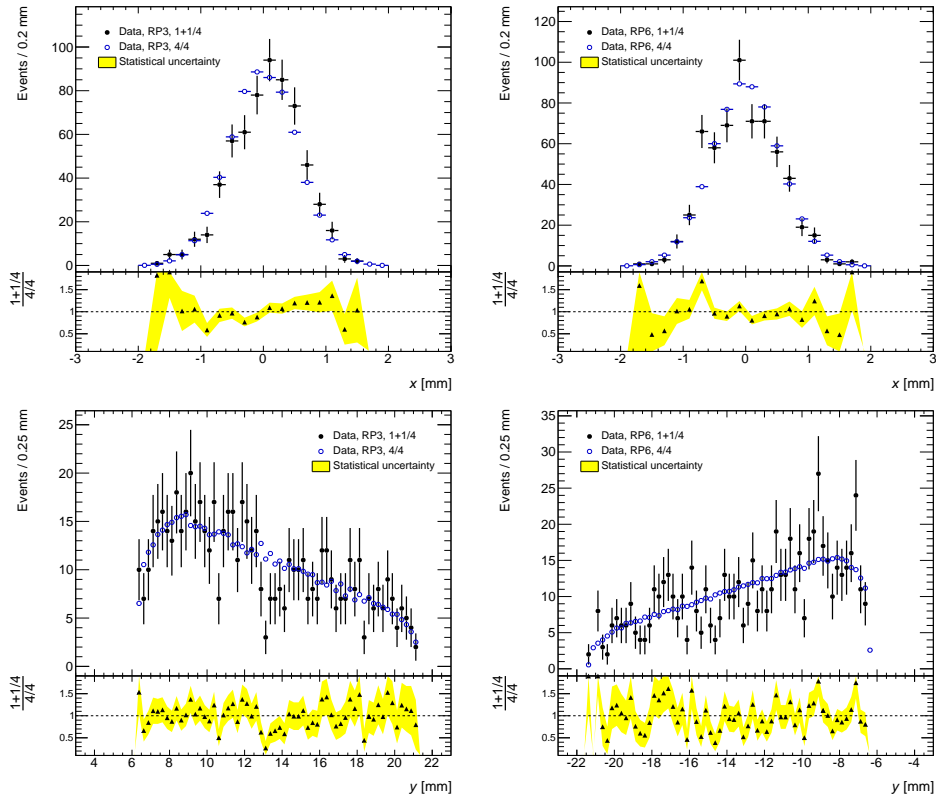


Figure A.36: Position distributions of case 1+1/4, sub-case 36.

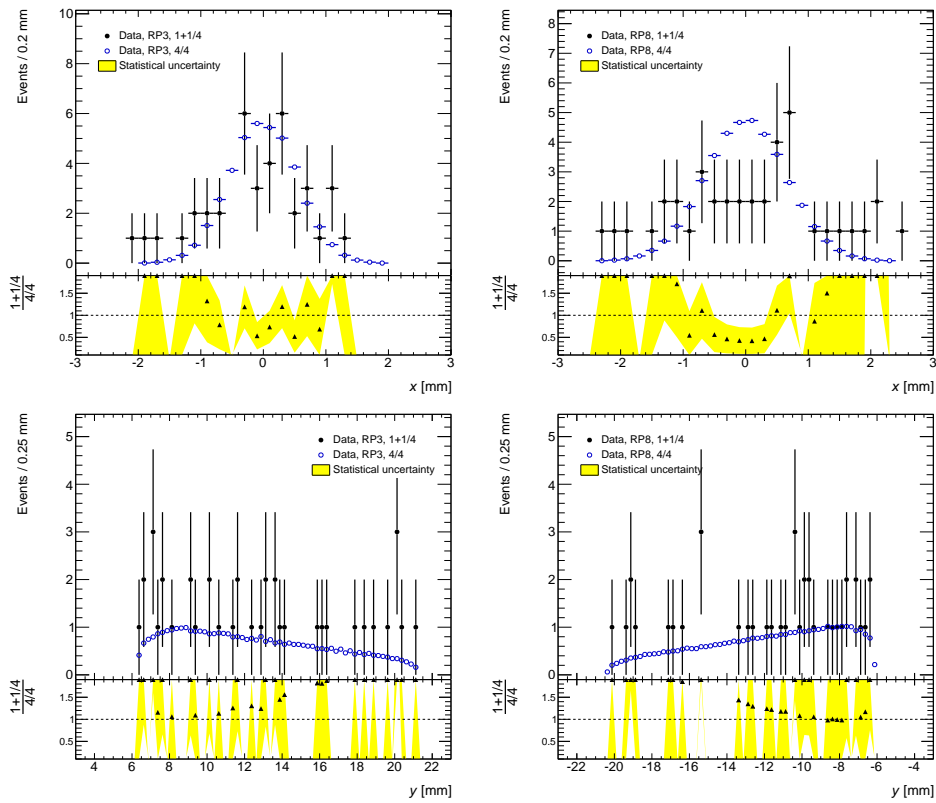


Figure A.37: Position distributions of case 1+1/4, sub-case 38.

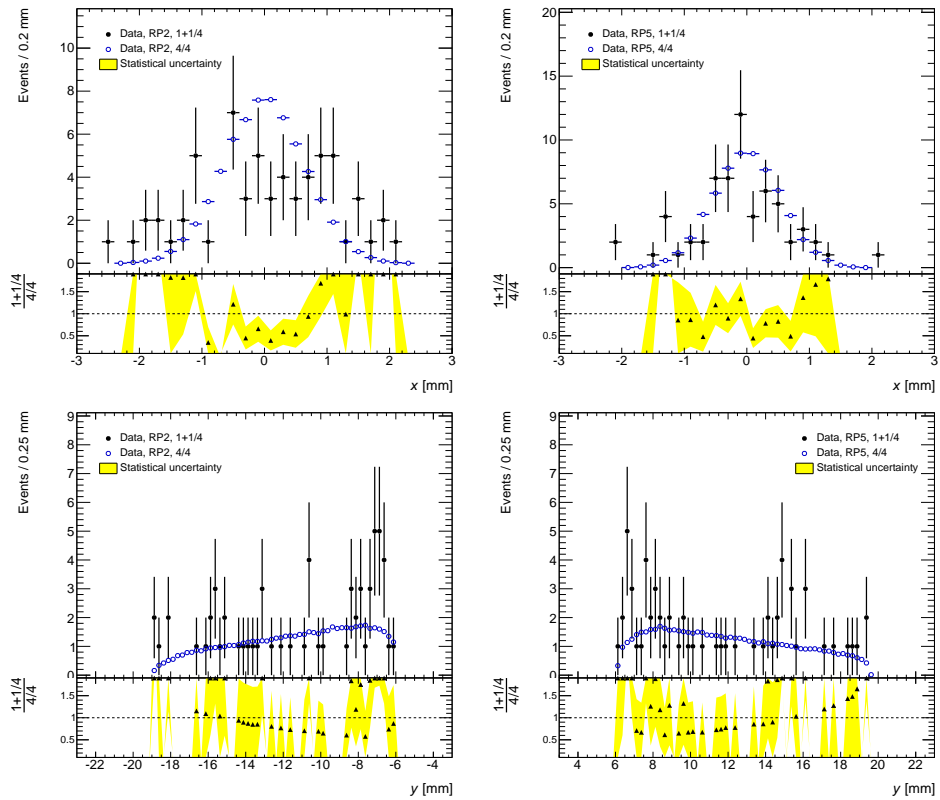


Figure A.38: Position distributions of case 1+1/4, sub-case 25.

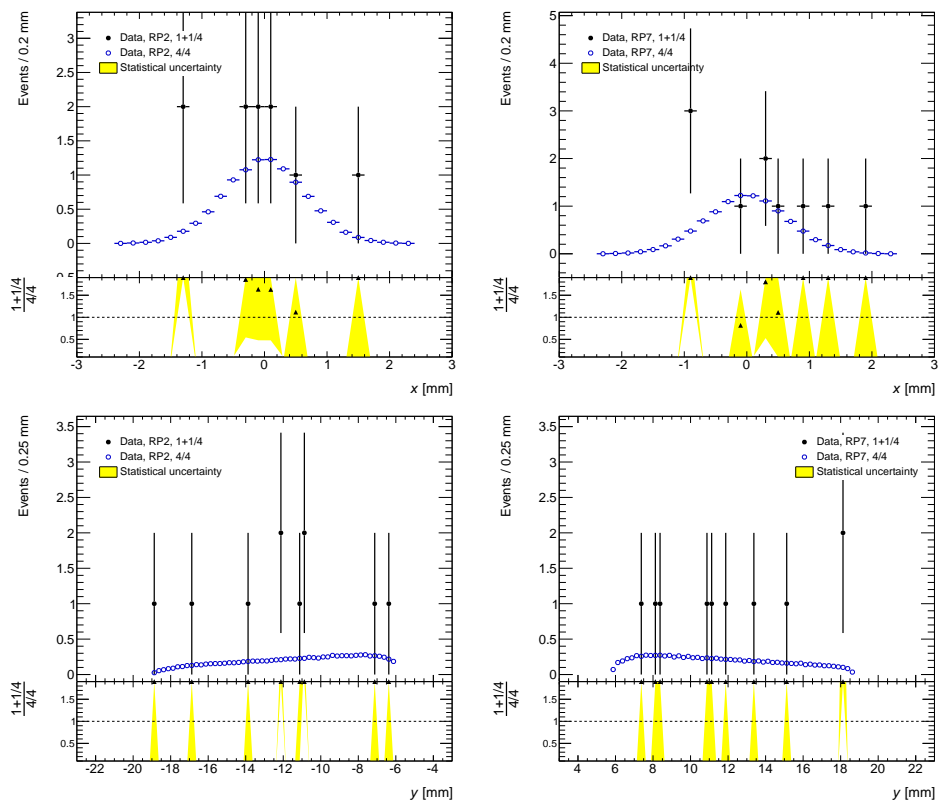


Figure A.39: Position distributions of case 1+1/4, sub-case 27.

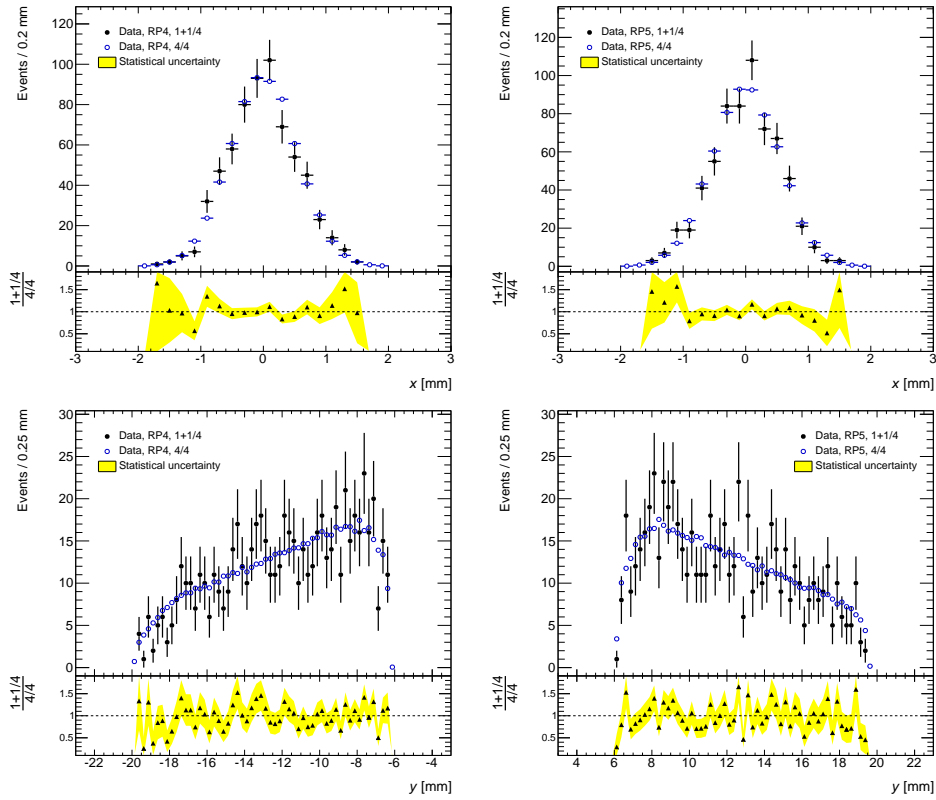


Figure A.40: Position distributions of case 1+1/4, sub-case 45.

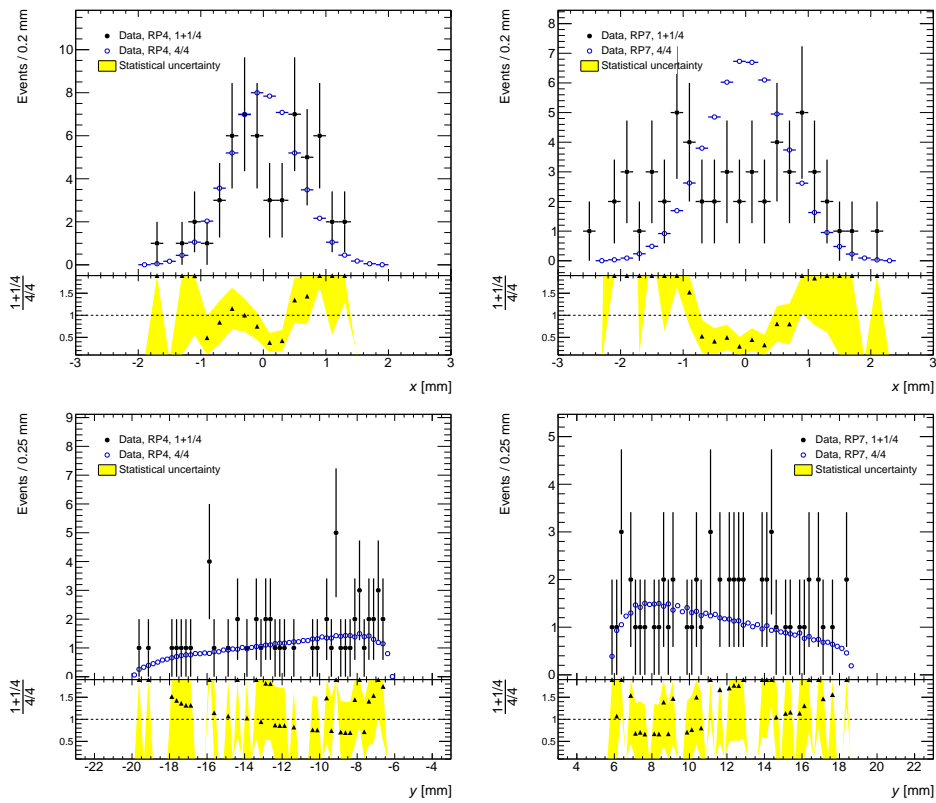


Figure A.41: Position distributions of case 1+1/4, sub-case 47.

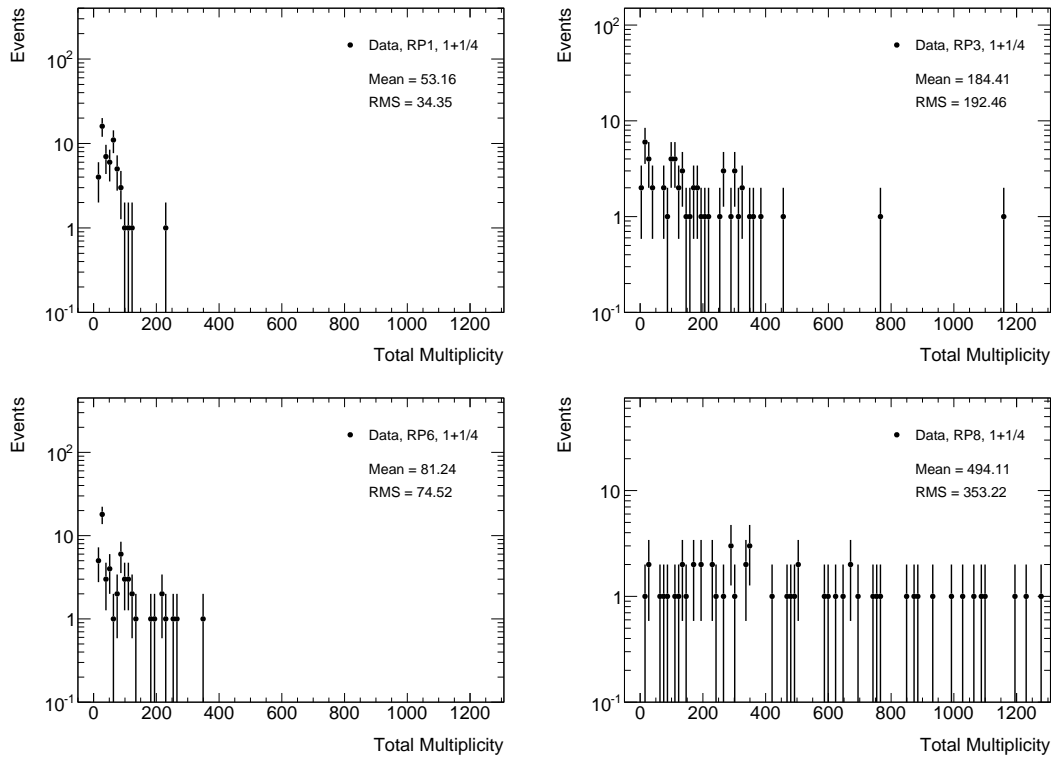


Figure A.42: Total multiplicity distributions of case 1+1/4, sub-case 16 where no track was reconstructed in RP3 and RP8.

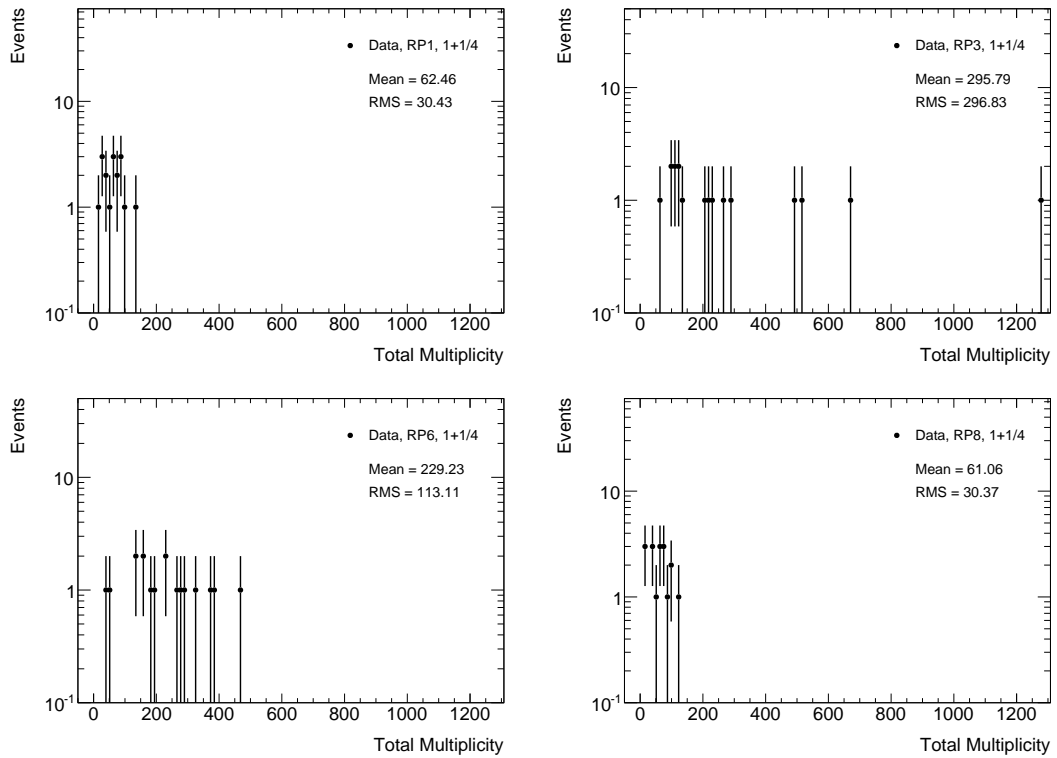


Figure A.43: Total multiplicity distributions of case 1+1/4, sub-case 18 where no track was reconstructed in RP3 and RP6.

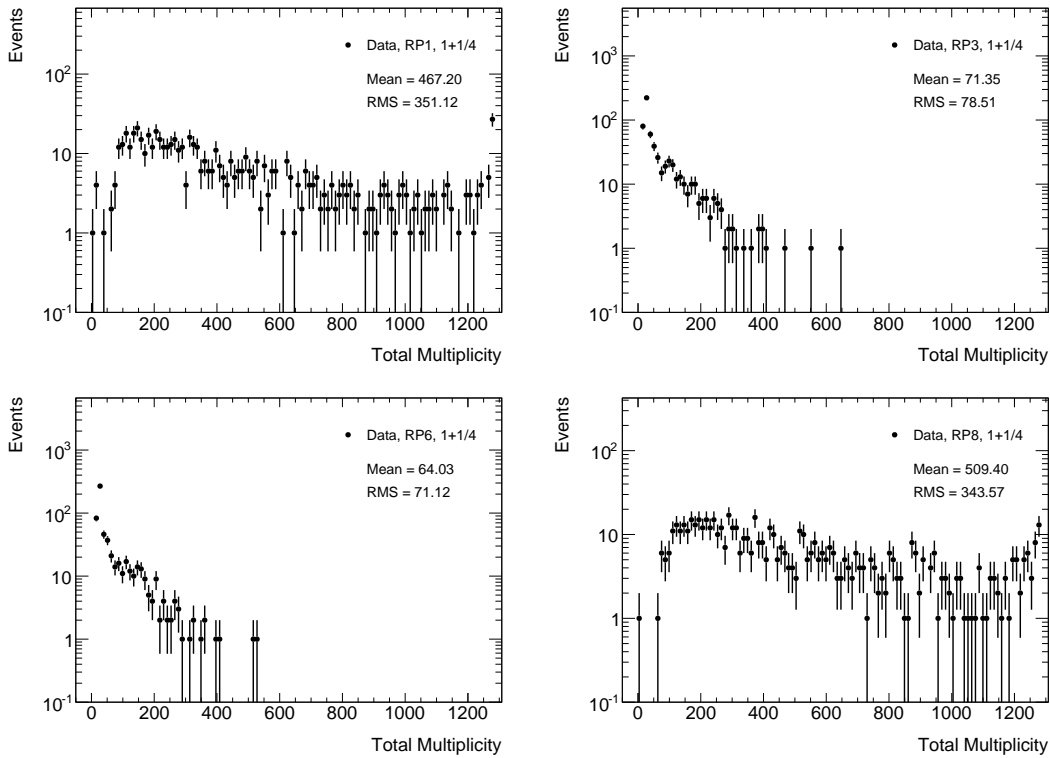


Figure A.44: Total multiplicity distributions of case 1+1/4, sub-case 36 where no track was reconstructed in RP1 and RP8.

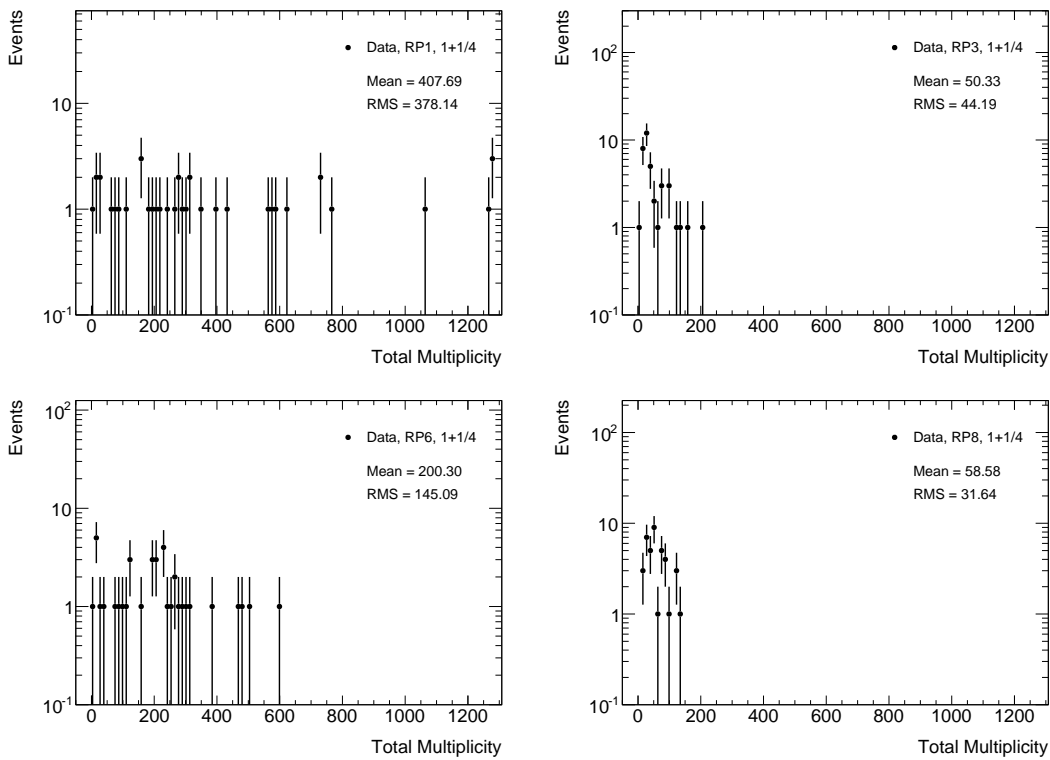


Figure A.45: Total multiplicity distributions of case 1+1/4, sub-case 38 where no track was reconstructed in RP1 and RP6.

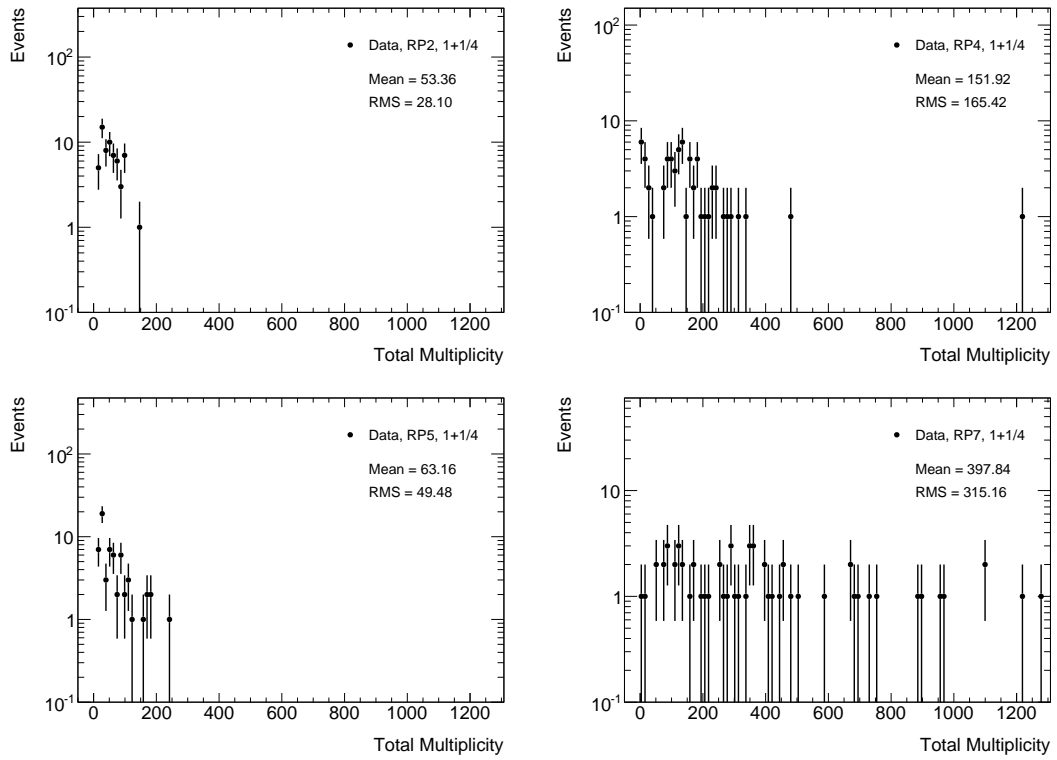


Figure A.46: Total multiplicity distributions of case 1+1/4, sub-case 25 where no track was reconstructed in RP4 and RP7.

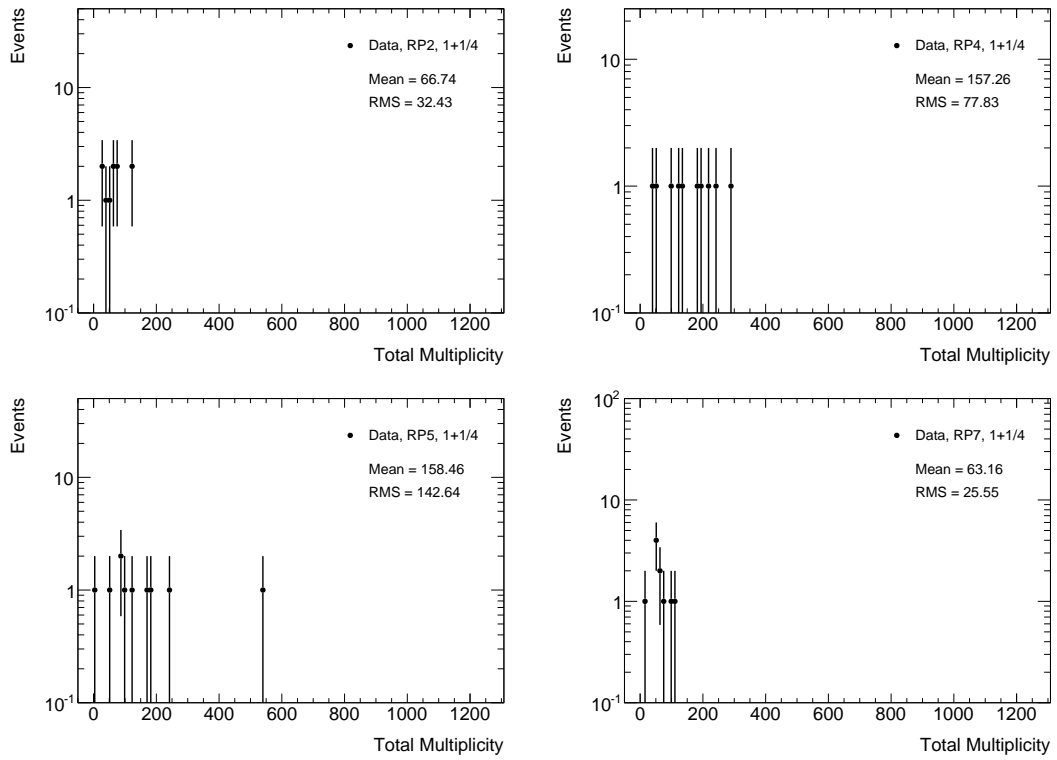


Figure A.47: Total multiplicity distributions of case 1+1/4, sub-case 27 where no track was reconstructed in RP4 and RP5.

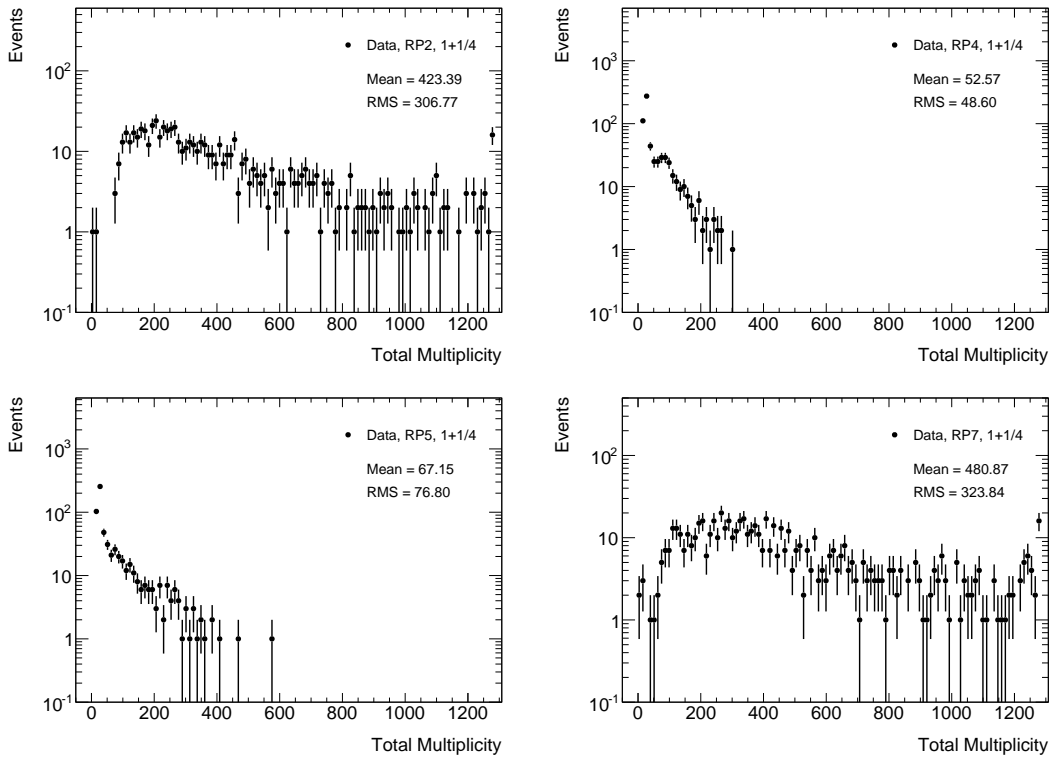


Figure A.48: Total multiplicity distributions of case 1+1/4, sub-case 45 where no track was reconstructed in RP2 and RP7.

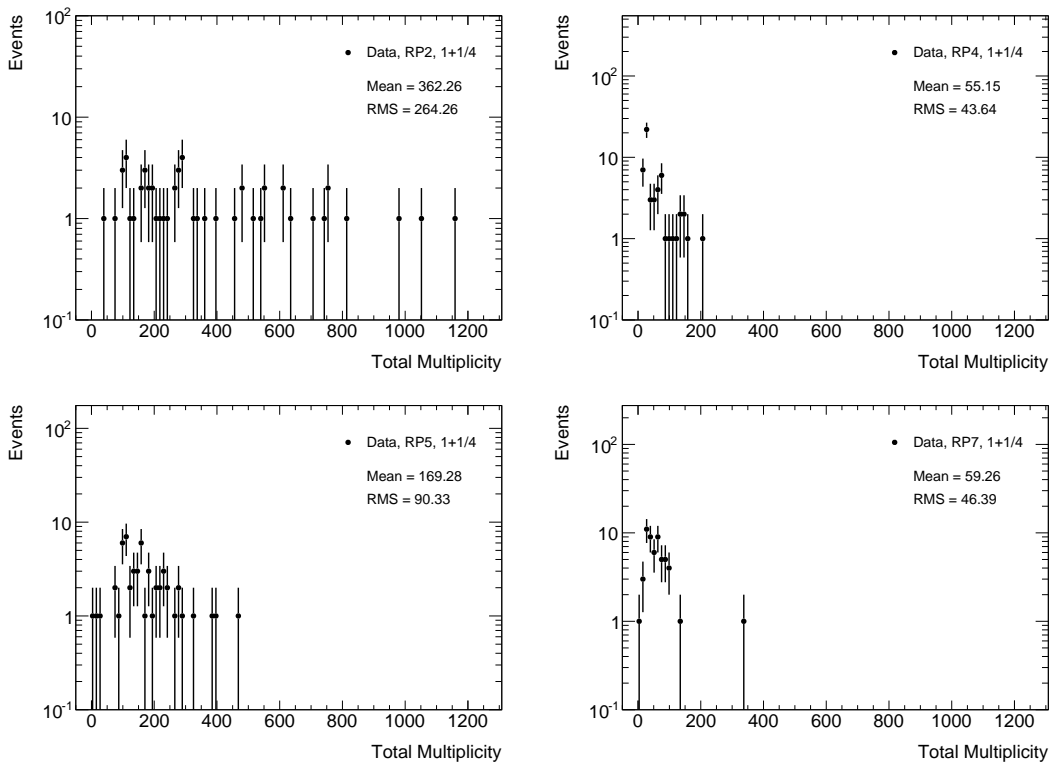


Figure A.49: Total multiplicity distributions of case 1+1/4, sub-case 47 where no track was reconstructed in RP2 and RP5.

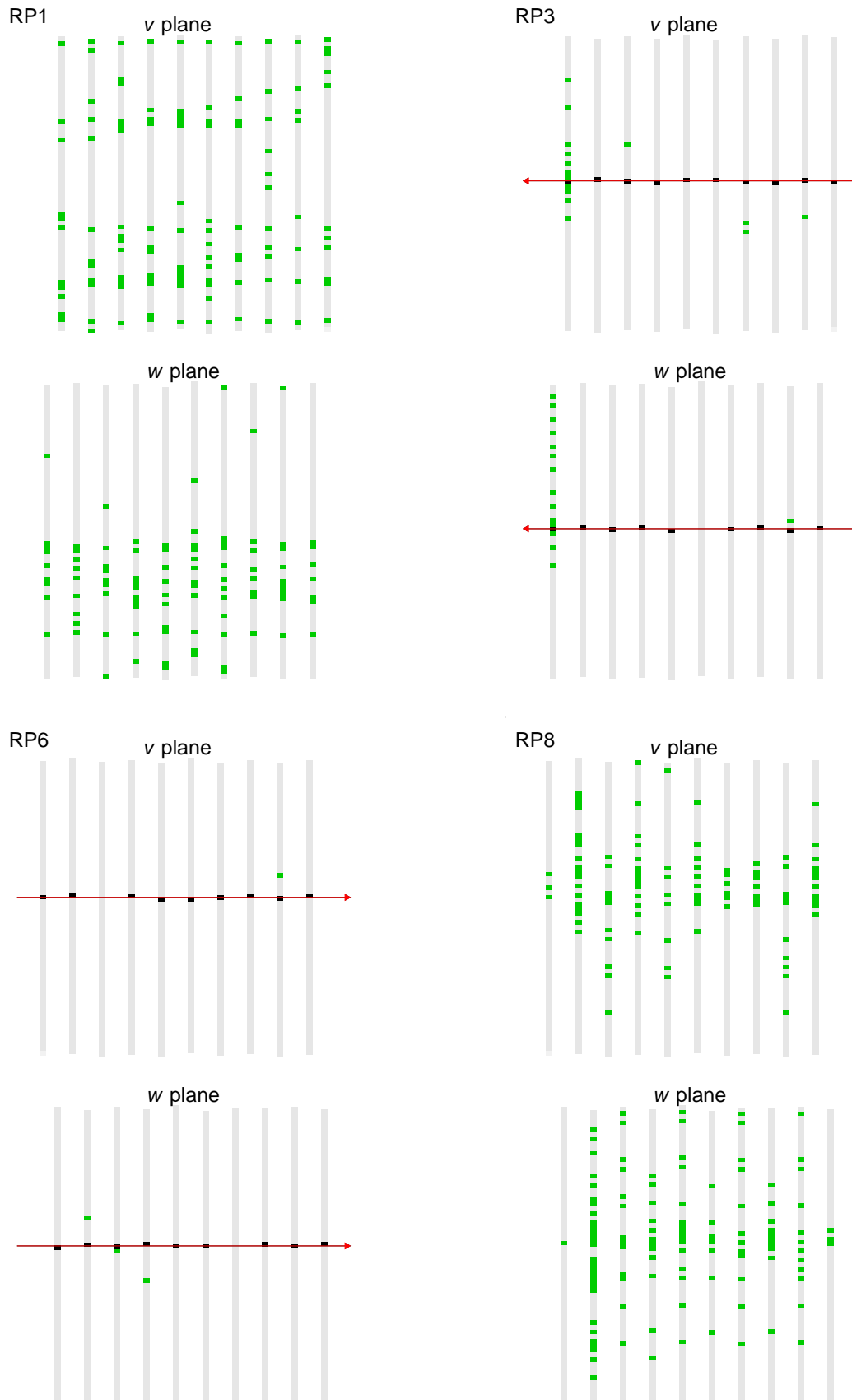


Figure A.50: Event displays of event 509298 (1+1/4, sub-case 36). A track is reconstructed in RP3 and RP6 but not in RP1 and RP8.

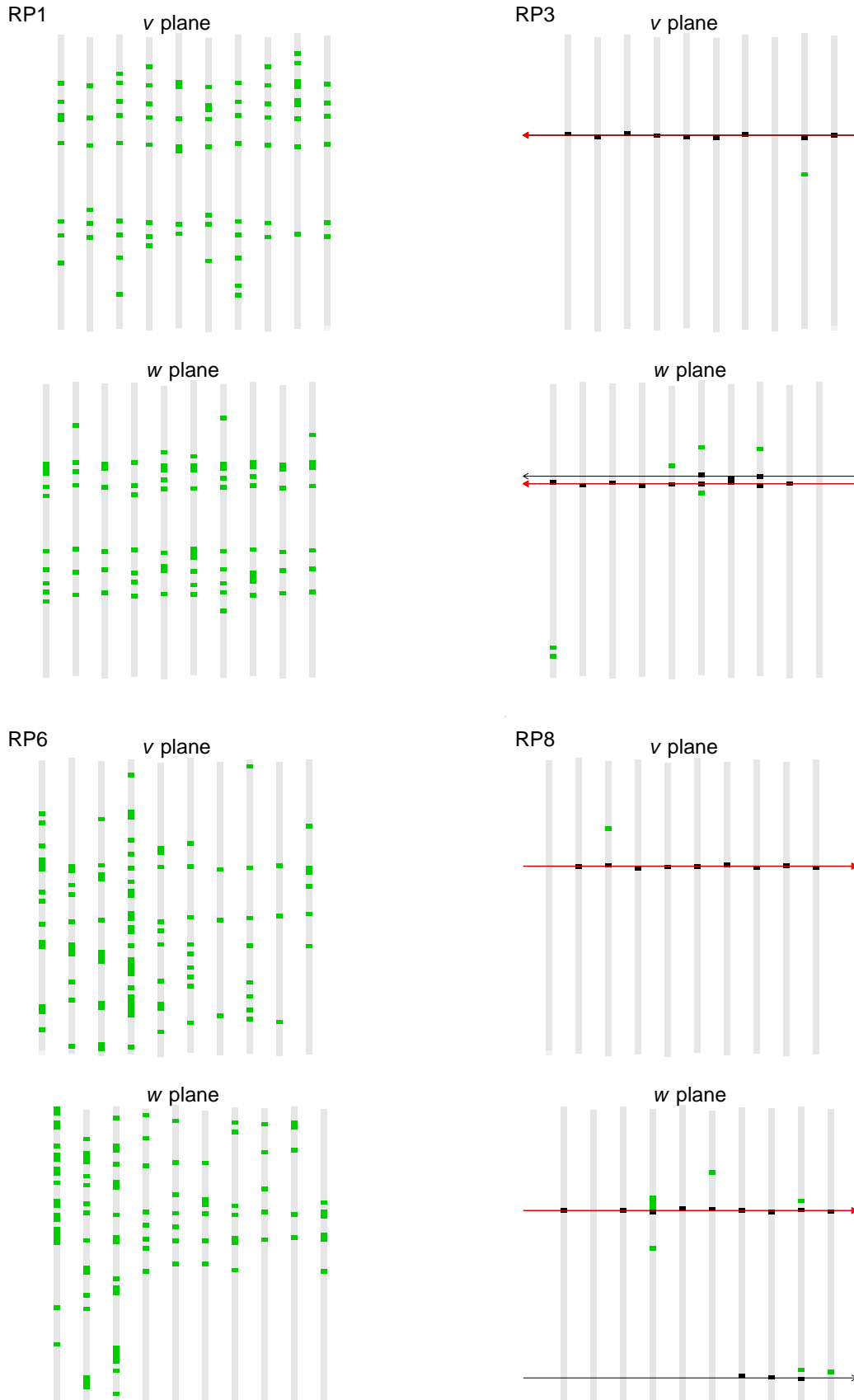


Figure A.51: Event displays of event 1079018 (1+1/4, sub-case 38). A track is reconstructed in RP3 and RP8 but not in RP1 and RP6.

A.5 Additional plots for reconstruction case 1/4

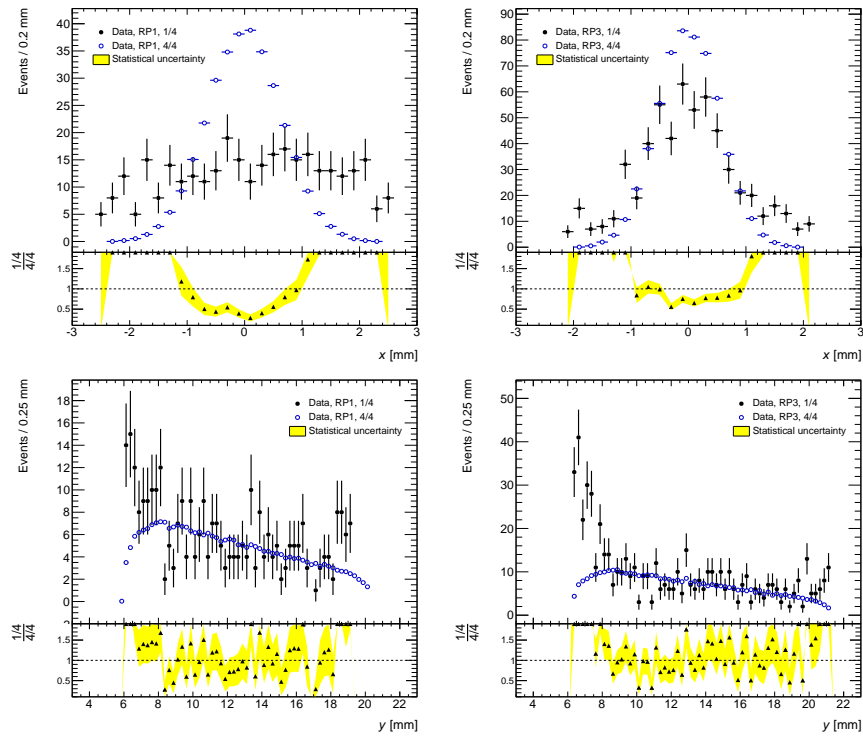


Figure A.52: Position distributions of case 1/4, sub-case 1 and 3.

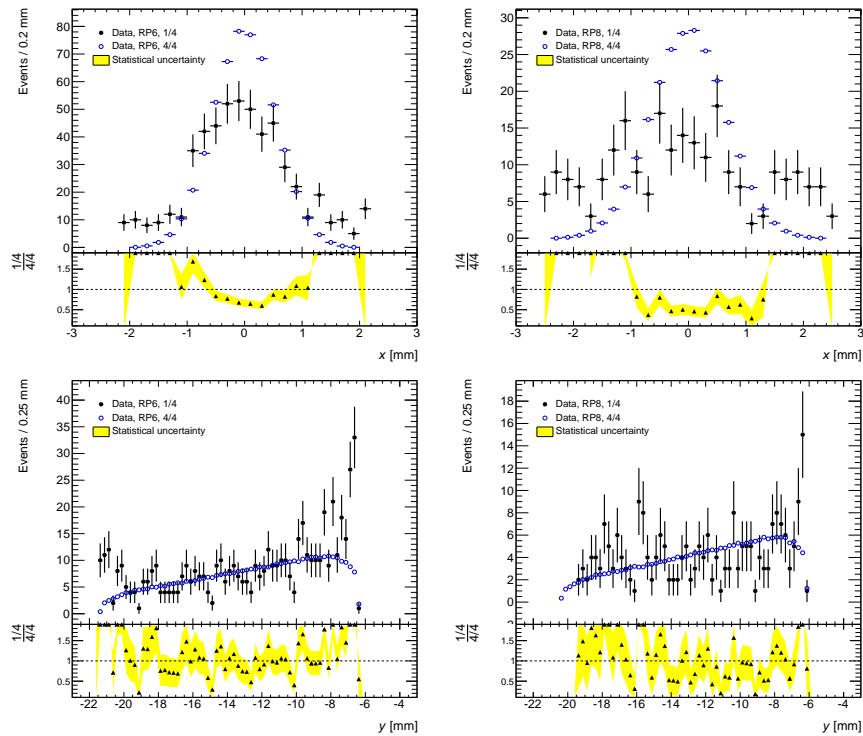


Figure A.53: Position distributions of case 1/4, sub-case 6 and 8.

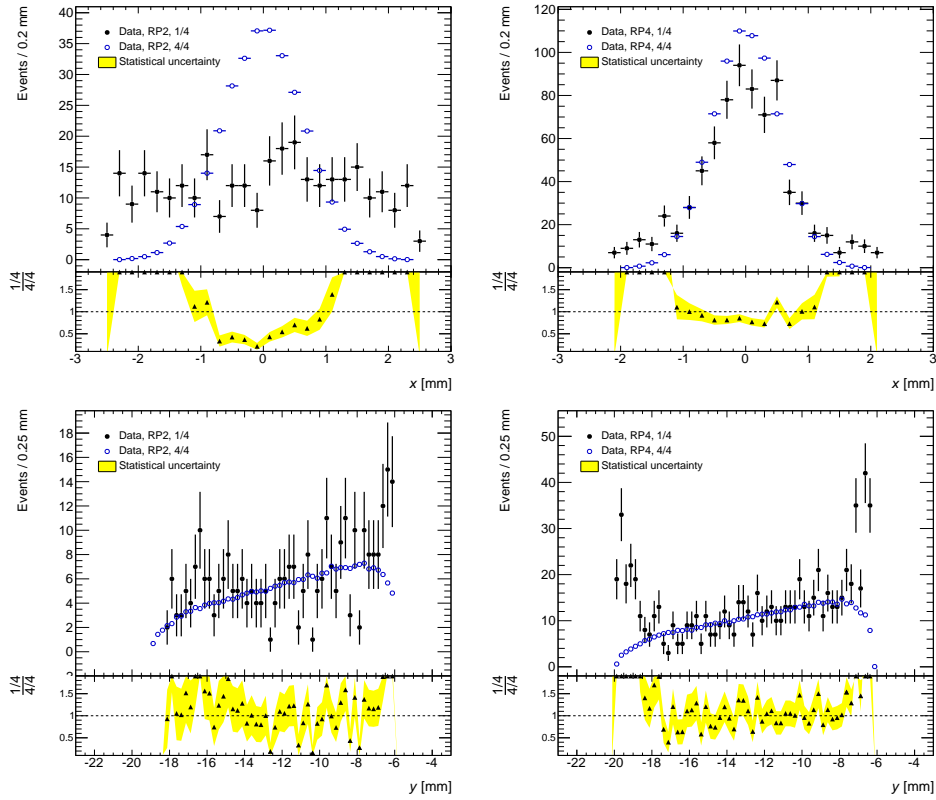


Figure A.54: Position distributions of case 1/4, sub-case 2 and 4.

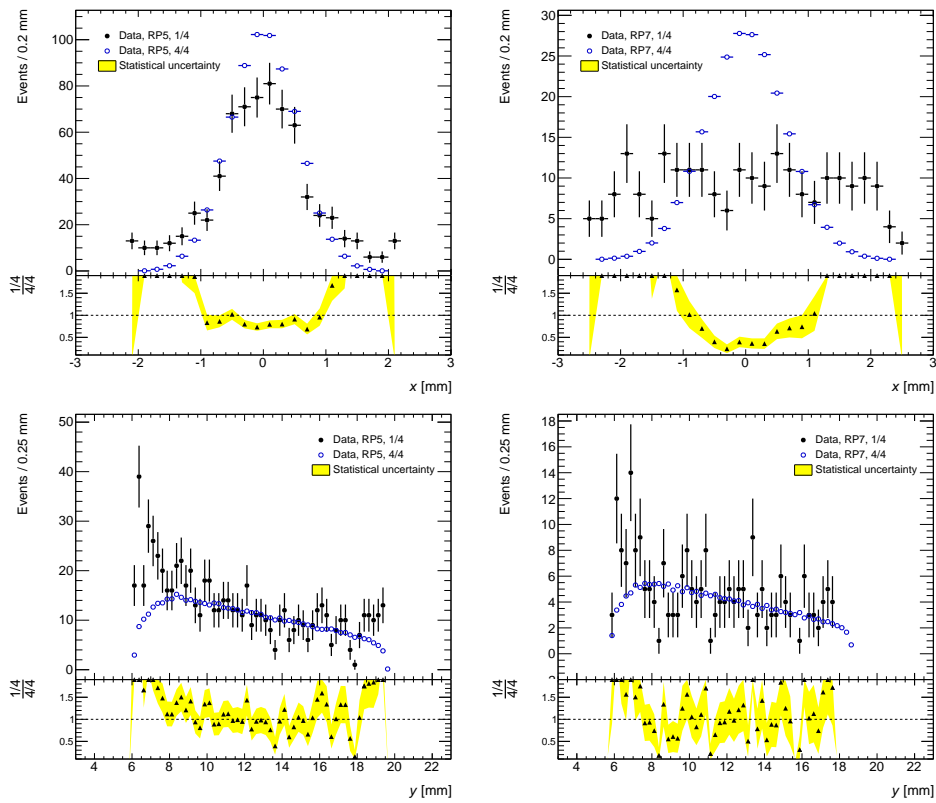


Figure A.55: Position distributions of case 1/4, sub-case 5 and 7.

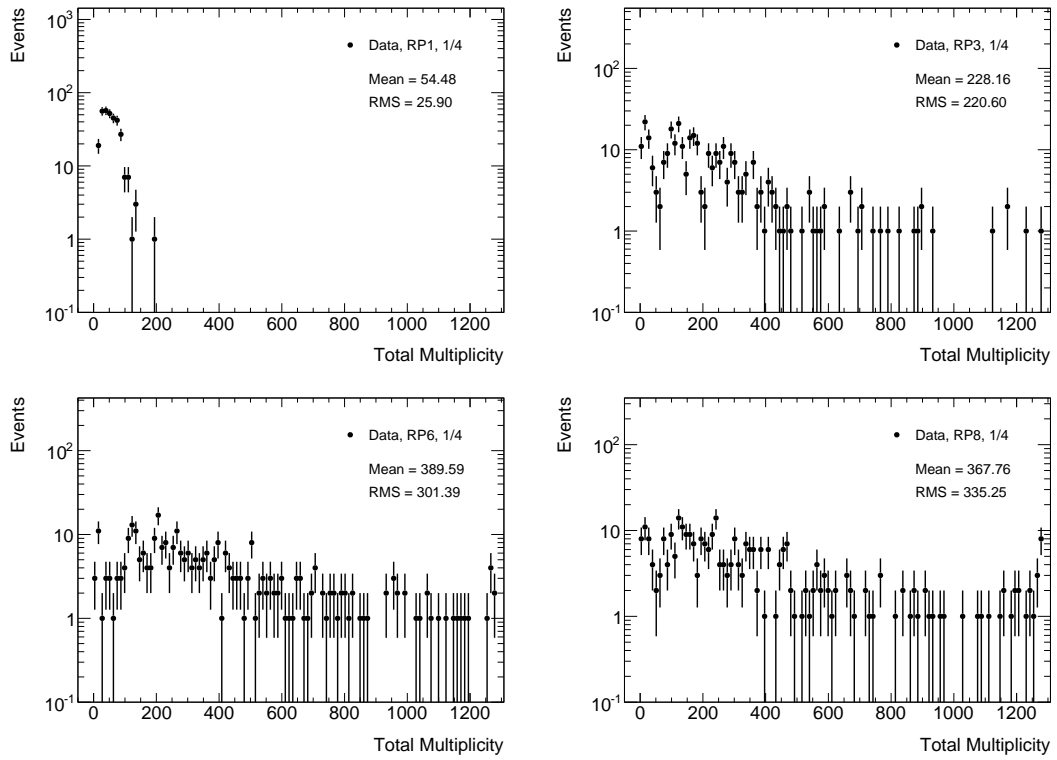


Figure A.56: Total multiplicity distributions of case 1/4, sub-case 1 where no track was reconstructed in RP3, RP6 and RP8.

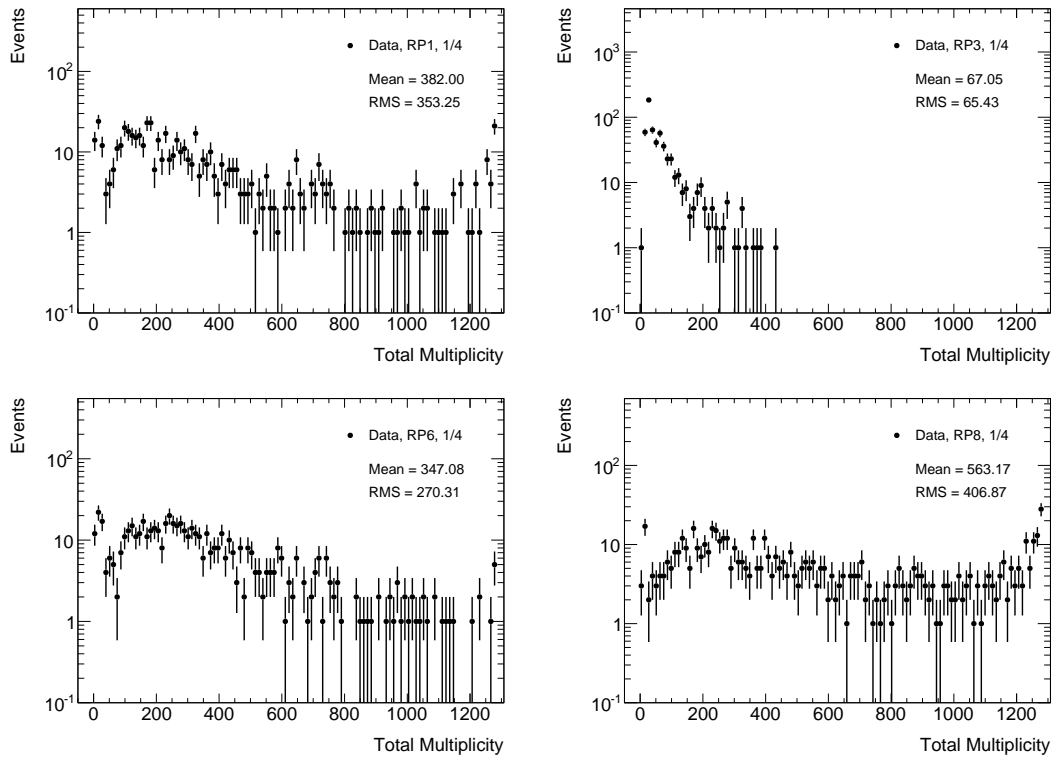


Figure A.57: Total multiplicity distributions of case 1/4, sub-case 3 where no track was reconstructed in RP1, RP6 and RP8.

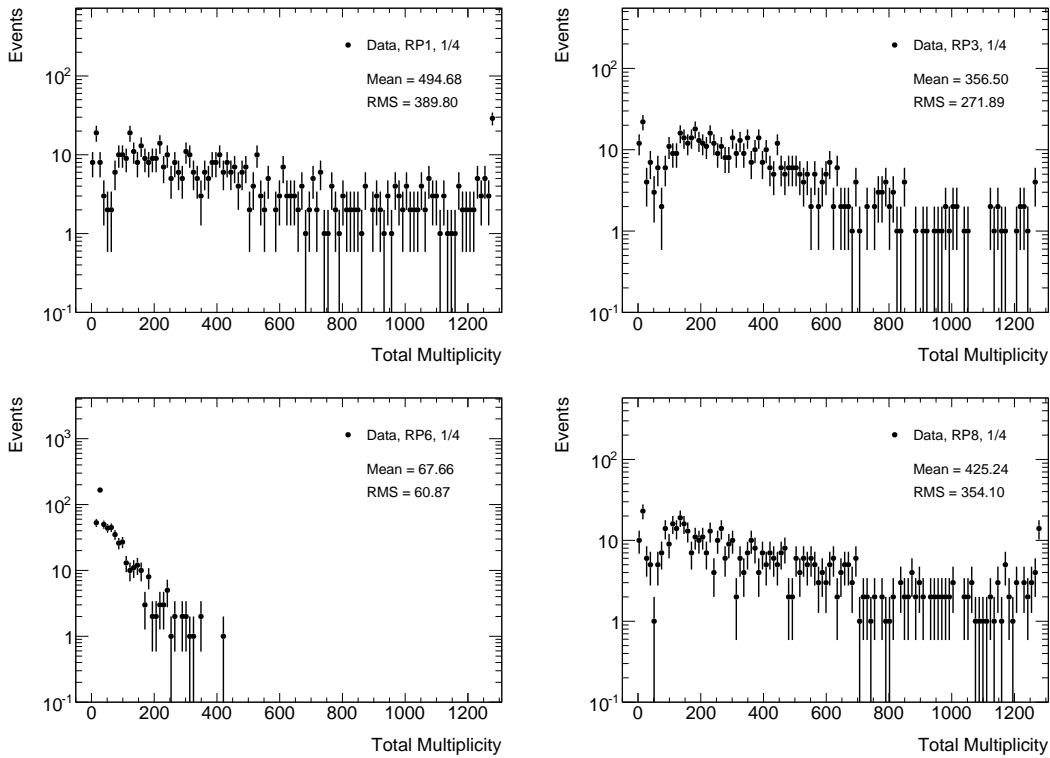


Figure A.58: Total multiplicity distributions of case 1/4, sub-case 6 where no track was reconstructed in RP1, RP3 and RP8.

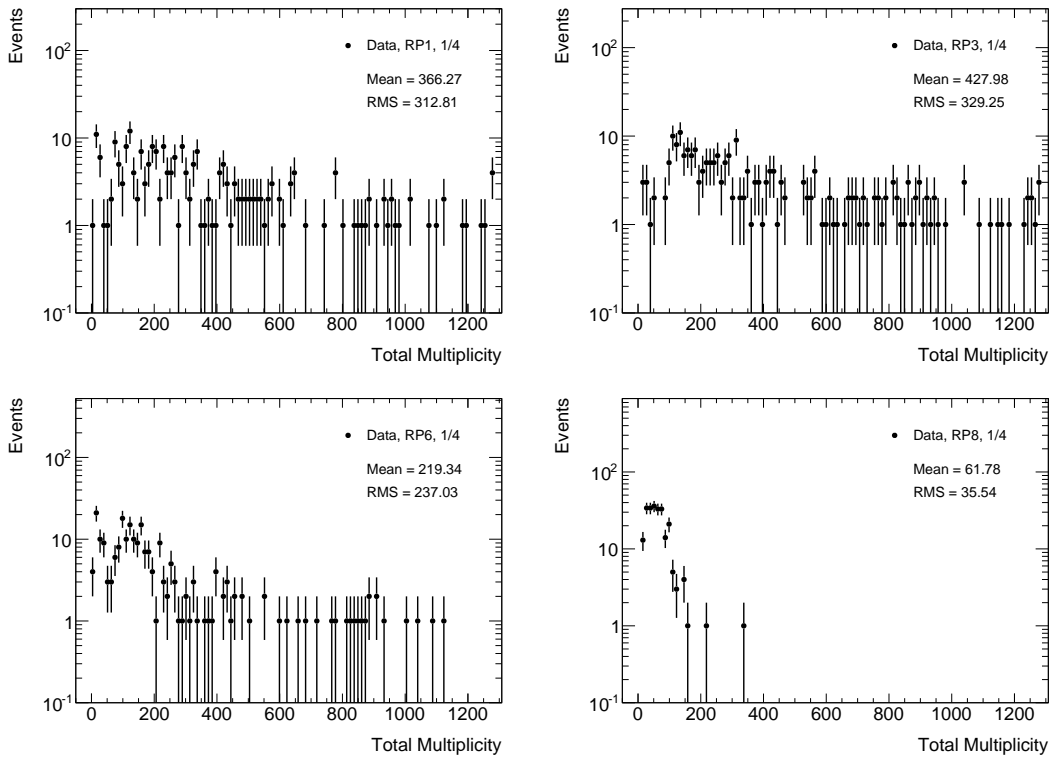


Figure A.59: Total multiplicity distributions of case 1/4, sub-case 8 where no track was reconstructed in RP1, RP3 and RP6.

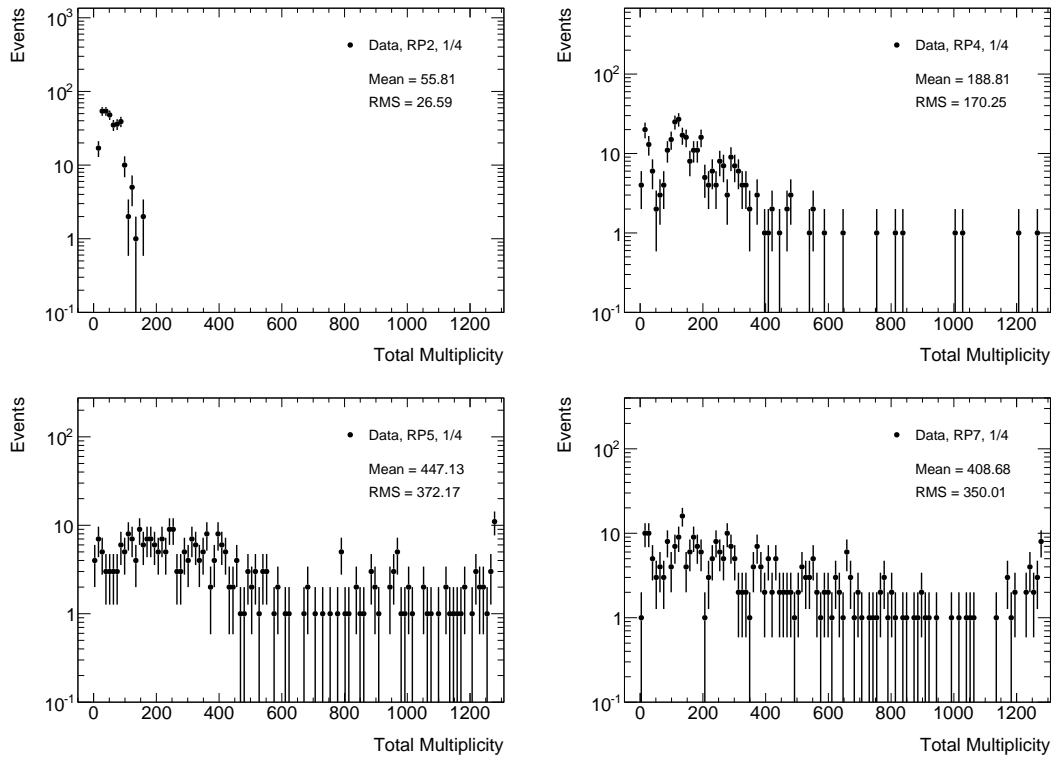


Figure A.60: Total multiplicity distributions of case 1/4, sub-case 2 where no track was reconstructed in RP4, RP5 and RP7.

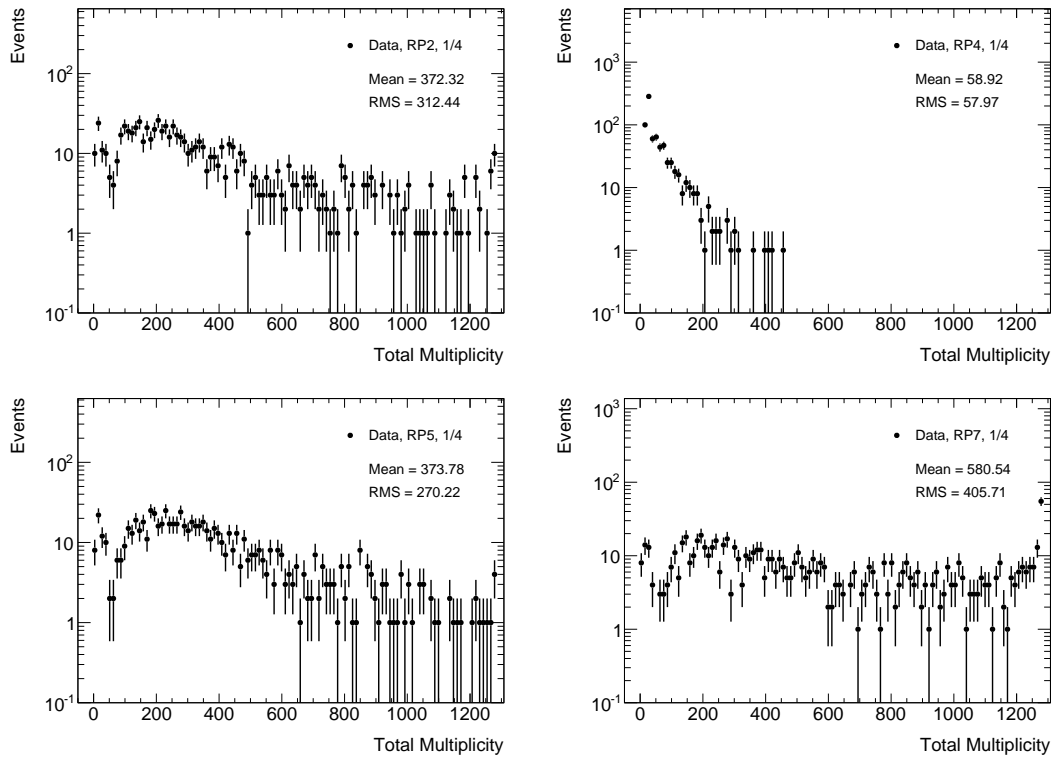


Figure A.61: Total multiplicity distributions of case 1/4, sub-case 4 where no track was reconstructed in RP2, RP5 and RP7.

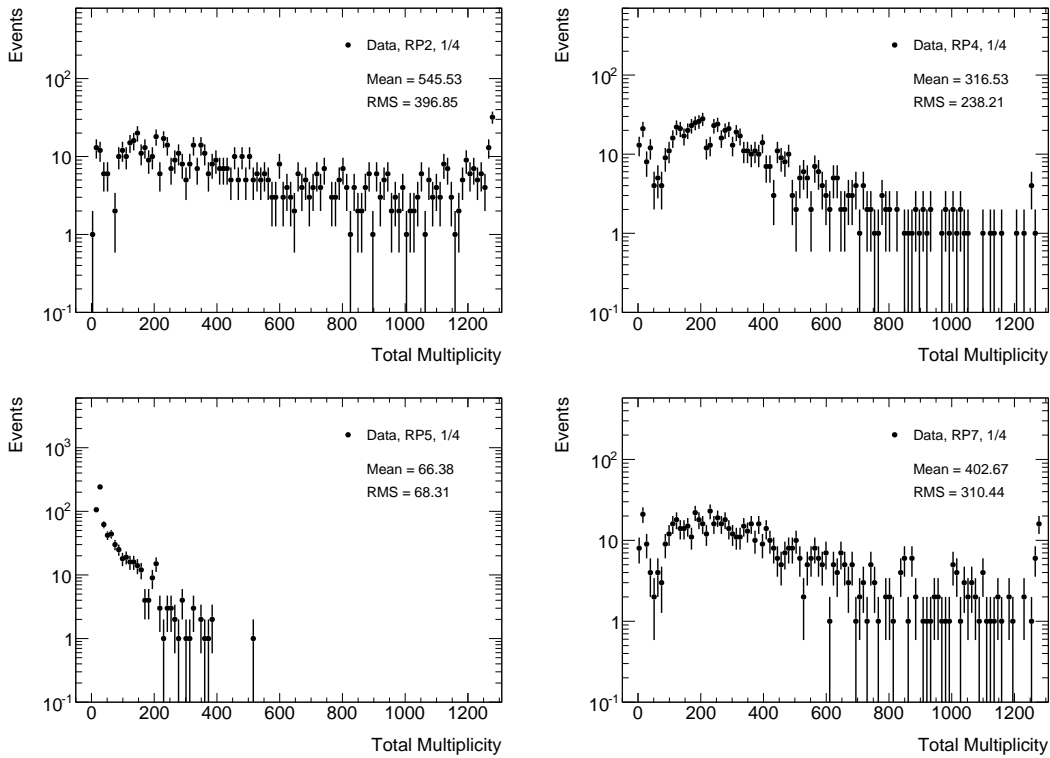


Figure A.62: Total multiplicity distributions of case 1/4, sub-case 5 where no track was reconstructed in RP2, RP4 and RP7.

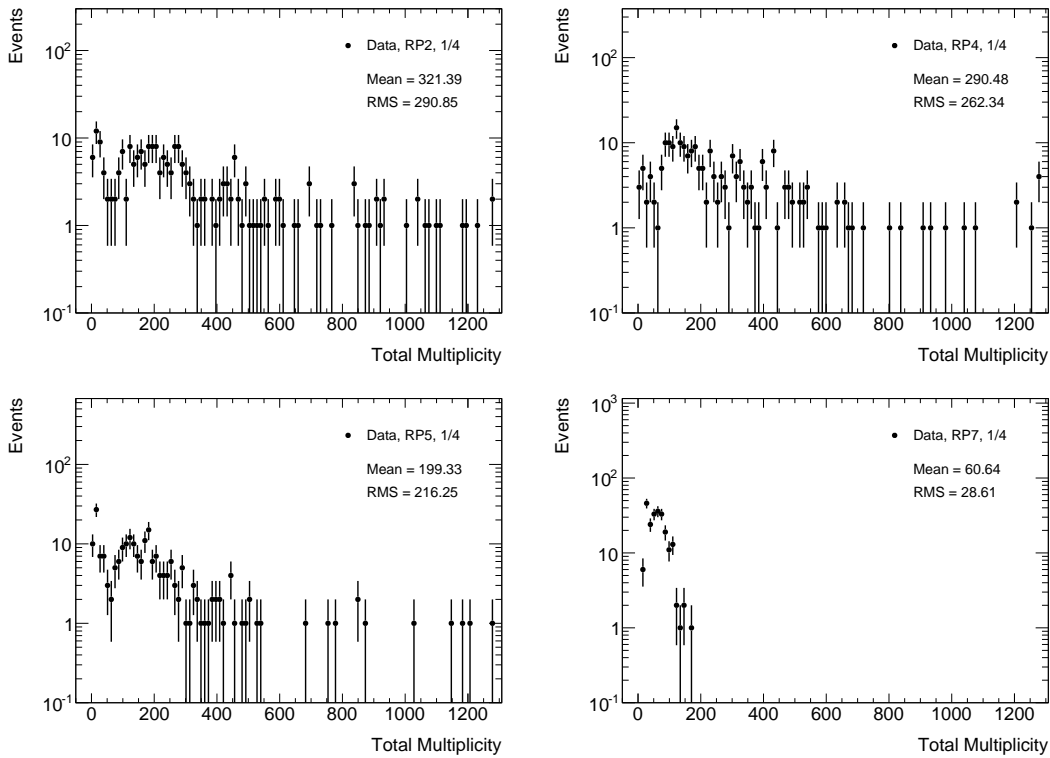


Figure A.63: Total multiplicity distributions of case 1/4, sub-case 7 where no track was reconstructed in RP2, RP4 and RP5.

A.6 Additional plots for reconstruction case 0/4

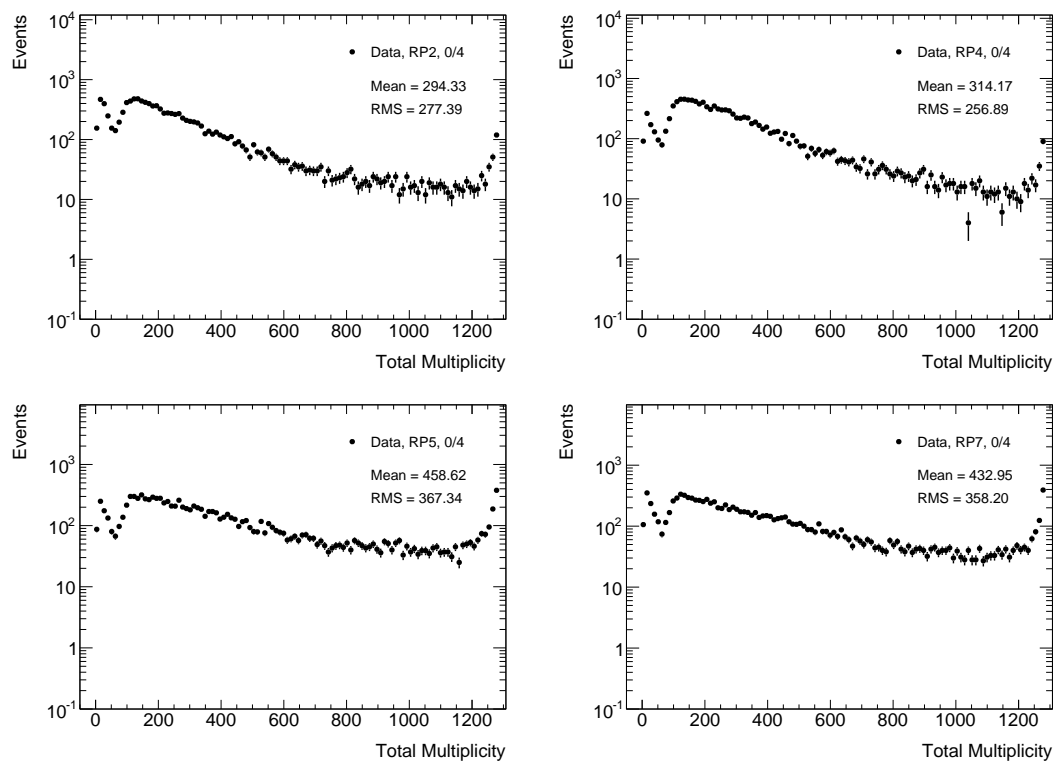


Figure A.64: Total multiplicity distributions of case 0/4, sub-case 2457.

A.7 Additional result tables

Table A.1: Measured values of $d\sigma_{\text{el}}/dt$ reconstructed with the nominal subtraction method with statistical, systematic and total uncertainties. The central $|t|$ -value in each bin is calculated from simulation, in which a slope parameter of $B = 19.5 \text{ GeV}^2$ is used.

$-t_{\text{lower}}$ [GeV ²]	$-t_{\text{upper}}$ [GeV ²]	$-t_{\text{central}}$ [GeV ²]	$d\sigma_{\text{el}}/dt$ [mb/GeV ²]	Stat. uncert. [mb/GeV ²]	Syst. uncert. [mb/GeV ²]	Total uncert. [mb/GeV ²]
0.0025	0.0100	0.0062	425.8	2.6	31.3	31.4
0.0100	0.0120	0.0110	382.6	1.9	17.7	17.8
0.0120	0.0145	0.0132	363.2	1.6	12.6	12.7
0.0145	0.0175	0.0160	342.0	1.4	10.6	10.7
0.0175	0.0210	0.0192	320.9	1.2	9.7	9.8
0.0210	0.0245	0.0227	300.3	1.1	8.6	8.6
0.0245	0.0285	0.0265	279.4	1.0	7.8	7.8
0.0285	0.0330	0.0307	256.1	0.9	7.0	7.0
0.0330	0.0375	0.0352	234.3	0.8	6.2	6.2
0.0375	0.0425	0.0400	213.2	0.7	5.5	5.6
0.0425	0.0475	0.0450	193.3	0.6	5.0	5.0
0.0475	0.0530	0.0502	175.1	0.6	4.5	4.5
0.0530	0.0590	0.0559	156.5	0.5	4.1	4.1
0.0590	0.0650	0.0619	139.8	0.5	4.1	4.1
0.0650	0.0710	0.0679	125.5	0.5	4.2	4.3
0.0710	0.0780	0.0744	110.2	0.5	3.9	3.9
0.0780	0.0850	0.0814	95.8	0.4	3.2	3.2
0.0850	0.0920	0.0884	83.9	0.4	2.9	2.9
0.0920	0.1000	0.0959	72.4	0.4	2.6	2.6
0.1000	0.1075	0.1037	62.0	0.4	2.2	2.2
0.1075	0.1150	0.1112	54.1	0.4	2.0	2.0
0.1150	0.1240	0.1194	46.4	0.3	1.8	1.8
0.1240	0.1330	0.1284	39.2	0.3	1.5	1.6
0.1330	0.1420	0.1374	33.0	0.3	1.4	1.4
0.1420	0.1520	0.1468	27.7	0.3	1.2	1.3
0.1520	0.1620	0.1568	22.8	0.2	1.1	1.1
0.1620	0.1720	0.1668	18.88	0.21	0.88	0.91
0.1720	0.1820	0.1768	15.58	0.19	0.83	0.85
0.1820	0.1930	0.1873	12.77	0.17	0.79	0.80
0.1930	0.2030	0.1978	10.45	0.16	0.68	0.70
0.2030	0.2140	0.2083	8.33	0.14	0.61	0.62
0.2140	0.2250	0.2193	6.70	0.13	0.49	0.50
0.2250	0.2360	0.2303	5.60	0.12	0.43	0.45
0.2360	0.2490	0.2422	4.45	0.11	0.39	0.41
0.2490	0.2620	0.2553	3.46	0.10	0.39	0.40
0.2620	0.2770	0.2691	2.53	0.08	0.41	0.41
0.2770	0.3000	0.2877	1.78	0.07	0.41	0.42
0.3000	0.3200	0.3094	1.21	0.07	0.37	0.38
0.3200	0.3500	0.3335	0.75	0.07	0.35	0.35
0.3500	0.3800	0.3636	0.47	0.13	0.34	0.36

Table A.2: Statistical, systematic experimental and extrapolation uncertainties of the total cross-section σ_{tot} for all four reconstruction methods.

Source	Subtraction	Local angle	Lattice	Local subtraction
σ_{tot} [mb]	95.35	95.57	95.03	94.98
Statistical uncert.	0.38	0.38	0.33	0.31
ALFA constraints	0.14	0.06	0.01	0.04
MAD-X	0.17	0.12	0.17	0.16
Q scan	0.13	0.14	0.06	0.06
$kQ2$ re-fit	0.04	0.00	0.01	0.13
$kQ5Q6$	0.18	0.14	0.17	0.15
Q misalignment	0.03	0.00	0.03	0.07
$kQ1Q3$ fit	0.16	0.04	0.02	0.07
Station 2	0.24	0.03	0.04	0.06
Distance	0.04	0.01	0.01	0.01
Lever arm	0.05	0.07	0.08	0.05
Vertical offset	0.03	0.09	0.04	0.10
Horizontal offset	0.01	0.03	0.03	0.07
Rotation	0.01	0.00	0.02	0.08
BG norm	0.11	0.03	0.05	0.05
BG shape	0.01	0.10	0.07	0.09
MC resolution	0.03	0.57	0.41	0.42
Physics Model	0.04	0.11	0.14	0.20
Emittance	0.16	0.10	0.09	0.08
Unfolding	0.03	0.09	0.04	0.09
Tracking algo	0.09	0.24	0.17	0.20
Crossing angle	0.07	0.05	0.11	0.12
Beam energy	0.43	0.51	0.43	0.41
Reco eff	0.44	0.46	0.46	0.46
Lumi	1.11	1.11	1.11	1.11
Experimental uncert.	1.25	1.36	1.30	1.30
ρ -parameter	0.08	0.07	0.07	0.07
Fit range	0.36	0.26	0.50	0.33
Coulomb phase	0.01	0.01	0.01	0.01
Form factor	0.01	0.01	0.01	0.01
Extrapolation uncert.	0.37	0.27	0.50	0.33
Total uncert.	1.36	1.44	1.43	1.38

Table A.3: Statistical, systematic experimental and extrapolation uncertainties of the nuclear slope B for all four reconstruction methods.

Source	Subtraction	Local angle	Lattice	Local subtraction
B [GeV ⁻²]	19.73	19.67	19.48	19.48
Statistical uncert.	0.14	0.15	0.14	0.15
ALFA constraints	0.06	0.02	0.00	0.01
MAD-X	0.07	0.04	0.06	0.05
Q scan	0.05	0.06	0.03	0.02
$kQ2$ re-fit	0.01	0.00	0.02	0.04
$kQ5Q6$	0.06	0.06	0.06	0.05
Q misalignment	0.00	0.00	0.01	0.04
$kQ1Q3$ fit	0.06	0.02	0.00	0.02
Station 2	0.06	0.01	0.01	0.01
Distance	0.01	0.01	0.00	0.01
Lever arm	0.01	0.02	0.02	0.02
Vertical offset	0.01	0.03	0.01	0.03
Horizontal offset	0.00	0.02	0.02	0.01
Rotation	0.00	0.01	0.01	0.02
BG norm	0.01	0.04	0.03	0.02
BG shape	0.00	0.04	0.03	0.03
MC resolution	0.01	0.20	0.15	0.15
Physics model	0.01	0.05	0.02	0.01
Emittance	0.05	0.03	0.02	0.01
Unfolding	0.01	0.00	0.01	0.03
Tracking algo	0.00	0.07	0.04	0.05
Crossing angle	0.07	0.02	0.08	0.08
Beam energy	0.19	0.21	0.19	0.18
Experimental uncert.	0.19	0.26	0.22	0.21
ρ -parameter	0.01	0.01	0.01	0.01
Fit range	0.17	0.17	0.26	0.18
Coulomb phase	0.00	0.00	0.00	0.00
Form factor	0.00	0.00	0.00	0.00
Extrapolation uncert.	0.17	0.17	0.26	0.18
Total uncert.	0.29	0.35	0.37	0.31